Structure-function relationships in the aortic valve

Anssari-Benam, Afshin

Structure-Function Relationships in the Aortic Valve

Afshin Anssari-Benam

Submitted for the degree of Doctor of Philosophy,
University of London

School of Engineering and Materials Science
Queen Mary, University of London

2012

Abstract

Globally, heart valve dysfunction constitutes a large portion of the cardiovascular disease load, causing high rates of mortality in European and industrialized countries. This is reflected in the database of the American Heart Association and the UK Valve Registry, showing a progressive increase in the number and age of patients in need of surgical interventions. Aortic valve (AV) dysfunction is significantly more prevalent than pathologies associated with other heart valves, accounting for approximately 43% of all patients having valvular disease. These statistics highlight the essential need for efficient and long term substitutes. However, the two types of replacement valves currently available in practice, i.e. mechanical and bioprosthetic valves, have only an estimated lifetime of around 10 years, after which the associated problems necessitate re-operation in at least 50-60% of the patients. Moreover, for patients under 35, the failure rate is nearly 100% within 5 years of the valve replacement surgery. The significant numbers of patients suffering from AV dysfunction, shortcomings to currently available valve substitutes, and the market demands for replacement valves has prompted increasing interest in the study of AV biomechanics.

A fundamental study of the AV structure-function biomechanics is presented in this thesis. The mechanical behaviour of the AV is characterised at the tissue level, and the associated microstructural mechanisms established. In addition to the experiments, in depth mathematical models are developed and presented, to explain the observed experimental data and elucidate the micromechanics of the AV constituents and their contribution to the tissue behaviour. Tissue-level results indicate that the AV shows 'shear-thinning' behaviour, as well as anisotropic time-dependent characteristics. The microstructural experimental data indicates that there is no direct translation of tissue level mechanical stimuli to the ECM, implying that strain transfer is non-affine. Modelling micro-structural mechanics has confirmed that collagen fibres do not need to become fully straight before they contribute to load bearing, while the elastin network has been shown to contribute to load bearing even at high strains, further exacerbating the non-linear stress-strain relationship of the valve. The structural mechanisms underlying time-dependent behaviour of the tissue can be explained at the fibre level, stemming from fibre sliding and the dissipative effects arising due to fibre-fibre and fibre-matrix frictional interactions, suggesting a unified structural mechanism for both the stress-relaxation and creep phenomena. These outcomes contribute to an improved understanding of the physiological biomechanics of the native AV, and may therefore assist in optimising the design processes for substitute valves and selecting appropriate materials to effectively mimic the native valve function. Understanding AV micromechanics also helps quantify the mechanical environment perceived by the residing cells, which can have significant implications for cell-mediated tissue engineering strategies.

Acknowledgments

I am most grateful to Dr. Hazel Screen, for her supervision and guidance through the course of this work, and her patience when things did not go according to plan! Her door was always open and she would always find time to discuss the results and new ideas. I'm also thankful for the help and support of Dr. Himadri Gupta, his point of views and stimulating discussions during our meetings. I would like to extend my appreciation to Prof. Dan Bader for providing his interesting views and ideas on the methodologies and data. I should also express my gratitude to the UK Engineering & Physical Sciences Research Council (EPSRC), the Discipline Bridging Initiative (DBI), and the Medical Research Council (MRC) for their funding of my research, without which it could not have taken place.

There are a number of people that I owe a debt of gratitude for their encouragement, support and care. My family, to whom my words fall short to express appreciation for all that they have done for me during this time, and to whom I dedicate this work; and my colleagues and friends in Queen Mary, whom created a friendly and an enjoyable working environment. My thanks should go to our lab manager and technician for taking me through and helping me with the lab protocols and procedures, and Mr. Balazs Ihracska for helping me prepare the technical drawings for the biaxial rig. To my colleagues in the lab I extend special thanks for all the good banter during the breaks! and to my friends Dr. Neveen Hosny, Dr. Henry Clarke, Dr. Kirsten Legerlotz, and Dr. Chavaunne Thorpe for being Nev, Henry, Kirsten and Chavaunne.

Finally, delivering this thesis within the three years' time (well, almost!), the volume of the practical and theoretical work that needed to be done, preparation and submission of research papers, and the highs and lows of my personal life have been a complimentary combination to attribute to a less than stress-free three years of my life! If you ever read this thesis and find any parts of it useful, please be sympathetic to my hard work and pain.

Contents

List of Figures

List of Tables

List of Acronyms

Aortic Valve . . . . . AV

Aortic Valve Interstitial Cell . . . . . AVIC

Atomic Force Microscopy . . . . . AFM

Dulbecco's Modified Eagle's Medium . . . . . DMEM

Extracellular Matrix . . . . . ECM

Fibrous Netwrok . . . . . FN

Fluid-Solid Interaction . . . . . FSI

Functional Tissue Engineering . . . . . FTE

Glycosaminoglycan . . . . . GAG

Heat Shock Protein 47 . . . . . HSP47

Numerical Aperture . . . . . NA

Pulmonary Valve . . . . . PV

Pulmonary Valve Interstitial Cell . . . . . PVIC

Small Angle Light Scattering . . . . . SALS

Small Angle X-ray Scattering . . . . . SAXS

Smooth muscle α -Actin . . . . . SMA

Quasi-Linear Viscoelasticity . . . . . QLV

United States National Committee on Biomechanics . . . . . USNCB

Valvular Endothelial Cell . . . . . VEC

Chapter 1

Aortic valve biomechanics: an introduction

1.1. Aortic valve physiology and function

Located between the left ventricle and aorta, the aortic valve (AV) is a cardiac tissue serving essentially as a check valve to prevent retrograde blood flow from the aorta to the left ventricle, in each cardiac cycle [1]. The anatomical position of the AV within the heart is shown in Figure 1.1, along with the other three heart valves: the pulmonary, mitral and tricuspid valves.

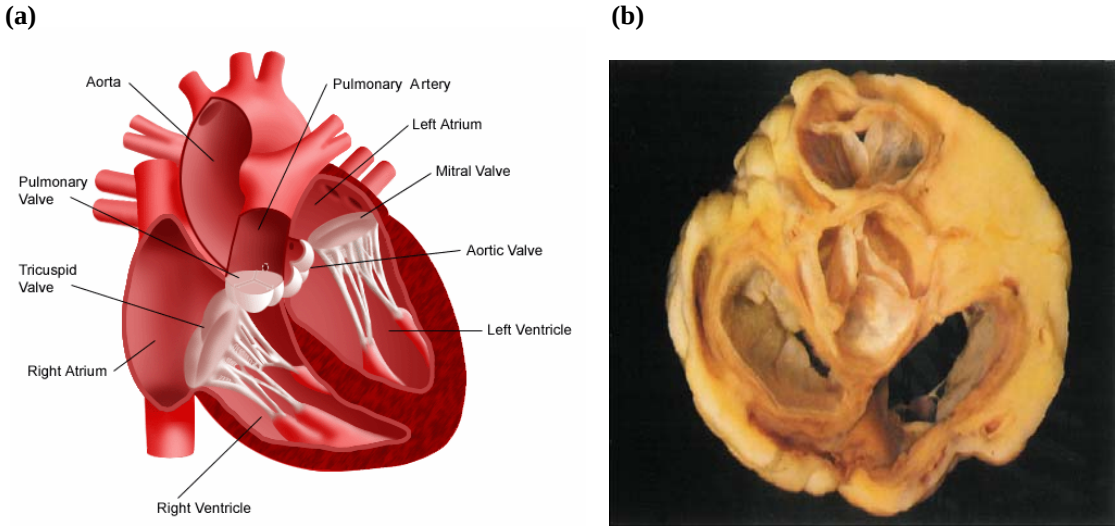

Figure 1.1 (a) Schematic of the anatomy of the heart valves. (b) All four valves lie in the same plane (adapted from [2], with permission).

Similar to the pulmonary valve (PV), the AV is also comprised of three separate leaflets. However, unlike the PV, the AV has coronary ostia[1] behind two of the leaflets in the aortic wall, giving rise to the nomenclature of the three leaflets [2]: right-, left- and non-coronary. The three leaflets are shown in Figure 1.2.

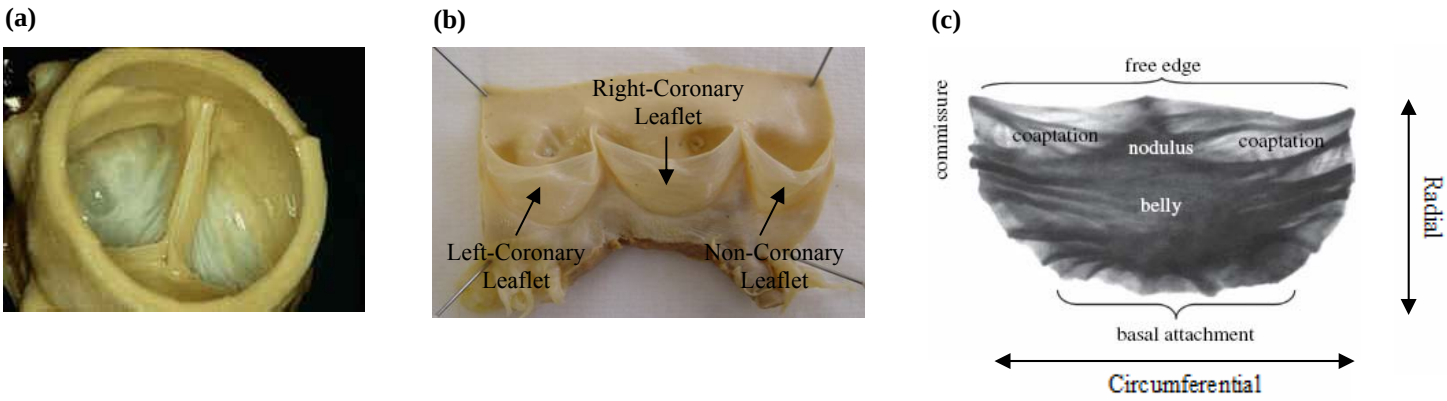

Figure 1.2 (a) AV attached to the aorta at the aortic root, (b) a view of the three leaflets of the AV in a longitudinal cut from the aortic root, (c) definition of the different regions of an AV leaflet, and the loading directions (adapted from [3] , with permission).

[1] The left and right coronary arteries originate at the base of the aorta from openings called the coronary ostia.

The AV is a passive cardiac structure, i.e. its opening and closure is controlled by the surrounding haemodynamic environment, driven by the change in cardiac pressure during each cycle [3]. The patterns of cardiac pressure waves within a cycle are shown in Figure 1.3.

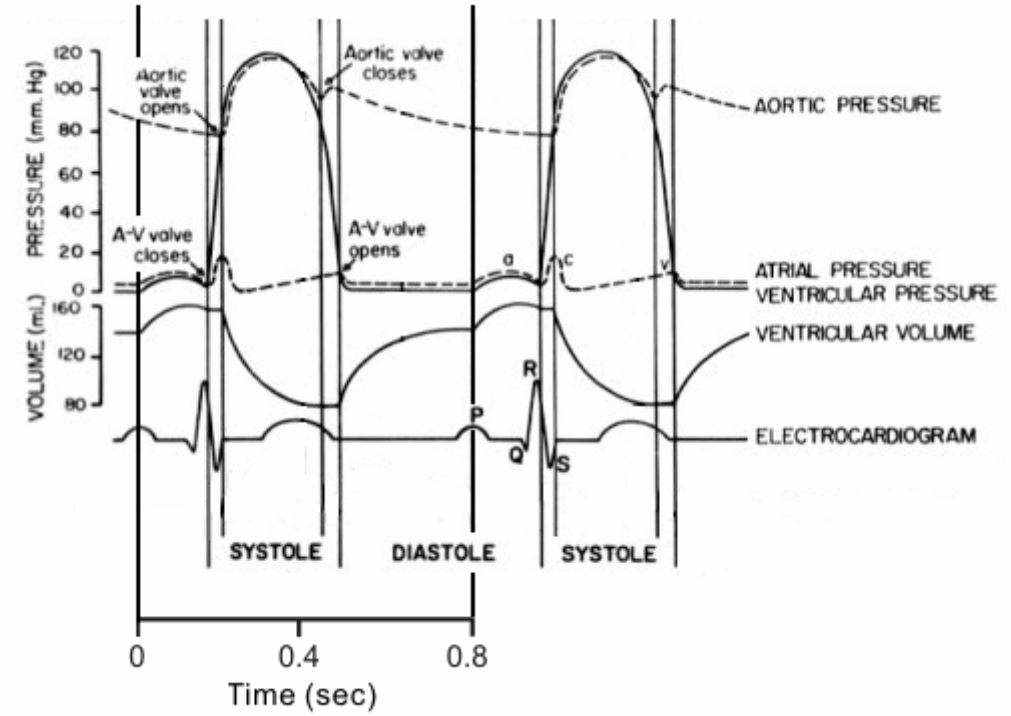

Figure 1.3 Cardiac pressure waves in each cycle. Each cycle is 0.8 s (adapted from [4]).

The AV opens in the systolic phase[1] of a cardiac cycle (Figure 1.4a), when the left ventricle contracts and ejects blood to the aorta. In healthy individuals, the blood flowing through the AV accelerates to a peak value of 1.35 ± 0.35 ms^{-1} [3]. The normal physiological transvalvular pressure on the AV is 80 mmHg at rest, 8-times higher than the other tri-leaflet valve, the PV [4]. Closure of the AV starts at the end-systolic phase, as the ventricle relaxes (Figure 1.4a). When closed, the free edges of the three leaflets coapt to prohibit back flow of blood to the ventricle. The leaflets are attached to the aortic wall at the 'basal attachment' (Figure 1.2). In such haemodynamic conditions, the opening and closure of the AV takes place over a time period of around 50 ms [3,5,6], during which the leaflets experience flexural bending that results in axial *in vivo* strains of approximately 10.1% and 30.8%, in the

[1] Systole is the phase of the cardiac cycle during which the left ventricle contracts. Conversely, diastole referred to the cardiac phase when the ventricle is relaxing and is filling with blood.

circumferential and radial directions, respectively [7,8]. A typical strain waveform experienced by the valve *in vivo* is presented in Figure 1.4b. The *in vivo* strain rates have been reported to be 440% ± 80% s^{-1} in the circumferential, and 1240% ± 160% s^{-1} in the radial direction [7,8], generating overall typical stresses in the range of 250-400 kPa *in vivo* [1,9]. The typical definitions for loading directions of leaflets are depicted in Figure 1.2 c.

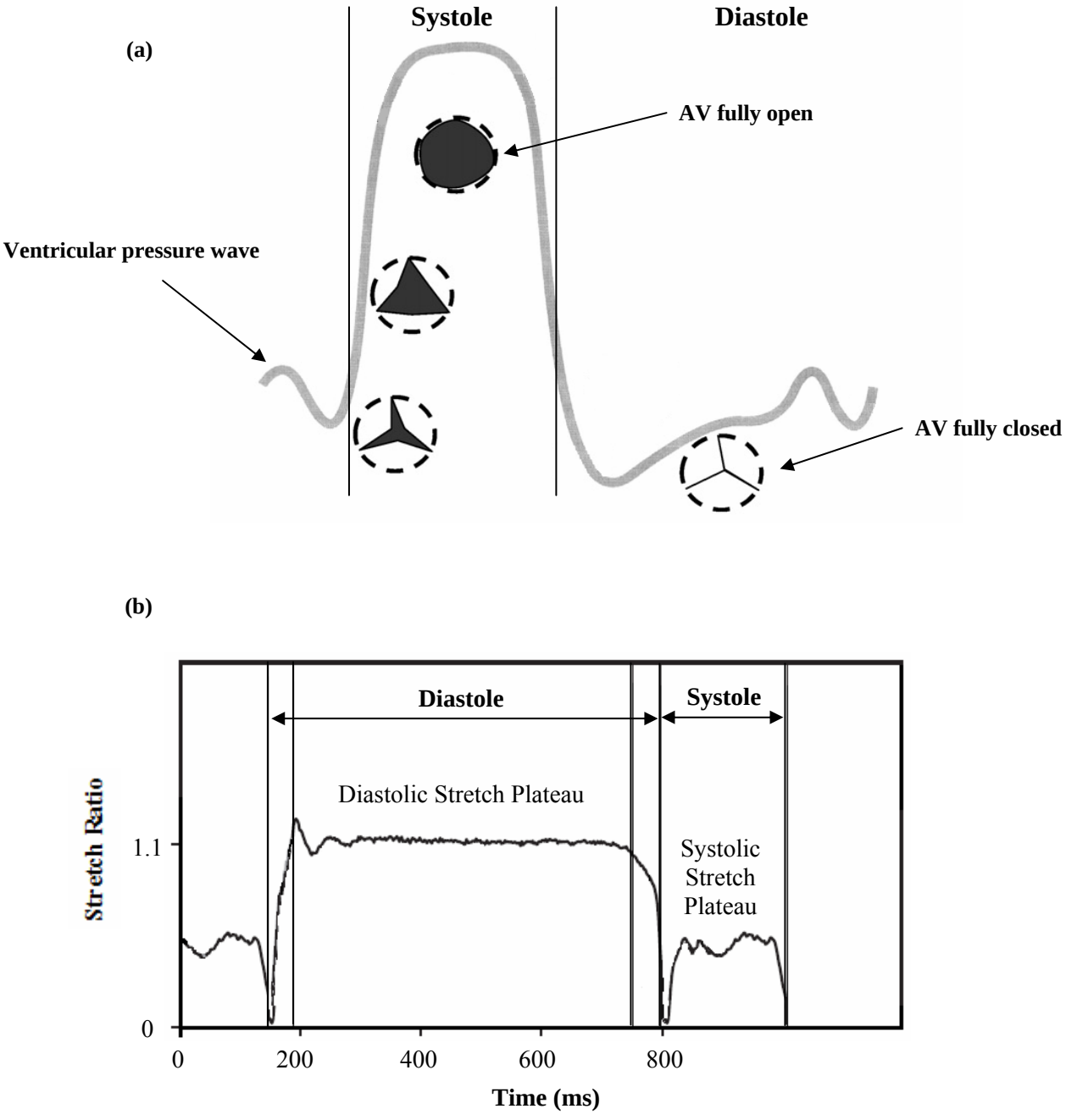

Figure 1.4 Functional and biomechanical characteristics of the AV: (a) opening and closure of the AV in relation to the ventricular pressure wave (adapted from [10], with permission), (b) a typical strain waveform of AV leaflet in a cardiac cycle in the circumferential direction (adapted from [11], with permission).

A normal functioning AV in a healthy human heart experiences around 40 million cardiac cycles per year, resulting to a total of 3×10^9 cycles in a lifetime [1]. Functioning under such repetitive and challenging haemodynamic loading conditions requires unique tissue properties and mechanical characteristics. To effectively meet its physiological and functional requirements, the AV has evolved into a complex and highly specialized tri-layered structure, able to accommodate repetitive and large strains throughout the cardiac cycle, and provide effective stress endurance within the tissue. The three morphologically distinct layers within the valve are termed the fibrosa, spongiosa and ventricularis [12].

The fibrosa is the thickest of the three layers, at approximately 317.1 μm [1], and faces the aorta. It is predominantly composed of circumferentially aligned, macroscopically crimped and densely packed type I collagen fibres [13], schematically shown in Figure 1.5. Owing to its high collagen fibre content, it is also the strongest and stiffest layer of the valve, functioning to endure high stresses and prevent excessive stretching of the valve in the systolic phase [14,15].

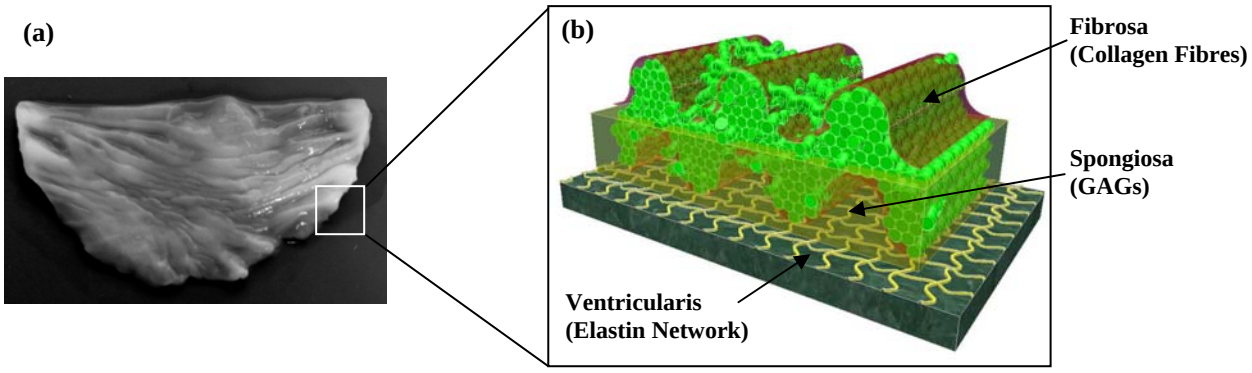

Figure 1.5 (a) intact AV leaflet, (b) schematic diagram of the layers of the AV leaflet (redrawn from [16]).

The centrally located spongiosa layer primarily contains glycosaminoglycans (GAGs), with a loosely arranged collagen fibre structure coupling it to the two outer layers of the valve [1,15]. The spongiosa layer is known to act as a damper, to reduce the impact created by sudden changes in pressure gradient in the transition from the end of the diastolic phase into the systole phase. It allows for relative movement between the other two valve layers as the valve opens and closes by enabling internal shearing [13,17,18].

As the name implies, the ventricularis layer faces the left ventricle chamber, and has a mean thickness of 158.2 μm [1]. It is mainly composed of elastin, present in the layer as a network of elastic fibres which are radially aligned [13]. The elastin network in this layer is thought to function as a 'return-spring mechanism', to restore the contracted configuration of the valve leaflet after the stretch induced in the diastolic phase of the cardiac cycle [19,20]. The ventricularis also contains some collagen fibres, but these are more sparse than in the fibrosa. However, the fibrous components of this layer enable the ventricularis to contribute to load bearing in the valve at low tissue strains and stresses.

Throughout the three layers of the valve extracellular matrix (ECM), there resides a heterogeneous population of cells known as the aortic valve interstitial cells (AVICs) [21-24]. The AVIC population consists of at least two distinct, but dynamic and interchangeable, phenotypes of cells: myofibroblasts and smooth muscle cells [15,22]. The distribution of the different phenotypes within the three layers remains unclear, with some studies indicating a random organisation of AVICs throughout the matrix [3]; whilst others suggest that myofibroblasts are predominantly located within the fibrosa [15]. However, it is believed that the phenotypic state of the AVICs at any time is likely related to the remodelling demands of the tissue, with studies showing that when the phenotype of the resident AVICs is 'myo-like', the cells are actively remodelling the ECM [25]. Figure 1.6 shows a confocal microscopy image of the cells.

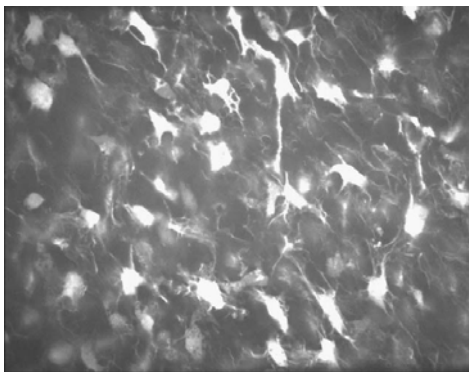

Figure 1.6 A confocal microscopy image of porcine AVICs stained with calcein AM (adapted from [24], with permission).

Also found within the AV are the valvular endothelial cells (VECs), which are morphologically different from the arterial endothelial cells [26,27]. They sheath the

surface of the AV leaflets, to create a non-thrombogenic interfacing surface between the cusp and the blood, allowing for transport of nutrients [22,27]. VECs are circumferentially aligned on the leaflet surface, perpendicular to the direction of blood flow [28]. Dysfunction of these cells has been linked to a number of disorders such as thrombosis and inflammation [29].

1.2. Aortic valve dysfunction and aetiology

Globally, heart valve dysfunction constitutes a large portion of the cardiovascular disease load, causing a high incidence of mortality in European and industrialized countries. This is reflected in the database of the American Heart Association and the UK Valve Registry, showing a progressive increase in the number and age of patients in need of surgical interventions [30,31]. AV dysfunction is significantly more prevalent than pathologies associated with other heart valves, accounting for approximately 43% of all patients with valvular disease, and resulting in higher mortality rates [30].

In a broad classification, there are two types of AV disease: congenital or acquired [32]. Congenital disease is an abnormality that develops before birth, and may result in improper valve size, malformed leaflets, or an irregularity in the way that the leaflets are attached [32]. The most common congenital defect is ‘bicuspid’ AV disease, where instead of the normal three leaflets, the bicuspid AV has only two. This defect is common worldwide, with a reported occurrence rate of 13.7 per 1000 people in industrialized countries such as the US [30]. It may not require immediate treatment in the infancy, but causes complications in the haemodynamics conditions later in the adulthood, requiring surgical intervention and valve replacements [30].

Acquired diseases are the AV pathologies that develop within the valve over time. These are typically referred to as age-related degenerative valve diseases. These AV diseases develop in an escalating fashion after the age of 65, with approximately 50% of the population having some form of acquired AV disease by the age of 85 [33]. The main acquired pathologies are valve calcification, stenosis and regurgitation [3,33]. It has been hypothesised that the main cause of these diseases is increasing

stiffness of the AV, which occurs as the AVIC-mediated tissue remodelling becomes disordered with age [33].

Aortic calcification, also known as aortic sclerosis, is a build-up of calcium deposits on the AV leaflets. It is thought to occur as a result of AV stiffening with age, which will result in the VECs on the surface of the leaflets being exposed to higher loading levels in each cardiac cycle, causing damage to the cell's membrane, and eventually haemolysis. Calcium is generally present in the solution surrounding the cells, since the membrane of healthy cells pump calcium ions out. However when cells become damaged, the phosphorus which is highly concentrated in the cell membrane will react with those calcium ions, forming calcium phosphate crystals that can deposit on the leaflets [34]. Over time, the calcium deposits thicken and cause narrowing at the opening of the aortic valve. This narrowing is referred to as aortic stenosis. This impairs blood flow through the valve, causing chest pain or a heart attack. Figure 1.7 shows a severely calcified AV.

Figure 1.7 Calcified AV leaflets.

Aortic valve regurgitation, also known as aortic insufficiency or aortic incompetence, is a condition that occurs owing to malcoaptation of the AV leaflets during valve closure, meaning that the AV does not close tightly, as shown in Figure 1.8. In this condition, some of the blood that was pumped out of the heart leaks back into the left ventricle. The malcoaptation of the valve occurs because the elastin network responsible for the elastic recoil of the normal valve, is no longer able to fully return the leaflets to their closed position because of the increase in the tissue stiffness with age.

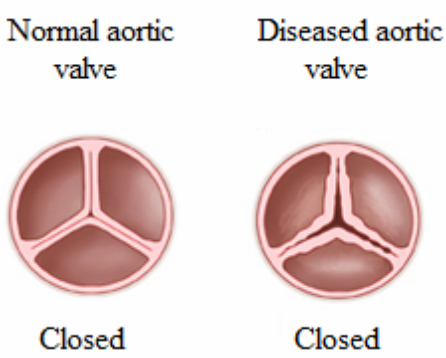

Figure 1.8 Schematic of diseased aortic valve with regurgitation.

The most common treatment for end stage valvular pathologies described above is surgical replacement of the native valve with a substitute. It is estimated that over 300,000 valves are replaced worldwide per year, creating a market turnover of $1 billion [16]. In practice, there are two types of replacement valves available to the patients: (1) mechanical valves; and (2) bioprosthetic valves.

The mechanical valves are available in different designs, however the 'ball and cage', the 'tilting disc' and the 'occluder leaflets' are the most commonly used [35]. An example of each of these replacements is shown in Figure 1.9. Mechanical valves are characterized by their good durability. However, they are associated with substantial risk of systemic thromboemboli and thrombotic occlusion, largely owing to their non-physiologic surfaces or the haemodynamic abnormalities created by their function as rigid occluders [13]. To minimise this risk, chronic anticoagulation therapy is required in all mechanical valve recipients. However, systemic anticoagulation renders patients vulnerable to potentially serious hemorrhagic complications. Thus, the combined risk of thromboembolic complications and hemorrhage remains the main disadvantages of mechanical prosthetic valves [13].

Bioprosthetic valves are made of chemically treated animal or human valvular tissue. There are three common types of bioprosthetic valves commercially available: (1) porcine xenograft valves, (2) bovine pericardial valves, and (3) allograft or homograft valves.

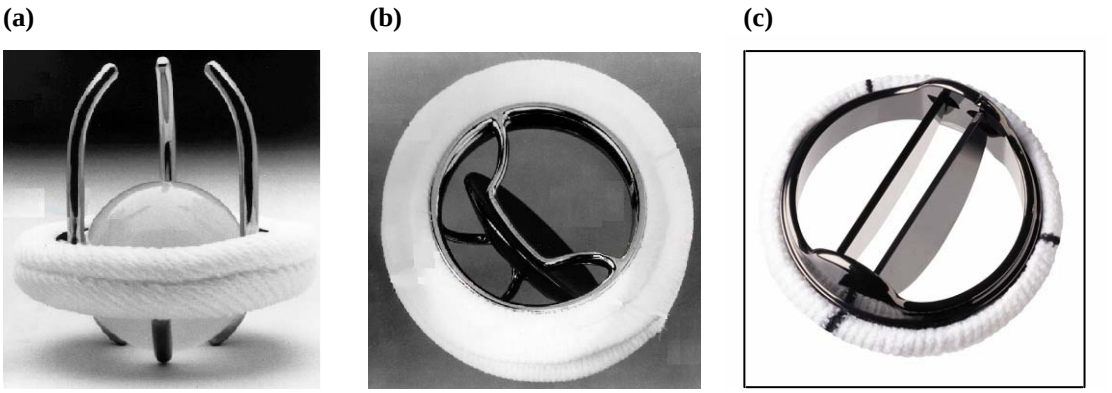

Figure 1.9 Mechanical valves: (a) ball and cage, (b) tilting disc, and (c) occluder leaflets.

The porcine xenograft valve consists of an intact pig aortic valve that is preserved in low-concentration glutaraldehyde solution [16]. The bovine pericardial valve is fabricated from three separate pieces of glutaraldehyde-treated calf pericardium, affixed to a supporting stent and sewing cuff, in a configuration similar to that of the porcine xenograft. Both the porcine and bovine valve tissues are cross-linked in low concentrations of glutaraldehyde to reduce their antigenicity and to stabilize the tissue against the proteolytic degradation that would otherwise occur following implantation into the recipient. Both types of valves are also treated with various other chemical agents to minimize their propensity to calcify over the duration of implantation and hence improve their longevity [34]. The homograft valves are intact human valves obtained from organ and tissue donors, usually stored cryopreserved as entire aortic root, and trimmed to size and shape before implantation in the recipient [16]. Figure 1.10 shows the three types of bioprosthetic valve.

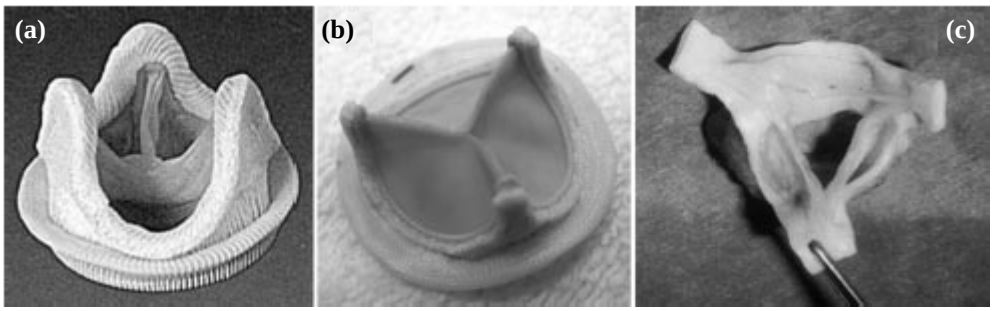

Figure 1.10 Images of a porcine bioprosthetic valve: (a) porcine xenograft, (b) bovine pericardial valve, and (c) a human aortic valve allograft, also known as a homograft (adapted from [16], with permission).

It is estimated that 50% to 55% of the replacement valves in recipients are mechanical and the rest are bioprosthetic [35]. In all cases, the estimated lifetime of a valve replacement is around 10 years, after which the associated problems necessitate re-operation in at least 50-60% of patients [13]. Moreover, for patients under 35, the failure rate is nearly 100% within 5 years of valve replacement surgery [35]. The rates of failure associated with the mechanical and bioprostheses valves are similar overall. Four categories of complications are commonly evident: (a) thromboembolism, thrombosis, and anticoagulation-related hemorrhage; (b) prosthetic valve endocarditis (infection); (c) structural dysfunction, i.e. failure or degeneration of the prosthesis biomaterials; and (d) non-structural dysfunction, i.e. a diverse array of complications which includes tissue overgrowth, paravalvular leak, hemolysis, and other extrinsic interactions of host tissues with a valve [36,37].

As a living alternative to the current substitutes, tissue-engineered heart valves attempt to overcome the limitations of the mechanical and bioprosthetic valves. The patient's own cells, isolated and expanded using standard cell culture techniques are seeded onto an appropriate carrier, termed the scaffold, manufactured in the shape of a heart valve. Subsequent stimulation, transmitted via the culture medium (biological stimuli) or via physiological loading (mechanical stimuli), promotes tissue development. In addition to biocompatibility, biodegradability and reproducibility, the scaffolds ideally possess appropriate cell adhesion and mechanical properties, matched to the native tissue [16]. The key vision of tissue-engineered valves is to develop a living implant, with the potential to grow and last a lifetime, rather than using external devices implanted inside the heart with numerous associated complications. However, to date it seems that "tissue engineering has promised much more than it has delivered" [16], and there has yet to be a successful clinical implantation of a tissue engineered valve.

The significant numbers of patients suffering from AV dysfunctions, shortcomings to all currently available valve substitutes [33,38], and the market demands for replacement valves [16] makes this a financially beneficial area of research, and has prompted increasing interest in the study of AV biomechanics. By studying the material properties and mechanical behaviour of the native AV, researchers have tried to create a platform to better understand the function of the valve under physiological

conditions, the causes associated with its pathology, and to design more successful tissue-engineering strategies. The literature related to AV biomechanics will be reviewed in the following section.

1.3. Aortic valve biomechanics

The biomechanics of the AV has been typically studied in three different capacities, with studies focused on [3,32]: (i) the valve-blood dynamic interactions, to understand the local haemodynamic environment and the loads exerted on the AV cusps by the blood flow at the organ level, (ii) the mechanical behaviour of the AV tissue, to understand its characteristic and properties at a tissue level, and (iii) the characterisation of the AVICs mechanical behaviour and properties, to understand their response to the applied loads and its relevance to their function, at a cellular level.

1.3.1. AV-Blood dynamic interactions

As discussed earlier, the mechanical function of the native AV is dictated by the surrounding haemodynamic environment, which controls the opening and closure of the valve. Mechanical loads arising from the haemodynamics at the organ level are transferred to the tissue and its cellular components. Thus understanding the interactions between the AV and the exerted haemodynamic forces is a key step towards characterising the mechanical environment of the AV under physiological conditions.

Different approaches have been adopted to investigate valve-blood dynamic interactions. The initial pioneering attempts employed fluoroscopy imaging techniques to monitor the dynamic AV function *in vivo* [7,8,39]. These experiments involved lead radiopaque markers sutured directly onto the valve leaflets. Using the mid-diastole configuration of the markers as the reference, the displacement of the circumferentially and radially oriented markers was measured. The results showed *in vivo* strains of 10.1% and 30.8% in the circumferential and radial directions,

respectively. The corresponding strain rates were also calculated to be 440%±80% s^{-1} circumferentially, and 1240%±160% radailly. More recent studies have used a more advanced biplane X-ray imaging technique to monitor AV movement *in vivo* [40]. Similar strain data was calculated, but images also revealed complex motion patterns of the valve in each cardiac cycle suggesting non-uniform valvular surface strains *in vivo* [40]. However, due to the insufficient imaging resolution and limitations in the number of the surface markers used, more detailed areal strain distribution measurements within the AV leaflets *in vivo* has not been possible [3].

Another approach to investigate the valve-blood dynamic interactions has been to use *in vitro* flow visualisation techniques [3]. Employing this technique, investigators have carried out flow measurements under different degrees of aortic valve stenosis *in vitro* [41]. Under physiological conditions of 70 heart beats per minute, systolic phase duration of 300 ms and mean aortic pressure of 90-100 mmHg, the results have shown that the blood ejects from the valve as a stream jet, in which the diameter of the jet decreases as the degree of stenosis increases. Moreover, using laser Doppler anemometry measurements, the jet flow velocity in the stenotic valve was measured to be 7.0 ms^{-1} at peak systolic phase, compared to 1.2 ms^{-1} for a normal valve [41]. The higher levels of jet velocity would elevate the turbulence and levels of shear stress downstream of the stenotic valve, potentially leading to damage to the cellular components of both the blood and the AV.

The highly dynamic motion of the AV leaflets, complex patterns of the haemodynamic forces, and the problems associated with the number of surface markers and resolution of the imaging techniques make the *in vivo* imaging of the AV leaflets very challenging and limits the capacity for more detailed analysis [32]. Computational models using finite element and fluid-solid interaction (FSI) analysis have been the popular alternative to investigate the heart valve-blood dynamic interactions, employed to calculate the stress distribution on the leaflets of native and bioprosthetic valves [42-45]. In such analysis, the fluid domain is described using an Eulerian reference frame, i.e. the fluid moves through a fixed mesh network, and the leaflet as the solid domain is described by Lagrangian formulation, i.e. the mesh moves together with the leaflet. For the complete simulation of AV function, the effects of blood flow are coupled to the deforming status of the AV leaflet. That is, at

every time step, the current location of the valve leaflet is described on the Cartesian grid. Based on the current conditions, the flow field is computed, incorporating the leaflet velocity at the previous time step as a boundary condition. The pressure and stress in the fluid are computed at the leaflet interface and are used as boundary conditions on the leaflet FE mesh. The leaflet deforms accordingly, and this deformation is fed to the fluid and the computation continues.

Different studies have developed and used different numerical techniques to couple the fluid and solid fields. Summarizing their findings, it has been established that:

- The stress, and accordingly the strain, distribution in AV leaflets upon opening and closure in each cardiac cycle is non-homogenous, with the belly region possessing higher values, reducing towards the commissure [46-49].

- Leaflets cycle between the fully unloaded to fully loaded state in every cardiac cycle, unlike some connective tissues that remain preloaded [50,51].

- Leaflets experience large, anisotropic strains in response to the transvalvular pressure gradient [46,50].

- Corresponding tension levels have been calculated to be in the range of 50-100 N/m at peak loading, with strain rates reaching 1000% s^{-1} [46-50].

- The collagen fibre architecture within the AV remodels according to the stress map of the leaflets [47-49].

- The mechanical properties of the aortic root at the annular ring highly influence the deformation of the AV leaflets [46,51].

1.3.2. Mechanical behaviour of the AV tissue

To achieve reliable modelling results, it is imperative to incorporate accurate material properties and mechanical characteristics of the modelled tissue into the computational models. As such, characterising the mechanical properties of the native AV is the necessary first step for both modelling the AV's haemodynamic environment, and the successful design of replacement valves that would closely

mimic the native valve's characteristics. This has been another area of interest concerning biomechanics of the AV. Studies in this area have been mainly performed using quasi-static uniaxial and biaxial loading protocols, as well as time-dependant loading regimes manifested by creep and stress-relaxation phenomena.

Quasi-static uniaxial tests

The initial attempts to characterise AV leaflet mechanics were carried out in the early 70's, utilizing quasi-static uniaxial tensile tests performed on fresh and frozen human AVs, and reporting a marked anisotropy in the mechanical behaviour of the tissue [52]. The samples withstood large deformations in the radial direction, whilst showing less extensibility and higher stiffness circumferentially [52]. Missirlis and Chong (1978) looked further at variations in strain across porcine AV samples, imaging the movement of ink marks along circumferential and radial strips of porcine AV leaflets under uniaxial strain, schematically shown in Figure 1.11 [53]. Their results confirmed the anisotropy of the tissue properties reported in [52], but also demonstrated that the middle section was the stiffest, particularly in the radial direction [53]. The samples were stretched at 2mm/min, which corresponded to strain rates of 20-45%/min for the radial strips and 14-21%/min for the circumferential strips. Although a clear failure point was not shown in their study, they reported that the radial samples sustained strains of 60% to 100%, compared to strains of 30% to 36% for circumferential samples.

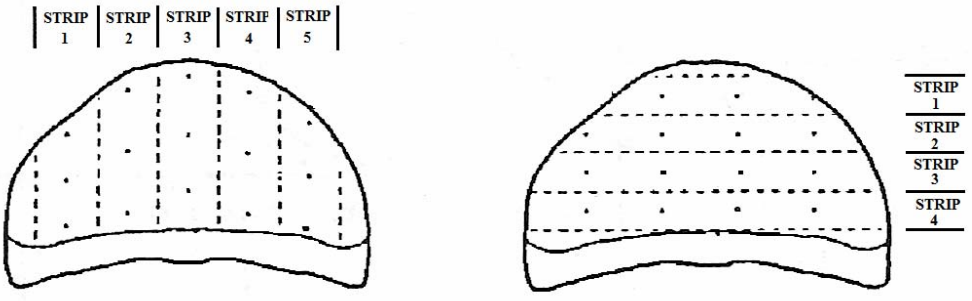

Figure 1.11 Schematic presentation of the AV leaflet, and the strips cut radially and circumferentially. The dots represent the ink-marks put on each strip. Strip 3 in each direction was reported to be stiffer than the other strips (redrawn from [53]).

In a follow on study, Chong and Missirlis (1978) presented a model of stress analysis in the AV tissue under deformation, where they incorporated a modified form of the thin membrane stress theory for a homogeneous linearly elastic and orthotropic lamina, based on Hooke's law [54]. This was the first attempt to propose a mathematical model to characterise the stress-strain behaviour of the AV tissue.

Further studies of these types have been carried out thereafter, employing uniaxial stretch tests to characterise the stress-strain relationship in the AV tissue, in both circumferential and radial loading directions. Studies performed by Sauren et al (1983) [5], Rousseau et al (1983) [55] and Mavrilas and Missirlis (1991) [6] are amongst the pioneering and most cited of such studies. The stress-strain curves in these studies have often been divided into three regions, namely pre-transition, transition and post-transition regions [5]. The definition of each region in a typical AV stress-strain curve is shown in Figure 1.12, adapted from [6].

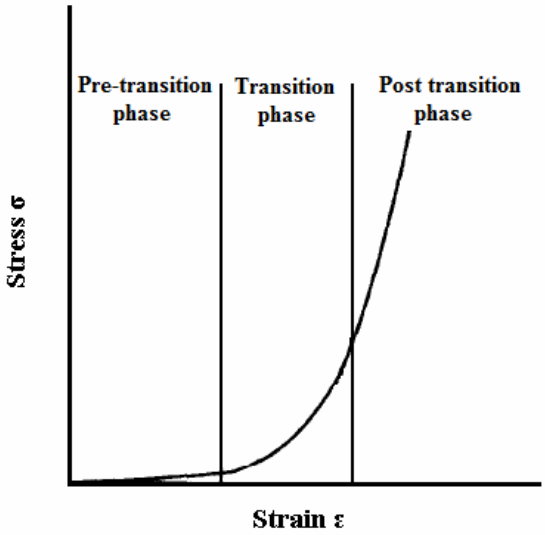

Figure 1.12 The three defined regions in the stress-strain curve of the AV leaflets (adapted from [6], with permission).

The observed non-linear stress-strain curve, manifested in the three defined regions, has been attributed to the structural re-organization of the ECM. The key ECM component is thought to be the collagen fibres, and their reorientation and reorganisation has been studied using light microscopy [56] and Scanning Electron Microscopy [57-59]. In the pre-transition phase, the collagen fibres are thought to be mainly crimped with negligible contribution to the load bearing mechanism of the

tissue [5,56]. The transmission of tensile force is thus provided mainly by the elastin component [5], hence the tissue behaviour is compliant in this phase. In the following transition phase, more collagen fibres gradually become recruited with the increasing applied load. As they are recruited, they become oriented in the loading direction and gradually become straight; increasingly contributing to stress transmission and the stiffening of the tissue. By the post transition phase, the collagen fibres have become predominantly aligned and uncrimped, acting as the main load bearing element of the tissue, and resulting in this phase to posses the highest stiffness [5].

The post transitional phase has generally been assumed to be linear and elastic. As such, the gradient of the line in this region has been typically used to calculate the elastic modulus. Table 1.1 summarizes the mechanical characteristics of the AV reported in the four above mentioned studies.

Under uniaxial loading conditions, there are also a few studies that have specifically investigated the effects of strain rate on the behaviour and the mechanical properties of the AV leaflet. Sauren et al (1983) is an example of one such study. The reported data are given in Table 1.1. The strain rate dependency of the mechanical properties of AV does not appear to follow a clear trend, as comparing the values in the table hardly concludes any consistant trends for the effect of strain rate on the reported values of maximum stress and strain, and E. The variation in the data provided in Table 1.1 further indicates that test conditions may drastically influence the observed mechanical behaviour of the AV and its reported properties. Factors such as loading protocols, gripping methods, sample geometry and pre-conditioning of the samples may all contribute to the variation of the results, as they are generally lab-specific.

Table 1.1 Reported mechanical properties of the AV samples, obtained from uniaxial loading tests, for different sample sizes and various loading rates. The values show a wide variation of data available concerning the mechanical properties of the AV tissue, specifically the elastic modulus.

Authors	Orientation	Strain Rate	Sample Size	E	Max. Reported Strain	Max. Reported Stress
Missirlis and Chong, 1978 [53]	Circumferential	2 mm/min	10 x 2 mm	3.35 MPa	~ 30-36%	~ 0.15 MPa
	Radial		6 x 2.4 mm	1.09 MPa	~ 70-100%	~ 0.12 MPa
Sauren et al 1983 [5]	Circumferential	0.069 s^{-1}	10 to 20 x 3 mm	~28 MPa	~ 7%	~ 0.8 MPa
		0.8 s^{-1}			~ 10%	~ 0.6 MPa
		0.08 s^{-1}			~ 10%	~ 0.5 MPa
	Radial	0.008 s^{-1}		---	~ 10%	~ 0.4 MPa
		3.2 s^{-1}		1.33 MPa	~ 12%	~ 0.07 MPa
Rousseau et al 1983 [55]	Circumferential	10 mms^{-1}	3 mm Wide	6.60 MPa	~ 10%	~ 0.3 MPa
Mavrilas and Missirlis 1991 [6]	Circumferential	2-3 s^{-1}	3 mm Wide	7.78 MPa	~ 25%	~ 1.5 MPa
	Radial			1.28 MPa	~ 22%	~ 0.2 MPa

As described in section 1.2, bioprosthetic valves obtained from porcine or bovine AV leaflets are often fixed in low-concentration glutaraldehyde solution to reduce their antigenicity [34,37]. Establishing the influence of fixation on the mechanical behaviour of the valves has also been the subject of a number of studies. Some of the most cited contributions include Broom and Thompson (1979) [60] and Rousseau et al (1983) [55], comparing the behaviour of fresh and fixed AV tissues. Results showed that the preserved tissues were stiffer (Figure 1.13), and withstood higher stresses but only extended to low strains [55,60].

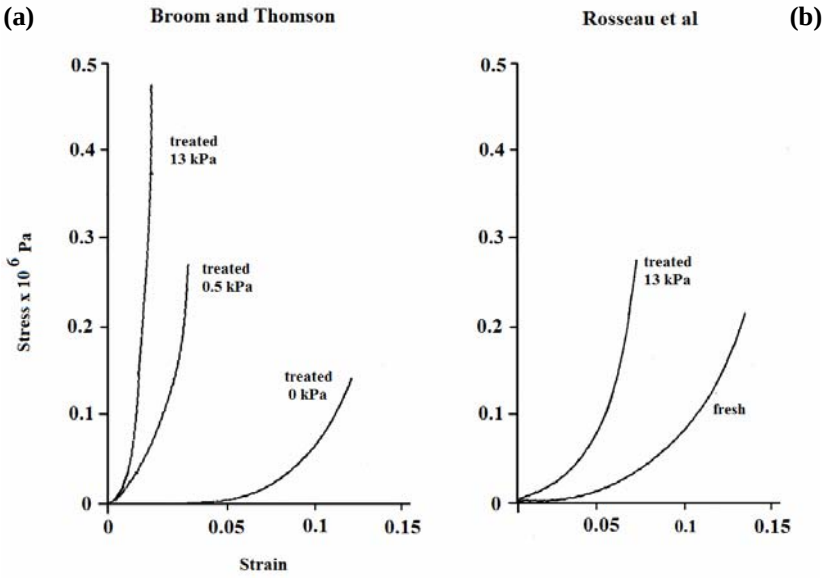

Figure 1.13 Stress-strain curves obtained by (a): Broom and Thompson (1979) [60], and (b) Rousseau et al (1983) [55]. The graphs show the results for circumferentially loaded samples (adapted from the indicated references with permission).

The increase in stiffness in preserved AV tissues has been attributed to the structural changes that occur due to the fixation, specifically the increased number of stable crosslinks between collagen fibrils. These are thought to decrease the compliance of the tissue structure by preventing relative movement between collagen fibres [55,60]. The effects of fixation pressure were also investigated in these studies, by applying a hydrostatic pressure of glutaraldehyde solution on the samples during fixation. Results showed that the stiffness of the samples was further increased by an increase in fixation pressure (Figure 1.13). Both studies have used circumferentially cut samples and have suggested the increasing alignment of collagen fibres with increasing fixation pressure as the cause for the stiffer behaviour of the samples at higher fixation pressures.

In another study of this type, Mavrilas and Missirlis 1991 performed the fixation process on radially cut strips from AV leaflets [6]. Interestingly, they reported an inverse influence of fixation, as their results showed that the radially fixed samples were more compliant, undergoing larger strains for lower stresses [6]. The reported graph is shown in Figure 1.14.

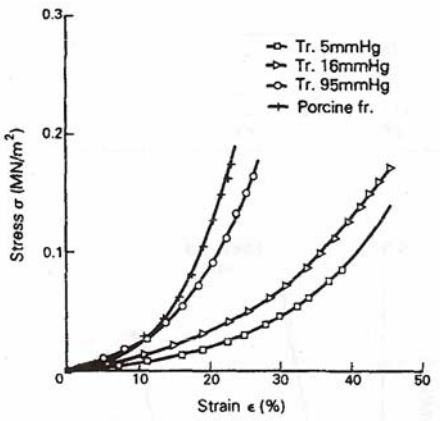

Figure 1.14 Representative stress-strain diagrams of radially cut strips from fresh and fixed porcine AV leaflets in different fixation pressures, as reported in [6] (adapted with permission).

More recent uniaxial studies regarding the mechanical behaviour of the AV tissue have attempted to investigate the structural reorganisation of the ECM under tensile deformation. Scott and Vesely (1995) focused on the reorganization of collagen fibres in the AV, performing a histological analysis of samples fixed under varying degrees of uniaxial tension [19]. They observed that the waviness of the collagen fibres allowed the structure to strain to approximately 17%, before the fibres become straightened and loaded. In addition, macroscopic crimping of collagen fibre bundles visible in the fibrosa layer allowed additional strains of up to approximately 23%, and the collagen fibre reorientation facilitated even larger deformations. Based on their study, they proposed that the collageneous structure of the AV leaflet tissue could undergo strains of nearly 40% without permanent deformation. They also proposed that the mechanism that returned the collagen fibre structure to its rest geometry when unloaded was the surrounding elastin matrix, which interconnects the collagen fibres and provides them with a return spring mechanism. A schematic of their model is presented in Figure 1.15.

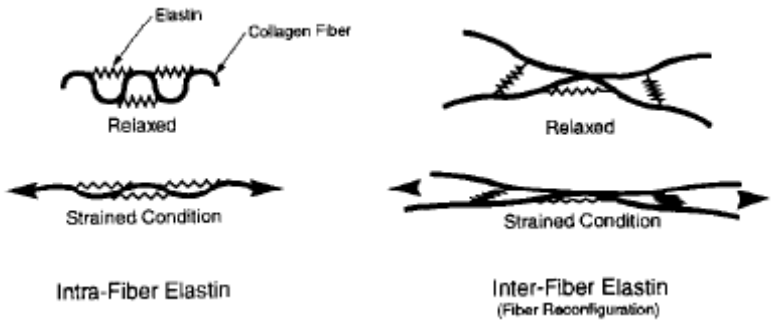

Figure 1.15 Collagen and elastin linkage model proposed in [19] (adapted with permission). Elastin may act as a return spring through one or both of the possible mechanisms shown. lntrafibre elastin would help return collagen fibres to their natural wavy state during unloading. Interfibre connections may act to return the collagen bundles to their crimped state when relaxed.

In this model, elastic springs run from one collagen crimp to the next. As the tissue is initially stretched, the elastin undergoes tension while the collagen develops small bending forces as the bundles straighten. Once straight, the stiff collagen fibres take up a larger proportion of the load in tension. When the load is released, the elastin acts to return the collagen to its undeformed geometry [19].

Vesely (1998) was the first to quantify the role of elastin in AV mechanics, by attempting to digest all ECM components except elastin, and assessing the subsequent changes in AV mechanical behaviour [20]. The tissue samples were digested in 0.1 N NaOH at 75 °C, after which loading tests were performed in both the circumferential and radial directions. In addition to whole valve tests, tensile tests on the individual layers of fibrosa and vetricularis were also carried out. The overall results are shown in the graphs of Figure 1.16. These data indicate that elastin is the main load bearing element in the ventricularis when stretched in the radial direction. By contrast, elastin plays a minor role in the fibrosa, under both radial and circumferential load. It was concluded that the aortic valve elastin: (i) has a minimal contribution to mechanics in the fibrosa layer; (ii) participates equally with collagen during the initial (pre-transition phase) stretching of the ventricularis circumferentially; and (iii) can totally dominate the mechanics in the radial ventricularis. Hence, whilst elastin is a relatively small structural component of the AV (the valve cusps contain about 50% collagen and only 13% elastin by dry weight), it could have a notable contribution to the mechanical behaviour of the whole leaflet.

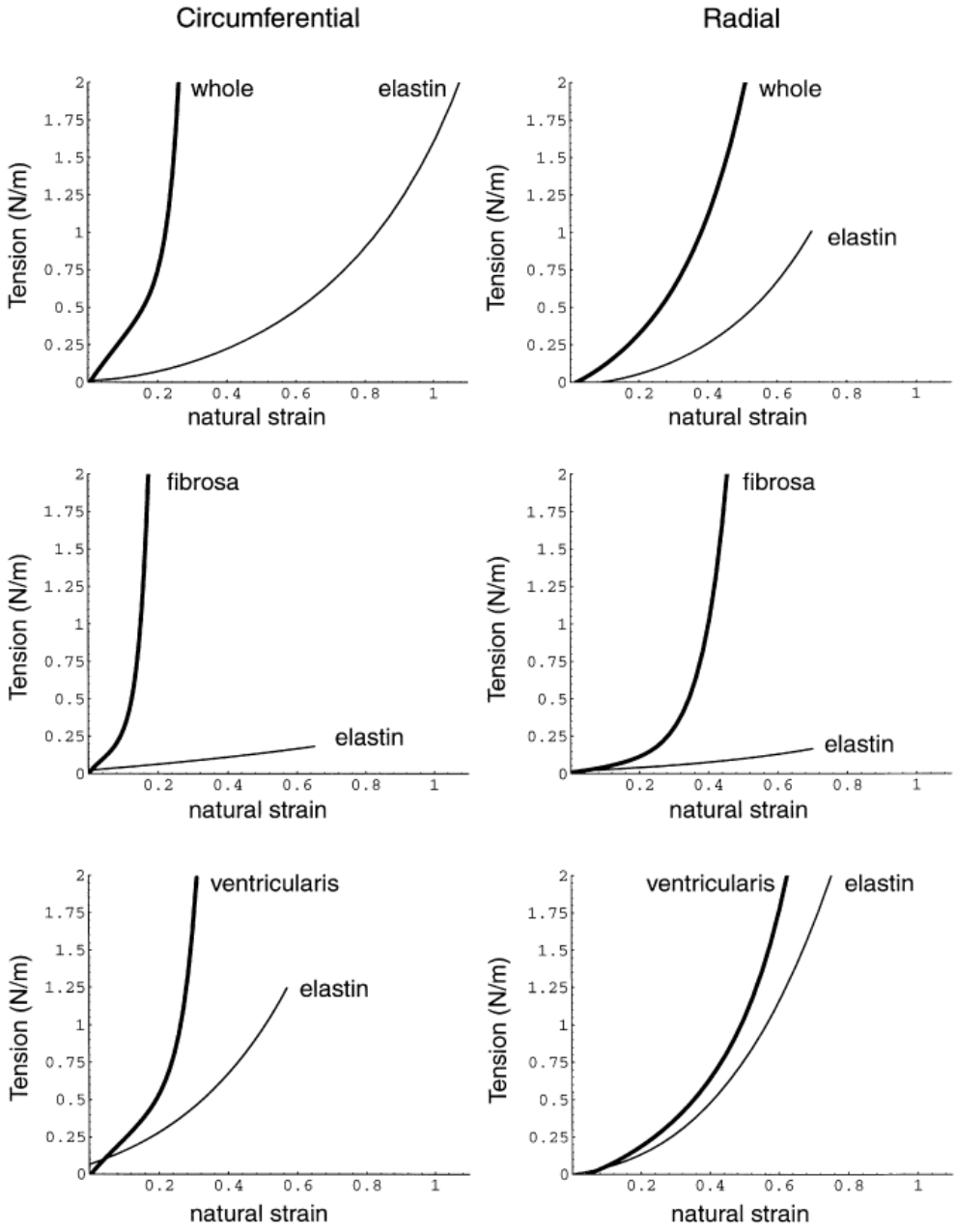

Figure 1.16 Plots of the uniaxial stress-strain curves describing the behaviour of fresh and digested tissues, reported in [20] (adapted with permission). These plots represent the relative contribution of elastin to the behaviour of the fibrosa and the ventricularis, as well as the whole tissue.

In a similar study, Lee et al (2001) performed tests to evaluate the effect of elastin damage on overall AV mechanics. For this purpose, they performed uniaxial tensile tests on AV leaflets, with and without elastin (digested with 10 ml of elastase solution for 36 h at 37˚C) [61]. Consistent with the previous studies [19,20], they showed that damage to elastin in aortic valves leads to a reduction in extensibility and an increase in the stiffness of the tissue.

Quasi-static biaxial tests

Although uniaxial experiments have provided the basis for the study and understanding of the mechanical behaviour and material properties of the AV leaflets, such tests do not reflect the multi-axial physiological loading conditions of the native functioning AV [3]. In order to address this, quasi-static biaxial mechanical testing has been adopted, to further contribute to the understanding of AV mechanical behaviour under more complex loading regimes. Biaxial studies of the AV are notably less prevalent than uniaxial studies, as they need more complicated experimental setups and techniques. The well accepted protocol for biaxial experiments has been to dissect a square sample from the belly region of the AV leaflets, and to transfer uniformly distributed loading to each of its four sides via surgical sutures [3], as shown in Figure 1.17. The sample is then subjected to either equi-biaxial (i.e. equal levels of tensile load applied to each loading axis) or non-equibiaxial loading regimes.

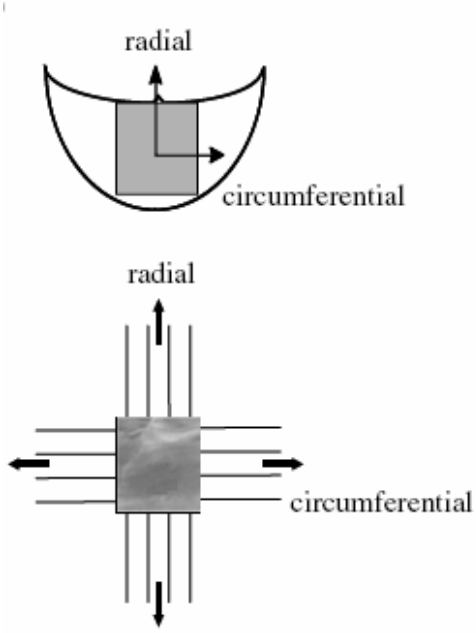

Figure 1.17 Schematic of the AV test specimen configuration in biaxial mechanical tests (adapted from [3], with permission).

The first attempts to carry out biaxial loading experiments on AV leaflets were completed by Christie and Barratt-Boyes (1995), in which they applied equi-biaxial loading to valve leaflets [62]. The mechanical behaviour of the pulmonary and aortic valves for both the fresh and fixed porcine tissues was compared in that study. The resulting data showed that the aortic valve is stiffer than the pulmonary valve, and that

fixed samples of both valves behaved in a less compliant manner than fresh samples, in a good agreement with the previously reported uniaxial results [6,55,57]. They also reported smaller strains and larger stresses in both circumferential and radial directions for AV test specimens, in comparison with the previously reported stress-strain levels for uniaxial loading tests, suggesting a less extensible mechanical behaviour of the AV leaflet when exposed to the biaxial deformation condition [62]. The obtained stress-strain plots are shown in Figure 1.18.

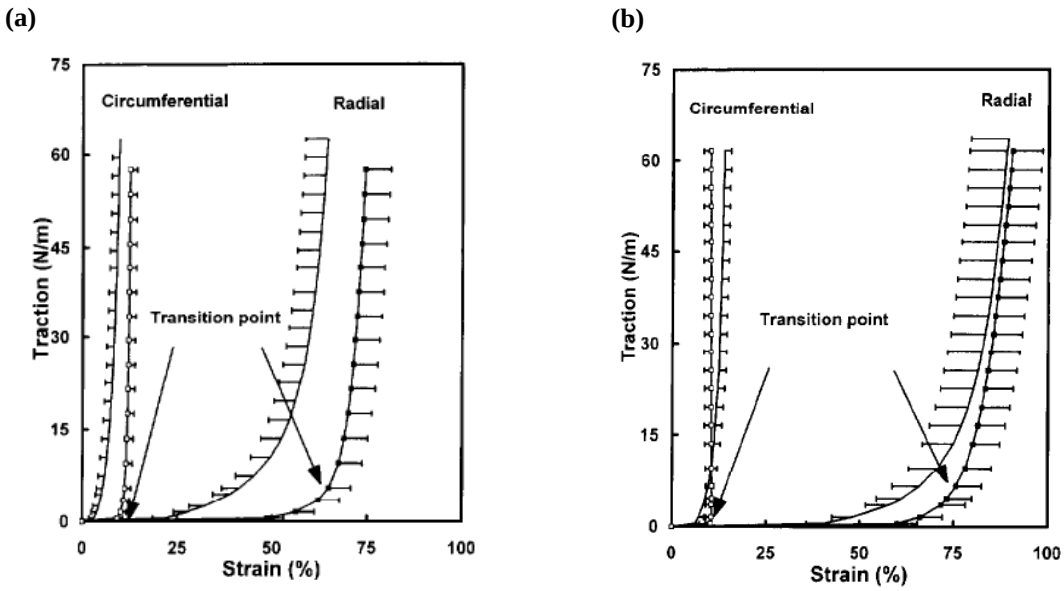

Figure 1.18 Stress-strain curves in biaxial loading test: (a) fresh and fixed porcine aortic leaflets. (b) fresh and fixed porcine pulmonary leaflets. The curves with symbols are the mean results for the 24 fresh samples (closed symbols = radial direction; open symbols = circumferential direction). The curves with no symbols are the corresponding curves for the fixed samples. The error bars show the standard deviation (adapted from [62], with permission).

In follow on studies from the same group, the age-related changes in deformation behaviour of the AV leaflets [63] and mechanical properties of explanted aortic allograft leaflets [64] under biaxial loading conditions were investigated. Consistent with their previous study, they reported lower strain and higher stress in AV tissue under biaxial loading tests, compared to uniaxial loading. They also determined that the AV tissue stiffens with increasing age, observing a nearly 50% decrease in extensibility for the subjects aged 60 compared with those aged 20 [63,64].

Perhaps the most comprehensive study of the mechanical behaviour of the AV under quasi-static biaxial testing has been carried out by Billiar and Sacks (2000), in which equibiaxial and non-equibiaxial loading experiments were performed on fresh

and glutaraldehyde fixed AV samples [65]. Using small angle light scattering (SALS), they also monitored the change in collagen fibre architecture of the test specimens at different levels of loading [65]. The obtained stress-strain curves under equi-biaxial loading are shown in Figure 1.19, in a good agreement with the results reported in [62]. The fixed samples appeared to be stiffer, with a smaller toe-in region [65].

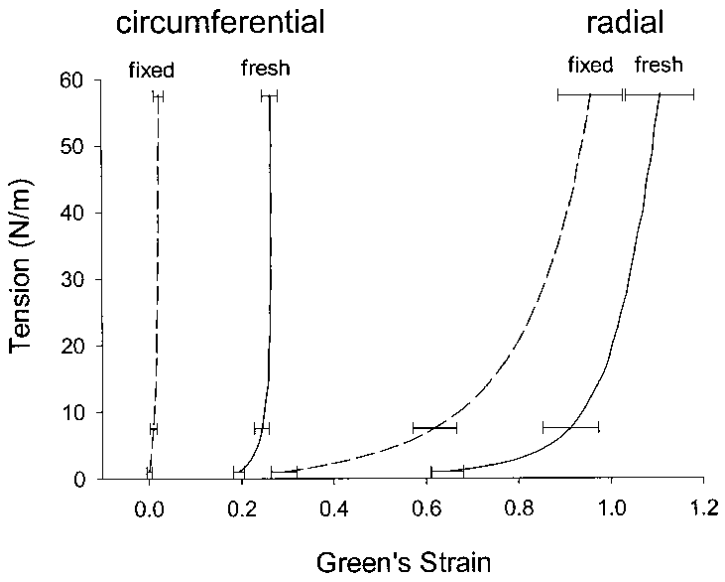

Figure 1.19 Mean stress–strain data for both fresh and glutaraldehyde treated AV test specimens (adapted from [65], with permission).

Although full details of the stress-strain curves under non-equibiaxial loads were not reported, the study did report a surprising response of the tissue when subjected to non-equibiaxial loads [65]. Interestingly, negative strains were seen in the circumferential direction with increase in loading in radial direction. Representative curves are shown in Figure 1.20.

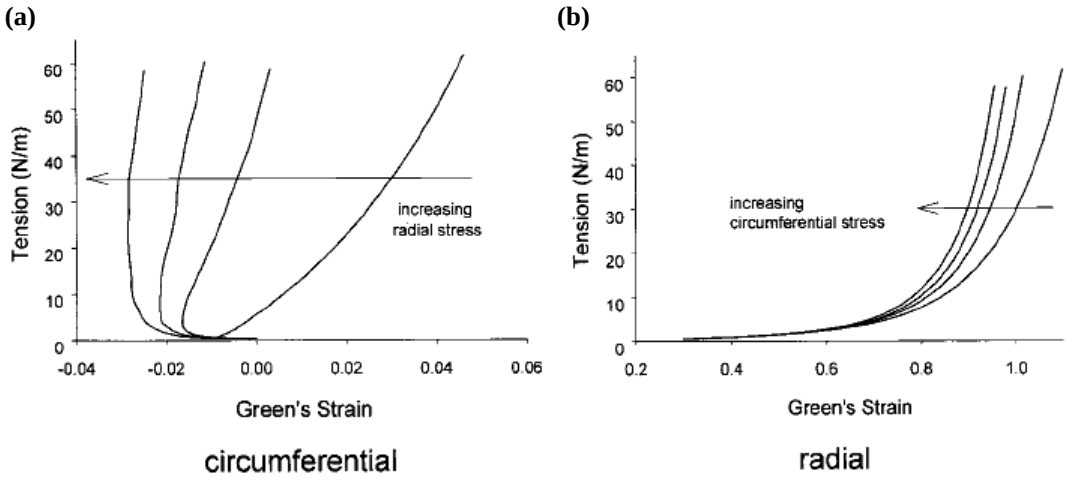

Figure 1.20 Stress–strain data for the AV test specimens under non-equibiaxial loading: (a) circumferential; and (b) radial directions (adapted from [65], with permission).

This complex behaviour of the tissue under biaxial loading was reported to be due to the tight angular distribution of collagen fibres [65]. As the radial axis is loaded, the forces cause the fibres to rotate, which in turn cause a contraction along the circumferential axis. This effect will become more pronounced as the radial loads become larger with respect to the circumferential loads. Figure 1.21 shows the process schematically. This effect illustrates that negative strains can be generated even though the stress magnitude is the same along both axes and no buckling of the tissue is observed. Thus, radial loads are ultimately resisted by the highly circumferentially aligned collagen fibres mainly present in the fibrosa layer, whose rotation into the loading direction facilitates very large strains prior to providing structural resistance [65].

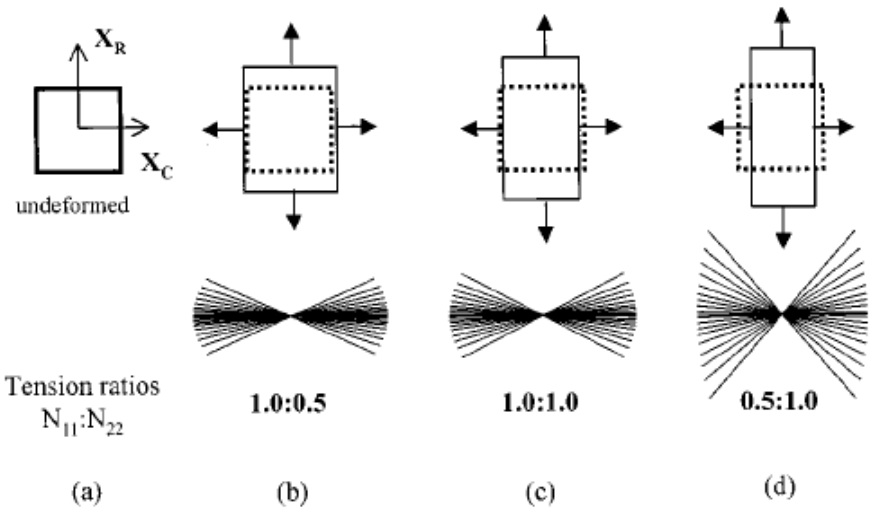

Figure 1.21 (a) A schematic of the biaxial test specimen, with the fibrous structure of the cusp depicting as the large collagen cords, which undergo large rotations with loading, (b-d) as the radial loads become larger with respect to the circumferential loads, the collagen fibres undergo large rotations. This causes contraction along the circumferential axis without buckling and allows for large strains (adapted from [65], with permission).

Similar to previous studies [19,20,61], Billiar and Sacks also favoured the hypothesis that the highly extensible elastin in the ventricularis allows the large radial compliance without yielding. In addition, they concluded that the strong axial mechanical coupling found between circumferential and radial loading of the AV is attributed to the alignment of the collagen fibres. Specifically, they described a scissor-like action of the fibres under load, which was responsible for the contraction along the aligned axis when its load magnitude is comparable or less than that of the perpendicular axis [65].

In a follow on study from the same group, a constitutive model based on the architecture and properties of the collagen fibre content of the AV ECM was developed, to describe the observed biaxial mechanical behaviour of the specimens [66]. They assumed a non-linear stress-strain relationship in a single collagen fibre, with stress exponentially related to strain. Furthermore, they assumed a normal angular distribution of collagen fibre orientation in the unloaded state, which remains unchanged during the loading [66]. This study was the first to attempt to formulate a constitutive equation for the biaxial mechanical behaviour of the AV, based on its microstructure.

More recently the mechanical behaviour of the separate valve layers has been investigated under equi-biaxial loading, and the behaviour of the isolated ventricularis and fibrosa layers compared with the intact tissue [1]. The study demonstrated that each AV leaflet exhibits a preloaded status: the fibrosa was observed to elongate while the ventricularis contracted after separation. This was in agreement with the findings of other studies [67], where the same phenomenon was observed upon dissection of the three layers of the AV leaflet. The stress-strain curves for the individual layers and the intact valve are shown in Figure 1.22. Several interesting results were observed: (i) the separated layers were very compliant at low strains; (ii) each of the separated layers exhibited significant anisotropic responses; (iii) the fibrosa in isolation behaved in a similar manner to the intact valve, with the exception that it was slightly less extensible in the radial direction; (iv) by contrast, the ventricularis exhibited extremely compliant equi-biaxial behaviour, with a very large toe region in the radial direction.

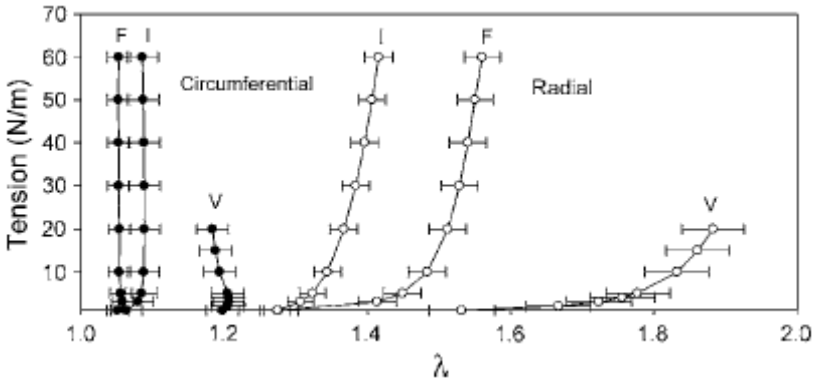

Figure 1.22 Mean equi-biaxial tissue responses of the intact, isolated fibrosa and ventricularis layers: I = intact, F = fibrosa, V = ventricularis (adapted from [1], with permission).

Time-dependent behaviour

Similar to other collagenous connective tissues such as the tendons and ligaments [68], the AV also exhibits time-dependent behaviour when subjected to specific loading conditions. Such behaviour can be realised through either stress-relaxation or creep tests. The former reflects a decrease in load (stress) which occurs when the tissues are subjected to a constant elongation, while creep describes the increasing elongation of the tissue under constant load (stress) [69,70]. In contrast to other soft

tissues such as skin and tendon, investigation of the time-dependent behaviour of AV has been the subject of a very few studies. The early contributions include the study of stress-relaxation in fresh AV tissue [5] and the comparison of stress-relaxation in fresh and glutaraldehyde fixed AV samples [55], employing the quasi-linear viscoelasticity (QLV) theory developed by Fung for soft tissues [71] to analyse the experimental data and quantify the relevant material parameters. Sauren et al. (1983) performed relaxation tests on circumferentially cut samples [5]. By fitting their experimental data to the QLV model, they reported that most of the relaxation occurs within the first 120s of the experiment, and the amount of relaxation is not significant thereafter [5]. 25% relaxation at an initial stress level of 0.8 MPa was reported in that study [5]. However they also argued that the QLV model was not able to accurately describe the experimental data. In a later study, Sauren and Rousseau (1983) performed a sensitivity analysis of the QLV model, and showed that there are some stress (strain) levels in which the QLV model will produce erroneous results. Furthermore, they showed that as the tissue tends to a more viscous-like behaviour, the resulting errors of the model would increase, until a limit was reached, at which point QLV could not determine the relaxation times [72].

Rousseau et al. (1983) compared the stress-relaxation behaviour of fresh and fixed AV tissue samples, and reported less relaxation in fixed tissue [55]. Fixation under pre-loading also affected the relaxation behaviour, as the samples fixed under 0.3 N preload were reported to have an approximately 60% decrease in total relaxation. The inaccuracy of using QLV to model stress-relaxation of the AV was again underlined in this study, reflected in the high standard deviations in the parameters calculated by the QLV model.

Other studies regarding stress-relaxation of the AV have investigated the effects of pre-conditioning and strain rates on the relaxation behaviour [73,74]. It was shown that preconditioning AV samples results in more identical stress-relaxation curves and less variation in the parameters, irrespective of the applied strain rate [73]. The proposed optimal protocol was at least 5 loading cycles up to loading level of 600g. However, this study highlighted that the lack of standard preconditioning protocol for stress-relaxation tests means that a direct comparison between different test data may prove problematic. In another study, it was suggested that the strain rate does not have

significant effects on the AV relaxation, as the QLV parameters were only 'moderately' affected by strain-rate [74]. Figure 1.23 shows the trend of the fast and slow relaxation times (Tau-1 and Tau-2 respectively) with increasing strain rates.

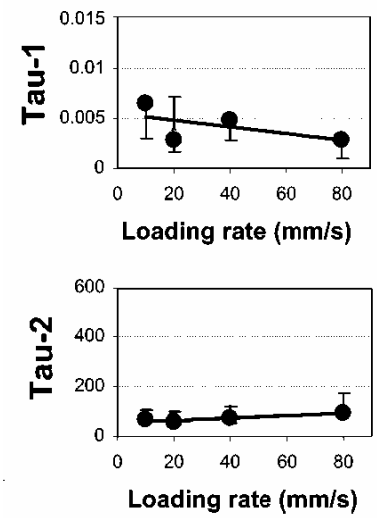

Figure 1.23 Mean and deviation of the fast and slow relaxation times at different strain rates, calculated by the QLV (adapted from [74], with permission).

Studies regarding the biaxial time-dependant behaviour of heart valves are very rare in the literature. Liao et al. (2007) looked at biaxial stress-relaxation of the mitral valve [75]. The specimens were loaded to 90 N/m equibiaxial tension and held at the fixed strain level, and the normalized stress-relaxation curves determined over a time course of 90 minutes (Figure 1.24). The overall relaxation values in the radial and circumferential directions were similar, with a reported 27.67% and 32.09% of relaxation in radial and circumferential directions, respectively [75].

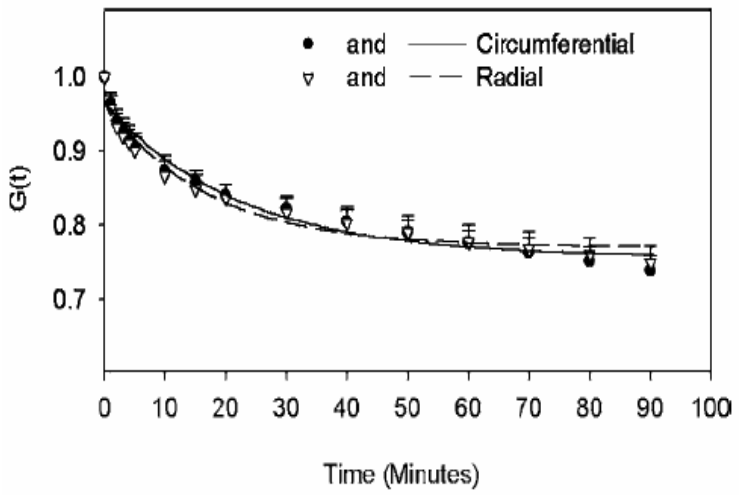

Figure 1.24 Normalized biaxial stress relaxation, $G(t)$, of mitral valve (adapted from [75], with permission).

Stella et al. (2007) performed a similar biaxial stress-relaxation study on AV samples, loading the specimens up to 60 N/m under equibiaxial tension and monitoring relaxation over 3 hours (Figure 1.25) [69]. These data indicate a more apparent difference in circumferential and radial relaxation, reporting 26.51% and 33.28% relaxation in the circumferential and radial directions, respectively [69].

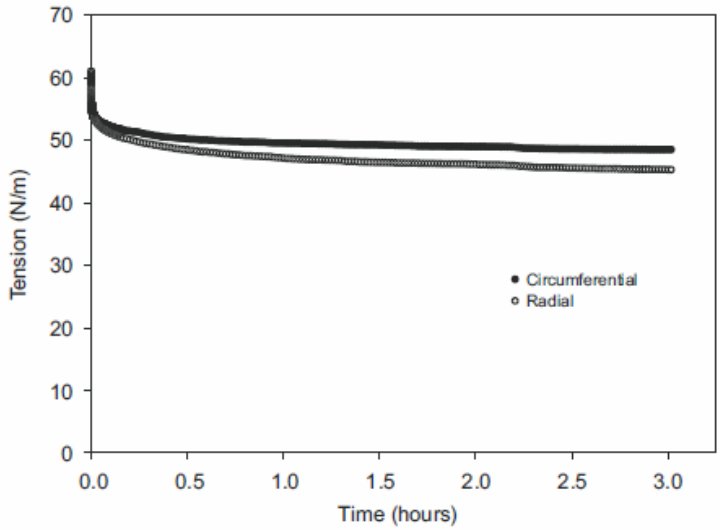

Figure 1.25 Representative biaxial stress-relaxation curves of the AV (adapted from [69], with permission).

Recently, Robinson and Tranquillo (2009) performed biaxial stress-relaxation tests, comparing equi- and non-equibiaxial loading regimes [76]. Their results indicated that as the ratio of radial load to circumferential load increased, the amount of relaxation decreased in both directions [76]. Interestingly, they did not find a significant

difference between the relaxation values in each direction, even under equibiaxial loading, in contrast to the previous study [69]. The reported relaxation values for different loading ratios are summarized in Figure 1.26. Possible reasons for this difference might be the geometry of the specimens and the gripping method, as they used cruciform test specimens and clamps for grips, compared to the square-shaped samples and the suture load-transfer mechanism employed by Stella et al. (2007) [69].

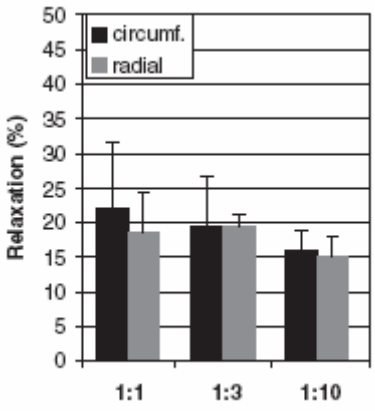

Figure 1.26 The percentage of relaxation in AV specimens at different loading ratios, in each direction (adapted from [76], with permission).

Most of the studies cited above, have used QLV theory to characterize the relaxation parameters. Within the QLV criteria, the creep function can be derived from stress-relaxation by a convolution using the Laplace transform [70,71]. On this basis, the time-dependent behaviour of the AV has been mostly characterised through stress relaxation experiments, and creep behaviour has rarely been investigated or characterised. Studies regarding uniaxial creep behaviour in the AV are not available in the literature to the knowledge of the author. However, there is one study investigating biaxial creep behaviour of the AV [69]. Noticeably, under equibiaxial loading, no measurable creep was reported over the time course of the experiment, as evident in Figure 1.27.

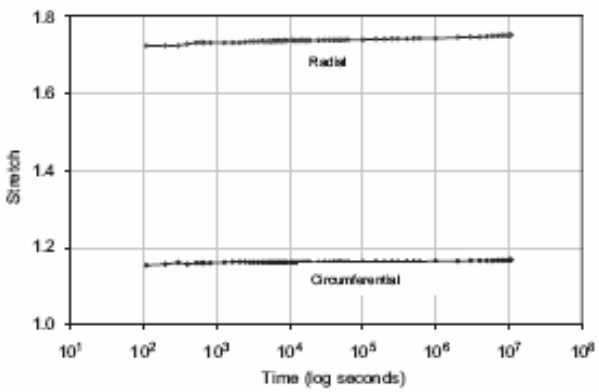

Figure 1.27 Representative AV planar biaxial creep behaviour for the circumferential and radial directions over the 3 h test (adapted from [69], with permission).

The authors suggested a possible structural mechanism for the observed lack of creep behaviour, which they termed the "fibril-level locking" mechanism [69,75]. This mechanism allows for stress to relax under constant strain, but does not allow for creep under constant stress, when subjected to equi-biaxial loading condition [69,75]. It describes the fact that the collagen fibril D-period decreases during stress-relaxation, while it remains approximately constant during creep, as observed through small angle X-ray scattering (SAXS) beamline patterns during the tissue relaxation and creep [69,75]. The biaxial time-dependent behaviour of the AV tissue further highlights that AV relaxation and creep may not be predicted from each other using the QLV theoey, and separate experiments are required to characterise each behaviour.

Flexural deformation

While uniaxial and biaxial quasi-static and time-dependent tests have elucidated valuable data on the in-plane mechanical behaviour of the AV tissue, the natural deformation mode of the valve *in vivo* is flexion, occurring as the leaflets open and close in each cardiac cycle. To quantify the flexural properties, Thubrikar et al. (1980) performed *in vivo* experiments on canine aortic valves [7]. Radiopaque markers were placed on the left coronary leaflet in the circumferential direction, and then tracked to determine the changes in leaflet length occurring during each cardiac cycle. The pressure changes were also measured and recorded using catheter pressure transducers. They reported the changes in the pressure and the length of the leaflet during the systolic and diastolic phase, and calculated the elastic modulus based on

the linear elasticity theory of thin cylindrical shells (Laplace law). The bending modulus was calculated to be 0.24 MPa at systole [7]. In another study by these authors, an analytical model was also proposed to correlate the radius of curvature of the leaflet to the applied stresses [77]. The calculated elastic moduli were in the range of those reported in [7].

More recently, 3-point bending tests have been performed on rectangular strips cut circumferentially from AV leaflets [78]. In their physiological unloaded position, the AV leaflets have a natural curvature (Figure 1.28a). During the tests, the specimens were bent either with the natural curvature or against it, by holding specimens stationary with two supporting posts, while a bending bar was applied to the centre of the tissue (Figure 1.28b). The relationship between the applied moment (M) and the change in the curvature of the specimens ($\Delta\kappa$) was obtained using the Bernoulli-Euler moment-curvature equation: $M = E_{eff}\, I\, \Delta\kappa$ [78], where E_{eff} is the instantaneous bending stiffness, and I is the second moment of inertia.

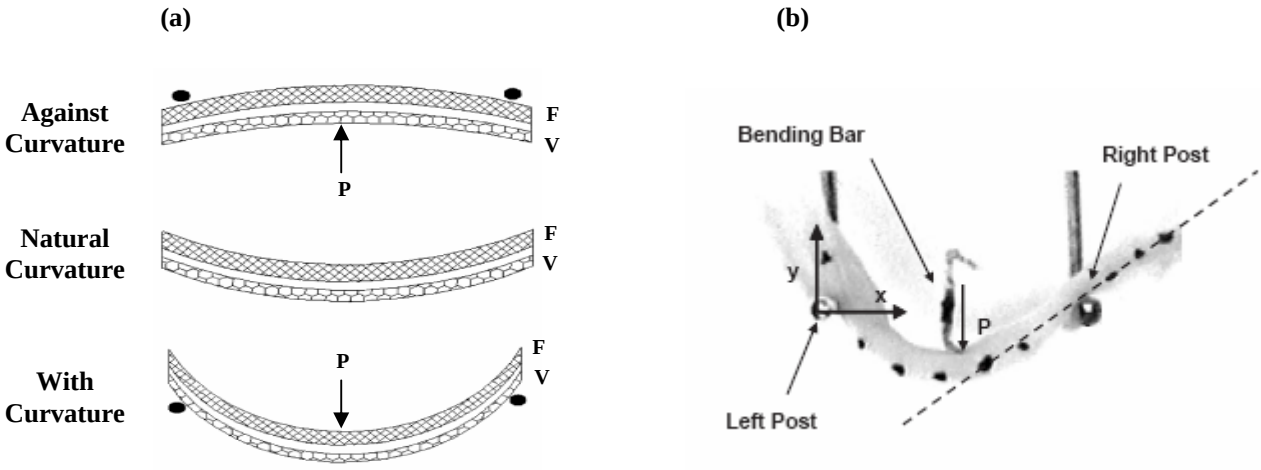

Figure 1.28 (a) Bending directions of AV leaflet. (V = Ventricularis layer, F = Fibrosa); (b) Schematic of leaflet specimen in the 3-point bending test configuration. P = applied load (adapted from [78], with permission).

The study concluded that when bent in the direction of the curvature, the effective stiffness of the specimens is dominated by the tension in the ventricularis layer, with little contribution from the fibrosa which is not designed to support compressive loads [78]. The reported value for the E_{eff} in this bending mode was 0.70±0.13 MPa. Conversely, when the specimens are bent against the natural curvature of the valve,

the fibrosa withstands tension while the ventricularis undergoes compression, with the reported value for E_{eff} = 0.49±0.13 MPa [78].

In a similar study, the flexural properties of the commissural region (where the upper portion of the leaflet joins the aortic root) were investigated, using the Bernoulli-Euler criterion [79]. The relationship between flexure angle (φ) and bending stiffness (E) was determined for angles up to φ = 40°, and reported to be linear in both the curvature and against-the-curvature directions. The slope of the φ-E line was shown to be negative, indicating that the bending stiffness decreased as the flexure angle increased. The value of E at a flexure angle of φ = 30° was taken as the 'representative' value, reporting E = 42.63±4.44 kPa in the curvature direction and E = 75.01±14.53 kPa in the direction against the curvature [79]. Their results showed that the commissural region is approximately 50% stiffer when bending against the natural curvature direction, suggesting the commissural region is functionally adapted for uni-directional physiological flexion.

1.3.3. Aortic Valve Interstitial Cells (AVICs) mechanical properties and function

In addition to AV mechanics at tissue level, there is a significant interest in the mechanical properties of the AVICs, the effects of applied loading on their function, and how they may influence the mechanical behaviour of the tissue itself. This has been another ground in studying the biomechanics of the AV [3]. Initial publications in this area have focused on characterising the deformation behaviour of the AVICs, quantifying their stiffness using micropipette aspiration or atomic force microscopy techniques [80,81].

The micropipette aspiration test is a well-established experimental technique for determining the properties of a variety of cell types [82,83]. Briefly, a defined level of hydrostatic pressure is applied to the surface of an isolated cell through a micropipette, and the aspirated length of the cell is then measured at that pressure. Merrymen et al (2006) employed this technique to determine the elastic modulus of porcine AVICs [80]. An initial tare pressure of 50 Pa was applied to ensure a seal

between the cell and the tip of the micropipette, and then a pressure step up to 500 Pa [80]. Under the assumption that AVIC is a homogeneous, isotropic, elastic and incompressible material, they calculated the elastic modulus of the cell to be 0.44 ± 0.02 kPa, using the relationship: $E = \varphi(\eta)\ [3r/2\pi]\ (\Delta P/L)$ [80]. E is the elastic modulus; r is the micropipette inner radius; P is the applied pressure; L is the aspirated length; and $\varphi(\eta)$ is called the wall function, a dimensionless coefficient calculated from the ratio of the pipette inner radius to the wall thickness, which in that study was 2.1 [80].

In another study, atomic force microscopy (AFM) was used to calculate the mechanical properties of AVICs seeded in monolayer [81]. In this technique, micro cantilever beams are utilized, which deflect through contact with the cells. By knowing the beam deflection and the applied force, the elastic modulus E can be determined. The cantilever probes used in that study had a spring constant values between 65.23 pN/nm and 72.93 pN/nm [81]. Following a series of assumptions, E was calculated by: $E = F/(0.594 \cdot \delta^2)$, where F is the applied load and δ is the amount of the cantilever beam deflection. The values for E were determined to be E = 55.06 ± 4.17 kPa, approximately 100 times more than that obtained via micropipette aspiration technique [81]. This variation is believed to result from the difference in the loading mechanisms. In the AFM technique, a localized force is applied to a focal point on the cell membrane, which is supported by the nearby structural components (microfilaments, nucleus, etc.). The resulting response is modelled from this small, highly localized deformation state. However, micropipette aspiration primarily examines the membrane of an isolated cell and unanchored cytoskeleton [81]. It has been argued that that the stiffness as measured with AFM allows for a more accurate representation of the cellular properties and architecture of the cell than micropipette aspiration. This is a result of the fact that the cells are seeded and attached to a substrate so that the cytoskeleton is extended and rigid as it is anchored at focal adhesions. This configuration is in contrast to testing with micropipette aspiration, where the cytoskeleton is freed and not in a physiologic state as the cells float in a solution [81].

In a more recent study, the viscoelastic behaviour of the AVICs was investigated using micropipette aspiration [9]. To model the viscoelastic behaviour, the Boltzmann superposition was incorporated into the standard linear solid model, to account for the stress-relaxation and creep during loading [9]. Creep and relaxation over a typical diastolic time period of 0.3 s were simulated [9], reporting average creep during diastole of 4.65±1.34%, and average stress-relaxation of 4.39±1.12% [9]. These results may imply that under physiological conditions, the loading time for the AVICs is sufficiently fast such that viscoelastic effects are negligible. However, these effects could become more significant in studies examining the mechanobiology of the AVICs in bioreactors *in vitro*, where the cyclic loads are applied at 1 Hz or less.

Another aspect of examining the AVICs function in the literature has been to investigate their mechanobiology, the relation between the biological responses of the cells to the change in their mechanical environment. One study has looked at this correlation by assessing the cellular stiffness and collagen biosynthesis through quantifying the smooth muscle α-actin (SMA) and heat shock protein 47 (HSP47) content, respectively, of the AVICs and pulmonary valve interstitial cells (PVICs) [80]. The results showed that the AVICs were significantly stiffer than the PVICs, and their cytoskeleton contained higher levels of SMA (616.77 ± 2.26 pg/ml) compared to PVICs (495.63 ± 2.37 pg/ml). Furthermore, the levels of HSP47 protein levels were higher in the AVIC cytoskeleton (411.57 ± 2.35 pg/ml) than the PVICs (317.63 ± 4.86 pg/ml) [80]. They concluded that the stiffer heart valve cells are likely to contribute more to ECM remodelling of the valves through collagen biosynthesis [80]. In another study from the same group, it was shown that the AVICs residing in the fibrosa layer are stiffer than those in the ventricularis layer, when the fibrosa was withstanding higher stresses than the ventricularis in a 3-point bending test [78]. The results of these two studies may be linked to conclude that the higher levels of collagen in the fibrosa could be due to the residence of stiffer AVICs in that layer, as an adaptive biological response to the higher stresses transferred to the fibrosa layer [80]. It is believed that when the phenotype of the AVICs is myo-like, they participate actively in ECM remodelling [32]. Thus, it can further be concluded that the phenotypical status of the AVICs may also be determined by their mechanical properties, i.e. their stiffness, which itself is determined by their loading environment [84].

At the tissue level, the contractile properties of the AVIC population has been shown to have an effect on the leaflets, generating modest contractile forces within the mN range, from 0.31 to 0.66 mN in the circumferential direction and 0.11 to 0.23 mN in the radial direction [85]. In another study it was determined that AVICs were able to generate larger contractile forces on the seeded substrate than PVICs [81]. While these forces may have a subtle effect on the deformation of the valves *in vivo*, their contribution to the mechanical behaviour of the AV is considered to be negligible, as these forces are orders of magnitude lower than the physiological loads on the valve [23].

The deformation of the AVICs *in situ* upon application of quasi-static physiological levels of transvalvular pressure has been the subject of some other studies [23]. In order to provide physiological loading to the aortic valve, tissue samples were fixed at pressures of 0 mmHg, i.e. free floating, 1 mm Hg, 2 mm Hg, 4 mm Hg, 60 mm Hg, and 90 mm Hg. As a measure of AVIC deformation, the nuclei of the cells were monitored, and the aspect ratio of the nuclei calculated at each pressure level from the photomicrographs along the transmural plane [23]. An image of the cell nuclei is shown in Figure 1.29a.

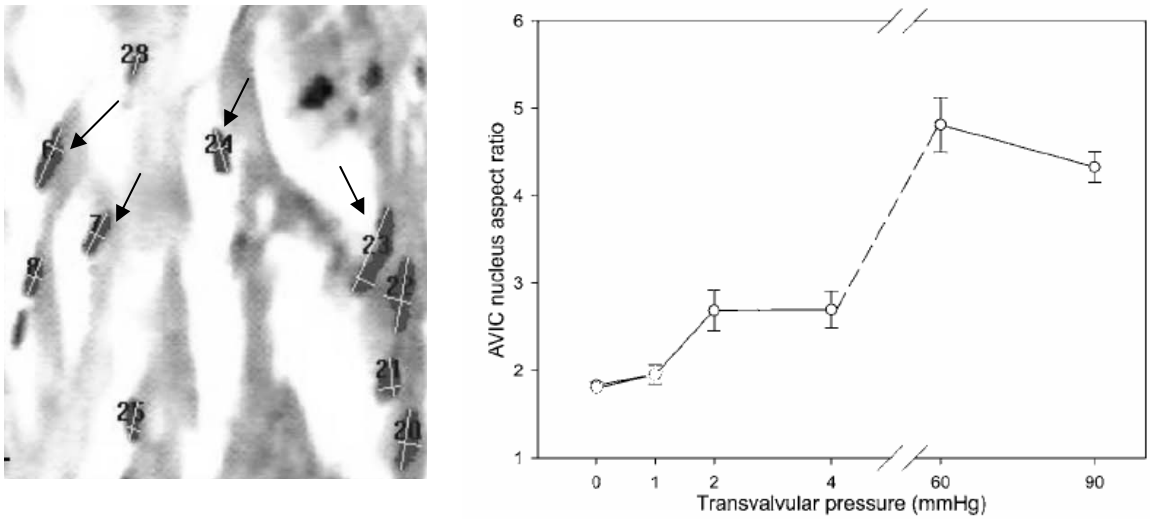

Figure 1.29 (a) A representative image of the AVIC nuclei (identified by arrows). The major- and minor-axis lengths used in calculating the aspect ratio are identified, (b) The change in nucleus aspect ratio with increase in pressure (adapted from [23], with permission).

The results of change in the nucleus aspect ratio against transvalvular pressure are given by the graph in Figure 1.29b, highlighting that nucleus aspect ratio generally increased with increasing applied pressure. Using small angle light scattering (SALS), the collagen architecture of each AV leaflet was also studied. It was concluded that once the collagen fibres straighten the AVICs begin to deform, and continued deformation of the AVIC nucleus was likely due to fibre-compaction effects that occur only when the collagen fibres are fully straightened and the valve leaflets are coapted [23].

1.4. Aims and scope of this study

As reviewed in §1.3, the analysis of AV biomechanics has mainly centred around three areas: the haemodynamic environment of the valve and the valve-blood interactions, its mechanical characteristics and behaviour, and the properties of its cellular constituents. A breakdown of these research areas is shown schematically in Figure 1.30. Data from these studies have led to an improved understanding of the complex functional aspects of the AV *in vivo*, and clarified some of the underlying mechanisms contributing to maintaining normal physiological function. However, a complete understanding of valve structure-function mechanics is currently lacking from the literature [23,32].

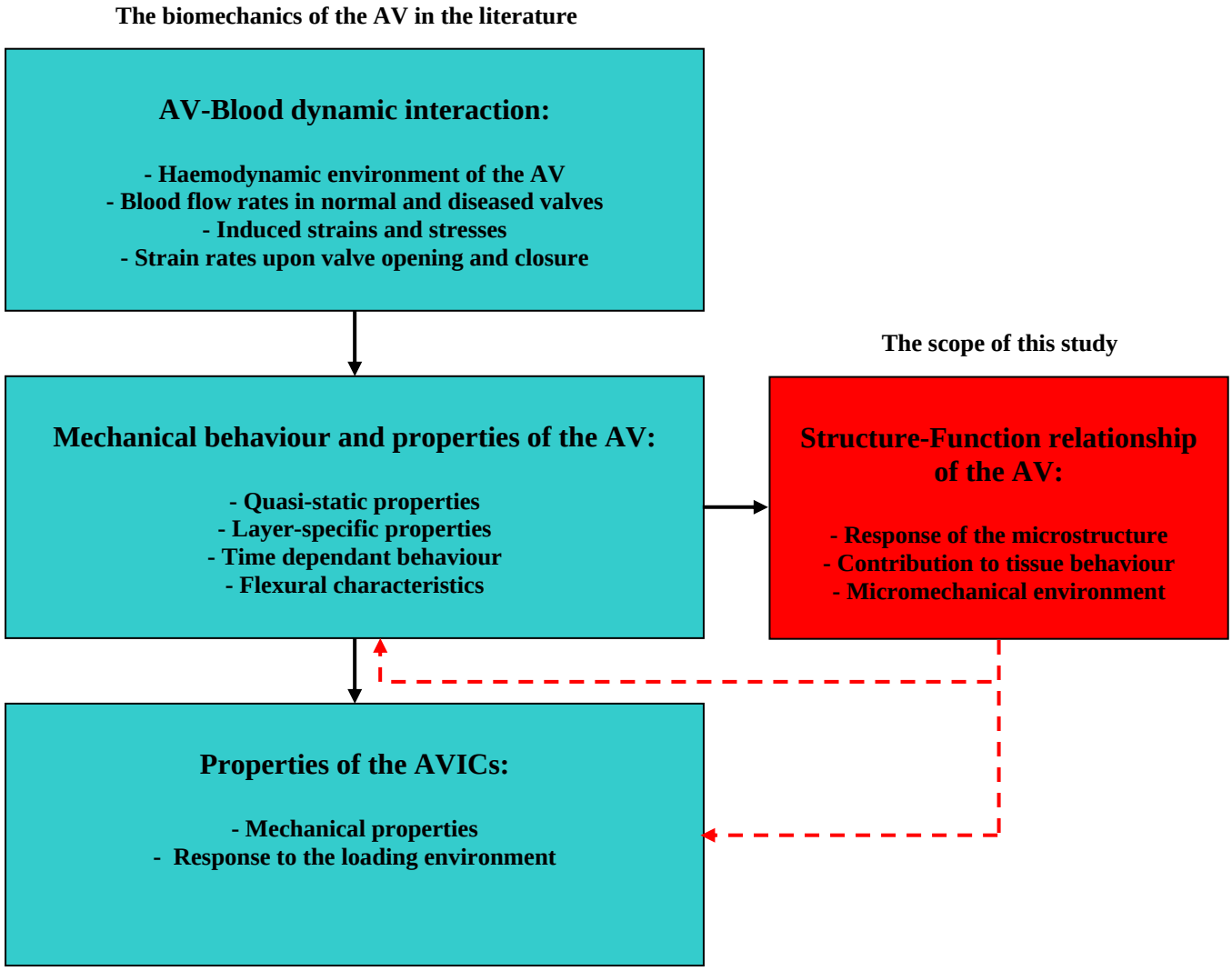

Figure 1.30 A schematic showing the approach in study of the biomechanics of the AV. The diagram on the left shows the available data on the literature, the box on the right represents the contribution of this thesis.

Knowledge of the structural mechanisms contributing to the observed mechanical behaviour at the tissue level would significantly improve our understanding of the physiological function of the native AV, and further improve the design of substitute valves and material selection processes, to effectively mimic the native valve function. Understanding the microstructural response of the valve ECM to applied loads would also help to quantify the micromechanical environment perceived by the residing AVICs. This is particularly important since the AVIC cellular function is known to be influenced and regulated by their local mechanical environment through mechanotransduction pathways. These include the regulation of cell-mediated ECM metabolism and remodelling [80,81], which is vital for maintaining homeostasis in the

native valve [80,81]. Furthermore, there is some evidence that inappropriate cell strains may contribute to the pathology of the valve by triggering responses which lead to valve degeneration and calcification [22,24,86].

It is therefore of critical importance to understand and characterise how the AV microstructure responds to the applied mechanical stimuli and how these microstructural responses would lead to the observed tissue behaviour. This thesis aims to investigate the mechanical behaviour of the AV at both tissue and microstructural levels, in order to establish structure-function relationships in the AV. The objectives of this study are to:

- Characterise the mechanical behaviour of the AV tissue.

- Investigate the response of the tissue microstructure to the applied loads, monitoring ECM reorganization.

- Quantify the contribution of the microstructural components to mechanical behaviour at the tissue level.

- Characterise the micro-mechanical environment within the valve matrix.

The mechanical behaviour is investigated under quasi-static and time-dependent loading modes, and the microstructure is studied using confocal laser microscopy imaging, with cell nuclei as micro-markers to monitor the ECM reorganisation. To formulate aspects of the structure-function relationships within the AV, mathematical models are also developed to explain the results analytically, and to quantify the associated mechanical and material parameters. The anticipated outcome of this study will be to provide more comprehensive and in depth quantitative data on the mechanical characteristics and material properties of the native valve, as well as the micro-structural mechanisms contributing to AV function. These data will help to design more efficient prosthetic and bioprosthetic substitutes. Additionally, the analytical information on the microstructural mechanisms will lead to a more detailed understanding of the micromechanical environment surrounding the AVICs, improving the understanding of mechanobiology in the native valve.

The research is presented in this thesis in the following format. Chapter 2 describes sample preparation techniques and general methodologies of the experiments used in this study. The mechanical testing and imaging setups, loading rig, and the ECM monitoring techniques are described and discussed in this chapter. Mechanical behaviour of the AV at tissue level is investigated and the results are presented in Chapters 3 and 4, under quasi-static and time-dependent loading modes, respectively. Chapter 5 addresses strain transfer from the tissue level to the microstructure, and how microstrain is distributed along the AV test specimens, as the first step to investigate the micromechanics of the AV. The role of collagen fibres in quasi-static behaviour of the valve is modelled and quantified in Chapter 6, followed by the analysis and characterisation of the role of the elastin network in Chapter 7. Chapter 8 discusses why QLV theory is insufficient in describing the time-dependent behaviour of the AV based on its microstructure. Accordingly, the response of the AV microstructure, alongside analytical explanations and new modelling criteria are presented in Chapters 9 and 10, to describe the micromechanics of AV stress-relaxation and creep behaviours, respectively. The overall conclusions and recommendations for future work are discussed in Chapter 11.

Chapter 2

General methodology:
Sample preparation, experimental equipment and techniques

In order to establish the objectives outlined in chapter 1, AV samples from porcine heart were utilised. To investigate different aspects of structure-function biomechanics within the samples, specific experimental equipment and protocols were employed in each set of experiments. The general methodologies for sample preparation are outlined in this chapter, alongside any repetitively adopted experimental equipment or techniques used in this study.

2.1. Sample preparation

Porcine hearts were obtained from animals ranging from 18 to 24 months, from a local abattoir within two hours of slaughter. The three AV leaflets were dissected from the aortic root and maintained in Dulbecco's Modified Eagle's Medium (DMEM, Sigma, Poole, UK) at room temperature (25° C). From each leaflet a 5 mm wide circumferential or radial strip was excised from the central (belly) region, as shown in Figure 2.1. For excision of the strips, each leaflet was placed and secured on a cutting board, and strips were cut out around a 5 mm wide solid block, placed tightly against the surface of the leaflet. Cutting through collagen fibres is known to inevitably reduce the structural integrity and strength of the sample [87]. In order to keep these cutting effects to a minimum, full sample length strips were cut along both the circumferential and radial directions (Figure 2.1b).

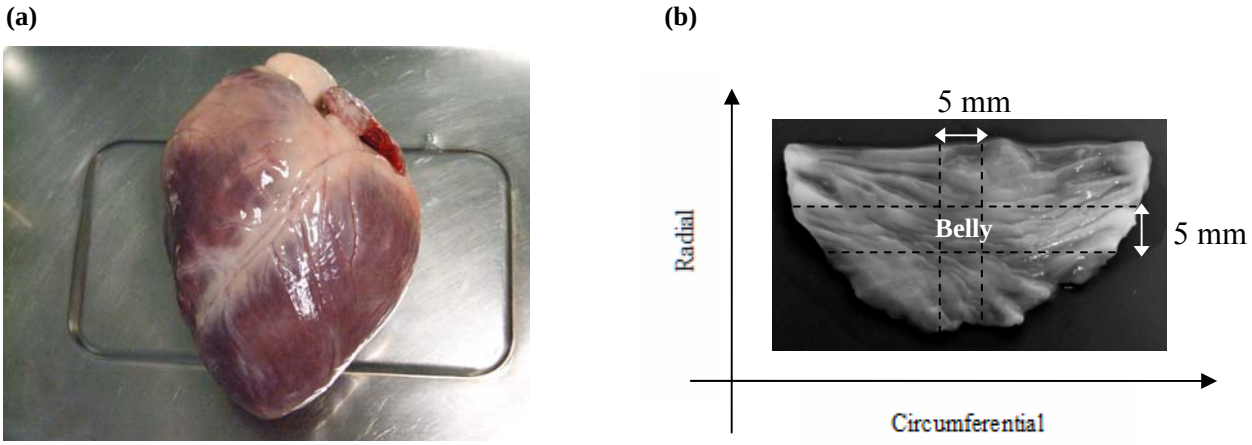

Figure 2.1 (a) Porcine heart obtained from an animal between 18 to 24 months; (b) 5 mm wide strips were cut from the belly region, in either the circumferential or radial direction.

The thickness of each strip was measured by moving it through the beam of a non-contact laser micrometer (LSM-501, Mitotuyo, Japan; resolution = 0.5 μm) and recording values at 1 mm increments. Mean thickness was used to determine the cross sectional area of each sample. The samples were then returned to DMEM before proceeding with the experiments.

2.2. Macro-mechanical tests

All mechanical tests (quasi-static and time-dependent) carried out at the macro (tissue) level, were performed on the strip specimens using the same material testing machine (Bionix 100, MTS, Cirencester, UK), fitted with custom designed pneumatic grips each with a corrugated surface (Figure 2.2). The pneumatic pressure was set to constantly grip samples with a pressure of 4 bar, preventing sample slippage during the experiments [88]. The corrugated surface increases the contact area between the sample and the grips, and together with the applied pressure, generates sufficient frictional force to hold the sample. The configuration of the gripping mechanism, holding a sample, is shown in Figure 2.2.

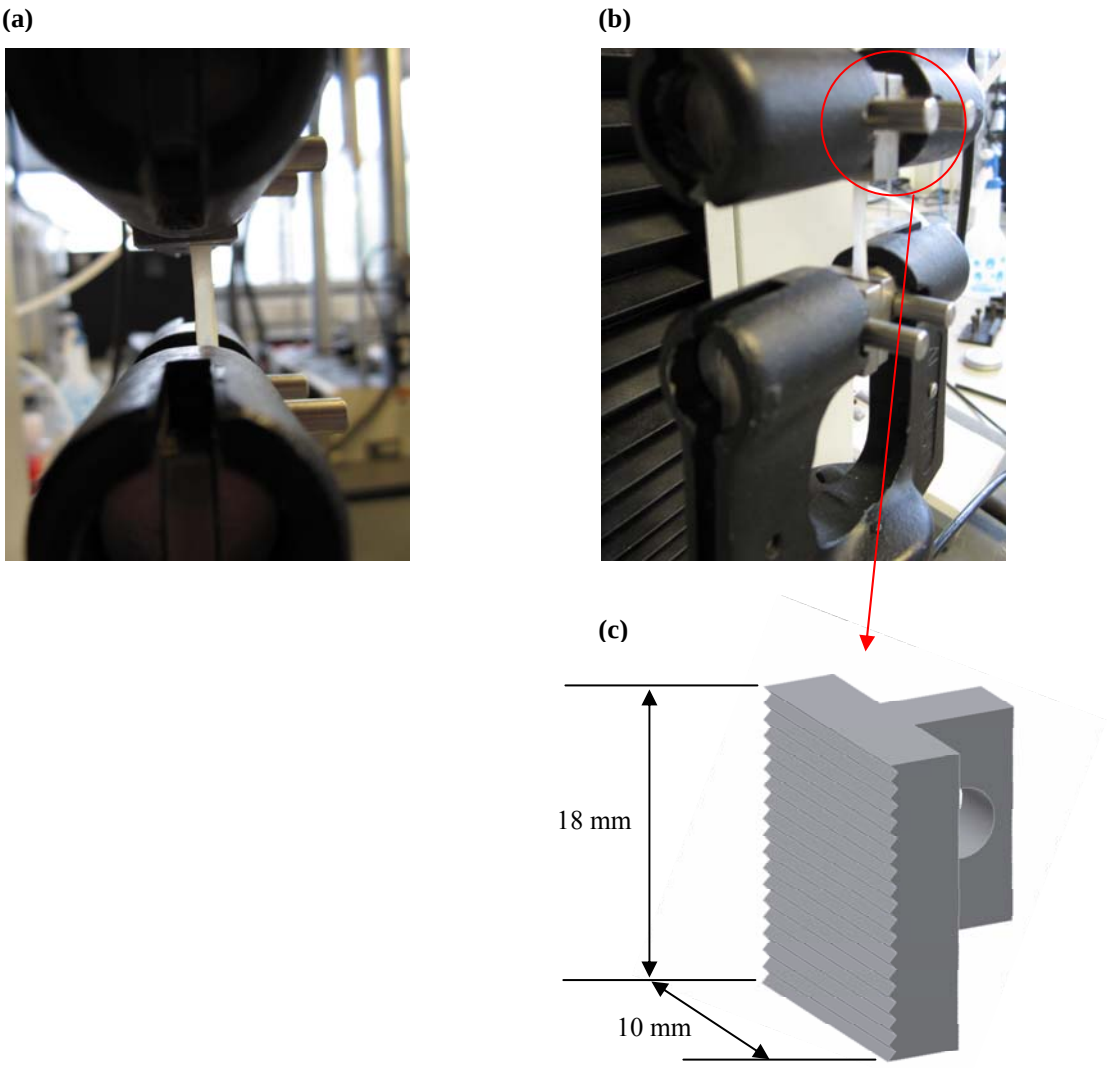

Figure 2.2 (a,b) The rectangular AV specimen strip mounted in the test machine and the gripping mechanism; (c) schematic and the dimensions of the grip.

The initial grip to grip distance was set to 10 mm, prior to start of the experiments, maintaining an initial sample length consistent with that adopted by previous research groups [5,19,20]. The machine allowed for strain rates of up to 1000%/min, and data acquisition frequencies of up to 20 Hz. A tare load of 0.01 N was applied to all test specimens, to maintain a consistent zero position. The adjusted distance between the grips was then used as the initial length to calculate the stretch ratios and resulting strains. The machine was programmed to apply the desired loading protocol, in quasi-static or time-dependant modes, according to the relevant experiments. Hydration of the samples was maintained by spraying Dulbecco's Modified Eagle's Medium (DMEM, Sigma, Poole, UK) over the samples during the experiments.

2.3. Micro-mechanical tests

Micro-structural mechanics within the AV extracellular matrix was investigated by adopting a previously established protocol from the host lab [87-89]. The technique uses the cell nuclei as micro-markers of the local microstructural changes, as the cells are known to be bonded to the surrounding ECM. Tissue samples are mounted within a custom made loading rig which is placed on the stage of a confocal scanning microscope. Under the application of mechanical stimuli, either quasi-static or time-dependent, the samples are imaged and the kinematics of the nuclei is recorded. The movement of each nucleus is tracked using particle tracking software. The relevant data regarding the movement of the cells are then extracted, and the reorganisation of the ECM is perceived accordingly. The imaging technique, the loading rig and the staining protocols to image cells are described in detail in the following sections of this chapter.

2.3.1. Confocal laser scanning microscopy

Confocal laser scanning microscopy is a type of fluorescence microscopy that facilitates the generation of high-resolution 3D images from viable tissue samples, enabling *in situ* characterisation of the microstructural architecture of the samples [90].

The majority of previous studies investigating the microstructure of the AV have used small angle light scattering (SALS) [1,63], or polarized light microscopy [54,57], imaging techniques. However, these imaging techniques require thin sections of the sample. Therefore the AV samples were fixed, generally using glutaraldehyde as the fixative agent, and thin sections were cut from the fixed samples to be investigated. However, fixation of the tissue is a destructive method, as it alters the number of cross-links within the ECM of the tissue resulting in changes in the mechanical behaviour of the tissue and the ECM, and the residing cells will no longer be viable [53,58]. Thus such techniques prevent the true examination of the tissue in its unaltered state, thereby limiting *in situ* observations of the response of the microstructure to the external mechanical stimuli. Confocal laser scanning

microscopy overcomes these limitations, making it a suitable imaging technique for investigating structure-function relationships in the AV for the purpose of this study.

A confocal laser scanning microscope uses a laser light source to excite a fluorescing contrasting agent within an imaged sample. The fluorescing contrasting agent is chosen for its ability to specifically bind to the structural component of interest within the tissue microstructure. An illumination light is launched from a gas or solid-state laser of a specific wavelength or several wavelengths and then filtered to produce the specific wavelengths required [92]. The operational principle of a confocal laser scanning microscope is shown schematically in Figure 2.3.

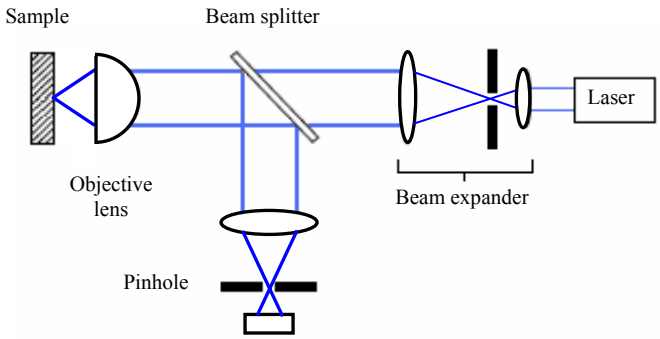

Figure 2.3 Schematic of a confocal microscope setup (redrawn from [92]).

The beam expander unit increases the diameter of the laser beam, to increase the resolution of the final image [92]. It also filters noise out of the beam, by passing the laser through a pinhole at the point within the expander where the light is focused into a neck. This focusing transfers the noise within the beam profile to the outside of the profile, thus causing the light to be truncated by the pinhole before the beam is fully expanded again. The light then enters the rear of the objective lens where it is focused into an area whose size is a function of the numerical aperture (NA)[1] of the lens [92]. That area is imaged using a specific excitation wavelength that is close to the contrasting agent's peak excitation wavelength. The contrasting agent, when excited by a light source, emits a longer wavelength that is then directed back along the same optical path as the illumination beam. A beam splitter or dichroic mirror, only

[1] NA is a measure of light focusing ability of a lens. It is a function of aperture diameter and focal length. It should be noted that objective lenses with higher NA have shorter working distances.

reflecting light below or above a certain wavelength, is then used to divert the florescent emission towards a photodetector. Before the light hits the photodetector, it passes through set of filters (low pass and high pass) allowing only a narrow bandwidth of light to pass constituting the wavelength range of the peak of the emission wavelength curve. The light is then focused though a detection aperture (confocal pinhole), enabling out of focus light to be eliminated before it is registered by the photodetector [92].

The confocal laser scanning microscope used in this study (UltraView; Perkin Elmer, Cambridge, UK) employs an argon laser as the illumination beam. Observations of the microstructure were made using a ×20 objective lens (Plan Apo; Nikon, Kingston-Upon-Thames, UK), with NA = 0.75. The excitation wave length of the argon laser beam was 488 nm, set up to approximately 60% of full laser power, and florescent images were recorded using a 586 nm emission band pass filter.

The nominal in-plane (x, y) resolution of a confocal laser scanning microscope is calculated by [93]:

$$Res = \frac{0.61\lambda}{NA} \tag{2.1}$$

where λ is the wavelength of the excitation beam. The microscopy setup described above enabled imaging resolution of $Res = 0.39\ \mu m$. The employed setup would thus provide detailed imaging of the micro-markers (AVIC nuclei) kinematics, as they are approximately 7 μm in length, ~20 times above the theoretical resolution.

2.3.2. Fluorescing labelling agent and protocol

With confocal scanning microscopy enabling the analysis of viable tissue samples, the development of fluorescing agents for labelling specific matrix and cell components has become desirable. Amongst the most frequently used dyes are calcein acetyl methyl (AM) and acridine orange, for marking the viable cell cytoplasm and nucleus respectively. For the purpose of employing AVIC nuclei as micro-markers in this study, acridine orange was used as the fluorescing labelling agent.

Acridine orange is a cell-permanent dye that provides a high contrast image of the cell nucleus when excited, by specifically binding to nucleic acids. It has been used in studies assessing the morphology of the AVICs [24], and also to label tenocyte nuclei to track micro strains within tendon [89-91]. In order to label AVIC nuclei within specimens in the current study, the excised AV strips were incubated in a 5 mM solution of acridine orange (Invitrogen, Oregon, USA) in DMEM for 1 hour at 25˚ C [89-91], prior to imaging.

2.3.3. Loading rig

The loading rig employed in this study was a custom made unaxial loading rig designed and developed in the host lab [94]. It can be placed on the stage of the confocal microscope, allowing samples to be imaged whilst subjected to controlled levels of the applied deformation (Figure 2.4).

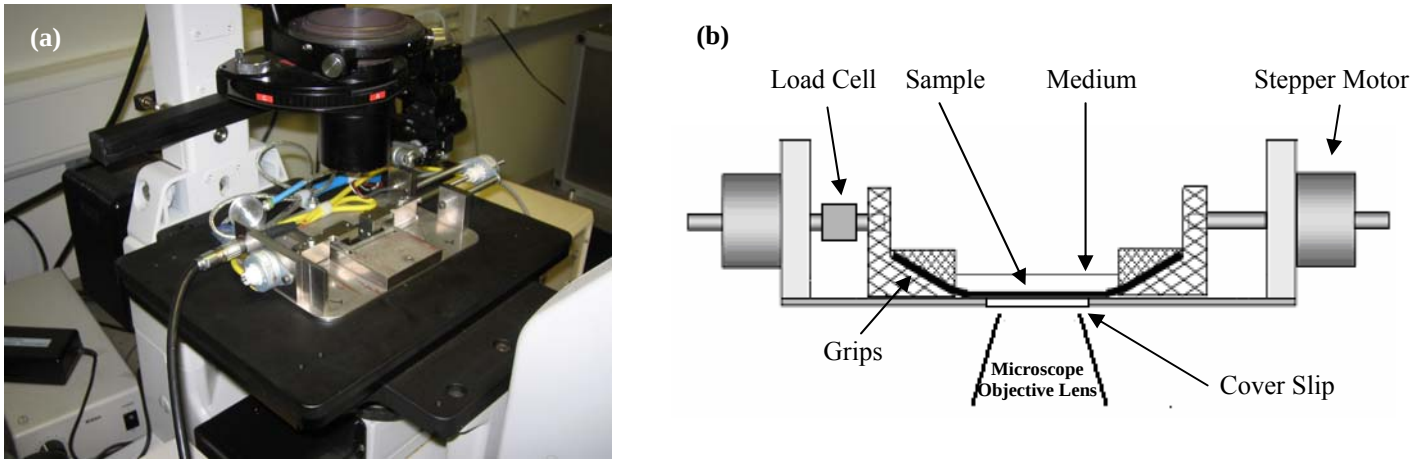

Figure 2.4 (a) Loading rig on the stage of the confocal microscope; (b) schematic of the rig and its components.

Samples are fixed between the grips and immersed in DMEM, to maintain hydration during imaging. Under displacement-control, the rig enables application of strains in both quasi-static and time-dependant modes, with user-defined strain magnitude, strain rate, holding times, etc [89-91]. Strains are applied to the tissue samples via a pair of in-line linear actuators (stepper motors, step resolution: ± 10%) located on both sides of the rig (Figure 2.4 b), transferring rotation of the spindle to linear movement of the grips. The force is measured by a 5N load cell (accuracy: ± 0.15%) attached to a grip at one side of the rig (Figure 2.4 b), with its upper limit set to 3.5N to prevent potential unwanted damage during the experiments. The initial grip to grip distance was set at 10 mm, for all samples. In order to ensure repeatability between experiments, the sample length was increased until the specimens straightened and were observed to subtly lift off the cover slip. This provided a consistent zero-strain starting position for the tests.

The schematic of the integrated set-up enabling microstructural analysis of the AV in this study is shown in Figure 2.5. The details of loading conditions used in each set of specific experiments are presented in the relevant following chapters.

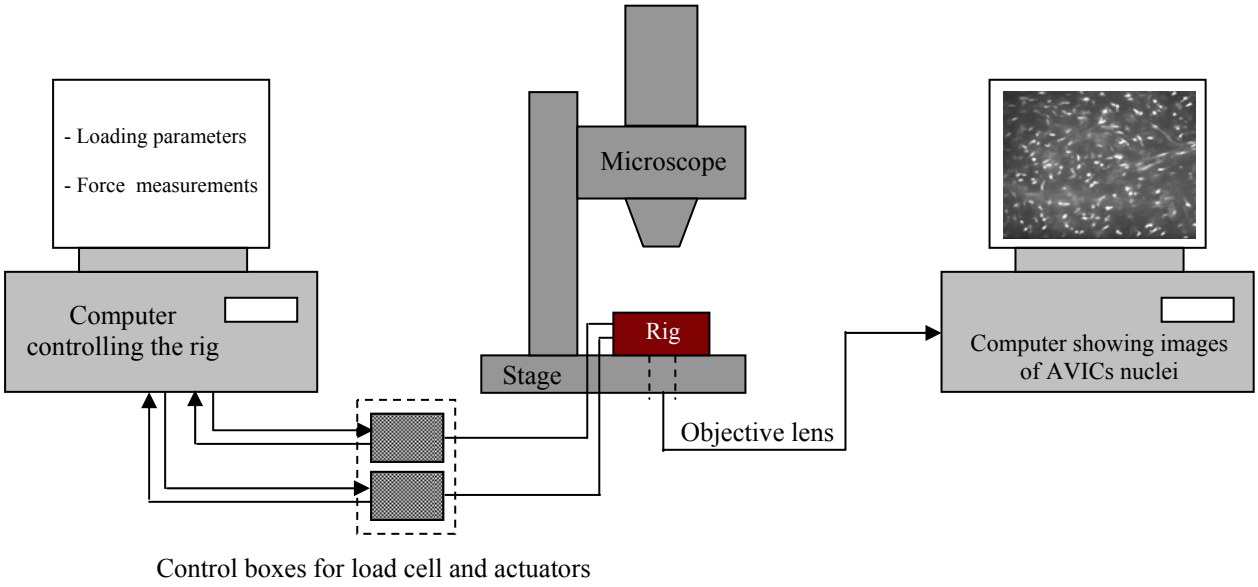

Figure 2.5 Schematic of the integrated setup used to image and study the AV microstructure.

Chapter 3

Aortic valve viscoelasticity in tensile deformation

The contents of this chapter have been published in:

Anssari-Benam, A., Bader, D. L., Screen, H. R. C. (2011) A combined experimental and modelling approach to aortic valve viscoelasticity in tensile deformation, J. Mater. Sci.: Mater. Med., 22, 253-262.

3.1. Synopsis

The quasi-static mechanical behaviour of the AV under tensile deformation is highly non-linear and anisotropic in nature, reflecting the complex collagen fibre kinematics in response to applied loading [5,52,62,65]. The mechanical behaviour and associated material properties under such loading conditions have mainly been characterised and quantified based on assumptions of elasticity, using thin membrane stress theory [54] or hyperelasticity [66]. However, as with many collagenous connective tissues, the AV is known to also exhibit viscoelastic behaviour and characteristics [5,69]. This has often been attributed to the glycosaminoglycan (GAG) component of the AV, mainly present in the spongiosa layer [1,17]. However, the viscoelastic behaviour of the AV in tensile deformation is generally less well characterised [32,95]. Important viscoelastic characteristics such as rate dependency in tissue stress-strain curves, hysteresis and resilience in loading cycles have not been fully evaluated, and the viscous effects of the AV structural constituents on its mechanical behaviour remain largely unknown. Furthermore, the majority of AV mechanical tests are performed on experimental equipments limited to loading rates considerably lower than those experienced during physiological function (15000%/min) [95]. As physiological loading rates are difficult to implement experimentally, it is important to develop a suitable viscoelastic model to accommodate the nature of rate dependency in AV tissue, and enable prediction of tissue response at high strain rates.

The viscoelastic behaviour of AV specimens subjected to uniaxial tensile deformation is investigated in this chapter, comparing the circumferential and radial loading directions, over a 100-fold range of strain rates. Hysteresis and resilience of the tissue are also examined in separate experiments. A constitutive viscoelastic model was then developed, based on the tri-layered structure of the AV using a Kelvin-Voigt solid, to predict the mechanical properties of the valve with varying strain rates.

3.2. Materials and methods

16 porcine hearts were used for the purpose of this study. Specimens were prepared according to the protocol described in §2.1, excised either circumferentially or radially from AV leaflets. This yielded a total of 24 pairs of samples. Measurements of sample thickness were made as described in §2.1. Samples were then mounted within the 'Bionix' material testing machine. The pre-experiment adjustments were performed according to §2.2.

3.2.1. Tensile tests

Tensile tests were carried out at 6%/min, 60%/min, and 600%/min, straining samples to failure. 12 samples were tested at each rate, 6 loaded circumferentially and 6 radially, and stress-strain curves obtained for each test.

3.2.2. Incremental one-cycle loading

In order to investigate hysteresis and resilience at different load levels, single cycle tests were performed on both circumferential and radial specimens ($n = 6$ for each group), at a constant strain rate of 60%/min. Each sample was subjected to a successive series of single cycle load tests at gradually increasing increments of load, returning to zero at the end of each cycle, and continuing until failure. Samples were loaded to nine different increments, between 5% and 80% of the previously established load at failure ($F_{failure}$), in the corresponding circumferential and radial directions.

3.3. Viscoelastic model

To model the viscoelastic behaviour of the AV, a constitutive equation of the tri-layered structure was developed using a spring and dashpot configuration, based on a Kelvin-Voigt model (Figure 3.1). Here, the two springs represent the elasticity of the ventricularis and fibrosa layers (E_1 and E_3), which are known to be the main load

bearing layers within the AV structure [1,20], while the dashpot represents the spongiosa layer.

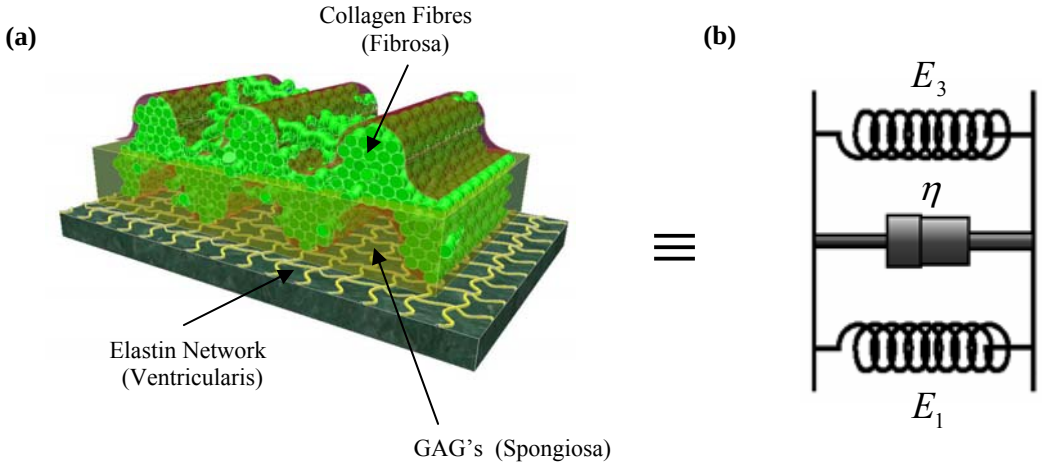

Figure 3.1 (a) schematic diagram of the structural configuration of the AV; and (b) viscoelastic representation of the AV leaflet with a Kelvin-Voigt model: the ventricularis and fibrosa are modelled with springs with elasticity of E_1 and E_3 respectively, and the spongiosa with a viscous damper with the coefficient of η.

For a Kelvin-Voigt model, the change in the viscoelastic stress tensor from time t_1 to t_2 during deformation can be characterized by superposition of the change in elastic and viscous shear resultants at each time point [96,97]:

$$\Delta T_{ij}\Big|_{t_1}^{t_2} = \Delta T_{ij}^{e} + \Delta T_{ij}^{v}\Big|_{t_1}^{t_2} = \left(T_{ij}^{e} + T_{ij}^{v}\right)_{t_2} - \left(T_{ij}^{e} + T_{ij}^{v}\right)_{t_1} \tag{3.1}$$

where the indices (i,j) represent the in-plane coordinates, either 1 or 2.

For an arbitrary time of deformation, substitution of the equivalent expressions for T_{ij}^{e} and T_{ij}^{v} in (3.1) yields:

$$T_{ij} = -P_h\delta_{ij} + E\varepsilon_{ij} + 2\eta V_{ij} \tag{3.2}$$

where T_{ij} is the Cauchy measure of stress [71], P_h is the hydrostatic pressure that represents the indeterminate part of the stress arising due to the constraint of incompressibility [98], E is the elastic modulus, η is the viscous dissipation coefficient, and ε_{ij} and V_{ij} are the deformation tand the rate of deformation tensors,

respectively. This equation assumes incompressibility, as is generally considered acceptable for biological soft tissues [71]. E is the equivalent elastic element, representing the sum of E_1 and E_3.

Cauchy stress T_{ij} is an objective measure and as such must be coupled with objective measures of strain and strain rate tensors in equation (3.2)[1]. Therefore, invariant measures of starin such as the Green starin tensor, and the corresponding invariant strain rate tensors can not be adopted in formulating a model by equation 3.2. To address this, we utilise objective measures of strain and rate of deformation tensors in equation 3.2, for a consistent parameterisation of the model from a continuum mechanics point of view.

The rate of deformation tensor, V, is an objective measure when defined as[1]:

$$\frac{\dot{\lambda}}{\lambda} = \vec{e} \cdot V \cdot \vec{e} \tag{3.3}$$

where λ is the stretch ratio, $\vec{e}$ is the direction of deformation, and operator $(\dot{})$ represents the time derivative. Assuming a uniaxial stretch, the rate deformation in the loading direction would simply become:

$$V = \frac{\dot{\lambda}}{\lambda} \tag{3.4}$$

An objective measure of strain for large deformations, coupled with the resulting objective Cauchy stress and the above definition of strain rate tensore is the Almansi strain defined as[1]:

$$\varepsilon = \frac{1}{2}\left(1 - \frac{1}{\lambda^2}\right) \tag{3.5}$$

After definig the objective parameters as above (equations 3.2 to 3.5), we now aim to formulate the model based on the equation 3.2.

[1] Baaijens, F. P. T. "Biomechanics: Concepts and Computation", pp. 200-207, internal communication, June 2012.

The stress tensor for directions 1 and 2 in (3.2) in component form can be written as:

$$\begin{cases} T_{11} = -P_h + E\varepsilon_{11} + 2\eta V_{11} \\ T_{22} = -P_h + E\varepsilon_{22} + 2\eta V_{22} \\ T_{12} = T_{21} = 0 \end{cases} \tag{3.6}$$

Subscripts 1 and 2 denote the loading directions, i.e. circumferential and radial respectively. Substituting for ε_{11} and ε_{22} from equation (3.5) and for V_{11} and V_{22} from equation (3.4) yields:

$$\begin{cases} T_{11} = -P_h + \left(\frac{E}{2}\right)\left(1 - \frac{1}{\lambda_1^2}\right) + 2\eta\left(\frac{\dot{\lambda}_1}{\lambda_1}\right) \\ T_{22} = -P_h + \left(\frac{E}{2}\right)\left(1 - \frac{1}{\lambda_2^2}\right) + 2\eta\left(\frac{\dot{\lambda}_2}{\lambda_2}\right) \end{cases} \tag{3.7}$$

The incompressibility constraint implies that $\lambda_1 \cdot \lambda_2 = 1$, thus T_{22} can be re-written as:

$$T_{22} = -P_h + \left(\frac{E}{2}\right)\left(1 - \lambda_1^{\,2}\right) - 2\eta\left(\frac{\dot{\lambda}_1}{\lambda_1}\right) \tag{3.8}$$

If the continuum experiences a uniaxial tension in direction 1 alone, T_{22} would be zero and thus:

$$P_h = \left(\frac{E}{2}\right)\left(1 - \lambda_1^{\,2}\right) - 2\eta\left(\frac{\dot{\lambda}_1}{\lambda_1}\right) \tag{3.9}$$

Substituting the above equation for T_{11} one gets:

$$T_{11} = \frac{E}{2}\left(\lambda_1^{\,2} - \lambda_1^{\,-2}\right) + 4\eta\left(\frac{\dot{\lambda}_1}{\lambda_1}\right) \tag{3.10}$$

The change in stress tensor in (3.1) can thus be rewritten using (3.10) as:

$$\Delta T_{11}\Big|_{t_1}^{t_2} = \left(\frac{E}{2}(\lambda_1^2 - \lambda_1^{-2}) + 4\eta\left(\frac{\dot{\lambda}_1}{\lambda_1}\right)\right)_{t_2} - \left(\frac{E}{2}(\lambda_1^2 - \lambda_1^{-2}) + 4\eta\left(\frac{\dot{\lambda}_1}{\lambda_1}\right)\right)_{t_1} \tag{3.11}$$

Setting the initial point of the deformation at $t_1 = 0$, where $\lambda_1 = 1$, the change in stress at time *t* will thus become:

$$T_{11} = \frac{E}{2}\left(\lambda_1^{\,2} - \lambda_1^{\,-2}\right) + 4\eta\left(\frac{\dot{\lambda}_1}{\lambda_1}\right) - 4\eta\dot{\lambda}_1 \qquad (3.12)$$

Equation (3.12) expresses the final form of the viscoelastic model, in the uniaxial tensile deformation. Since the principal directions for the AV leaflet are defined as circumferential and radial, equation (3.12) can be re-written for the two directions as:

$$T_{cir} = \frac{E_{cir}}{2}\left(\lambda_{cir}^{2} - \lambda_{cir}^{-2}\right) + 4\eta_{cir}\left(\frac{\dot{\lambda}}{\lambda_{cir}}\right) - 4\eta_{cir}\dot{\lambda} \qquad (3.13a)$$

and

$$T_{rad} = \frac{E_{rad}}{2}\left(\lambda_{rad}^{2} - \lambda_{rad}^{-2}\right) + 4\eta_{rad}\left(\frac{\dot{\lambda}}{\lambda_{rad}}\right) - 4\eta_{rad}\dot{\lambda} \qquad (3.13b)$$

The inhomogeneous and anisotropic nature of the AV necessitates the use of different elastic and damping coefficients in the two orthogonal directions [5,6,99], as reflected in the above two equations (3.13a, 3.13b).

Equations (3.13a) and (3.13b) were fitted to the experimental stress-strain data sets at each strain rate, for each direction, using the Levenberg-Marquardt algorithm by Origin 8.0 software (Microcal™ Software Inc. USA), for respective parameter estimations.

3.4 Results

Figure 3.2 represents typical stress-strain curves for both circumferential and radial tests to failure, at the three strain rates. It is evident that increasing strain rate leads to an associated increase in failure stress and decrease in failure strain in both the radial and circumferential directions. The mean failure data with standard deviations are compared at each strain rate for both loading directions in Table 3.1.

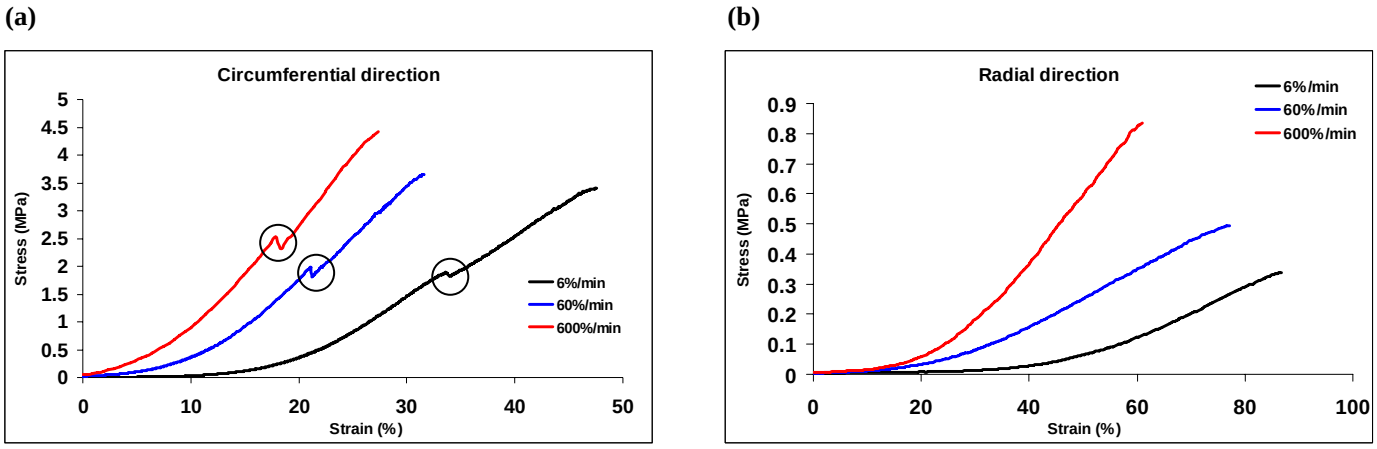

Figure 3.2 Typical $\sigma - \varepsilon$ curves for the AV strips loaded at 6%/min, 60%/min and 600%/min, showing: (a) circumferential specimens, and (b) radial specimens. Circles indicate the highly repeatable stress drop in the circumferential direction at all the tested strain rates. Note that due to the highly anisotropic behaviour of the AV, the scale of the axis in the graphs are not the same.

Only one example curve is shown at each strain rate in the graphs in Figure 3.2. However, very small variations were seen between the 6 samples tested at each rate [88], as reflected in the standard deviations presented in Table 3.1. A sudden transient decrease in stress was observed in the circumferentially loaded specimens at each rate, designated by circles in Figure. This will be further discussed later in this section.

Table 3.1 Values (mean ± SD) of the ultimate tensile stress (UTS) and failure strains in both directions and at different rates.

Sample	Strain Rate (%/min)	UTS (MPa)	Failure Strain (%)
Circumferential	6	3.44 ± 0.57	45.07 ± 1.25
	60	3.68 ± 0.12	31.54 ± 1.69
	600	4.45 ± 0.13	27.56 ± 1.96
Radial	6	0.34 ± 0.03	87.6 ± 1.78
	60	0.50 ± 0.03	77.15 ± 0.03
	600	0.84 ± 0.05	61.11 ± 0.63

In order to investigate the extent of non-linearity in the material response under tensile deformation, the tangent modulus E (also referred to as the instantaneous elastic modulus), was numerically estimated from the first derivative of the $\sigma - \varepsilon$ curve at each data point, following a strategy adopted in a previous study [90]. Typical curves of $E - \varepsilon$, for circumferential and radial samples, at each of the three strain rates are shown in Figure 3.3. In each modulus curve, three distinct regions were identified (indicated by the dotted lines in the Figure 3.3) in which the pattern of E values changed notably. In order to analytically define these regions, the gradient of each successive point established from the $E - \varepsilon$ graphs. If the gradient for 5 successive points identified an increasing trend in E values, the first point was considered the starting point of the second region. All the previous points were considered to be in the first region. Conversely, if the gradient remained zero in all of the 5 successive points, or alternated in sign in four points, the first point was considered the starting point of the third region. This resulted in:

(1) an initial region in which the modulus is constant (the modulus in this region will be referred to as E_1), implying that the respective $\sigma - \varepsilon$ curve is linear up to a strain of ε_1;
(2) a region in which the value of E increases with the increase in strain, up to a strain of ε_2, resulting in nonlinear behaviour in the respective $\sigma - \varepsilon$ curve; and
(3) a region of constant modulus (referred to as E_3), which results in a second linear section of the $\sigma - \varepsilon$ curve, up to the strain ε_3.

Beyond ε_3, there was a decrease in modulus (Figure 3.3), suggesting the initiation of microstructure failure which will subsequently lead to gross specimen failure. The values for ε_1, ε_2 and ε_3 at each strain rate are summarized in Table 3.2.

Recalling the typical stress-strain curves at different strain rates shown in Figure 3.2, a sudden transient decrease in stress was seen in the circumferentially loaded specimens at all strain rates. This can be seen to consistently occur in the second linear region of the $\sigma - \varepsilon$ curves, between ε_2 and ε_3. Further inspection highlighted

that the decrease occurred between $0.45 < \frac{\sigma_d}{\sigma_f} < 0.6$, where σ_d is the stress at which the decrease occurs and σ_f is the failure stress. No corresponding decrease was observed in the radially oriented specimens.

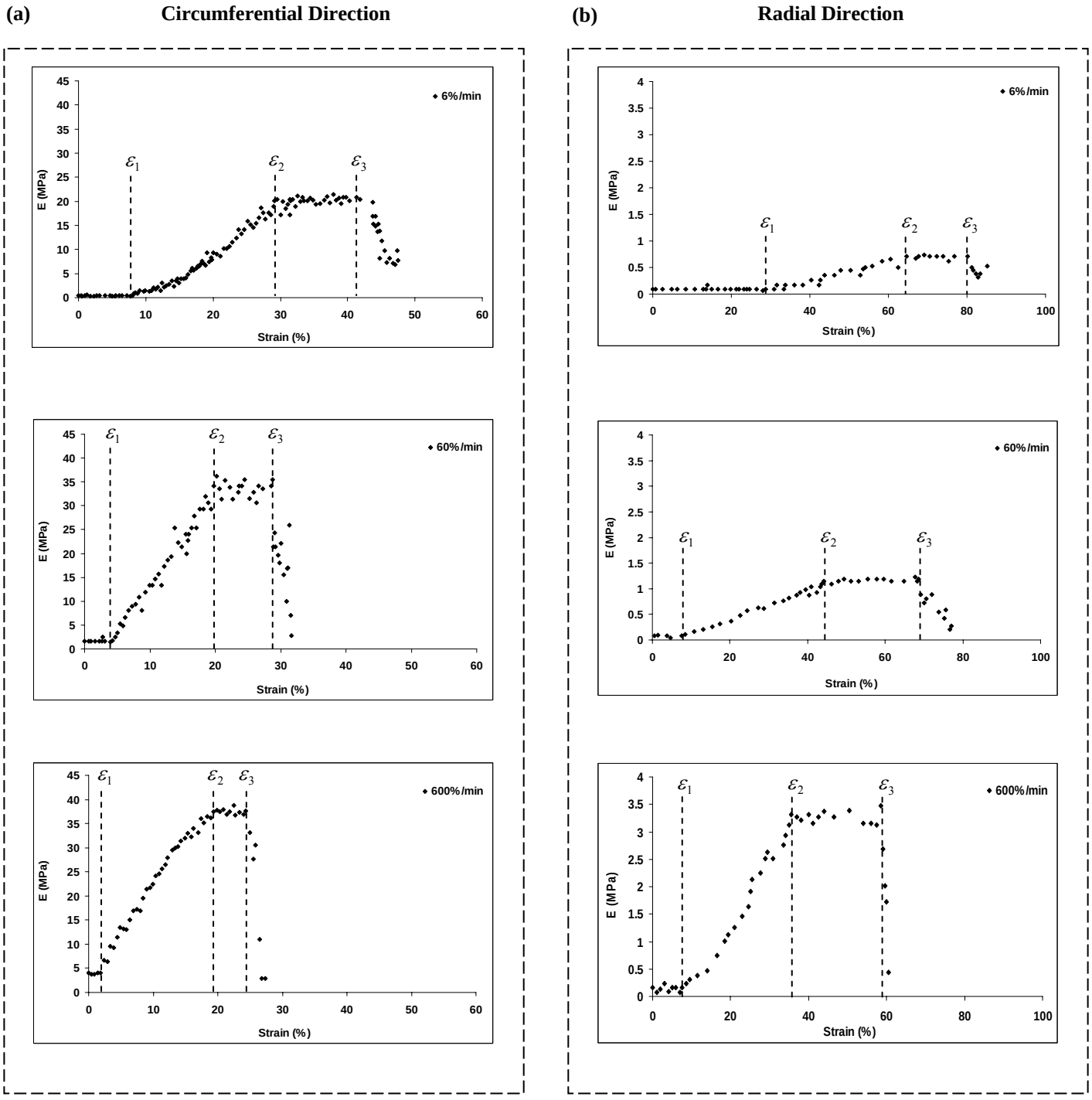

Figure 3.3 Typical $E-\varepsilon$ diagrams for the AV strips comparing: (a) circumferential specimens; and (b) radial specimens. The top, middle and bottom panels show the results at 6%/min, 60%/min and 600%/min strain rates respectively.

Table 3.2 Values (mean ± SD) of the mechanical parameters for each of the three regions of the stress-strain curves, evaluated experimentally in both directions and at different rates. The indices 1, 2, 3 indicate the first, second and third regions of the stress-strain curves, respectively.

Sample	Strain Rate (%/min)	E_1 (MPa)	ε_1 (%)	ε_2 (%)	E_3 (MPa)	ε_3 (%)
Circumferential	6	0.42 ± 0.16	8.05 ± 1.63	28.01 ± 2.61	20.4 ± 0.86	41.25 ± 2.06
	60	1.63 ± 0.14	4.28 ± 0.88	19.68 ± 2.22	34.07 ± 1.98	28.59 ± 1.77
	600	4.01 ± 0.42	1.91 ± 0.49	18.69 ± 2.37	37.54 ± 1.45	24.32 ± 1.36
Radial	6	0.085 ± 0.021	30.8 ± 2.95	64 ± 1.97	0.71 ± 0.8	80.5 ± 2.41
	60	0.088 ± 0.015	7.73 ± 0.16	44.62 ± 3.2	1.21 ± 0.09	69.11 ± 1.38
	600	0.15 ± 0.01	6.83 ± 0.04	35.58 ± 1.65	3.36 ± 0.10	58.52 ± 1.24

With increasing strain rate, larger values of E were evident in all regions, while the strain range for the initial linear region of the graphs decreased, quantitatively showing that the material becomes stiffer, in both directions (Figure 3.3, Table 3.2).

Stress-elongation $(\sigma - \lambda)$ data were fitted to the model in equations (3.13a) and (3.13b), for circumferential and radial specimens, respectively. E_{cir} and E_{rad} were determined by $(E_1 + E_3)$, obtained for each loading direction and strain rate (Table 3.2). The corresponding values for η_{cir} and η_{rad} were then estimated by the model. The model provided a good fit, as illustrated in Figure 3.4, with the R^2 values in excess of 0.98 for all of the experimental data sets. The values for the two parameters in each direction (E and η) are indicated in Table 3.3. The model clearly predicts a decrease in damping coefficient with an increase in strain rate for both circumferential and radial directions, indicating a 'shear-thinning' behaviour of the tissue.

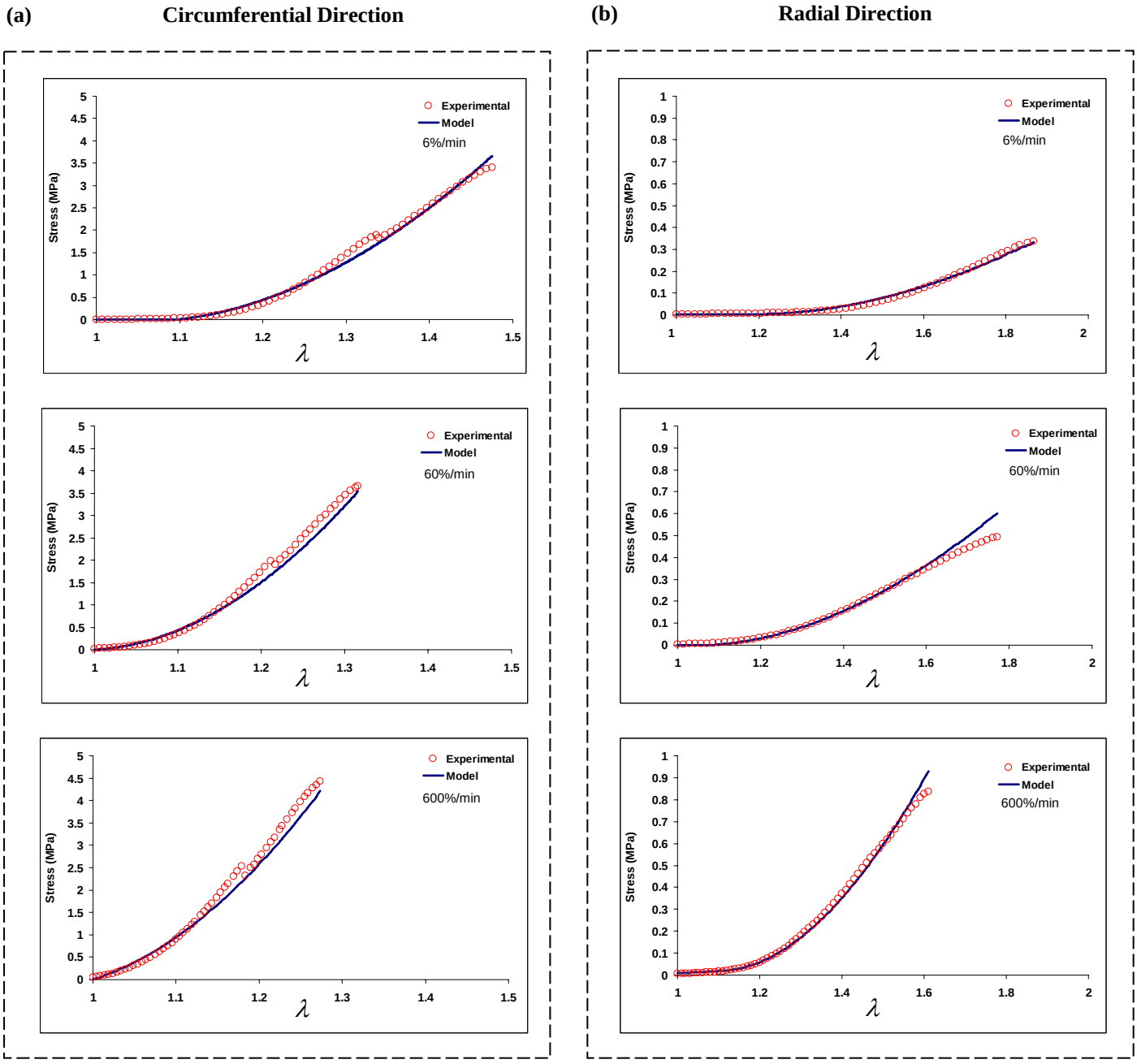

Figure 3.4 Typical experimental $\sigma - \lambda$ curves plotted alongside the model (equation (3.13)): (a) circumferential specimens; and (b) radial specimens. The top, middle and bottom panels show the curves at 6%/min, 60%/min and 600%/min strain rates respectively.

Table 3.3 The E and η values (mean ± SD) in both directions, at the different strain rates.

Strain Rate (%/min)	E_{cir} (MPa)	η_{cir} (MPa s)	E_{rad} (MPa)	η_{rad} (MPa s)
6	20.55 ± 2.45	675.06 ± 82.15	0.75 ± 0.28	49.12 ± 3.47
60	35.62 ± 0.97	152.50 ± 6.57	1.26 ± 0.08	6.17 ± 0.37
600	40.84 ± 2.05	18.48 ± 0.99	3.39 ± 0.53	4.59 ± 0.66

In order to investigate the hysteresis effects and associated irreversibility, AV specimens were subjected to single cycle loading and unloading tests, applying incrementally increasing loads until failure (§3.2.2). Figures 3.5a and 3.5b illustrate the typical resulting force-elongation $(F-\lambda)$ curves, where force is described as a percentage of the failure load ($F_{failure}$). The sudden transient decrease in force in the circumferentially loaded samples was again evident, within the same range as reported in quasi-static tensile tests (Figure 3.5a). The ratio of the unloading to loading area was calculated for each cycle, in both loading directions, as shown in Figure 3.5c. This ratio, which reflects the degree of specimen resilience, was consistently smaller in the circumferential direction, suggesting less circumferential resilience. In addition, the cycle associated with the sudden decrease in force consistently reported the minimum ratio, suggesting that this phenomenon is contributing to a further reduction in resilience within circumferentially loaded specimens.

It has been previously shown that the dissipation of deformation energy will lead to irreversible elongation of the continuum [100]. This could be examined in the present study by relating the percentage of change in sample length estimated from the difference between the length at the end of the cycle from that at the beginning (Figure 3.5d). These data demonstrate that the irreversibility of sample length is present in both loading directions even at small applied loads. However, the corresponding values are generally higher under circumferential loading.

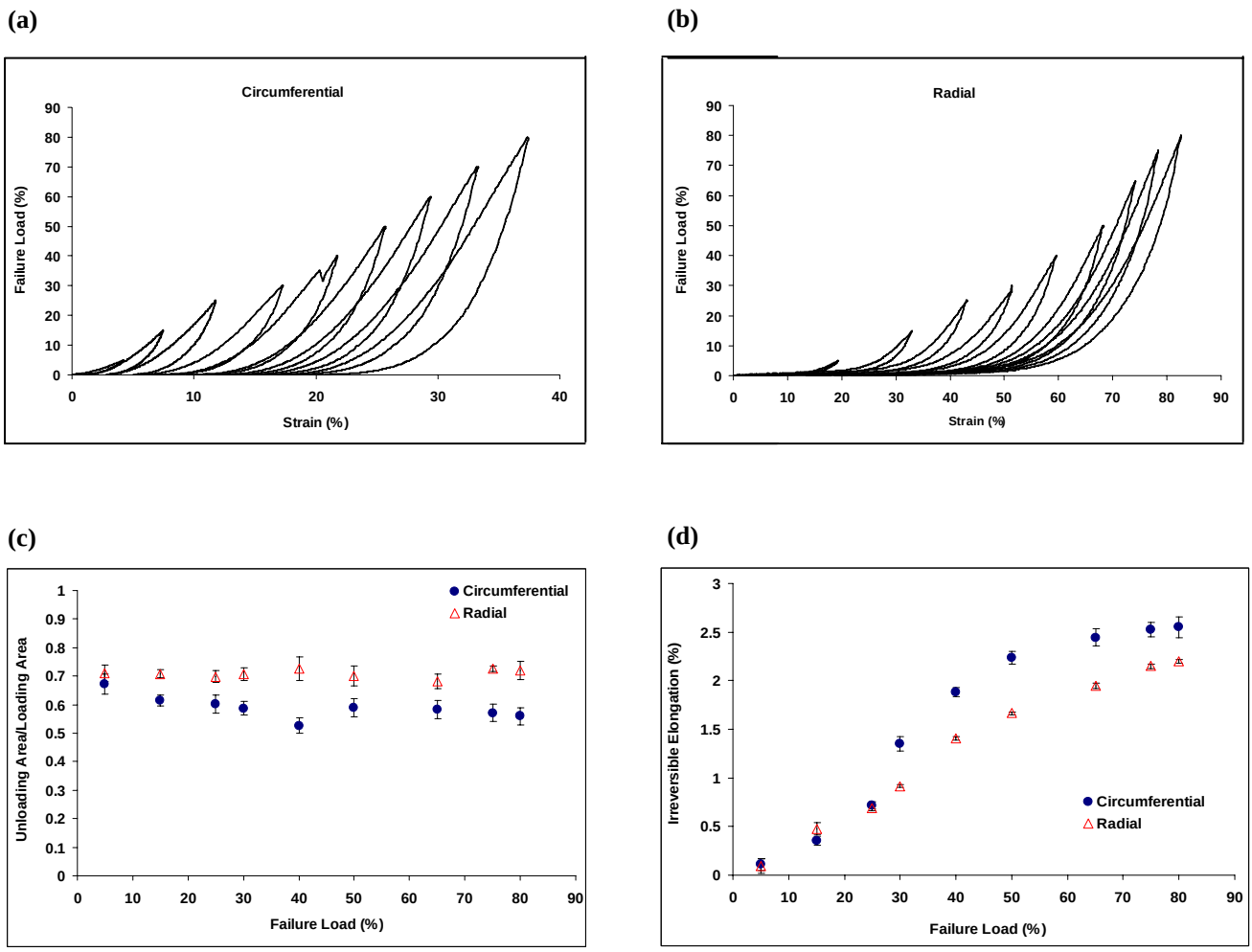

Figure 3.5 Hysteresis and recoverability of the AV strips. Typical force - extension curves for the incremental one-cycle loading-unloading tests for: (a) the circumferential; and (b) the radial specimens. (c) recoverability of the specimens (defined as the area underneath each loading curve divided by its unloading curve) in both directions. (d) irreversible elongation at the loading cycles for both directions.

3.5. Discussion

The viscoelastic response of the AV under tensile deformation was investigated and quantified in this chapter, using quasi-static mechanical tests, performed at different strain rates and under hysteresis loading. These tests have confirmed the previously reported nonlinear and anisotropic behaviour of the AV, with a stiffer response in the circumferential direction [5,65]. However, the present data have additionally demonstrated viscous damping effects, strain rate sensitivity and evidence of hysteresis and irreversibility during loading/unloading cycles, all of which also show dependence on the loading direction.

To maintain a definable and repeatable reference position for stress-strain curves, a tare load of 0.01 N was applied to all test specimens prior to start of the tests and recording the data, as described in §2.2. Application of a tare load will inevitably affect the extent of the observed pre-transition and transition phases of the stress-strain curves (defined in §1.3.2, Figure 1.12), also known as the toe-in region. However, the adopted tare load was two orders of magnitude smaller than the ultimate failure load of the samples (Table 3.1). Furthermore, comparisons with other uniaxial stress-strain curves reported in the literature, e.g. Sauren et al, 1983 [5], indicate similar trends and values. For a comparison within the toe-in region, Sauren et al report a stress value of ~ 300 kPa, at a strain level of 10%, in the circumferential direction under a uniaxial strain rate of 48%/min [5], which is closely matched with the 330 kPa value of stress in the current study at a strain rate of 60%/min (Figure 3.2). It is therefore reasonable to suggest that, while application of a tare load could influence the extent of the natural toe-in region of the tissue, the adopted level in this study did not have significant effects on the overall stress-strain behaviour and the failure properties of the samples.

A repeatable transient decrease in stress was observed in the $\sigma - \varepsilon$ response of the samples loaded circumferentially (Figure 3.2), not reported before in studies examining the AV mechanics. To establish whether this transient decrease was an intrinsic tissue property, or an artefact arising due to the sample slippage, two additional sets of tests were carried out. In the first set, ink markers were placed on the samples, adjacent to the grips, and filmed during the tests to failure (n = 6). Analysis of these videos, using image processing software (ImageJ, NIH), revealed no detectable change of relative marker positions during the tests. In the second series of tests, the corrugated surface of the grips were altered to reduce the surface friction coefficient, and establish if this led to change in the point at which the transient decrease occurred. The test was repeated on 6 samples, and the decrease consistently occurred within the same range. Taken together, the data indicate that it was an intrinsic aspect of the AV material behaviour in the circumferential direction. Indeed, a similar phenomenon has been reported when testing some other multi-layered collagenous tissues, such as carotid arteries [101], in which the sudden decrease in stress has been attributed to failure of the media layer, prior to the adventitia [101]. Analogous to the arteries, the AV also has two main load bearing layers, the

ventricularis and the fibrosa. The ventricularis contains less collagen and more elastin compared to the fibrosa, and is thus likely to fail first at lower stresses, prior to the ultimate failure point of the specimen. The repeated occurrence of this transient decrease in the specific stress range of $0.45 < \frac{\sigma_d}{\sigma_f} < 0.6$ further suggests this hypothesis, as it implies that it represents an intrinsic failure parameter of the tissue. Such a decrease was not observed in the radial direction. It is likely that since the collagen fibres are aligned circumferentially, the stiffness of the two layers is more uniform in the radial direction and, as a result, the failure strength of the layers is more closely matched.

A Kelvin-Voigt element-based model was introduced to describe AV viscoelasticity based on the three morphological layers of the valve (equations 3.13a and 3.13b). Incorporating the rate effects, the model revealed that the tissue shows 'shear-thinning' behaviour, with reduced effective viscosity at higher strain rates (Table 3.3). Such a behaviour can not be investigated and characterised under elastic deformation assumptions, and has not previously been reported for AV tissue. Nonetheless, a similar trend of behaviour has been observed and reported for concentrated proteoglycan solutions [101]. It seems reasonable to suggest that this behaviour in AV tissue could be attributed to the GAGs associated with the proteoglycans, mainly present within the spongiosa layer [17].

Extrapolating the value of η to a physiological strain rate of 15000%/min would predict values of $\eta_{cir} \cong 8.3$ MPa s and $\eta_{rad} \cong 3.9$ MPa s in the circumferential and radial loading directions, respectively. This would imply that the native AV tissue offers minimal resistance to internal shear forces induced by blood flow. It seems highly likely that such a property constitutes a fundamental requirement for any valve replacement. Indeed a material that does not exhibit sufficient shear thinning at physiological loads would perceive markedly increased shear stresses acting on the leaflet surface. This would inevitably reduce the effective lifetime of the substitute structure and further contribute to complications associated with haemolysis and blood coagulation.

With respect to the rate dependency, the stress-strain response indicate a pronounced rate sensitivity in both directions, with a 100-fold increase in strain rate leading to a 23% increase in mean UTS in the circumferential direction, compared to a 60% increase under radial loading (Table 3.1). This contrasts with previous studies which have reported negligible rate effects on the mechanical behaviour of the AV tissue [55,74]. However, this discrepancy may be a result of previous testing protocols employing a smaller range of strain rates, and may further be exacerbated by the modelling criteria. Indeed some of the well established viscoelastic models, such as quasi-linear viscoelasticity theory (QLV), would only accurately incorporate rate effects if an ideal step or ramp displacement is applied, which is impossible to achieve in experimental protocols [74].

The hysteresis experiments demonstrated greater resilience in samples loaded in the radial than circumferential direction (Figure 3.5c), suggesting lower radial dissipative damping effects. These data positively reinforce the modelling calculations, which predicted much lower damping coefficients for radially strained samples (Table 3.3). Furthermore, it was notable that samples did not show full reversibility in either loading direction at any of the prescribed strain rates. However, the continual loss of resilience in each cycle might not necessarily imply plastic deformation; it could be attributed to the reorganisation of the AV microstructure during loading/unloading cycles.

Chapter 4

Time-dependent behaviour of the aortic valve

The contents of this chapter have been published in:

Anssari-Benam, A., Bader, D. L., Screen, H. R. C. (2011) Anisotropic time-dependant behaviour of the aortic valve, J. Mech. Behav. Biomed. Mat., 4, 1603-1610.

4.1. Synopsis

The mechanical behaviour and material properties of the native AV were characterised under quasi-static loading conditions in chapter 3. However, similar to other collagenous connective tissues, the AV also exhibits time-dependent behaviour when subjected to specific loading conditions [5,55,69]. Time-dependent behaviour can be realised through either stress-relaxation or creep tests. The former reflects a decrease in load (stress) which occurs when the tissues are subjected to a constant elongation (strain), while creep describes the increasing elongation (strain) of the tissue under constant load (stress). These processes will also occur when samples are subjected to continuous cyclic perturbations, under either load or strain control [70].

Time-dependent spectra cannot be measured directly in experiments [103] and thus experimental data must generally be fitted to viscoelastic models, to estimate the associated moduli and characteristic times [69,74,103]. As reviewed in §1.3.2, studies investigating stress-relaxation of the AV under uniaxial strain, have generally adopted the QLV criterion to estimate the associated parameters. However, these studies have also indicated that stress-relaxation of AV cannot be fully described by the QLV model [5,69,72]. Indeed, QLV assumes that stress relaxation is independent of applied strain [104], an assumption which has not been confirmed in the relevant experiments.

The few studies examining biaxial time-dependent behaviour of heart valves have mainly employed equi-biaxial loading protocols, indicating that the valves may not exhibit a complete range of time-dependant phenomena under a equi-biaxial loading mode [69,75]. No measurable creep has been reported to occur within the time course of those experiments [69,75], suggesting that such loading boundary condition may not facilitate experimental observations of the complete range of time-dependent behaviour of the valves.

In light of these data, adoption of a uniaxial loading mode and alternative modelling criteria may be beneficial in assessing the time-dependent behaviour of the AV. Accordingly, this chapter investigates stress-relaxation and creep behaviour of the AV under uniaxial load, within the generalised Maxwell model criteria. Different strain and load increments are employed to assess how stress-relaxation and creep

parameters, respectively, depend on the level of applied stimuli. The experimental data are modelled with a generalised Maxwell model to determine the associated parameters, and gain insights into the underlying microstructural mechanisms.

4.2. Materials and methods

12 porcine hearts were used for this study. Test specimens were prepared according to the protocol described in §2.1, excised either circumferentially or radially from AV leaflets. This yielded a total 18 pairs of samples.

Sample thickness was measured as described in §2.1, and samples were then mounted and prepared for testing in the 'Bionix' material testing machine, to perform the stress-relaxation or the creep tests. The failure data obtained from tensile deformation tests at the strain rate of 60%/min (Table 3.1) were used to identify the range of load or strain increments for stress-relaxation and creep tests, each given as a percentage of the ultimate failure parameters. The pre-experiment adjustments were performed according to §2.2.

4.2.1. Incremental Stress-Relaxation Protocol

9 pairs of samples were subjected to incremental tensile stress-relaxation tests. Each sample was strained to eight increasing increments of strain, between 3% and 90% of the strain at failure ($\varepsilon_{failure}$), in both the circumferential and radial directions. The straining pattern is shown schematically in Figure 4.1, while details of the adopted strain increments are summarized in Table 4.1. A constant strain rate of 60%/min was used, and samples were held at each strain increment for 300 seconds.

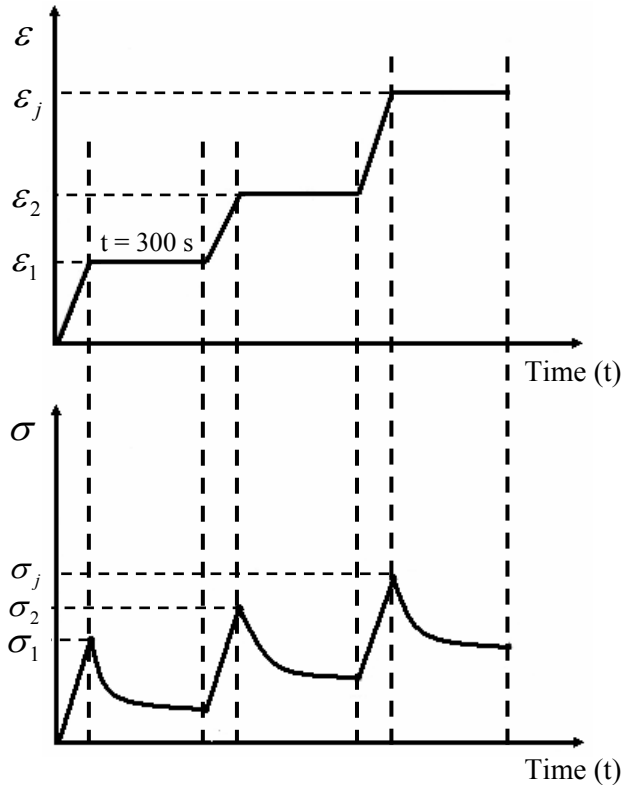

Figure 4.1 Schematic of the incremental stress-relaxation tests: uniaxial strain (ε) is applied to the tissue sample as a ramp up to a specific percentage of failure strain and then is kept constant for 300 seconds; the stress (σ) relaxes over the holding time in each increment.

Table 4.1 Details of strain increments for stress-relaxation tests.

	Circumferential Direction	**Radial Direction**
$(\%\varepsilon_{failure})$	Corresponding Strain (%)	Corresponding Strain (%)
3	1	2
5	2	4
10	3	---
15	5	10
20	7	15
30	10	25
40	---	30
50	15	40
60	20	---
80	25	60
90	---	70

4.2.2. Incremental Creep Protocol

9 pairs of samples were subjected to incremental tensile creep tests. Each sample was loaded to ten increasing increments of load, between 1% and 80% of the tensile load at failure ($L_{failure}$), in both directions. The loading pattern is shown schematically in Figure 4.2, and details of the adopted load increments are summarized in Table 4.2. A constant strain rate of 60%/min was used, and samples held at each loading increment for 300 seconds.

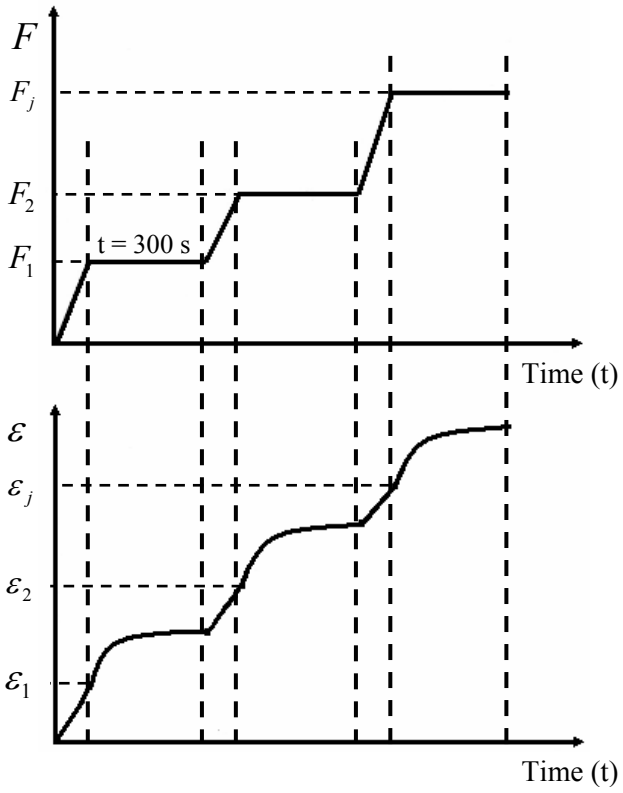

Figure 4.2 Schematic of the incremental creep test: uniaxial load (F) is applied to the tissue sample up to a specific value and then is kept constant for 300 seconds; the strain (ε) increases over the holding time in each increment.

Table 4.2 Details of load increments for creep tests.

Load Increment ($\%L_{failure}$)	Circumferential Direction	Radial Direction
	Corresponding Load (N)	Corresponding Load (N)
1	0.1	---
5	0.5	0.05
10	1.0	0.1
20	2.0	0.25
30	---	0.4
40	4.0	0.5
45	4.5	0.6
50	5.0	0.7
60	---	0.8
70	7.0	0.9
80	8.0	---

4.2.3. Model and Analysis

In order to estimate a series of time-dependant parameters, a generalized Maxwell model was employed, to analyse data from both stress-relaxation and creep experiments. For a generalized solid, composed of *n* Maxwell elements in parallel (Figure 4.3a), the relaxation spectrum is expressed by [103,105]:

$$\sigma(t) = \sigma_{\infty} + \sum_{i=0}^{n} \sigma_i \exp(-t/\tau_i) \tag{4.1}$$

where σ_{∞} is the value of stress at equilibrium, σ_i is the initial value of stress in *i*th element, and τ_i is the respective relaxation time of the *i*th element.

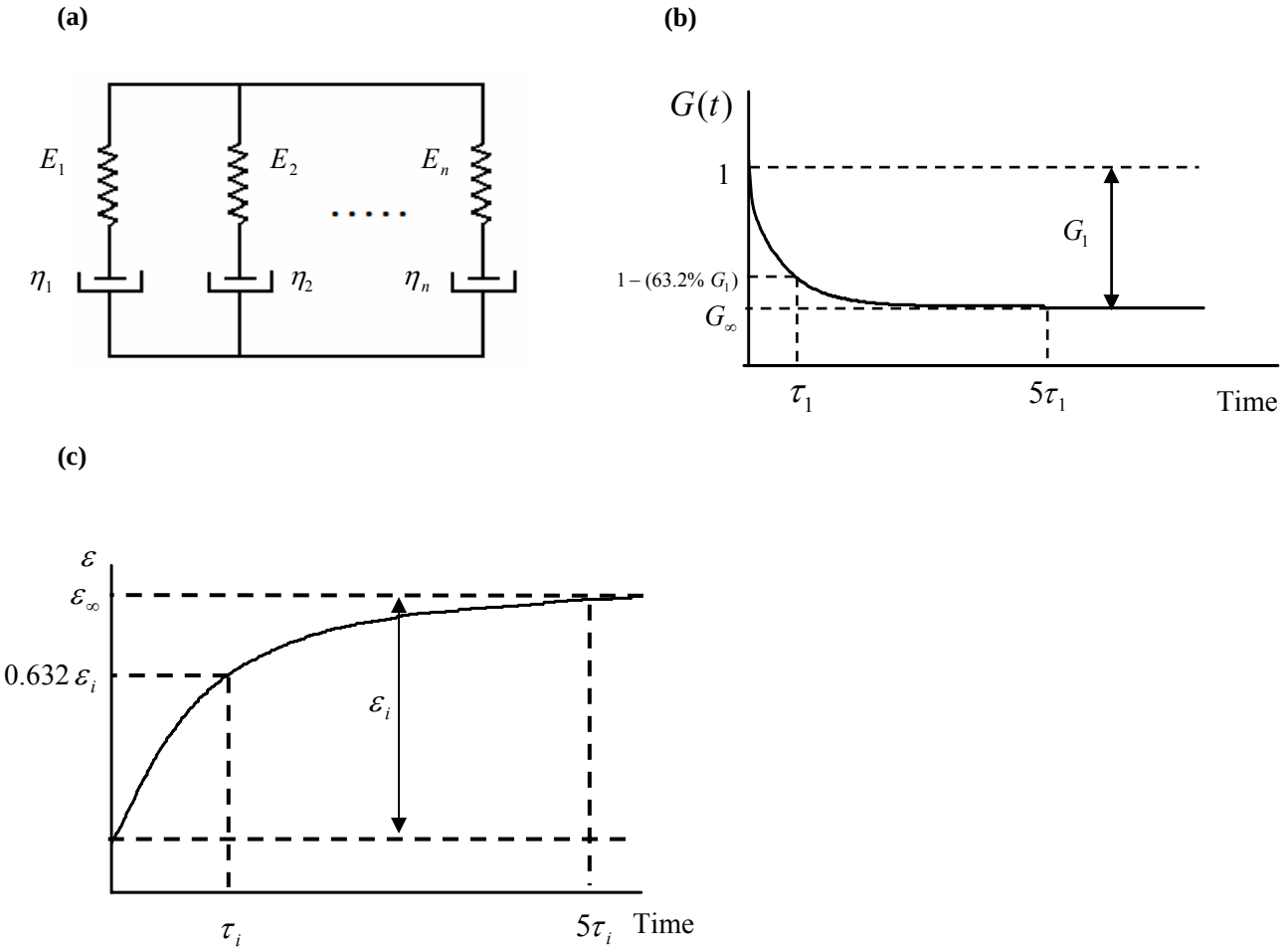

Figure 4.3 (a) schematic of a generalized Maxwell solid with *n* parallel Maxwell elements; (b) a typical single mode Maxwell relaxation curve; (c) a typical Maxwell creep curve.

The "normalized" stress relaxation function, $G(t)$, is found by dividing both sides of equation (4.1) by the initial value of stress in the relaxation process (σ_0), which yields:

$$G(t) = G_\infty + \sum_{i=0}^{n} G_i \exp(-t/\tau_i) \tag{4.2}$$

where G_∞ represents the normalized stress value at equilibrium and G_i is the amplitude of the relaxation mode of the *i*th element. τ_i indicates the time at which approximately 63.2% of the relaxation of the *i*th element has taken place, while 99% of the relaxation occurs within $5\tau_i$ [75], as indicated with a typical Maxwell-mode exponential decay curve in Figure 4.3b.

The generalised Maxwell model can be adapted to describe a creep response as [106,107]:

$$\varepsilon_{primary}(t) = \varepsilon_{\infty} - \sum_{i=1}^{m} \varepsilon_i \exp\left(\frac{-t}{\tau_i}\right) \tag{4.3}$$

where ε_{∞} is the asymptotic value of creep strain for the primary stage, ε_i is the amplitude of the creep strain of the *i*th element, and τ_i is the time for approximately 63.2% retardation of the *i*th element, as indicated with a typical Maxwell creep curve in Figure 4.3c.

However, this equation will only describe primary creep. In order to accommodate secondary creep, equation (4.3) must be adapted. It has previously been demonstrated that primary creep followed by a linear secondary creep, can be characterized in the form [108]:

$$\varepsilon_c(t) = \varepsilon_{primary}(t) + \dot{\varepsilon}_s t \tag{4.4}$$

where $\dot{\varepsilon}_s$ is the creep rate during the secondary creep stage [108]. The creep model describing primary and secondary creep regimes can therefore take the form:

$$\varepsilon_c(t) = \varepsilon_{\infty} - \sum_{i=1}^{m} \varepsilon_i \exp\left(\frac{-t}{\tau_i}\right) + \dot{\varepsilon}_s t \tag{4.5}$$

For the calculation of stress relaxation and creep parameters, equations (4.2) and (4.5) were curve fitted to the experimental data for each increment in the test protocols, using the Levenberg-Marquardt algorithm by Origin 8.0 software (Microcal™ Software Inc. USA). The number of time-dependant terms required to fit the data was determined based on the change in the chi-squared (χ^2) values of the fit. Starting from $i = 1$ in equations (4.2) and (4.5), the fitting process was iterated by the addition of a time-dependant term, and the corresponding χ^2 value was calculated at each i. The iteration was stopped when the reduction in the χ^2 value was less than an order of magnitude compared to the previous step, hence producing no significant further improvement in the fit [109].

4.3. Results

4.3.1. Stress-Relaxation

Typical normalized relaxation curves for samples loaded in both directions at different increments of failure strain ($\varepsilon_{failure}$) are shown as open circles in Figures 4.4a and 4.4b. All curves show a rapid initial relaxation, for each of the strain increments. In addition, samples show greater levels of relaxation in the initial low strains in both radial and circumferential directions. The variations between the 6 samples tested at each strain were small; all relaxation curves at $\varepsilon = 5\%\varepsilon_{failure}$ for each direction are shown in Figure 4.4c, as an example, but this is also reflected in the small standard deviations presented in Table 4.3, for all other strain increments.

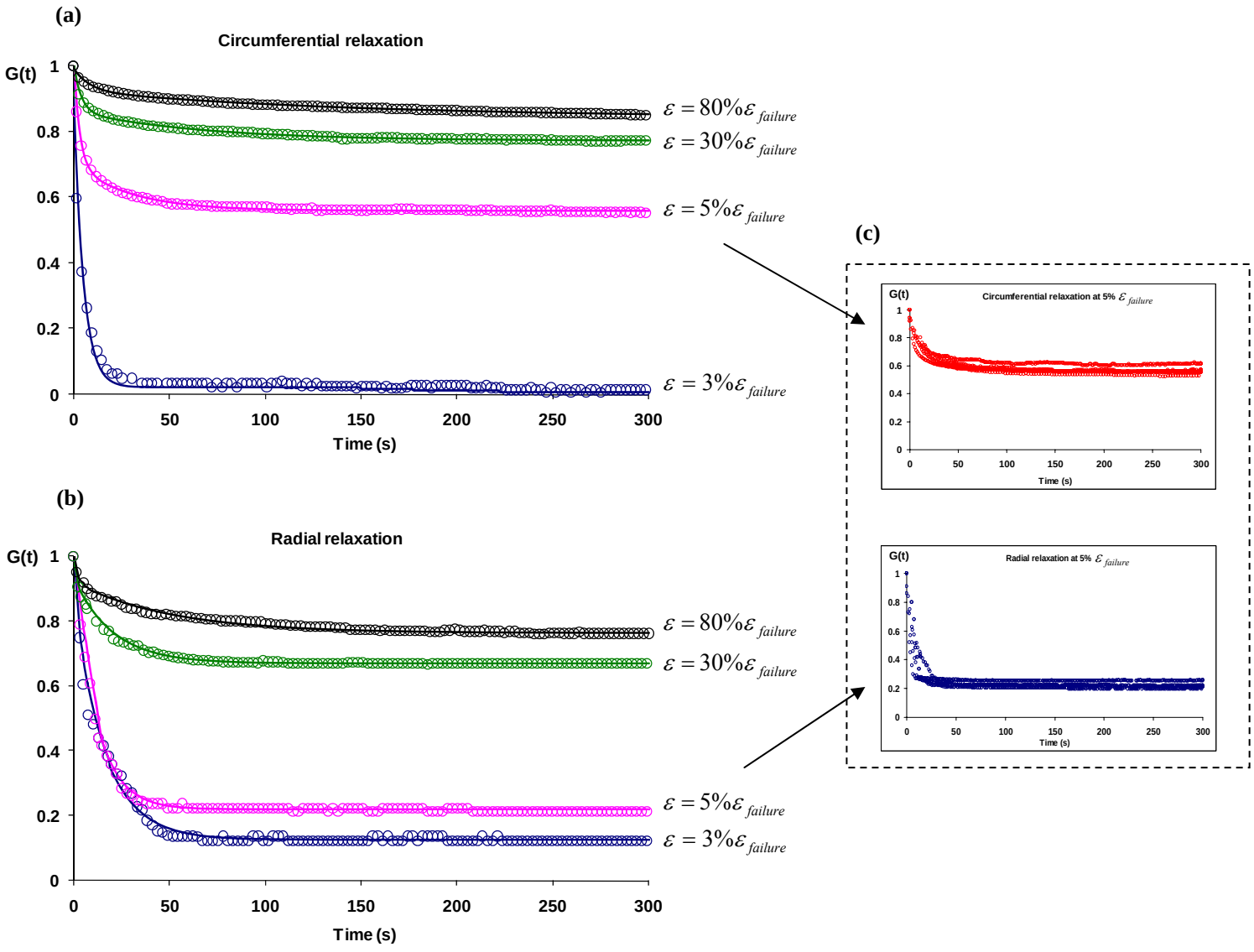

Figure 4.4 Typical normalized stress-relaxation curves for circumferential and radial samples. Experimental data are shown with circles (○), and the model with a continuous line (━). Graphs show: (a) relaxation in circumferential direction; (b) relaxation in radial direction; (c) stress-relaxation curves for the 6 repeats at $5\%\varepsilon_{failure}$ in both directions, to show the typical variation between the repeats.

The experimental data sets for both directions were fitted to the Maxwell model and plotted as continuous lines on Figures 4.4a and 4.4b. The model provided a good fit with the experimental data, with R^2 values in excess of 0.98 for all strain increments. However, modelling the data highlighted differences in the relaxation modes required to appropriately model the data, as summarized in Table 4.3. While a single mode describes the stress relaxation spectrum for strains below 5% of $\varepsilon_{failure}$ in the circumferential direction, a double mode is required for higher increments. By contrast, in the radial direction, a single mode was adequate to describe relaxation at all strain levels.

Table 4.3 Details of the test increments for stress-relaxation experiments: the resulting relaxation modes, and total amount (mean ± SD) of relaxation each increment.

Stress-relaxation				
	Specimen			
	Circumferential		**Radial**	
Strain Increments ($\%\varepsilon_{failure}$)	**Relaxation Modes***	**Relaxation at 300s (%)**	**Relaxation Modes***	**Relaxation at 300s (%)**
3	S	95.80 ± 2.91	S	85.09 ± 3.45
5	S	41.25 ± 3.56	S	76.96 ± 2.13
10	D	34.75 ± 2.04	---	---
15	D	29.72 ± 1.40	S	41.20 ± 1.44
20	D	26.35 ± 1.78	S	38.49 ± 2.13
30	D	22.80 ± 2.86	S	34.08 ± 2.22
40	---	---	S	30.01 ± 2.01
50	D	19.81 ± 1.28	S	26.59 ± 1.82
60	D	18.22 ± 1.71	---	---
80	D	16.38 ± 1.82	S	21.48 ± 2.80
90	---	---	S	18.85 ± 2.27

* S: Single, D: Double
--- : Not measured

The total percentage of relaxation at 300s for each strain increment is also given in Table 4.3. It is evident that the high relaxation values were associated with the smaller initial strains, with relaxation reducing with increasing strain increments, to values of 16.38% and 18.85 % in the circumferential and the radial directions, respectively. The relaxation times calculated by the model for circumferential and radial directions are illustrated in Figures 4.5a and 4.5b, respectively. Two relaxation times are indicated for strains above 5% of $\varepsilon_{failure}$ in the circumferential direction, referred to as 'fast' and 'slow' relaxation times, as the specimens showed a double relaxation mode (Figure 4.5a), while a single value is indicated for the radial direction (Figure 4.5b). As the applied strain increases, the amount of relaxation decreases, while the relaxation times increase, indicating a clear retardation in the relaxation process.

(a)

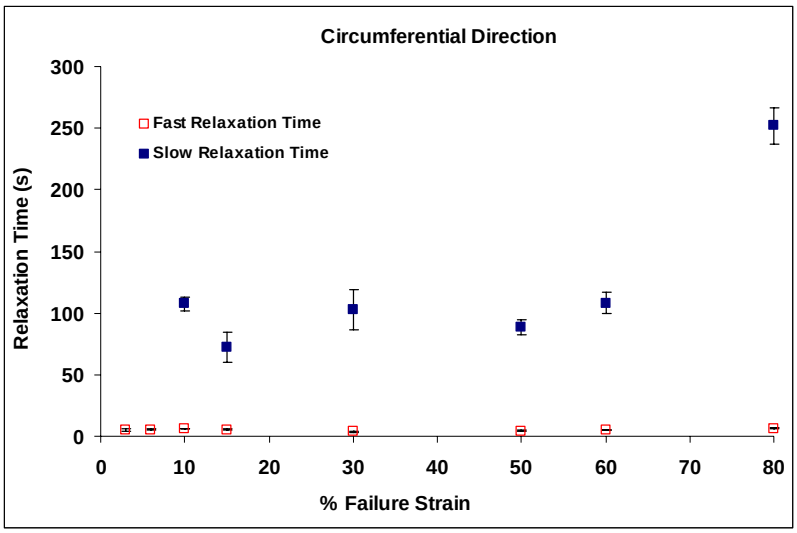

(b)

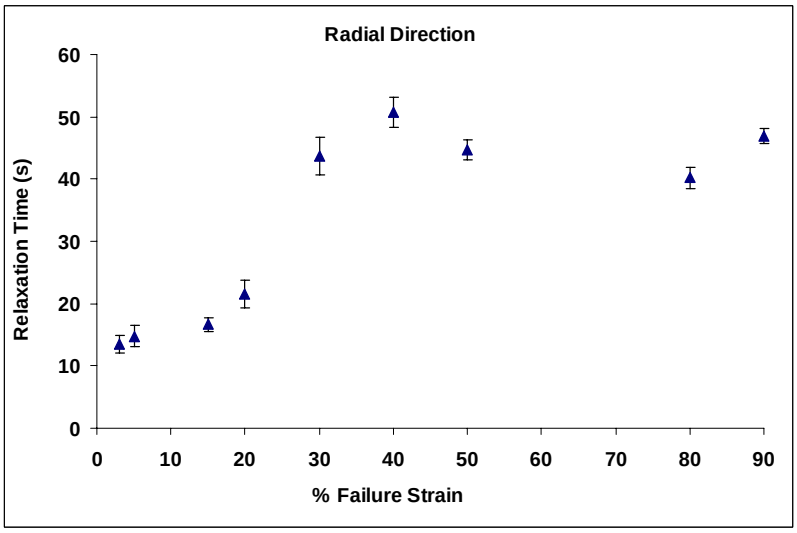

Figure 4.5 Stress-relaxation parameters as determined by the model for: (a) the circumferential direction; and (b) the radial direction. Two relaxation times (fast and slow) are given for the circumferential samples. All data points are presented as mean ± SD.

4.3.2. Creep

Typical creep curves for circumferential and radial samples at different increments of the tensile load at failure ($L_{failure}$) are illustrated in Figures 4.6a and 4.6b. The variations between the 6 samples tested at each load were small, as represented for the creep at $F = 5\%L_{failure}$ in Figure 4.6c as an example, but also reflected in the small standard deviations presented in Table 4.4, for all other loading increments.

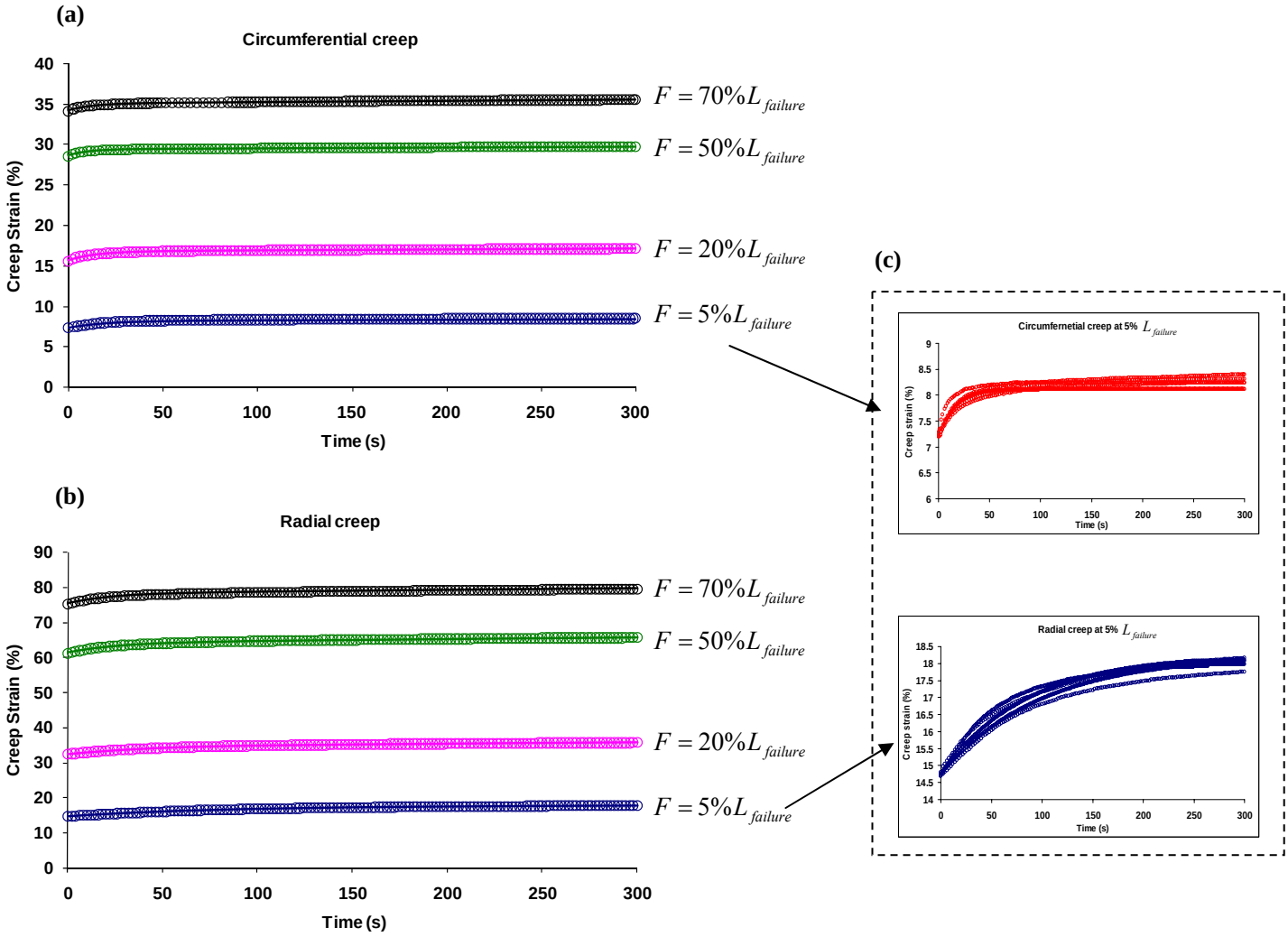

Figure 4.6 Typical creep curves from circumferential and radial samples. Experimental data are shown with circles (○), and the model with a continuous line (▬). Graphs show (a) creep strain in circumferential direction; and (b) creep strain in radial direction; (c) creep curves for the 6 repeats at $5\%L_{failure}$ in both directions, to show the typical variation between the repeats.

Samples show typical creep behaviour for soft tissues, with primary creep dominating the 300 seconds duration of every load increment, in both loading directions. The fitting of experimental data to the model (equation 4.5) yielded R^2 values greater than 0.98 for all load increments (Figures 4.6a and 4.6b). However, in the process of fitting, it became evident that a secondary creep mode was necessary to describe creep in all samples, with the exception of the data at low values of circumferential load ($F < 5\%\ L_{failure}$, Table 4.4).

The total amount of creep strain at 300s for each load increment is summarized in Table 4.4. There is a small increase in creep amplitude with increasing load increments for both directions. However, the radial direction showed consistently higher levels of creep compared to the circumferential direction, with values 3-4 fold higher at each corresponding load level (Table 4.4).

Table 4.4 Details of the test increments for creep experiments: the resulting creep behaviour, and total amount (mean ± SD) of creep strain each increment.

Creep				
	Specimen			
	Circumferential		**Radial**	
Load Increment ($\%L_{failure}$)	**Creep behaviour****	**Creep at 300s (%)**	**Creep behaviour** **	**Creep at 300s (%)**
1	P	1.05 ± 0.18	---	---
5	P	1.09 ± 0.18	P + S	3.06 ± 0.48
10	P + S	1.08 ± 0.16	P + S	3.18 ± 0.26
20	P + S	1.13 ± 0.16	P + S	3.36 ± 0.25
30	---	---	P + S	3.52 ± 0.26
40	P + S	1.23 ± 0.16	P + S	3.86 ± 0.32
45	P + S	---	P + S	4.06 ± 0.28
50	P + S	1.33 ± 0.17	P + S	4.35 ± 0.23
60	---	---	P + S	4.41 ± 0.34
70	P + S	1.52 ± 0.17	P + S	4.62 ± 21
80	P + S	1.85 ± 0.18	---	---

** P: Primary, S: Secondary
--- : Not measured

The creep retardation times (τ), as calculated by the model, are shown for each loading increment in Figure 4.7a. It is evident that retardation times generally decrease with the magnitude of the load increment in both loading directions. However, the nature of the decrease varies such that circumferential samples demonstrate a rapid decrease in retardation time, reaching a steady state value of approximately 11 s. By contrast, there is a monotonic decrease in retardation time of radial specimens, with a value of approximately 25 s at 70% of the $L_{failure}$ (Figure 4.7a).

The relationship between the secondary creep rate, $\dot{\varepsilon}_s$, and the load levels is illustrated in Figure 4.7b. While the secondary creep rate in the circumferential direction increases with increase in applied load, the values in the radial direction are notably higher at all corresponding load levels (Figure 4.7b).

(a)

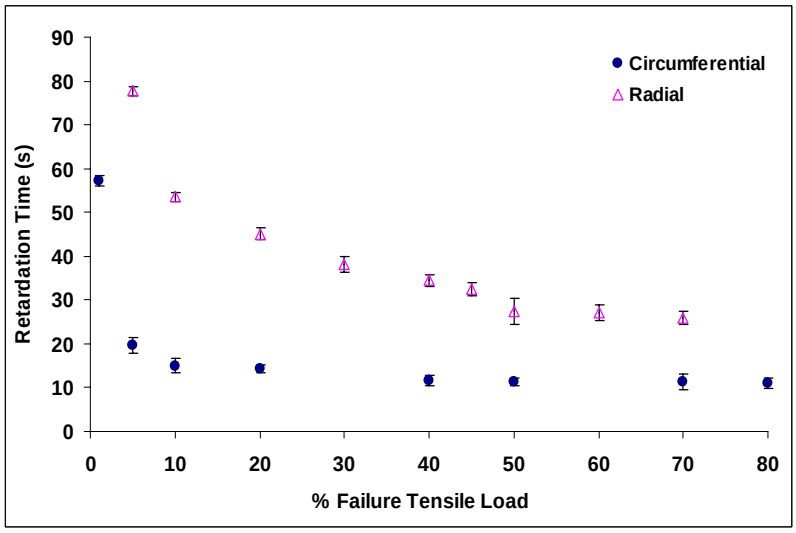

(b)

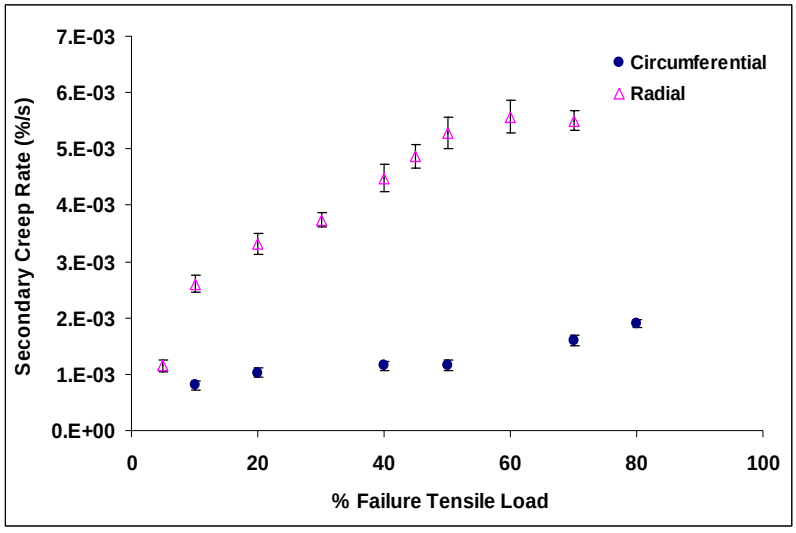

Figure 4.7 Creep parameters as determined by the model for different applied loads (% $L_{failure}$), comparing both loading directions: (a) the calculated retardation times; and (b) secondary creep rates. All data points are presented as mean ± SD.

4.4. Discussion

This chapter has considered the time-dependent behaviour of the AV in response to incremental tensile stimuli in both circumferential and radial loading directions. Both experimental and modelling data highlight that the time-dependent parameters show directional dependency. In addition, the data also indicates that stress-relaxation and creep behaviours both vary with the magnitude of applied strain or load, respectively.

In vitro biaxial loading protocols may more closely represent the complex physiological loading environment of the native valve. However, it has been previously shown that heart valve tissues may not exhibit creep behaviour under biaxial loading mode [32,69,75], and subsequently the underlying mechanisms of time-dependant behaviour may not be completely elucidated from biaxial test data. An assessment of uniaxial properties provides insights into both stress-relaxation and creep behaviours of the AV, and the underpinning knowledge necessary to analyse the mechanical behaviour of the native valve under more complex loading regimes.

As incremental strain and load protocols were employed in the current analysis, it is likely that the observed time-dependent behaviour is influenced by the history of the previous applied increments. However, previous studies of stress-relaxation behaviour in the AV have reported circumferential relaxation of approximately 25% under a direct strain of 30% of $\varepsilon_{failure}$ [5], which corresponds well with the value of the present study (Figure 4.4a, Table 4.3). Notably, the data is also in agreement with that reported for other collagenous tissues, such as tendons and ligaments, subjected to direct relaxation testing. Relaxations of about 40% have been reported within 300s at a strain level of approximately 2.5% [110], while 30% relaxation was reported at a strain level of approximately 5% [70]. In a supplementary test in the present work, two sets of samples were strained directly to a single increment of 60% or 80% of $\varepsilon_{failure}$, in the circumferential or radial direction respectively. The corresponding modes and values of relaxation were similar to those seen in the equivalent incremental tests, with total mean relaxation values of 21.6% and 26.2% respectively. Previous studies have also demonstrated that the estimated values of the time-dependent parameters will be influenced by the preconditioning protocols applied to

specimens of AV tissue [73,111]. Whilst no preconditioning was employed in this study, the relaxation tests at lower strain increments may arguably act as preconditioning load at higher strains. A recent study has indicated that if a sample does not fully relax prior to commencing another increment in a stress-relaxation test, the resulting relaxation curve will not reach equilibrium within the estimated relaxation time [111]. However the present data indicates that specimens consistently attained an equilibrium state within the estimated relaxation times (Figure 4.4), suggesting that the previous load history did not impose a pronounced preconditioning effect on specimen relaxation.

Considering the stress-relaxation data, the relaxation modes differed with respect to sample orientation, and also with strain increment in the circumferential direction (Figure 4.4, Table 4.3). It is well established that different viscoelastic modes represent different structural mechanisms involved in time-dependent spectra [110,112,113]. The current data would indicate that two structural mechanisms are activated during relaxation in the circumferential direction for strain levels above 5% of $\varepsilon_{failure}$, while a single mechanism is appropriate in describing relaxation for lower strains and when valve tissue is tested in the radial direction. Structurally, collagen fibres in the AV are predominantly aligned in the circumferential direction, and are primarily crimped in the unloaded state [5]. Hence, the single relaxation mode observed in the radial direction and for low strains in the circumferential direction might be attributed to the structural influence of GAG within the tissue, as it was established in chapter 3 that the viscous shear-thinning behaviour of GAG also influences the quasi-static behaviour of the AV samples. The uptake of a secondary relaxation mode occurs at increasing circumferential strains, where the structural crimp of the collagen fibres within the tissue is eliminated, and fibres become more straight and stretched [5]. Indeed, it has previously been shown that sliding between the stretched collagen fibres may represent a mechanism for stress relaxation in some connective tissues [113].

The experimental creep data showed that higher creep values, and subsequently higher creep compliance (defined as $\varepsilon(t)$ divided by σ [114]) were consistently observed in the radial direction (Table 4.4). When loaded circumferentially, samples

only exhibited primary creep over the 300s period for loading levels below 5% $L_{failure}$, implying that the primary creep rates are noticeably lower at those loading levels in the circumferential direction, and it takes more time to enter into the secondary creep stage. Additionally, the secondary creep rates in the radial direction were also higher than those seen circumferentially. These data further highlight a directional dependency to the time-dependent behaviour of the AV, with a greater probability of creep accumulation in the radial direction.

There is currently very limited literature regarding the creep phenomena in heart valves. Whilst no measurable levels of creep response are observed to occur under equi-biaxial loading conditions [32,69,75], the aortic valve is known to be strained non-equibiaxially *in vivo* [115,116], under which conditions some creep may well occur. The creep behaviour seen in the current uniaxial study indicates that the creep is an intrinsic time-dependent property of the aortic valve tissue. However, direct comparison between biaxial loading results and the results of the present study is problematic, as fibre kinematics under biaxial loading regimes are distinctly different to those under uniaxial load [1,65], and do not enable circumferential and radial strain responses to be independently established.

The primary and secondary creep behaviour observed in the present work is similar to that reported for other collagenous tissues under uniaxial loading [117-119]. Indeed, the present values for secondary creep rates of AV tissue in the circumferential direction were comparable to those reported for tendons [118]. As tendon is composed predominantly of collagen, the current data may indicate that it is the collagen fibre content of the valve which dominates the circumferential creep phenomena.

Recent studies investigating the structural origins of time-dependant behaviour within heart valves have reported that the collagen fibril D-period decreases during stress-relaxation, but remains approximately constant during creep [69,75]. This has been referred to as the ‘fibre-level locking’ mechanism, and has been suggested to be a possible structural mechanism responsible for the observed time-dependent behaviour of the valves at the tissue level [69,75]. However, it is currently not clearly

understood how, and if, this phenomenon is related to the time-dependent modes observed at the tissue level. The microstructural mechanisms involved in the time-dependent behaviour of the AV will be studied experimentally in more detail and analytically modelled in chapters 10 and 11.

Chapter 5

Strain transfer through the aortic valve:
from tissue to the fibrous network

The contents of this chapter have been presented at:

Anssari-Benam, A., Bader, D. L., Screen, H. R. C., Inhomogeneous local micro strain fields in aortic valve leaflet, *6th World Congress on Biomechanics*, August 2010, Singapore.

and published in:

Anssari-Benam, A., Gupta, H. S., Screen, H. R. C. (2012) Strain transfer through the aortic valve, J. Biomech. Eng., 134 (6), 061003, doi: 10.1115/1.4006812.

5.1. Synopsis

The quasi-static and time-dependent behaviours of the AV at the tissue level were investigated in chapters 3 and 4. In the following chapters, AV micromechanics will be investigated, and the response of the valve microstructure and how it contributes to the observed tissue level behaviour will be established and discussed.

In the first step, the strain transfer from the tissue level to the fibrous network (FN) within the AV will be investigated. Collagen and elastic fibres (elastin) [13] provide the main structural elements of the AV matrix, and their combined network, referred to as the fibrous network (FN) here, provides the main load bearing element of the valve ECM. However, it is currently unclear how the externally applied deformations at the tissue level are transmitted through the layers of the valve microstructure [120], with little data on strain mapping within the FN to correlate the tissue-level deformations to the local structural deformations [23,80].

Investigating this correlation can prove significant as it further clarifies two important aspects of structure-function relationships within the AV tissue:

(i) from the tissue mechanics point of view, it addresses the mode of strain transfer, i.e. affine or non-affine, from the tissue level to the microstructure. The mode of strain transfer is a key feature of microstructural based models, and is important for a more accurate characterisation of the role of the FN in the mechanical behaviour of the tissue. Furthermore, quantifying the strain distribution across the FN will establish the extent of strain inhomogeneity throughout the AV matrix; and

(ii) from a cell mechanobiology perspective, it is a key step towards quantifying the local mechanical environment surrounding the valve cells. Cells are known to be attached to the FN [23,85,121], thus deformation within the FN may induce deformation in the residing cells [23,85]. This is of particular interest, as aortic valve interstitial cells (AVICs) have been documented to perceive and react to their local mechanical environment, altering ECM metabolism and remodelling [80,81], cell phenotype [24,84,86] and cell stiffness [80,85]. This range of cellular functions plays an important role in maintaining homeostasis in the native valve [80,81], and affect the mechanical behaviour of the AV leaflet *in vivo* [80,82]. AVICs are also likely to

play a role in pathology of the AV, possibly triggering responses which lead to valve degeneration and calcification, if exposed to inappropriate deformations [22,24,86]. These data suggest that quantifying the local mechanical environment perceived by the AVICs *in situ* is key in understanding and interpreting their mechanotransductive behaviour in the native AV. It will also provide primary knowledge for a successful cell-mediated tissue engineering strategy [120].

Studies employing microstructural based models for characterising mechanical behaviour of AV tissue, as well as those examining mechanobiology in valve cells, have generally utilised the assumption of a direct transformation of mechanical stimuli from the tissue to the collagen fibres [66,122], and to the cells [80,123], respectively. However, the complex structural organization of the ECM within the AV may not facilitate a model of direct transformation or translation of tissue level mechanical stimuli through the AV matrix. This is due to the non-uniformity of the fibre kinematics in the ventricularis and fibrosa [1,32,124], and the relative movement of the two layers provided by the spongiosa layer, resulting in internal shearing [13,18].

To address this, the present chapter investigates the correlation between applied strains at the tissue level, macrostrains across the AV tissue surface, and FN deformations. The distribution of strain fields throughout the FN is characterised, to establish the inhomogeniety and non-uniformity of FN strains, comparing the behaviour of the ventricularis and fibrosa layers.

5.2. Materials and methods

32 porcine hearts were used for this study. Specimens were prepared according to the protocol described in §2.1, excised either circumferentially or radially from AV leaflets. This yielded a total of 48 radial and 48 circumferential samples.

5.2.1. Fibrous network strain mapping

The technique for mapping strains within the tissue matrix followed that discussed in §2.3. A total of 36 pairs of circumferential and radial cut strip samples were used for mapping the strains within the FN, with each set divided in two further analysis groups in order to investigate strain across the FN in either the ventricularis or fibrosa layer of the valve. The resulting 4 test groups, each containing 18 samples, were: (i) circumferentially cut samples viewed from the ventricularis side, (ii) circumferentially cut samples viewed from the fibrosa side, (iii) radially cut samples viewed from the ventricularis side; and (iv) radially cut samples viewed from the fibrosa side. Imaging was carried out at a depth of 50 to 80 μm into the designated valve layer. A typical image of the cell nuclei captured using the described set up is presented in Figure 5.1.

In order to investigate the distribution of local strains across the FN of each specimen strip, samples were divided into 5 hypothetical equidistance regions as shown in Figure 1b: C denotes the central region, and RI, RII, LI and LII, the two regions to the right and left to the central region, respectively. The boundary regions between each of these areas were then selected for imaging, giving 6 imaging locations along the sample length (Figures 5.1). Samples were incrementally strained in 2% increments from 0% to 20% in the circumferential direction, and from 0% to 40% radially, at a rate of 60%/min consistent with the previous macro-mechanical experiments discussed in chapters 3 and 4. Cells within the selected sample regions were imaged at each increment. Any individual test looked at a sample cut either circumferentially or radially, viewed from either the fibrosa or ventricularis side at one of the 6 locations. 3 repeat samples were tested for each imaging location.

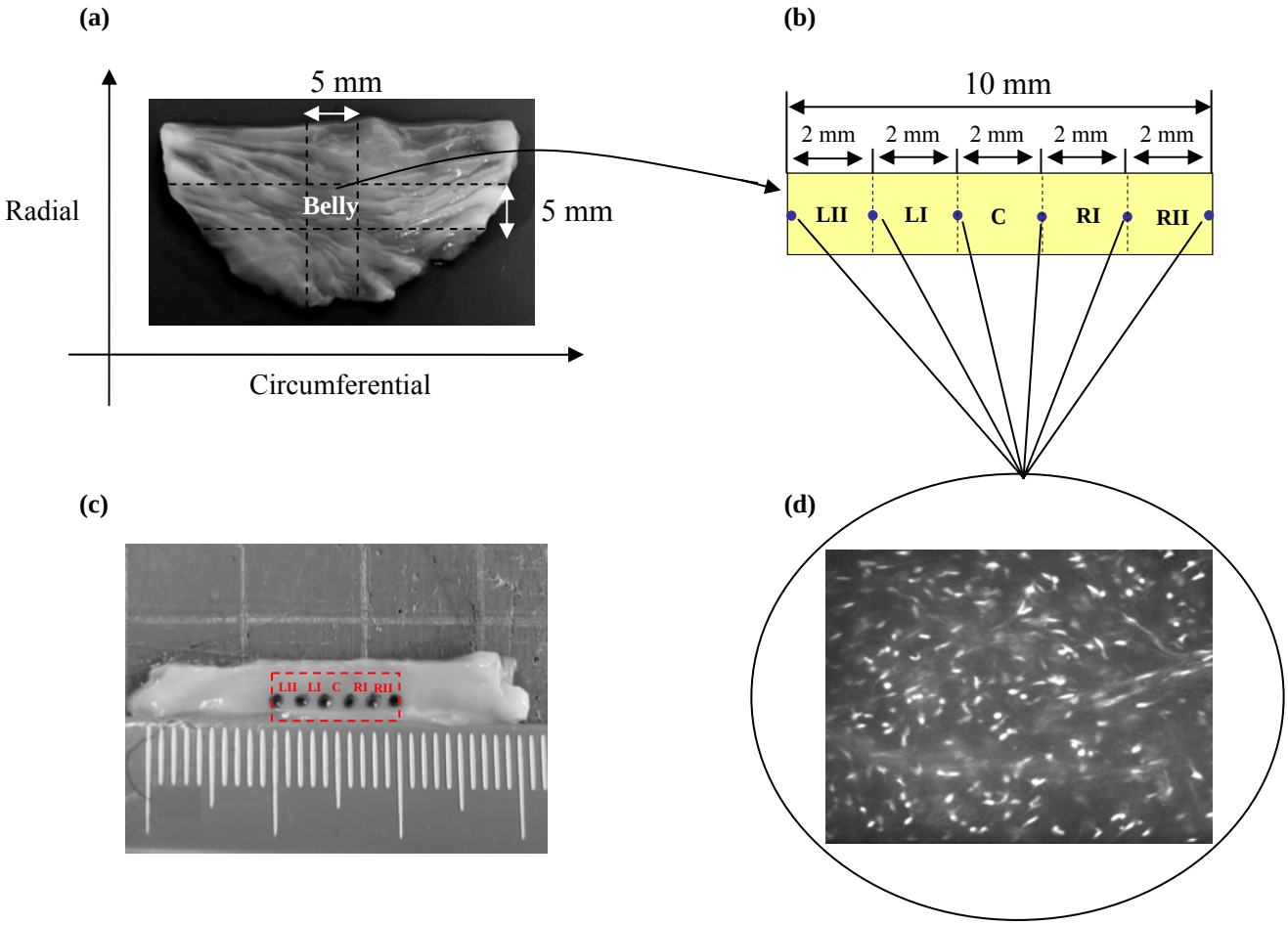

Figure 5.1 (a) An AV leaflet: 5 mm wide strips are cut from the belly region, in either the circumferential or radial direction; (b) Schematic of a strip specimen showing the 5 defined equidistance regions. Blue circles represent the boundary regions that were tracked by the confocal microscope; (c) For macro analysis, the specimen strips were ink marked every 2 mm over a 10 mm length, resulting in 5 equidistance regions designated by C, RI, RII, LI and LII, similar to the defined regions for analysis of FN strains; (d) A typical confocal microscopy image of cell nuclei within a boundary region.

From each resulting set of images, the movement of all the cells within the field of view (670 μm × 500 μm) was tracked with increasing strain increment, using particle tracking software (IMARIS®, Bitplane AG) to determine the (x, y) coordinates of the centroid of each nucleus at every strain increment. Using these positions, the displacement of each nucleus at each strain increment was calculated in the loading direction, resulting in a frequency distribution of nuclei displacements at each increment (Figure 5.2). To determine the mean nuclei displacement at each increment, the weighted average of each distribution was calculated as:

$$\bar{d} = \frac{\sum_{i=1}^{n} x_i d_i}{\sum_{i=1}^{n} x_i} \tag{5.1}$$

where n is the binning (i.e. number of groups of the nuclei having the same range of displacement), i indicates each group, x_i and d_i are the number of cell nuclei and the displacement of the ith group, respectively. The accumulative displacement of nuclei with increasing strain increment was then calculated by summing the mean nuclei displacement at each increment $\bar{d}$. As the cells are bonded to the fibres, the displacement of cells indicates the elongation of the FN as the tissue is strained, shown schematically in Figure 5.3 for one local region. To finally achieve the strains within the FN of each sample region, the mean relative displacement of cells at each end of that region were subtracted to establish the mean elongation, and strains calculated accordingly.

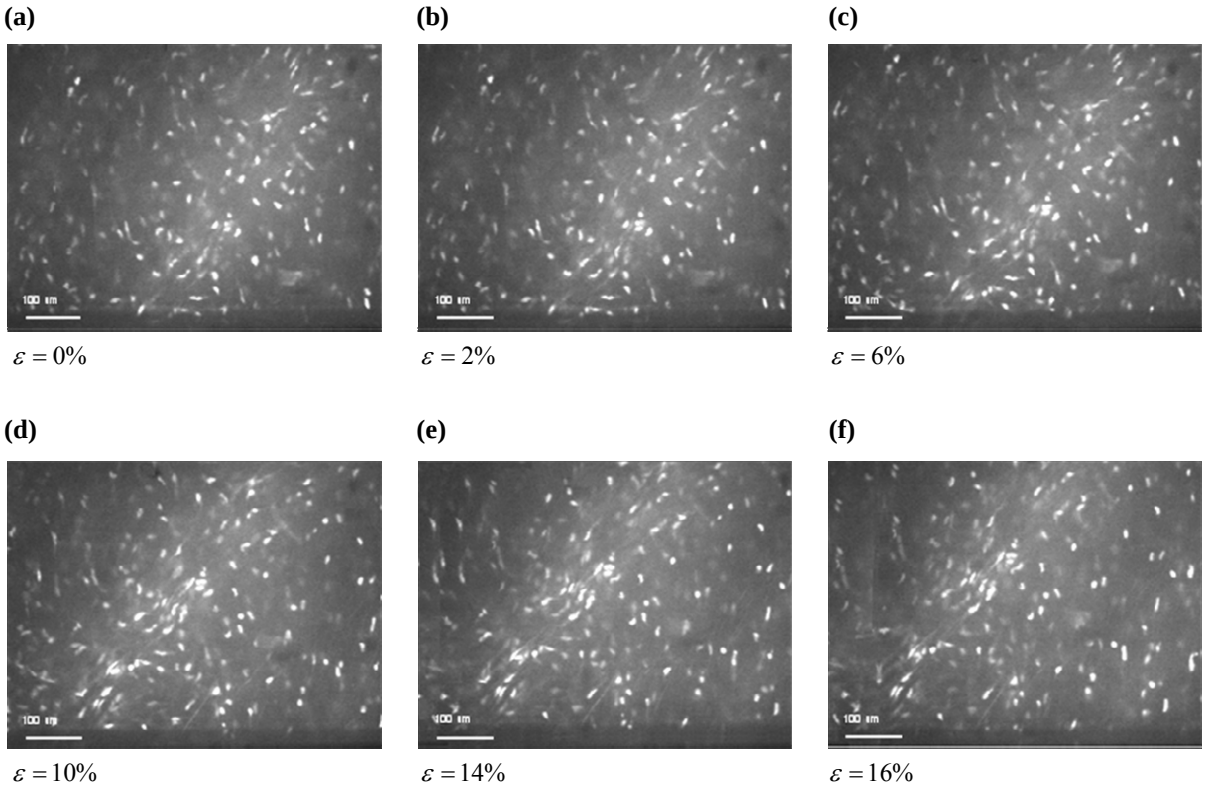

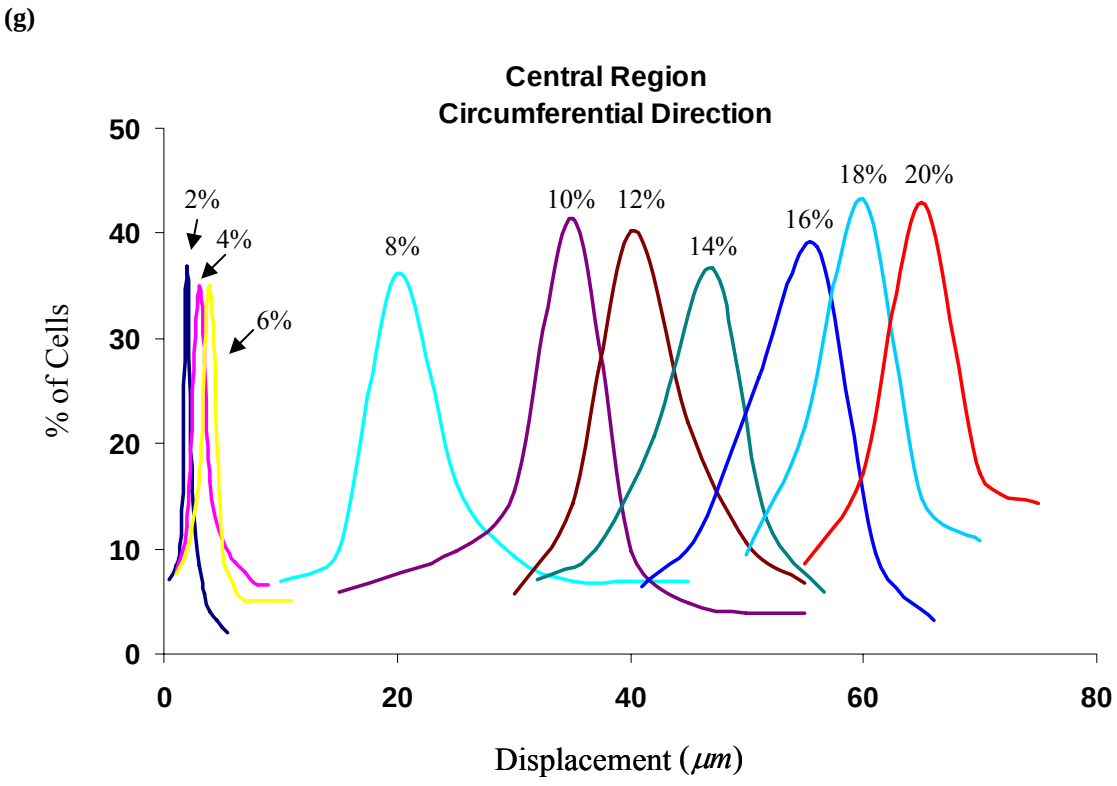

Figure 5.2 (a-f) A typical sequence of images of a group of cells tracked at each applied strain increment. The strain increases from (a) to (f), as given next to each image. (g) The frequency plot of nuclei displacement at each strain increment for the same group of cells. The strain increment is shown next to each distribution. Each distribution shows only the displacement occurring during that increment, and is not cumulative.

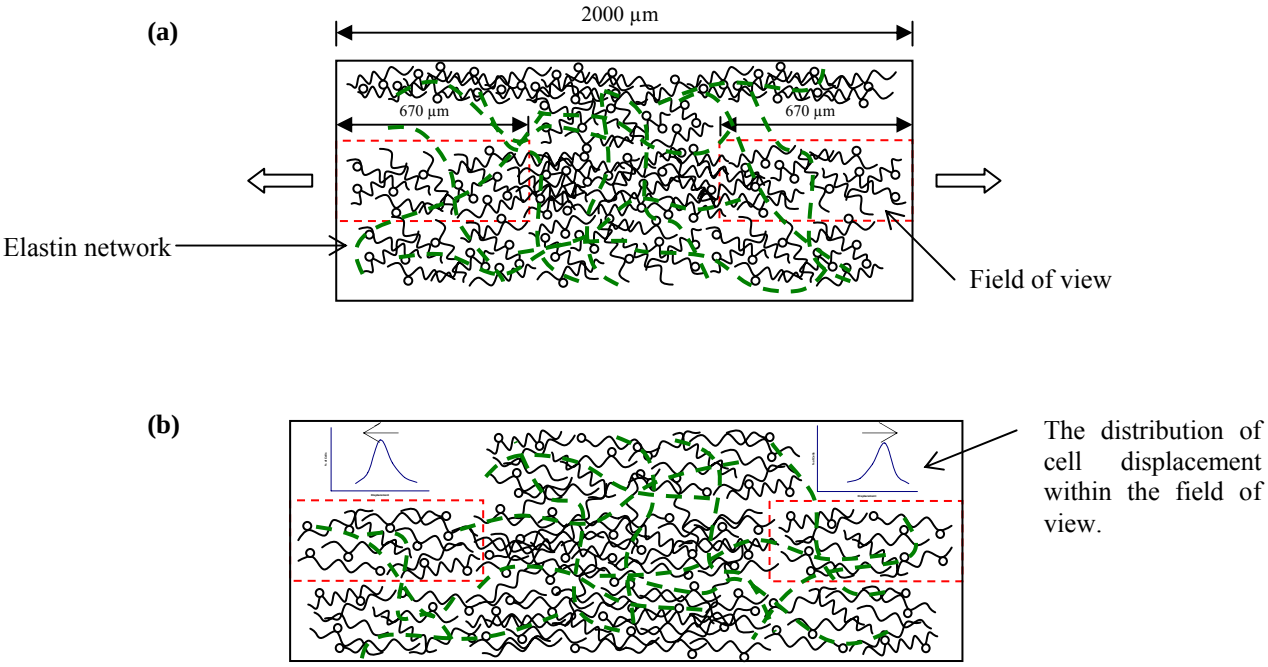

Figure 5.3 Schematic depicting the fibrous network within one of the defined regions of the specimen, under tissue level deformation. Upon the application of strain to the sample (3a), fibres rotate and displace, resulting in elongation of the entire network (3b). The movement of the fibres can be inferred through monitoring the movement of the cell nuclei, as the cells (hollow circles) are attached to the fibres. Dashed boxes highlight the size of the field of view at either end of a specimen region.

5.2.2. Macrostrain mapping

In order to assist in the interpretation of the FN strain data, macrostrains across the sample surface were correlated with the applied grip to grip strains, by tracking surface makers. 12 circumferential and 12 radial strips were ink marked every 2 mm over a 10 mm length (Figure 5.1c); 6 on the fibrosa surface and 6 on the ventricularis surface. The 5 resulting equidistance regions across the strip matched the regions used for the FN strain mapping (Figure 5.1). Following the protocol outlined for the FN strain analysis, samples were secured in the rig, strained in 2% increments at 60%/min, and imaged at each increment. The images were analyzed using image analysis software (ImageJ, NIH, USA), and the relative displacements of the adjacent markers used to calculate macrostrains in each region.

5.2.3. Statistical analysis

Statistical comparisons between the FN strain values in each region were performed using paired *t*-tests. The statistical significance was set at $p < 0.05$. Data in the figures are presented as the mean and standard error of the mean $(n = 3)$.

5.3. Results

5.3.1. Fibrous network strain mapping

A typical series of images tracking nuclei displacement with increasing strain increment are shown in Figure 5.2, taken from the central region of a circumferentially loaded sample. The frequency distribution plot showing nuclei displacement at each strain increment for this typical sample is shown in Figure 5.2g. Each distribution shows only the displacement occurring during that increment, and is not cumulative.

Frequency distributions of nuclei displacement were drawn for each applied strain increment in every test, from which the mean accumulative FN strain in each of the 5 test regions was calculated. Graphs comparing these FN strains in circumferentially and radially cut samples from both the ventricularis and fibrosa sides of the valve are shown in Figure 5.4. It is immediately evident that the relationships between applied strain and FN strains are non-linear, particularly in the circumferential direction, in which there are very low initial network strains. Comparing strains across the length of the samples, the FN strain in the central region was greatest in all cases, decreasing nearer to the gripping points (RII and LII regions). Under circumferential loading, for applied strains in excess of 8% and 10% in the ventricularis and fibrosa layers respectively, the network in the central region strains significantly more than in the other four regions (Figures 5.4a and 5.4b). However, the central region strains only became significantly larger at strain levels above 18% and 24% for the ventricularis and fibrosa layers, respectively, under radial direction loading (Figures 5.4c and 5.4d). It is notable that no significant differences were seen when comparing the FN strain

values between the symmetrically opposing regions, i.e. between RI and LI and between RII and LII, in the two layers in either loading direction.

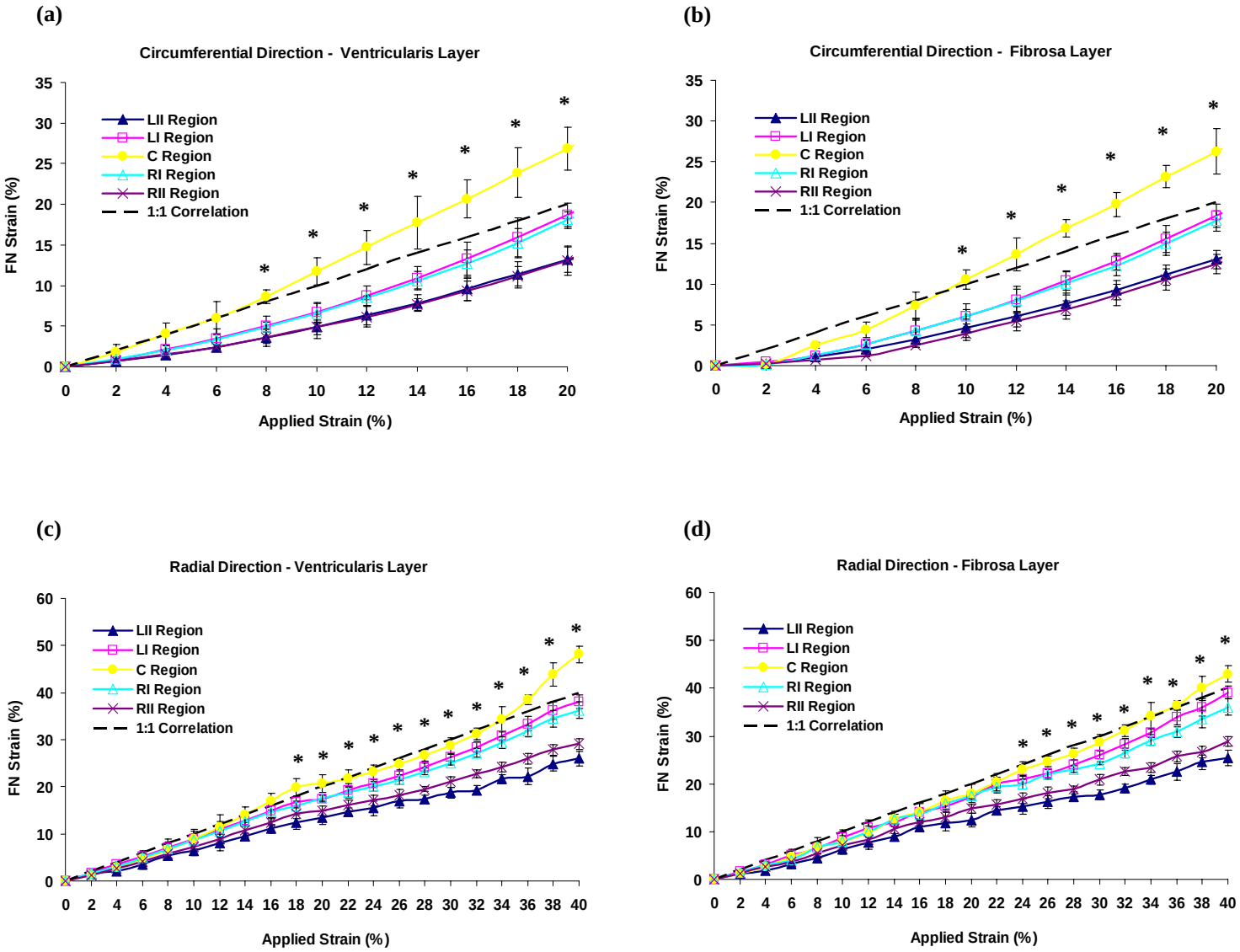

Figure 5.4 FN strains at different applied strains for specimens viewed from: (a) the ventricularis layer; and (b) the fibrosa layer, loaded in the circumferential direction. The network strains in the central region are significantly higher compared to those in other regions at applied strain levels above 8% and 10%, in the ventricularis and fibrosa layers, respectively. FN strains for samples viewed from (c) the ventricularis layer; and (d) the fibrosa layer, loaded in the radial direction. FN strains in central region become significantly higher than the other regions at strain levels above 18% and 24% for the ventricularis and fibrosa layers respectively. No significant differences between microstrains in the symmetrical regions (RI-LI and RII-LII) were seen. Dashed lines indicate the 1:1 linear correlation between the applied strain and FN strain. The asterisks indicate statistical significance ($p < 0.05$) between the central region and all other regions.

5.3.2. Macrostrain mapping

In order to establish if the distribution of strain within the FN is also reflected at the macro level, the macrostrains in each sample region were also calculated with increasing applied strain (Figure 5.5), comparing circumferential and radial loading directions from both the ventricularis and fibrosa sides. The 1:1 correlation is shown as a dotted line in the graphs. It is notable that macro strains across the samples were smaller than the overall applied strains. However, strains in the central region more closely matched the applied strains (Figure 5.5).

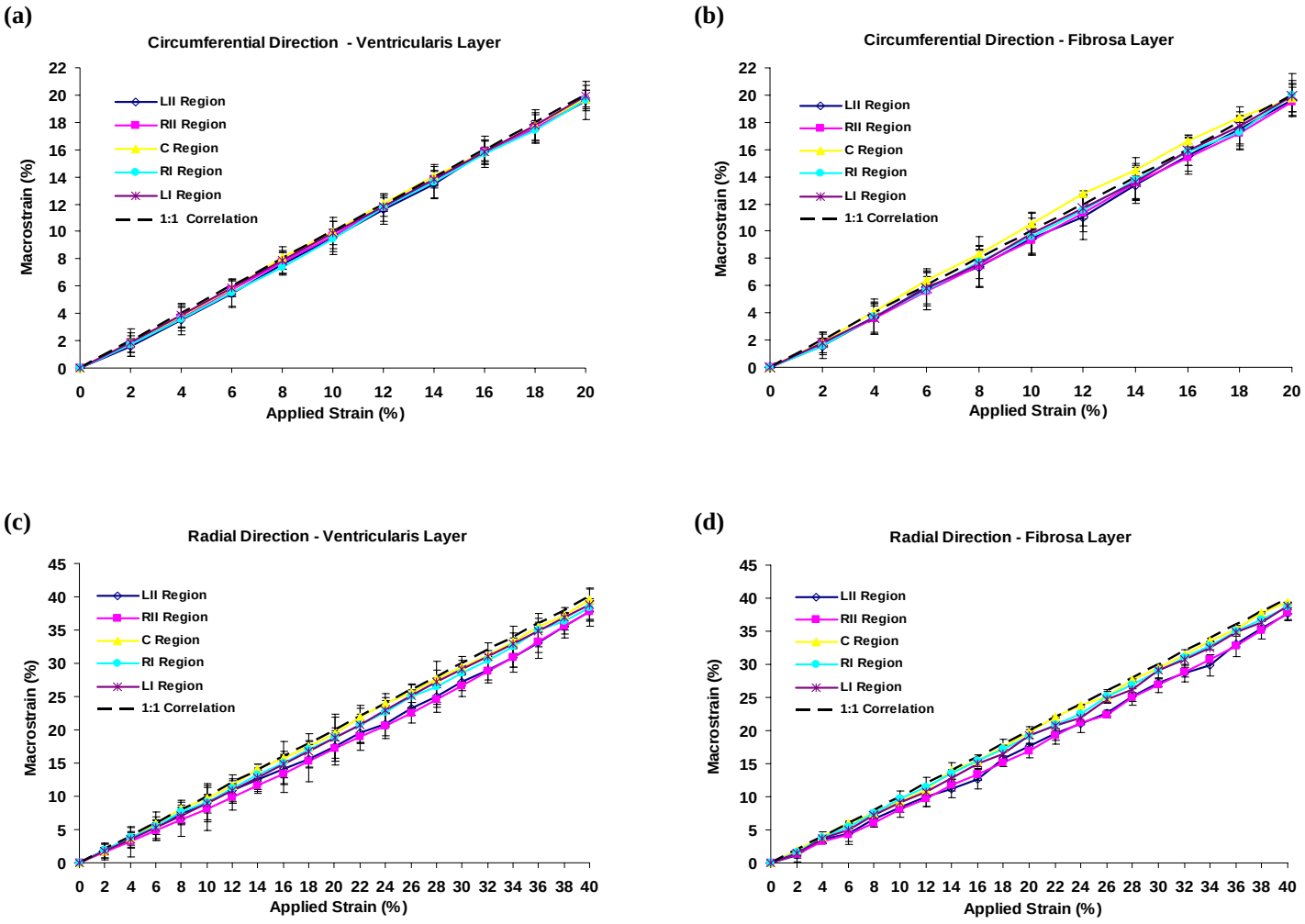

Figure 5.5 Macrostrains across each sample region measured from: (a) the ventricularis side, and (b) the fibrosa side, loaded in the circumferential direction, and (c) the ventricularis side, and (d) the fibrosa side, loaded in the radial direction. Dashed lines indicate the 1:1 linear correlation between macrostrains and applied strains.

Macrostrains are evidently more uniform across the sample length than the FN strains. However, emulating the FN strains, the central region of the samples possessed slightly higher strains than the regions nearer the grips, more closely correlating with applied strains. While this difference is more pronounced in the radial direction (Figure 5.5), it was not significant in any samples. Comparing the two loading directions, macrostrains are more uniform in the circumferential direction (Figure 5.5), with a higher correlation factor, r, between the macrostrains and the applied strains. Indeed, the mean difference between the macrostrains and the applied strains in the radial direction was observed to be an order of magnitude higher than that in the circumferential direction.

5.4. Discussion

Applied strains were compared with macrostrains across the AV sample surface, and FN strains established from cell nuclei movement. While the central region reported slightly higher macrostrains than the regions near the grips, the distribution of macrostrains was generally homogenous, correlating strongly with the applied strains in both loading directions, in both layers (Figure 5.5). The correlation factor r was in excess of 0.96 for all the cases, except in the fibrosa layer under the circumferential loading, in which a weaker correlation with the applied strain was evident ($r = 0.93$). This is likely to be a result of the significantly higher collagen fibre content of the fibrosa, which will give rise to a more non-uniform behaviour as a result of more pronounced effects of fibre recruitment and reorientation.

By contrast, the FN strain field was inhomogeneous both along the length of each layer, and between the layers, under both circumferential and radial loading. Furthermore, the FN strains in both loading directions reported a pronounced non-linear correlation with the applied strains, particularly in the circumferential direction, in both layers.

Cells are known to bond to fibrous proteins, particularly collagen, through a number of different integrins [23,85,121]. By monitoring the movement of the cells at each applied increment of strain, the movement of the FN and subsequently the FN

elongation was established (Figure 5.3). The nominal in-plane (x, y) resolution of the confocal images in the current study was determined to be $Res = 0.39\ \mu m$ (§2.3.1), whilst the smallest detected movement of the cell nuclei was observed to be $1.16\ \mu m$. With movements at least three times the image resolution, the microscopy technique provides sufficient imaging resolution for tracking the cell nuclei movement, even at lower strain increments.

In both loading directions, from both the ventricularis and fibrosa sides of the valve, the FN in the central region strained the most, reducing towards the gripping points. The observed distribution of strains within the FN is likely to be strongly influenced by the end effects concept, addressed by the Saint-Venant's principle. This principal demonstrates that the strain field at sites closer to the gripping points may be confined due to the gripping effects, only becoming uniform at distances away from the points of gripping [125]. For any given sample, gripping effects have been shown to decay at a certain length along the test specimen, known as the characteristic decay length [126]. The characteristic decay length defines how rapidly end effects decay in a sample, from which point the strain across the sample is considered uniform. While this length is of comparable length to the width of the test specimen for most engineering materials such as steel and some polymers [127], it can be more significant in soft biological tissues, specifically in samples for which dimensions are confined, due to the limitations in the size of the subject tissue.

The mathematical criteria for calculating the characteristic decay length based on the Saint-Venant's principal have been established through the works of Knowles [128] and Horgan [129]. Based on these criteria, and to address this effect analytically, it is shown in Appendix A that the following relationship can be used to determine this distance for a planar fibrous connective tissue sample:

$$l = O\left((E/G)^{0.5} b\right) \tag{5.2}$$

where l is the characteristic decay length, E and G are the elastic and shear modulus of the tissue respectively, b is the width of the specimen, and the operator $O(\ )$ is the 'order of' the value in the brackets.

The instantaneous elastic modulus E and the viscous damping coefficient η of the porcine AV samples were quantified in chapter 3, demonstrating that the AV shows a shear-thinning behaviour. The shear modulus G for a shear-thinning material can be calculated by [130]:

$$G = \frac{\eta_0}{\tau} \tag{5.3}$$

where τ and η_0 are the characteristic relaxation time and viscosity at very low shear rates, respectively [130]. By extrapolating the results obtained in chapter 3 for η at low strain rates of 1%/min, and using the relaxation times characterised previously in chapter 4 as $\tau_{circ} = 5.20 \pm 1.3$ s in circumferential and $\tau_{rad} = 34.88 \pm 10.2$ s in radial direction, the shear moduli were determined to be approximately 598 MPa and 119 MPa in the circumferential and radial directions, respectively. Substituting these, alongside the values of 20 MPa (circumferential) and 0.75 MPa (radial) for instantaneous elastic modulus (E) at low strain rates from chapter 3, the characteristic decay lengths from each grip are determined to be in order of 0.9 mm in the circumferential direction, and 2 mm in the radial direction.

Subsequently, the strain fields can be considered to be independent of gripping effects within the middle 8 mm of circumferential specimens, and the middle 4 mm for radial samples. These data correlate positively with macrostrain findings, in which circumferentially loaded samples reported more uniform distributions than radial samples, while the central region of all samples reported macrostrains more closely matched to the applied strains. Indeed, the confinement of strain fields at regions closer to the grips, due to gripping effects, has also been reported in other studies investigating the *in vitro* mechanical behaviour of soft tissues [131-134]. Using strain gauges [134], and markers and video imaging techniques together with finite element method [131-133,135], studies have confirmed that tissue specimens generally appear less extensible towards the clamping sites, with concentration of stress at the gripping points [131-1333,135].

Neither the macro nor the FN strains across the sample regions add up to the applied strain at each increment, potentially stemming from the confining effects of the grips on the local strains. Data suggest that longer specimens would be more appropriate to

achieve a more extensive sample region unaffected by gripping, and more uniformity between the local and applied strains. However, the physical dimensions of the AV impose a limit on the length of test specimens, especially in radial direction. The strain distribution in the radial direction should be treated with caution, and correction factors may be required for a more realistic interpretation of the FN strain results in this direction.

However, the data indicates that the inhomogeneous and non-uniform distribution of FN strains across each layer may not stem solely from end effects. Comparing the FN strains of LI, RI and the central regions (C) in Figure 5.4 indicates a clear inhomogeneity, where the gripping effects are theoretically minimal. This additional effect may be due to the AV collagen fibre architecture, as suggested in some finite element modelling studies of AV micromechanics [47,48]. In the regions close to the commissures, the preferred direction of fibres is more uniformly oriented towards the circumferential principal axes, while the fibres in the belly region are more randomly oriented [47-49]. The belly region of the AV leaflet forms the central region of the strip specimens used in this study (Figure 5.1), hence the reorientation of the fibres in this region would allow more displacement of the cells and larger FN strains. Conversely, in regions away from the centre near the commissures, where the fibres are already more uniformly aligned, less reorientation would occur.

The difference in the FN elongation between the two layers can be calculated from the strain data presented in the graphs in Figure 5.4, for both the loading directions. However, owing to the extreme end effects in the radial direction (60% of the length of the sample), only the circumferential direction is considered for additional analysis. Considering the FN strains across the middle 8 mm of the circumferential samples (thus excluding LII and RII regions which are within the characteristic decay length), the elongation of the FN within the ventricularis layer was consistently larger than the fibrosa, across each equivalent specimen region (Figure 5.6). The summed difference in elongation of the two layers over the three regions is shown in Figure 5.6b.

In each sample region, the difference in FN elongation is largest in the initial applied strain increments, reducing as the applied strain increases (Figure 5.6a). Such a response seems reasonable, considering the macroscopic crimp which is localised to

the fibrosa [1,13]. At initial strains, the ventricularis has less macro crimp and is less stiff, hence the FN in this layer would displace more than in the fibrosa, resulting in larger FN elongations of the ventricularis relative to the fibrosa. As the applied strain increases, the macro crimp in the fibrosa straightens out, and the displacement of the FN in the two layers becomes steadily more uniform.

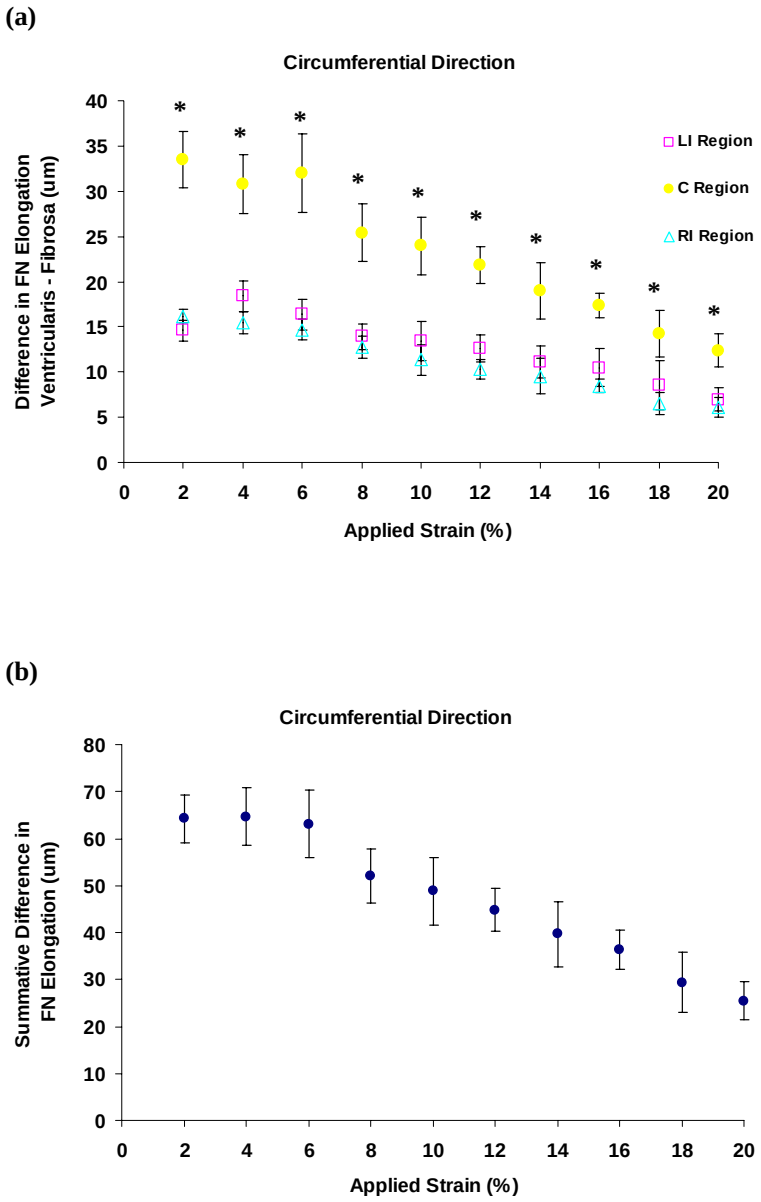

Figure 5.6 Difference in the FN elongation between the ventricularis and fibrosa layers in the circumferential direction: (a) the difference in each region that is unaffected by end effects (RI, C, LI), and (b) the summative difference in matrix elongation between the two layers, from these 3 regions. The asterisks indicate a statistically significant difference ($p < 0.05$) between the central region and RI or LI.

A key aspect of the non-uniform elongation of the FN within the ventricularis and fibrosa, shown schematically in Figure 5.7, is that it will result in internal shearing induced in the 1-3 plane within the network. Using the mean difference in total FN elongation between the layers, the internal shear strain (γ) was calculated at each strain increment. Previous studies of collagen shearing have assumed the modulus for the network internal shear, G_i, to be 50 KPa [136]. Using these values, the resulting internal shear stresses, $\tau_i = G_i\gamma$, are shown in Figure 5.8, for each strain increment. These calculations are based on the assumption that the orders of the characteristic decay lengths of the ventricularis and the fibrosa layers are similar, and equal to the calculated 0.9 mm from each gripping point by equation (5.2). This assumption may be considered reasonable, as the elastic moduli of the two layers have been reported to be in the same order of magnitude within the strain range used in this study [1,124].

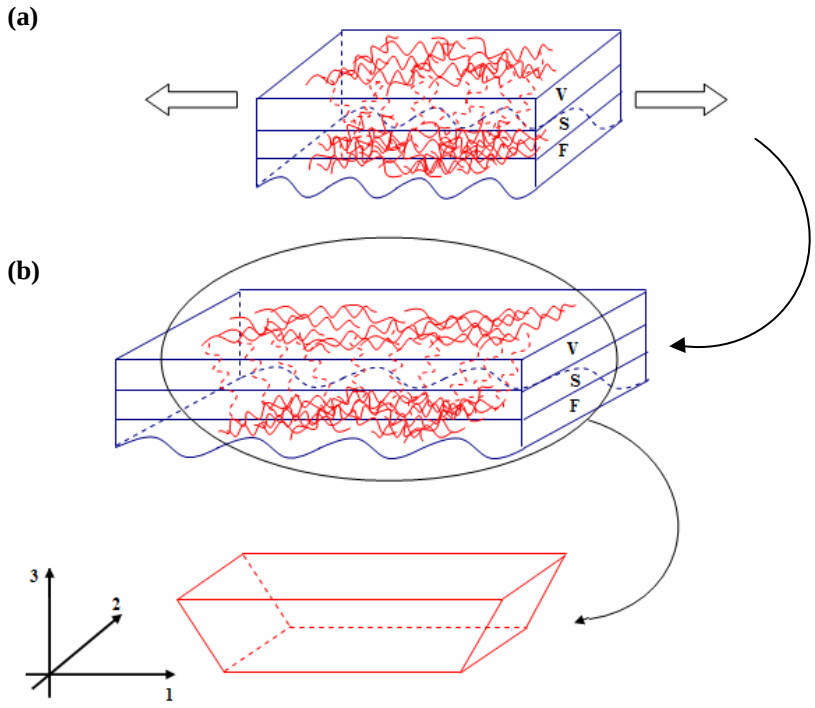

Figure 5.7 Schematic showing the effect of the difference in elongation of the FN within the AV layers: the network (a) before; and (b) after deformation. The FN is elongated more in ventricularis layer (V) compared to the fibrosa (F). This will lead to internal shearing in the 1-3 plane.

To establish how the experimentally derived internal shear stress values correlate with well-established viscoelastic criteria, the data are compared with theoretical

values calculated using a Kelvin-Voigt model (Appendix B). Chapter 3 showed that the deformation behaviour of AV specimens under uniaxial tensile loading can be described by a Kelvin-Voigt model. For a 3D Kelvin-Voigt viscoelastic solid under uniaxial stress, it can be shown that the shear strain in the 1-3 plane is related to the tensile deformation in direction 1 as (Appendix B):

$$\gamma_{13} = \frac{\eta_1}{E_1}\dot{\varepsilon}_1 \tag{5.4}$$

where γ_{13} is the shear strain in 1-3 plane, E_1 and η_1 are the elastic modulus and the viscous damping coefficients in the loading direction 1, respectively, and $\dot{\varepsilon}_1$ is the strain rate in that direction.

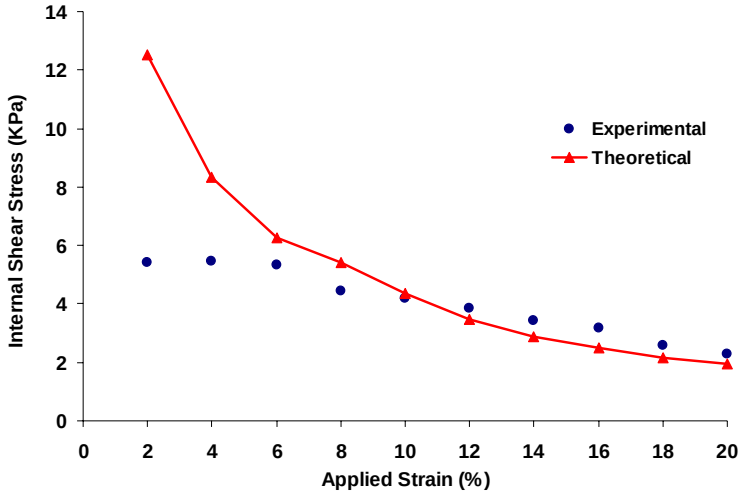

Figure 5.8 Internal shearing in the specimens at each applied strain increment: experimental data are compared to theoretical values.

Taking the values of E_1 and η_1 at each strain level from chapter 3, the calculated shear stress at each strain increment is compared to the experimental values in Figure 5.8. A good agreement is observed between the theoretical and experimental values, especially at increasing strains. The differences at low strain levels could be due to the fact that, similar to the instantaneous elastic modulus E, G_i is also likely to be strain dependent, and its value should vary at different strain levels. The single value used for these calculations may well be more appropriate for the higher strains. Nevertheless, the experimental internal shear stress values obtained in this study are

within the range of those previously reported for porcine AV specimens, with a maximum value of approximately 5 KPa [18,137].

In vitro biaxial or flexural loading modes may represent the physiological loading conditions of the AV more closely. However, the mode of strain transfer within the tissue is primarily influenced and determined by the ECM organization and the associated structural responses, and not the loading boundary conditions. This study aimed to provide a fundamental understanding of the distribution of local FN strains across and between each of the main load-bearing layers within the AV. It constructs the first 3D map of the local strains to the knowledge of the author and experimentally elucidates the internal shearing occurring as a result of tensile deformation at the macro level. The results of this study may therefore assist the interpretation of data obtained through more relaxed or constrained loading boundary conditions. Quantification of internal shear stress within the layers of the AV could also have implications for understanding AVIC mechanobiology, providing a better understanding of the local mechanical environment perceived by the cells.

It was established in this chapter that the distribution of strain within the FN across the AV is inhomogeneous, as well as anisotropic. The FN within the central region appears to possess the maximum values of strain, decreasing towards the commissures. Strain transfer from the macro level to the FN is not direct, with results indicating a non-linear correlation between the macro- and micro-strains (Figure 5.4). Additionally, shear strains and stresses are induced within the FN between the layers, upon the application of tensile strains at macro level. These results suggest that the strain transfer from the tissue to the microstructure is non-affine. Furthermore, they indicate that the AVICs are possibly exposed to additional stress modes beyond those applied at the tissue level. These findings provide a better understanding of stress transfer from the tissue level to the microstructure.

Chapter 6

The role of collagen fibres in the structure-function relationship of the aortic valve:

Fibre contribution to tissue mechanics from the crimped to the fully straight state

6.1. Synopsis

Strain transfer from the tissue to the fibrous network (FN) within the AV was investigated in chapter 5. FN strains were characterised, with results suggesting that the strain transfer is non-affine. In this chapter, this information is incorporated into the development of a micro-structural based model, to address the non-linearity of the quasi-static stress-strain behaviour of the valve, observed in chapter 3. Constitutive modelling of the mechanical behaviour of soft tissues based on their microstructure provides a powerful tool for predicting how microstructure influences tissue behaviour, particularly when *in situ* investigation of the microstructural properties is experimentally challenging.

Due to their complex structural organization, planar soft tissues generally exhibit highly non-linear and anisotropic mechanical behaviour, and often require derivation of new mathematical relationships to describe their behaviour. This, in turn, necessitates the development of specific constitutive models to effectively describe how the gross-level macromechanics is related to the behaviour of the material constituents within the tissue. In chapter 3, a phenomenological model was developed (equations 3.13a and 3.13b) to describe the behaviour of the AV based on its three morphological layers. Despite the good fit to experimental data and ability to characterise some of the material parameters of the tissue, no information and interpretation of the underlying structural mechanisms could be elucidated from the model.

In the structural-based modelling approach, as its name implies, the structural components of the tissue are incorporated in modelling its behaviour [143]. A structural model addresses the relationships between tissue structure and function, explaining the mechanical properties of the tissue based on the microstructure, such as the anisotropy and non-linearity [144,145]. Thus, structural models are advantageous in that they elucidate the contribution of microstructural components to the overall tissue mechanical behaviour, and provide physically meaningful material parameters based on the actual composition of the tissue [143-145]. The emerging role of tissue engineering in providing living replacement implants for AV tissue further strengthens the importance and application of structural models, as they can assist

estimations of the mechanical environment of the living cells residing within and bonded to the micro-structure of native tissue. With cells controlling matrix metabolism in response to their mechanical environment [80,81], understanding the localized strain environment surrounding the cells becomes critical. Such localized structural information can also provide design features for cell seeded scaffolds, to help reproduce physiological loading environments [146].

The main theoretical criterion for the structural modelling approach in soft tissues has been established through the pioneering work of Lanir [143,147], based on the assumption that the mechanical behaviour of soft tissues can be characterised through the summation of the response of its individual constituent collagen fibres under deformation. The deformation and stress of each fibre is determined during the tissue deformation, and the overall tissue stress can be determined by integrating the effect of all fibres [111,121]. An important aspect when incorporating such structural theory is thus the consideration of fibre stress-strain law, i.e. how the individual fibres deform under the applied tissue level strain/stress, and subsequently how they would contribute to the load bearing characteristics of the tissue.

In the currently available structural models, the laws governing fibre stress-strain behaviour have mainly employed one of two different assumptions:

1- Collagen fibres have been assumed to be linear elastic; however only contributing to load bearing in the tissue when fully uncrimped. The initially wavy fibres will elongate homogenously until they are fully straight, and will then strain linearly with respect to the induced stress on the fibre. This assumption has been widely used in Lanir's work, with the different straight length of the fibres presented by a distribution function [111,143,147]. As the applied strain on the tissue increases, more fibres would progressively become straight, giving rise to the non-linear stress-strain relationship observed in soft tissues (Figure 6.1a).

Or;

2- The stress-strain relationship in a fibre is intrinsically non-linear, mainly assumed to be of exponential form [66,122]. This assumption is prevalent for micro-structural based models describing the behaviour of the AV.

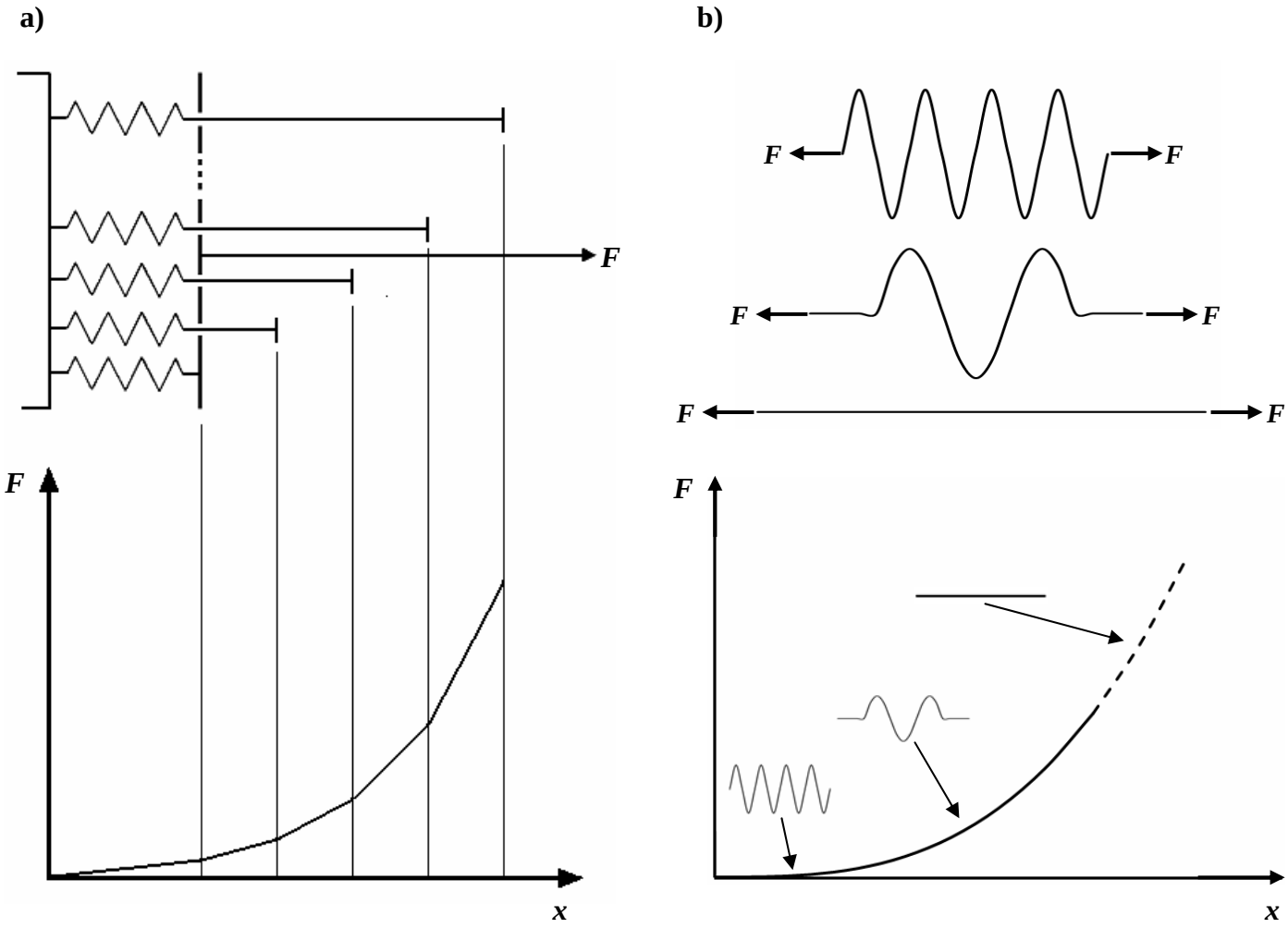

Figure 6.1 Schematic representation of the structural mechanism causing non-linear behaviour of fibrous soft tissues: (a) a model of nonlinear elasticity demonstrating the progressive recruitment of individual collagen fibres acting as linear components (redrawn from [148]). (b) Continuous gradual straightening, giving a gradually increasing stiffness. When fully straight, the fibres behaves linearly and possess the highest stiffness (dashed lines).

However, difficulties can be identified with both of these assumptions. It is has been well established that individual fibres within soft tissues do not have a uniform crimp wavelength and amplitude [149,150]. This has also been established for samples in the current study, with histological sections showing a range of crimp characteristics for individual fibres (Figure 6.2). This non-uniform organisation means that the initially wavy fibres will elongate in a non-uniform fashion, i.e. fractions of a fibre may become straight while the fibre is not yet fully uncrimped [149,150]. These straight fractions of the fibres will then be able to strain and subsequently contribute to the load bearing features of the tissue; a factor not considered under assumption (1) described above.

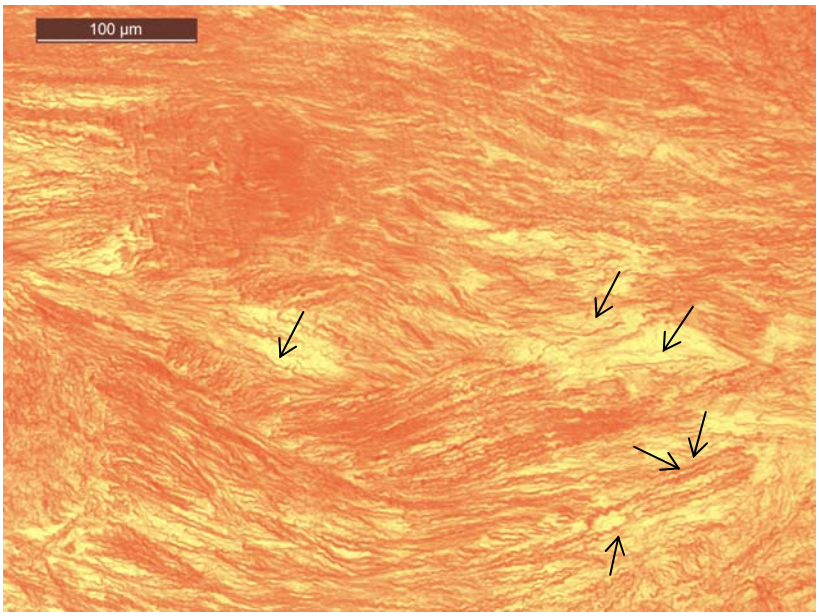

Figure 6.2 A histological image of wavy collagen fibres in unloaded AV tissue, stained using Picro Sirius Red and imaged by a x10 magnification objective. Fibres do not have a uniform crimp wavelength. Arrows show some of the fibres that have straight fractions even in an unloaded state.

With respect to assumption (2), an exponential relationship between stress and strain in a single collagen fibre is not in accordance with the experimental observations, where linear elastic features have been reported for straight collagen fibres [151,152].

Thus, even though the models developed based on the above two assumptions have widely been successful in characterising the mechanical behaviour of a variety of soft tissues, neither of the two assumptions seem to fully comply with the experimentally observed behaviour of the fibres under deformation.

In order to address this, an alternative approach is presented and formulated in this chapter, which considers each individual collagen fibre becoming straight in stages, and thus straight sections strain and contribute to load bearing in the tissue, even though the whole fibre may still not be fully uncrimped. The elastic modulus of fibres is derived based on their straightened length, and the fibre strain is calculated with respect to the applied tissue strain. The angular distribution of collagen fibres in planar tissue is derived and incorporated into the model. The experimental stress-

strain data of porcine aortic valve tissue, characterised in chapter 3, is used to verify the outcomes of the developed model.

6.2. Formulation of the model

Following the pioneering work of Lanir [143,147], the 2nd Piola-Kirchhoff stress of a fibrous soft tissue can be expressed as (Appendix C):

$$S = \int_{-\frac{\pi}{2}}^{\frac{\pi}{2}} R(\theta) S_{fibre} [\vec{N} \otimes \vec{N}] d\theta \tag{6.1}$$

where $R(\theta)$ is the statistical distribution function of the angular distribution of the collagen fibres, in which the θ is the Eulerian angle describing the direction of oriented fibres, S_{fibre} is the 2nd Piola-Kirchhoff stress of the population of fibres in tissue, and $\vec{N}$ is the unit vector representing the direction of the fibre. Derivation of the mathematical relationship for S_{fibre} is described in the following section.

6.2.1. The stress-strain relationship for a fibre

When crimped, collagen fibres adopt a helical form, as shown schematically in Figure 6.3, which can only bear tension along the axis of the helix. The internal forces induced within the fibre upon the application of external tensile force are shear and torsion (Figure 6.3b). Thus, the total displacement energy of the fibre under tensile deformation would be obtained by the superposition of the strain energy functions due to each individual stress [141]:

$$U = U_{Shear} + U_{Torsion} \tag{6.2}$$

with:

$$U_{Shear} = \int \frac{F^2}{2AG_{fibre}} dl \ , \ U_{Torsion} = \int \frac{M^2}{2G_{fibre}J} dl \tag{6.3}$$

In the above equations, F is the tensile force on the fibre, M is the torsion, G_{fibre} is the shear modulus of the fibre, A is the fibre cross-sectional area, and J is the second polar moment of area.

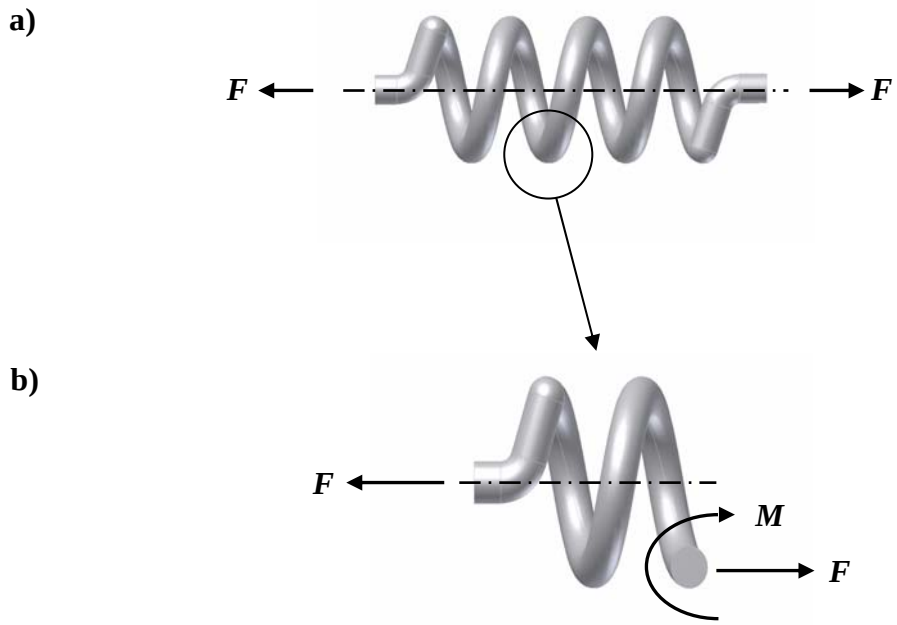

Figure 6.3 Schematic of a crimped fibre: (a) the fibre possesses a helical form that can be approximated by a sinusoidal function. (b) The internal loads induced within a fibre upon the application of an external load ***F*** on the fibre.

The wavy shape of the crimped fibre can be approximated by a sinusoidal function in the form $y = a\sin bx$, where a is the amplitude and b is the frequency, calculated as $2\pi / Wavelength$ [153,154]. Assuming that the cross-section of the fibre is circular with radius r which remains uniform along the fibre, it follows:

$$M = Fa \;,\; A = \pi r^2 \;,\; J = \frac{\pi r^4}{2} \tag{6.4}$$

substituting (6.4) into (6.3):

$$U_{Shear} = \frac{F^2}{2\pi r^2 G_{fibre}} \int_0^{x_0} dl \tag{6.5a}$$

and

$$U_{Torsion} = \frac{F^2 a^2}{\pi r^4 G_{fibre}} \int_0^{x_0} dl \tag{6.5b}$$

where x_0 is the crimped length of fibre (Figure 6.4), and $\int_0^{x_0} dl$ is the straight length of the fibre, L, which would be:

$$L = \int_0^{x_0} \sqrt{1 + y'^2}\, dx \;\Rightarrow\; L = \int_0^{x_0} \sqrt{1 + a^2 b^2 \cos^2 bx}\; dx \tag{6.6}$$

substituting equations (6.5a), (6.5b) and (6.6) into (6.2) gives the total strain energy function in terms of the properties of the fibre as:

$$U = \frac{F^2 (r^2 + 2a^2)}{2 G_{fibre} \pi r^4} \int_0^{x_0} \sqrt{1 + a^2 b^2 \cos^2 bx}\; dx \tag{6.7}$$

The relationship between displacement and force in the fibre can now be determined using Castigliano's theorem, as [141]:

$$\delta = \frac{dU}{dF} \tag{6.8}$$

where δ is the displacement. Using equation (6.7) one would get:

$$\delta = \frac{(r^2 + 2a^2)F}{G_{fibre} \pi r^4} \int_0^{x_0} \sqrt{1 + a^2 b^2 \cos^2 bx}\; dx \tag{6.9}$$

Collagen fibres are known to be linearly elastic [151,152,155]. In a linear elastic solid, the relationship between force and displacement is characterised by the well known equation $F = K\delta$, where K is the stiffness constant. Thus, using equation (6.9):

$$K = \frac{G_{fibre} \pi r^4}{r^2 + 2a^2} \cdot \frac{1}{\int_0^{x_0} \sqrt{1 + a^2 b^2 \cos^2 bx}\; dx} \tag{6.10}$$

Accordingly, the elastic modulus of fibre E_{fibre} will be determined from its stiffness constant ($K = AE_{fibre}$) [23] as:

$$E_{fibre} = \frac{G_{fibre}\pi r^4}{A(r^2 + 2a^2)} \cdot \frac{1}{\int_0^{x_0} \sqrt{1 + a^2 b^2 \cos^2 bx} \; dx} \tag{6.11}$$

There exists experimental evidence suggesting that wavy fibres do not necessarily have to become fully straight in order to to contribute to the load bearing status of the tissue. Instead, even if a fraction of a fibre straightens upon the application of mechanical stimuli, this straight part of the fibre will be strained, even when the rest of the fibre is not yet fully uncrimped [149,150]. Thus, it is possible to consider that a fraction of a fibre would contribute to load bearing of the overall tissue, with this fractional contribution increasing as more of the fibre becomes straight. To model this effect, the concept of gradual straightening of a fibre must be incorporated into the equations describing the stress of fibre, S_{fibre}, and subsequently the overall stress of the tissue, S, in equation (6.1). The next step is thus to derive the mathematical relationships for fibre stiffness and strain with respect to the straight length of the fibre.

Consider the arbitrary wavy fibre at the zero stress state shown in Figure 6.4. The crimped length of the fibre is x_0. Upon the application of some force, the fibre's new length becomes X. In the most general status, a portion of the fibre becomes straight and strains, while the wavy length of the fibre also changes to a new coordinate x_1 (Figure 6.4). It is easily perceived that as larger portions of a fibre become straight, the overall change in fibre length X reduces. This is due to the fact that the straight part would deform much less than the wavy portion. Thus, considering the whole fibre as a mechanical element, it becomes stiffer as it straightens. Equivalently, its instantaneous elastic modulus will depend on how much of the fibre has become straight, with the fibre becoming increasingly stiffer with increase in the straight portion. It reaches its highest stiffness when fully straight, and remains constant from this point forward, and the element acts linearly (Figure 6.1b).

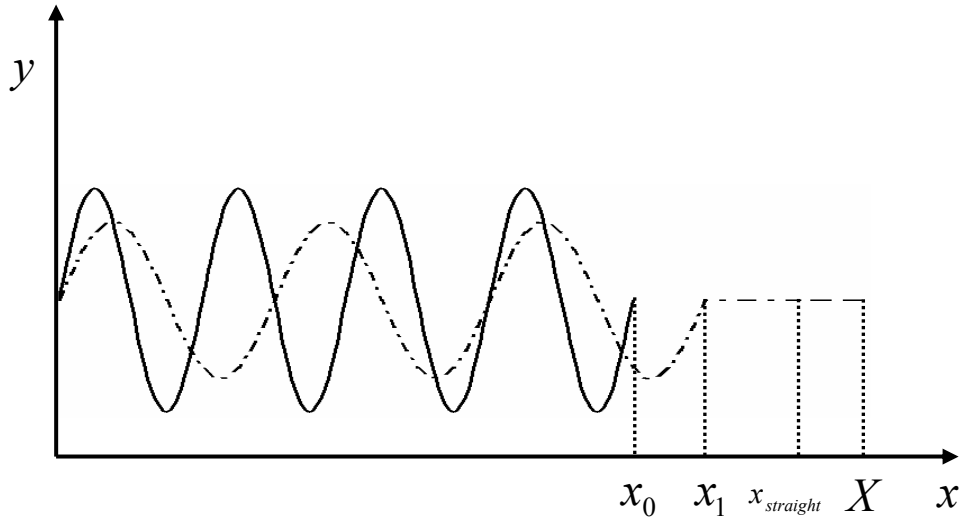

Figure 6.4 Coordination of a fibre under deformation. The total length of a wavy fibre before deformation (continuous line) is x_0. After deformation (dotted line), the length of the wavy part of the fibre becomes x_1, and its overall length, including the straight part and the strained part, is X.

Let $e_{fibre}(p)$ be the instantaneous elastic modulus of the fibre, where p is the portion of fibre which is straight, with respect to its current wavy length x. Thus:

$$p = qx \ , \ 0 \le q \le 1 \tag{6.12}$$

Equation (6.11) gives the elastic modulus of a fibre when it is fully straight, i.e. where the fibre has its maximum stiffness and acts linearly, as explained earlier above. The relationship between the instantaneous modulus of the fibre $e_{fibre}(p)$ and E_{fibre} may thus be written as:

$$\int \frac{e_{fibre}(p)}{L} dp = E_{fibre} \ , \ p = qx \tag{6.13}$$

It is evident from equation (6.13) that when the fibre is fully straight ($q = 1$), $e_{fibre}(p) = E_{fibre}$. Thus, the instantaneous elastic modulus of the fibre $e_{fibre}(p)$ can be determined by differentiating both sides of the above equation with respect to variable x, upon substituting for E_{fibre} from equation (6.11):

$$q \cdot e_{fibre}(x) \cdot \frac{1}{L} = \frac{G_{fibre}\pi r^4}{qA(r^2+2a^2)} \cdot \left(\frac{q(\sqrt{1+a^2b^2} - \sqrt{1+a^2b^2\cos^2 bqx})}{(\int_0^{qx} \sqrt{1+a^2b^2\cos^2 b(qx)}\ dx)^2} \right) \tag{6.14}$$

The denominator in the brackets of the right hand side of the above equation is equal to L, as given by equation (6.6). Thus equation (6.14) can be re-written as:

$$e_{fibre}(x) = \frac{G_{fibre}\pi r^4}{qA(r^2+2a^2)L}\left(\sqrt{1+a^2b^2} - \sqrt{1+a^2b^2\cos^2(bqx)}\right) \tag{6.15}$$

Equation (6.15) characterises the instantaneous elastic modulus of a fibre based on the proportion of its length that is straight.

As shown in Figure 6.4, upon application of an arbitrary load, a fibre of initial length x_0 will elongate to a new length X. This additional length, i.e. $X - x_0$, can be broken down into: (i) new additional wavy length ($x_1 - x_0$ as shown in Figure 6.4), (ii) the portion that has become straight $x_{straight}$, and (iii) the straight portion that becomes strained, which is the true fibre strain ε_{fibre}. The portion of a fibre that becomes straight would thus depend on the magnitude of the global finite Lagrangian strain $\varepsilon_{Lag.}$. In general, stochastic approaches have been proposed to model the gradual recruitment of wavy fibres. Following the previous studies [111,122,147,156], the same approach was employed, incorporating a gamma function in describing the distribution of the gradual straightened portion of the fibre at different applied global strains $\varepsilon_{Lag.}$, denoted by $D(\varepsilon_{Lag.})$, with respect to the initial length of the fibre x_0. This approach is also supported by the experimental results obtained in chapter 5, as the strain transfer from gross tissue level to the microstructure was shown to be non-affine, and therefore a direct deterministic relationship may not represent the correlation realistically.

Thus the straight length of the fibre at each $\varepsilon_{Lag.}$ would be:

$$x_{straight} = x_0 \cdot D(\varepsilon_{Lag.}) \tag{6.16}$$

where:

$$D(\varepsilon_{Lag.}) = \frac{1}{\beta^{\alpha}\Gamma(\alpha)} \varepsilon_{Lag.}^{\alpha-1} \exp\left(-\frac{\varepsilon_{Lag.}}{\beta}\right) \tag{6.17}$$

The parameters α and β are positive constants determining the shape of the distribution.

By definition, the fibre true strain, ε_{fibre}, is the change in the length of the straight portion of the fibre Δl divided by the initial straight length $x_{straight}$:

$$\varepsilon_{fibre} = \frac{\Delta l}{x_{straight}} \tag{6.18}$$

For calculating the change in the wavy length of the fibre, let us define ε_{wavy} as the change in the wavy length of the fibre divided by the initial wavy length, at each global Lagrangian strain:

$$\varepsilon_{wavy} = \frac{\Delta \text{ wavy length of the fibre}}{\text{initial wavy length}} \tag{6.19}$$

For simplicity in notation, Δ wavy length of the fibre will be shown by Δ. However, the initial wavy length of the fibre at every $\varepsilon_{Lag.}$ can be calculated by:

$$\text{initial wavy length of the fibre} = (1 - D(\varepsilon_{Lag.}))x_0 + L \times D(\varepsilon_{Lag.}) \tag{6.20}$$

where, by the definition of the parameters, the first term represents the length of the remainder of the wavy fibre, and the second term accounts for the part of the fibre that elongates to become straight. One should notice that at zero deformation state, where $D(\varepsilon_{Lag.}) = 0$, equation (6.20) returns x_0, which is the initial wavy length of fibre. When all the fibre is straight, $D(\varepsilon_{Lag.}) = 1$, and the equation (6.20) calculates L. Substituting into (6.19):

$$\varepsilon_{wavy} = \frac{\Delta}{(1 - D(\varepsilon_{Lag.}))x_0 + L \times D(\varepsilon_{Lag.})} \tag{6.21}$$

From geometrical point of view, the values of ε_{wavy} and ε_{fibre} should be related at each $\varepsilon_{Lag.}$, since the length that becomes straight to account for ε_{fibre}, comes from the

initially wavy length of the fibre in ε_{wavy}. However, it is not a linear relationship, and the proportionality varies at each $\varepsilon_{Lag.}$. Hence, mathematically:

$$\varepsilon_{wavy} = c(\varepsilon_{Lag.}) \cdot \varepsilon_{fibre} \tag{6.22}$$

where $c(\varepsilon_{Lag.})$ is a proportionality coefficient. It is evident that $c(\varepsilon_{Lag.}) \geq 1$ at each $\varepsilon_{Lag.}$.

By its definition:

$$\varepsilon_{Lag.} = \frac{X - x_0}{x_0} \tag{6.23}$$

$X - x_0$ can now be calculated from the equations (6.16), (6.18), (6.21) and (6.22), hence:

$$x_0\varepsilon_{Lag.} = x_0 D(\varepsilon_{Lag.}) + \varepsilon_{fibre} x_0 D(\varepsilon_{Lag.}) + \varepsilon_{fibre} \cdot c(\varepsilon_{Lag.}) \cdot \left[(1 - D(\varepsilon_{Lag.}))x_0 + L \times D(\varepsilon_{Lag.})\right] \tag{6.24}$$

and by re-arranging the above:

$$\varepsilon_{fibre} = \frac{x_0\varepsilon_{Lag.} - x_0 D(\varepsilon_{Lag.})}{x_0 D(\varepsilon_{Lag.}) + c(\varepsilon_{Lag.}) \ \left[(1 - D(\varepsilon_{Lag.}))x_0 + L \times D(\varepsilon_{Lag.})\right]} \tag{6.25}$$

Thus, stress in a single fibre at each global Lagrangian strain $\varepsilon_{Lag.}$, s_{fibre}, can be calculated by incorporating the definition of $D(\varepsilon_{Lag.})$ into equations (6.15), and equation (6.25) as:

$$s_{fibre} = e_{fibre} \cdot \varepsilon_{fibre} \ \Rightarrow$$

$$s_{fibre} = \frac{G_{fibre}\pi r^4}{AL(r^2 + 2a^2)D(\varepsilon_{Lag.})}\left(\sqrt{1 + a^2b^2} - \sqrt{1 + a^2b^2\cos^2(bD(\varepsilon_{Lag.})x)}\right) \cdot \frac{x_0\varepsilon_{Lag.} - x_0 D(\varepsilon_{Lag.})}{x_0 D(\varepsilon_{Lag.}) + c(\varepsilon_{Lag.}) \ \left[(1 - D(\varepsilon_{Lag.}))x_0 + L \times D(\varepsilon_{Lag.})\right]} \tag{6.26}$$

6.2.2. Stress-strain relationship for the population of fibres in tissue

Physically, it is evident that not all fibres in a tissue will start to contribute to load bearing at a same $\varepsilon_{Lag.}$, since the initial length and the waviness of fibres varies in tissue. Hence [122,156]:

$$S_{fibre} = \int_0^{\varepsilon_{fibre}} P(\varepsilon_{Lag.})\, s_{fibre}\, d\varepsilon_{Lag.} \tag{6.27}$$

where $P(\varepsilon_{Lag.})$ is a statistical distribution function representing the fibres that are active in load bearing within the tissue at $\varepsilon_{Lag.}$, and $P(\varepsilon_{Lag.})d\varepsilon_{Lag.}$ by definition is the total fraction of the fibres that are contributing to the load bearing status of the tissue [111,122]. Assuming that $P(\varepsilon_{Lag.})$ can be approximated by a Weibull distribution, following previous studies [157]:

$$P(\varepsilon_{Lag.}) = \frac{\kappa}{\psi}\left(\frac{\varepsilon_{Lag.}}{\psi}\right)^{\kappa-1} \exp\left[-\left(\frac{\varepsilon_{Lag.}}{\psi}\right)^{\kappa}\right] \tag{6.28}$$

where κ and ψ are shape and scale parameters [157].

Thus, the complete form of S_{fibre} is:

$$\begin{cases} S_{fibre} = \int_0^{\varepsilon_{fibre}} P(\varepsilon_{Lag.})\, s_{fibre}\, d\varepsilon_{Lag.} \\ s_{fibre} = \dfrac{G_{fibre}\pi r^4}{AL(r^2+2a^2)D(\varepsilon_{Lag.})}\left(\sqrt{1+a^2b^2} - \sqrt{1+a^2b^2\cos^2(bD(\varepsilon_{Lag.})x)}\right)\cdot \\ \qquad \dfrac{x_0\varepsilon_{Lag.} - x_0 D(\varepsilon_{Lag.})}{x_0 D(\varepsilon_{Lag.}) + c(\varepsilon_{Lag.})\ \left[(1-D(\varepsilon_{Lag.}))x_0 + L\times D(\varepsilon_{Lag.})\right]} \\ P(\varepsilon_{Lag.}) = \dfrac{\kappa}{\psi}\left(\dfrac{\varepsilon_{Lag.}}{\psi}\right)^{\kappa-1} \exp\left[-\left(\dfrac{\varepsilon_{Lag.}}{\psi}\right)^{\kappa}\right] \end{cases} \tag{6.29}$$

Substituting equation (6.29) into (6.1) gives the 2nd Piola-Kirchhoff stress of the whole fibrous soft tissue:

$$\begin{cases} S = \int_{-\frac{\pi}{2}}^{\frac{\pi}{2}} R(\theta) S_{fibre} [\bar{N} \otimes \bar{N}] d\theta \\ S_{fibre} = \int_{0}^{\varepsilon_{fibre}} P(\varepsilon_{Lag.})\, s_{fibre}\, d\varepsilon_{Lag.} \\ s_{fibre} = \dfrac{G_{fibre} \pi r^4}{AL(r^2 + 2a^2) D(\varepsilon_{Lag.})} \left(\sqrt{1 + a^2 b^2} - \sqrt{1 + a^2 b^2 \cos^2(bD(\varepsilon_{Lag.})x)} \right) \cdot \\ \qquad \dfrac{x_0 \varepsilon_{Lag.} - x_0 D(\varepsilon_{Lag.})}{x_0 D(\varepsilon_{Lag.}) + c(\varepsilon_{Lag.}) \left[(1 - D(\varepsilon_{Lag.})) x_0 + L \times D(\varepsilon_{Lag.}) \right]} \\ P(\varepsilon_{Lag.}) = \dfrac{\kappa}{\psi} \left(\dfrac{\varepsilon_{Lag.}}{\psi} \right)^{\kappa - 1} \exp\left[- \left(\dfrac{\varepsilon_{Lag.}}{\psi} \right)^{\kappa} \right] \end{cases} \tag{6.30}$$

6.2.3. Angular distribution of fibres

Nearly all of the currently available structural models for soft tissues have considered the angular distribution of fibres to be a 'normal' distribution [122,144,145,156]. Despite the good fit of these structural models to the experimental stress-strain data, it will be shown in this section that a normal distribution may not be consistent with the physical fibre kinetmatics *in situ*. Alternatively, a new angular distribution function is derived for fibres based on the physical conditions and kinematics of the fibres within the tissue, for a more accurate description.

Consider that the vectors $\vec{V}_1$ and $\vec{V}_2$ in Figure 6.5 represent the position vector of a fibre before and after the application of an increment of external load to the tissue, and θ and α are the vector's angle with the x axis before and after strain, respectively. The fibre has been fixed from one end and rotates around this point. Let us assume that the applied strain increment has been small (any given increment of strain can be applied as a series of infinitely small strain increments). Under such a

condition, one can consider that the projection of the two vectors on the x axis remains unchanged; whilst the position along the y direction changes (Figure 6.5).

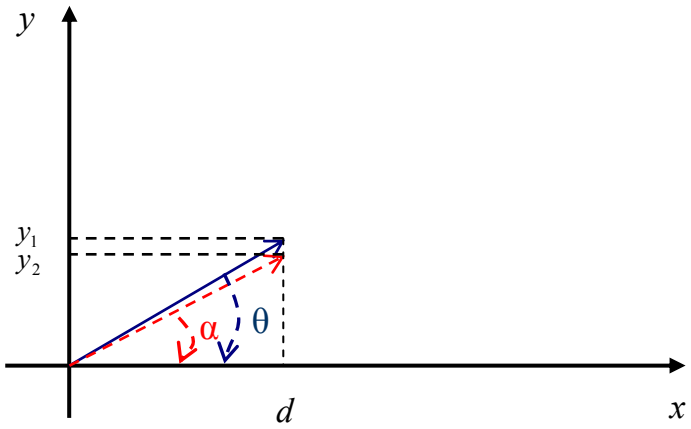

Figure 6.5 Position vector of a fibre before (continuous blue arrow) and after (dotted red arrow) the application of external load on the tissue. The fibre is shown to be rotating around its end at origin.

Thus:

$$\tan\theta = \frac{y}{d} \Rightarrow \theta = \arctan\left(\frac{y}{d}\right) \tag{6.31}$$

and:

$$d\theta = \frac{d}{d^2 + y^2} dy \tag{6.32}$$

Dividing both sides of above equation by π:

$$\frac{d\theta}{\pi} = \frac{1}{\pi}\frac{d}{d^2 + y^2} dy \tag{6.33}$$

Satisfying the condition in equation C2 (Appendix C), interestingly $\frac{d\theta}{\pi}$ in equation (6.33) has the form of a Lorentzian distribution function. Its physical meaning is that the angular orientation of a fibre with respect to the coordinate axis, in small deformations resulting to small rotations around a fixed point at one of its ends, would change in a way that the coordinate variables, x and y, will have a Lorentzian distribution. Since the sum of Lorentzian variables would also have a Lorentzian

distribution [158], the θ itself would follow a Lorentzian distribution pattern. Thus, the angular distribution of the fibres in a planar tissue at each increment of small deformation would follow a Lorentzian distribution pattern as:

$$R(\theta) = \frac{1}{\pi} \frac{\gamma}{(\theta - \theta_0)^2 + \gamma^2} \tag{6.34}$$

where θ_0 specifies the location of the peak of the distribution, and γ specifies the half-width at half-maximum.

Substituting equation (6.34) into (6.30), the final form of the 2nd Piola-Kirchhoff stress of the whole fibrous soft tissue would be:

$$\begin{cases} S = \int_{-\frac{\pi}{2}}^{\frac{\pi}{2}} R(\theta) S_{fibre} [\vec{N} \otimes \vec{N}] d\theta \\ S_{fibre} = \int_0^{\varepsilon_{fibre}} P(\varepsilon_{Lag.})\, s_{fibre}\, d\varepsilon_{Lag.} \\ s_{fibre} = \frac{G_{fibre} \pi r^4}{AL(r^2 + 2a^2) D(\varepsilon_{Lag.})} \left(\sqrt{1 + a^2 b^2} - \sqrt{1 + a^2 b^2 \cos^2(bD(\varepsilon_{Lag.})x)} \right) \cdot \\ \qquad \frac{x_0 \varepsilon_{Lag.} - x_0 D(\varepsilon_{Lag.})}{x_0 D(\varepsilon_{Lag.}) + c(\varepsilon_{Lag.}) \left[(1 - D(\varepsilon_{Lag.})) x_0 + L \times D(\varepsilon_{Lag.}) \right]} \\ P(\varepsilon_{Lag.}) = \frac{\kappa}{\psi} \left(\frac{\varepsilon_{Lag.}}{\psi} \right)^{\kappa - 1} \exp\left[- \left(\frac{\varepsilon_{Lag.}}{\psi} \right)^{\kappa} \right] \\ R(\theta) = \frac{1}{\pi} \frac{\gamma}{(\theta - \theta_0)^2 + \gamma^2} \end{cases} \tag{6.35}$$

6.2.4. Stress-strain equation in fibrous soft tissues

For parameter estimation, the model in equation (6.35) should be fitted to the experimental stress-strain data of the tissue. Generally, in mechanical uniaxial

or biaxial deformation tests, the data set is presented either in engineering stress or true stress, versus strain. Thus, the 2nd Piola-Kirchhof stress of the continuum in equation (6.35) needs to be converted accordingly to describe the data set:

a) if the engineering stress is used in presenting the experimental stress data, the model should express the 1st Piola-Kirchhoff stress, where [138]:

$$\sigma = f\ S \tag{6.36}$$

σ and f are the 1st Piola-Kirchhoff stress and deformation gradient tensors respectively. Thus:

$$\sigma = f \int_{-\frac{\pi}{2}}^{\frac{\pi}{2}} R(\theta) S_{fibre} [\vec{N} \otimes \vec{N}] d\theta \tag{6.37}$$

or equivalently in component format, using the equation (C8, Appendix C):

$$\begin{cases} \sigma_{11} = \lambda_1 \int_{-\frac{\pi}{2}}^{\frac{\pi}{2}} R(\theta) S_{fibre} \cos^2\theta\ d\theta \\ \sigma_{22} = \lambda_2 \int_{-\frac{\pi}{2}}^{\frac{\pi}{2}} R(\theta) S_{fibre} \sin^2\theta\ d\theta \\ \sigma_{12} = \sigma_{21} = \dfrac{1}{\sqrt{\lambda_1 \lambda_2}} \int_{-\frac{\pi}{2}}^{\frac{\pi}{2}} R(\theta) S_{fibre} \cos\theta \sin\theta\ d\theta \end{cases} \tag{6.38}$$

where λ is the stretch ratio.

b) if the true stress is the measure of stress used in experimental data, the model should express the Cauchy stress, where [138]:

$$T = f\ S\ f^T \tag{6.39}$$

T and f are the Cauchy stress and deformation gradient tensors, respectively. Thus:

$$T = f \int_{-\frac{\pi}{2}}^{\frac{\pi}{2}} R(\theta) S_{fibre} [\vec{N} \otimes \vec{N}] d\theta \; f^T \tag{6.40}$$

or equivalently in component format, using the equation (C8, Appendix C):

$$\begin{cases} T_{11} = \lambda_1^2 \int_{-\frac{\pi}{2}}^{\frac{\pi}{2}} R(\theta) S_{fibre} \cos^2 \theta \; d\theta \\ T_{22} = \lambda_2^2 \int_{-\frac{\pi}{2}}^{\frac{\pi}{2}} R(\theta) S_{fibre} \sin^2 \theta \; d\theta \\ T_{12} = T_{21} = \dfrac{1}{\lambda_1 \lambda_2} \int_{-\frac{\pi}{2}}^{\frac{\pi}{2}} R(\theta) S_{fibre} \cos\theta \sin\theta \; d\theta \end{cases} \tag{6.41}$$

where λ is the stretch ratio.

6.3. Results and analysis

The first step in determining the resultant stresses by either equations (6.38) or (6.41) is to calculate the e_{fibre} and s_{fibre} (equations 6.15 and 6.26), which requires the geometrical and mechanical properties of the collagen fibre as inputs. However, the literature is diverse concerning the values reported for a single fibre, leading to uncertainty in choosing a single suitable value for calculations [155]. In addition, the properties of fibres seem to show subject dependence (i.e. species, age, etc) [151], and no data specific to 18 to 24 months old porcine valves is available. Thus, and in order to develop an understanding of the capabilities of the model for different fibre properties reflected in different AV samples, the minimum and maximum reported values for the mechanical properties (E_{fibre} and G_{fibre}) of a single fibre are incorporated into model calculations, and the results presented for the two cases.

The shear modulus of collagen fibre G_{fibre} has been reported to be of the order of magnitude of 10^8 Pa [155], with the elastic modulus E_{fibre} in order of magnitude

between 100 MPa to 1 GPa [153,155,159]. As for the geometrical properties, the amplitude of the fibre waviness (a) ranges between 1 μm to 10 μm, the frequency values (b) range approximately from 698131 to 69813, and radius (r) between 50 nm to 500 nm [153]. However, histological analysis of the AV samples enabled quantification of a, b and the crimped length (x_0) of the collagen fibres in samples used in this study, with the average values of $a = 3$ μm, $x_0 = 100$ μm and $b = 628318$. For the purpose of modelling, these values were utilised, which fall well within the reported range in the literature. In addition, two values for G_{fibre} were selected, equating to the minimum and maximum values of E_{fibre} in the literature. Table 6.1 summarizes the reported values for the mechanical and geometrical properties of a fibre, and the values selected in this study.

Table 6.1 Geometrical and mechanical properties of a single fibre: reported data and values used in the model.

	a (μm)	b	r (nm)	x_0 (μm)	G_{fibre} (Pa)
Reported Values	1 - 10	698131 - 69813	50 - 500	---	$O^*(10^8)$
Used Values	3	628318.4	100	100.6	1.3×10^8 3.7×10^8

* Order of magnitude.

Figure 6.6 shows how the elastic modulus of a fibre changes as it becomes straighter, calculated from equation (6.15) with the values given in Table 6.1. When it becomes fully straight, the modulus reaches its maximum, and remains constant thereafter (straight line in the Figure 6.6). For shear modulus values of $G_{fibre} = 1.3 \times 10^8$ Pa and $G_{fibre} = 3.7 \times 10^8$ Pa, the values for E_{fibre} correspond to 3.41×10^8 Pa and 1.04×10^9 Pa respectively according to the equation, which are the minimum and maximum values reported in the literature for the elastic modulus of a fibre [153,155].

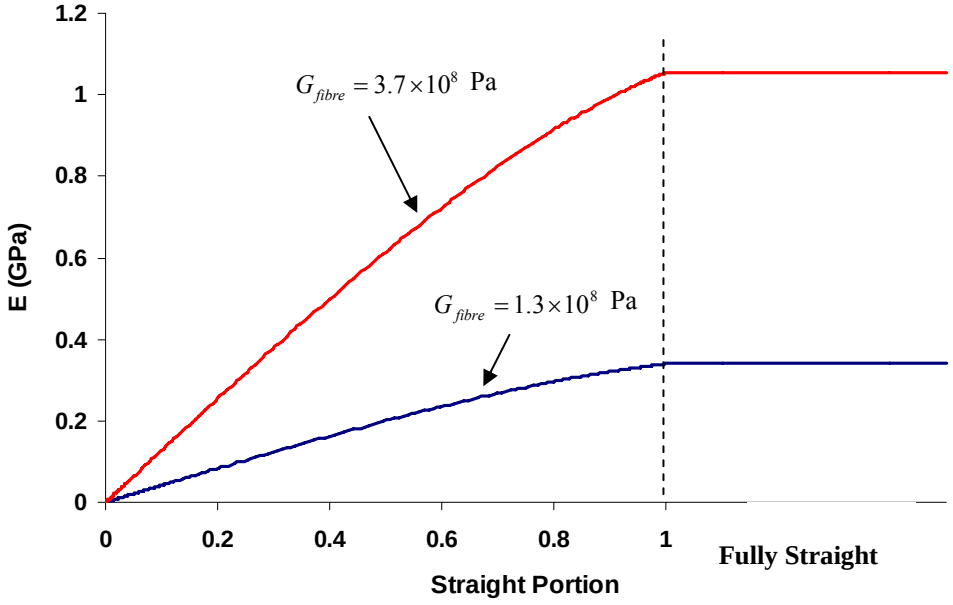

Figure 6.6 Elastic modulus of a fibre as it becomes straight, calculated by equation (6.15).

The engineering stress-strain curve for a circumferentially loaded sample at 60%/min (Chapter 3) was fitted to the model in equation (6.38) for σ_{11}, since the tests were performed uniaxially and thus $\sigma_{22} = \sigma_{12} = 0$. The estimation of parameters was optimised using a code in MATLAB^{TM}, employing a genetic algorithm application. The optimised parameters were obtained by the best fit to experimental data, through minimisation of an objective function defined as the normalized sum of the squared errors between each experimental data point and the model estimate. The sudden transient reduction in stress, due to the partial failure of ventricularis layer of the valve tissue (§3.5) could not be followed by the model, as layer dependant properties have not been incorporated.

The straight portion of the fibre at each applied tissue strain ($\varepsilon_{Lag.}$), given by equation (6.17), is shown in Figure 6.7a for both fibre properties considered. As expected, the stiffer fibre becomes straighter at higher strains compared to the softer fibre. While the model predicts that the softer fibre becomes fully straight at approximately $\varepsilon_{Lag.} = 0.26$, it predicts that only approximately 60% of the stiffer fibre is straight at the same strain (Figure 6.7a). The fibre strain ε_{fibre} against the applied

strain $\varepsilon_{Lag.}$ is shown in Figure 6.7b, determined by equation (6.25). It is evident that the stiffer fibre undergoes lower strains at each $\varepsilon_{Lag.}$. This was also reflected in the values for the proportionality coefficient $c(\varepsilon_{Lag.})$, as the values calculated by the model were 1.86 ± 0.33 and 1.31 ± 0.12 for the stiffer and softer fibre, respectively. This, in the light of equation (6.22), physically means that shorter lengths of the stiffer fibre become straight at each applied strain increment $\varepsilon_{Lag.}$, compared to the softer fibre. The current literature suggests that the failure strain for a fibre is around 10% [155]. As shown in Figure 6.7b, the model calculates that the fibres will reach their failure strain at an applied strain $\varepsilon_{Lag.}$ of approximately 0.26 or 0.34, for softer or stiffer fibres respectively. However, the failure strain for the tissue was observed to be around 0.31 (Chapter 3, Table 3.1), which would perhaps imply that the fibres in the tested AV samples possess an elastic modulus lower than 10^9 Pa, the upper limit reported in the literature.

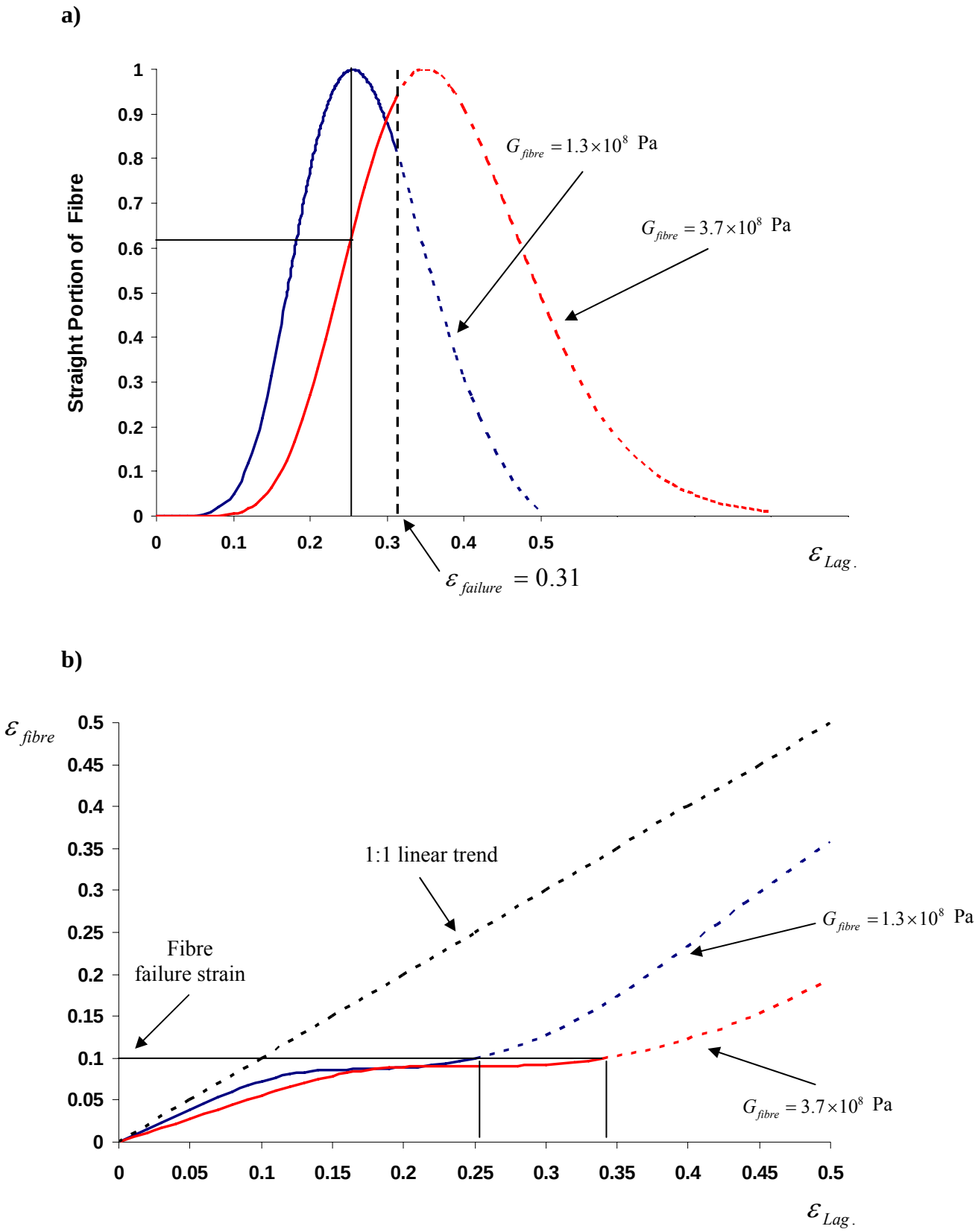

Figure 6.7 (a) The straight portion of a fibre at each applied strain. The dashed line indicates the tissue failure strain at 0.31. Only approximately 60% of the stiffer fibre is straight at the same tissue strain $\varepsilon_{Lag.}$ where the softer fibre is fully straight. (b) Fibre strain ε_{fibre} against $\varepsilon_{Lag.}$. The dashed line indicates the 1 to 1 linear relationship. The failure strain of fibre is 10% [155], which occurs at approximately $\varepsilon_{Lag.} = 0.26$ or $\varepsilon_{Lag.} = 0.34$.

The stress-strain curves for a single fibre s_{fibre} at the two boundary stiffness conditions are shown in Figure 6.8, calculated by equation (6.26). The elastic modulus of the two fibres has approximately a 3 fold difference, when fibres are fully straight, as presented in Figure 6.6. This difference can also be observed in the values for s_{fibre} (Figure 6.8).

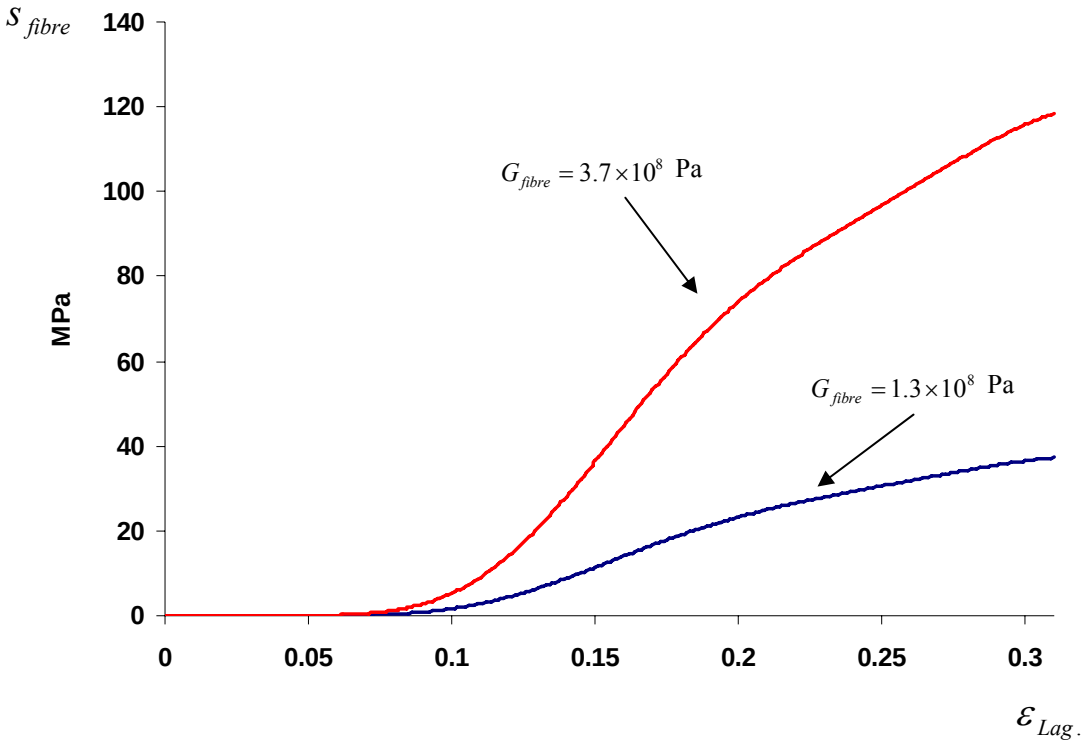

Figure 6.8 Stress-strain curve in a single fibre calculated by the model in equation (6.26).

With the stress-strain relationship for a single fibre now quantified, the stress in a group of fibres in the tissue, S_{fibre}, was calculated using equation (6.29). The corresponding stress-strain curves at the two boundary stiffness conditions are shown in Figure 6.9a. However, the model calculated that the total fraction of fibres that are active in these two boundry conditions are significantly different. By definition, the total fraction of fibres can be calculated from the $P(\varepsilon_{Lag.})$ defined in equation (6.28), by $\int P(\varepsilon_{Lag.})d\varepsilon_{Lag.}$ [111,156]. The total fraction of active fibres for each case is shown in Figure 6.9b. The results indicate that at the point of gross sample failure, while approximately 80% of the total fraction of fibres in the tissue are active for the soft fibre case, only approximately 30% of the fibres are contributing to the load

bearing in the tissue with the stiffer fibre characteristics (Figure 6.9b).

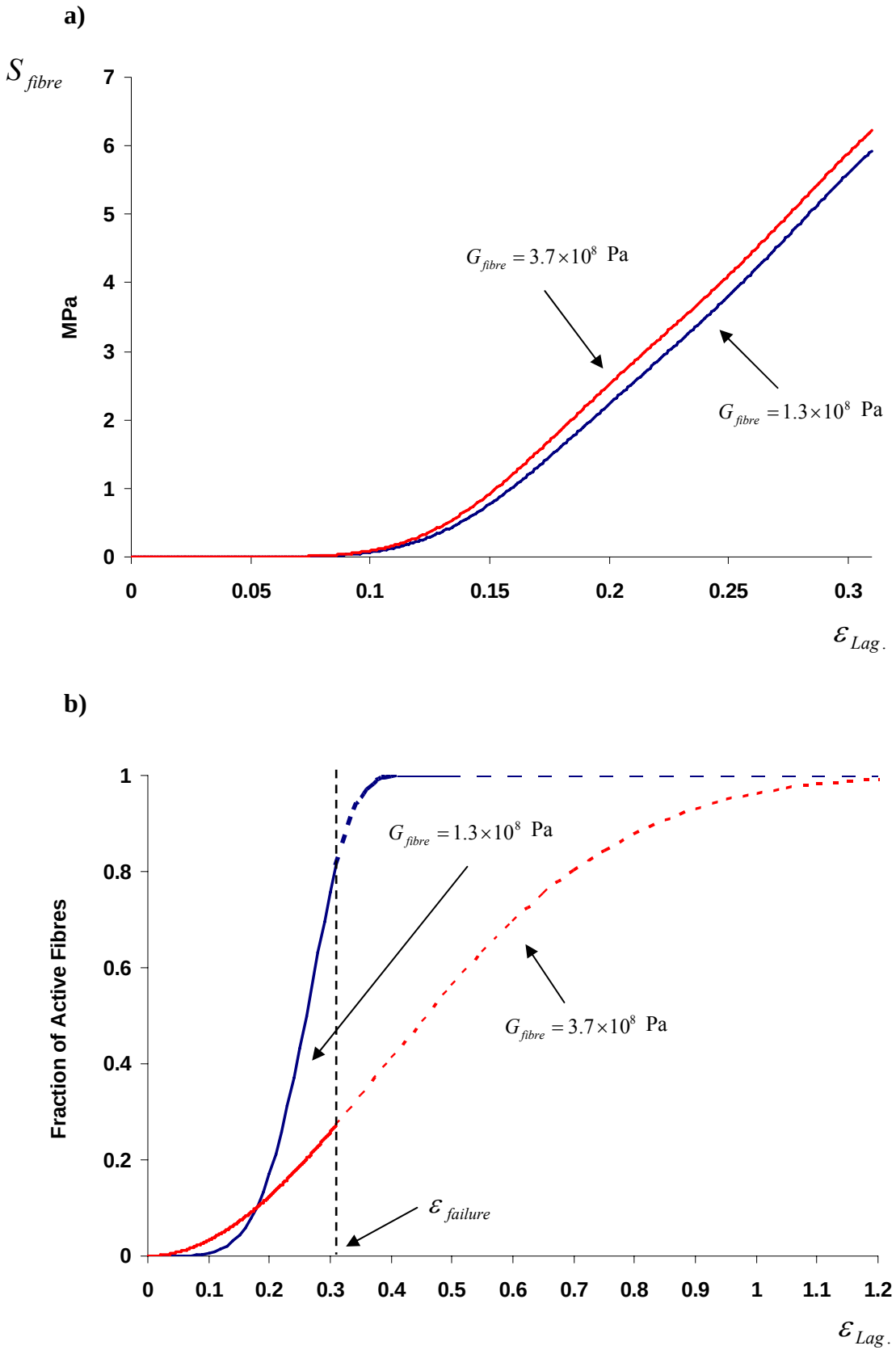

Figure 6.9 (a) Stress-strain curves calculated using the two boundary stiffness conditions for the active fibres in load bearing of the tissue, (b) The total fraction of fibres which are active within the tissue at each strain level.

To calculate the 1st Piola-Kirchhoff stress of the tissue σ_{11} in equation (6.38), the angular distribution of fibres should be incorporated into the equation. All the previous studies regarding the microarchitecture of AV tissue have assumed a normal distribution [66,122], hence the previously available data cannot be used directly in the model, as the current study has shown that the angular distribution of fibres should follow a Lorentzian pattern. However, using the experimental data given in [122], the angular distribution of fibres within porcine AV tissue is symmetrical around the peak at zero degree, which translates to $\theta_0 = 0$ and $\gamma = \frac{\pi}{4}$ for a Lorentzian distribution. By incorporating these values into equation (6.34) and subsequently (6.38), the modelling results for the stress-strain curve of the whole tissue in the circumferential direction are presented in Figure 6.10, compred with the experimental data from chapter 3. The R^2 values were 0.97 and 0.98 for the case of soft and stiff fibres, respectively. The values adopted for each model parameter are summarized in Table 6.2, for the case of the two fibres.

Table 6.2 The model parameters for the two types of fibres considered.

	α	β	$c(\varepsilon_{Lag.})$	κ	ψ	θ_0	γ	R^2
For $G_{fibre} = 1.3 \times 10^8$	9.38 ± 0.43	0.03 ± 0.01	1.31 ± 0.12	5.56 ± 0.38	0.28 ± 0.02	0	$\frac{\pi}{4}$	0.97 ± 0.017
For $G_{fibre} = 3.7 \times 10^8$	11.72 ± 0.58	0.04 ± 0.01	1.86 ± 0.33	2.36 ± 0.27	0.55 ± 0.05	0	$\frac{\pi}{4}$	0.98 ± 0.004

a)

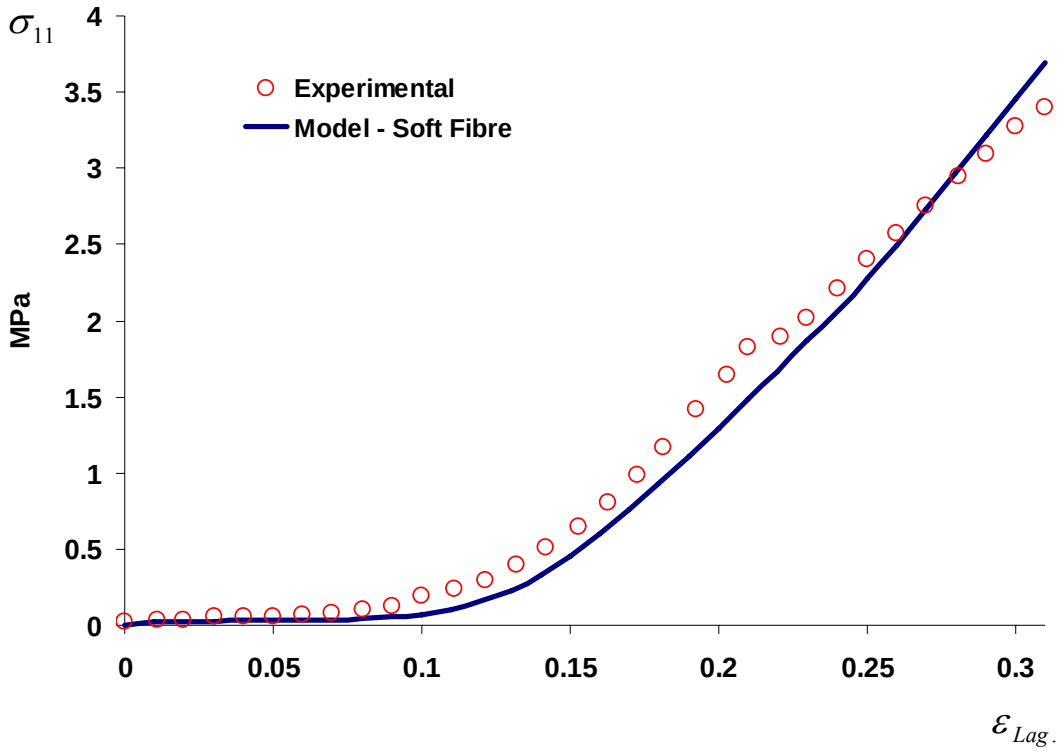

b)

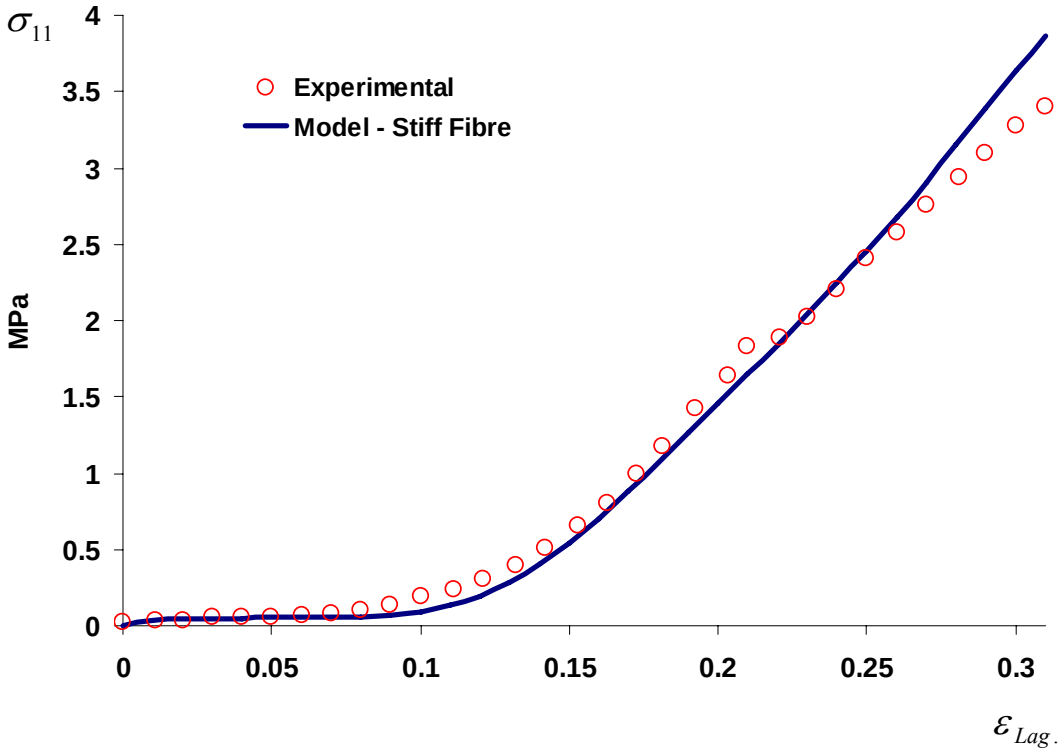

Figure 6.10 Experimental stress-strain curves and the modelling results for: (a) softer fibre; (b) stiffer fibre. The experimental data are shown with circles, and the modelling results by a continuous line. The curves represent the stress-strain data in the circumferential direction.

6.4. Discussion

A new modelling criterion was developed and presented in this chapter which considers the contribution of wavy fibres in the overall mechanical behaviour of fibrous tissues. As the fibres become straighter, their effective stiffness and contribution to the load bearing status of the tissue increases, reaching a maximum when they become fully straight. Previous structure-function modelling approaches have considered the gradual recruitment of the fibres, with fibres only contributing to the tissue mechanics once straight. However, the modelling approach presented in the current chapter has considered the gradual straightening of individual fibres, steadily increasing their contribution to the mechanical behaviour of the tissue as they become straighter. The model successfully fitted the experimental data, and quantified physically meaningful parameters, which provide more insights into the response of microstructure of the AV under deformation. These include properties of a single fibre as it becomes increasingly straight, stress-strain parameters in a single fibre, and the fraction of the fibre population that contributes to the tissue mechanics at each strain/stress level.

A specific angular distribution function was presented as a part of the model, derived from the possible changes in coordinates of a fibre during rotation, for a planar tissue such as AV. Analysis showed that the angular distribution function of fibres should follow a Lorentzian distribution pattern, and can not therefore be chosen arbitrarily. A new relationship between fibre strain and applied strain at the tissue level was also introduced, based on the findings presented in chapter 5, which demonstrated that strain transfer is non-affine. This adds to the accuracy in quantifying fibre strains even at low tissue-level applied loads.

To assess the capability of the model in providing meaningful results for different fibre properties, reflecting different types of tissue characteristics, the upper and lower limits of the mechanical properties of a single fibre reported in the literature were incorporated into the equations, to compare the extreme cases of modelling parameters. The model provided a good fit with the experimental data in both cases, and quantified how the response of the microstructure would differ with different fibre properties.

One of the ultimate goals of modelling the microstructural mechanics of tissues is to be able to quantify the loading environment encountered by the cells residing within the microstructure. Such information would have valuable implications in cell-mediated tissue engineering applications, and can not be measured by experimentation alone. The correlation between the tissue level strain and the fibre strain is presented in the graph in Figure 6.7b. Since it is well accepted that the AVICs are tightly bonded to the fibres [22,23], it is reasonable to suggest that the maximum tensile strain levels transferred to the attached cells may be closer to those seen at fibre level. However, cells are likely to withstand additional compressive and shear strains, as the whole ECM reorganizes during tissue deformation.

It must be noted that only the data related to the circumferential loading direction was considered for the modelling in this chapter, as the preferred principal direction of the collagen fibres within the AV is the circumferential direction. The micromechanics of the fibres and their contribution to the tissue behaviour are significantly more pronounced in this direction, and can therefore be better analysed by a fibre mechanics based model in more details. However, the stress/strain relationships have been derived for both loading directions, as presented in equations (6.38) and (6.41).

The improvements introduced by the modelling criteria presented in this chapter will lead to a more accurate quantification of the microstructure response, especially at lower applied loads on the tissue, where the fibres would still be more wavy rather than straight.

The modelling approach developed in this chapter was based on the hyperelasticity assumption introduced by Lanir (equation 6.1) [143,147]. While this is a well accepted criterion for the structural-based models of soft tissues, it does not take into account the shearing effects due to the non-fibrous components of the ECM (e.g. GAG). Indeed, the interactions between the fibres and the GAG content of the tissue matrix during deformation is known to induce shear on the fibres, which further contributes to their gradual straightening [155]. However, due to the random nature of the size, shape and content of the fibres in the tissue ECM, deterministic approaches in characterising such shearing effects may prove very challenging, and further

simplifying assumptions may be required [155]. Nevertheless, the stochastic formulations incorporated in microstructural based models to represent the gradual fibre straightening and recruitment, integrate the overall straightening effects irrespective of the underlying causes, e.g. the shearing between fibres and the GAG substance, the inter-connections of the fibres, or simply straightening of the fibres due to stretch of the whole tissue.

Chapter 7

The role of the elastin network in the mechanical behaviour of the aortic valve

7.1. Synopsis

The two main load-bearing constituents of the aortic valve (AV) are the collagen fibres and elastin, as reviewed in chapter 1. The role of collagen fibres in the mechanical behaviour of the AV was modelled and analysed in chapters 6 and 7. The role of elastin network will be considered in this chapter.

The contribution of the elastin network to the mechanical behaviour of the AV has generally been described in a qualititative fashion in the literature, limited to two main descriptions: (i) it contributes to the load-bearing capacity of the tissue at small strains, where the collagen fibres are wavy and bear minimal loads and the tissue stress-strain relationship is quasi-linear [5]; and (ii) it restores the contracted configuration of the valve leaflet after the stretch induced during the diastolic phase of each cardiac cycle [19,20]. A more thorough characterisation of structure-function relationships in the AV requires the contribution of the elastin network to the mechanical behaviour of the AV to be quantified. Models regarding the elastin network deformation and its connection to the total deformation of the AV tissue are currently lacking in the literature. This chapter introduces and develops a theoretical criterion to understand and quantify the role of the elastin network in AV mechanical behaviour. A strain energy function is formulated for the elastin network, and the force-elongation relationship derived from the strain energy function accordingly.

7.2. Theoretical criterion and formalism

The modelling criteria used here are based on the principles of statistical mechanics of worm-like molecular chains theories originally developed for entropic rubber elasticity [161,162]. Concisely, the theory applies to flexible molecular chain network structures that are formed by occasional cross-links between the chains [163-165]. In their undeformed state, chains can have many arbitrary configurations of nearly equal entropy, typically represented by statistical distributions. Perturbing the chains away from their equilibrium conformations generates entropic forces that oppose these deformations, which forms the basis of their mechanical behaviour and stress-strain response [164,165]. The elastin network in soft tissues is thought to provide a close

analogy to the worm-like chain networks [163,165,166]. A typical histological image of the elastin network in the porcine AV samples used in the current study is shown in Figure 7.1, depicting the random and worm-like shape of the elastic fibres. The elastin network in the AV is known to be in the form of a flat network providing inter-fibre connections with collagen fibres [19,20]. A schematic of this configuration is shown in Figure 8.2a. Following this analogy, the principles of statistical mechanics of worm-like molecular chains are applied to the elastin network within the AV tissue.

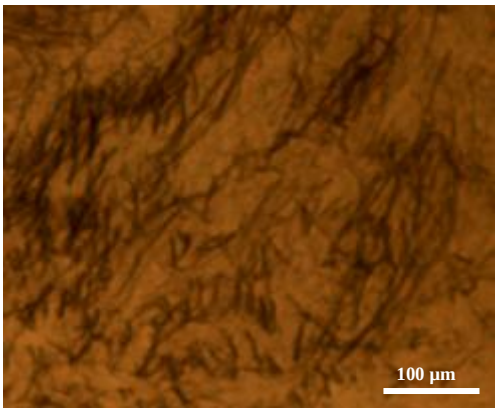

Figure 7.1 A histological image of the elastin network in an unloaded AV tissue sample, stained using Millers Elastic and imaged by a x20 magnification objective. Elastic fibres have a random shape, close to the worm-like chain configuration.

The fundamental assumption of the chain network theory is that the free energy of a network of n chains per unit volume is equal to the sum of the elastic free energy of the individual chains [161,164]. Thus the entire network may be replaced by a system of a single chain in the local Cartesian coordinate system [164]. For a planar tissue such as the AV, let us consider the system to be a square area element with sides of initial length a_0, oriented along the coordinate axes of x and y, and having a single elastin chain along its diagonal as shown in Figure 7.2b. The two end points, *A* and *B*, are the fixed points of inter-fibre connection with the collagen fibres (Figure 7.2a), and the chain can assume any arbitrary configuration without changing the end points.

(a)

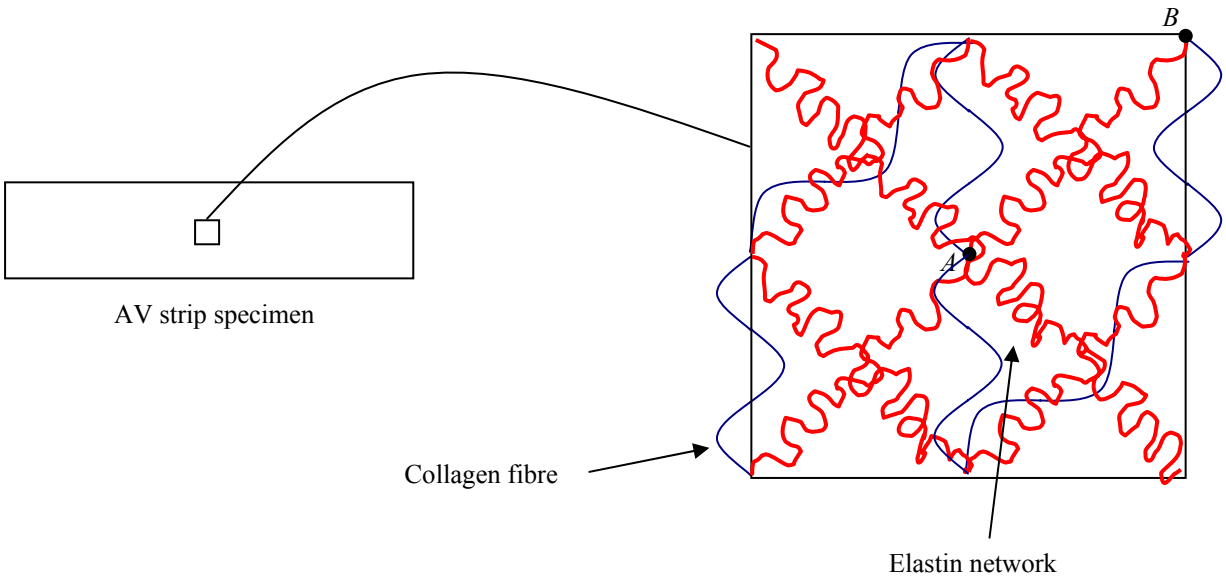

(b)

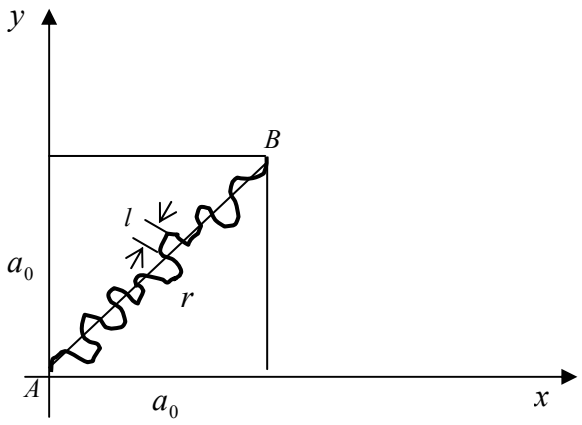

Figure 7.2 (a) Schematic of the elastin network structure within the AV (red lines), and its inter-fibre connections with the wavy collagen fibres (blue lines), as proposed in [19,20] (b) Geometry of a single chain in a 2D square element.

In the statistical treatment of a single chain, its geometrical structure is idealized to be composed of N segments of equal length l, also known as the Kuhn segment length, as shown in Figure 7.2b. The contour length L of the chain is then $L = Nl$.

Let r depict the current end to end distance of the chain, and r_0 the unstrained free chain distance. The chain stretch is therefore:

$$\lambda = \frac{r}{r_0} \tag{7.1}$$

The next key step is to determine the entropy of the chain. As previously mentioned, the chain can assume any arbitrary configuration between the two end points *A* and *B*. Let us introduce the probability density $p(\lambda)$, which essentially describes the probability that a chain of contour length L takes a configuration characterised by the end to end distance r. Then the entropy of that chain is governed by the Boltzmann's equation as:

$$s = k \ln p(\lambda) \tag{7.2}$$

where k is the boltzmann constant. For a purely entropic response the free energy ψ_c of the chain is obtained by [100]:

$$\psi_c = -Ts \tag{7.3}$$

where T is the absolute temperature. Inserting equation (7.2) into (7.3):

$$\psi_c = -kT \ln p(\lambda) \tag{7.4}$$

ψ_c is the free energy for the unconstrained deformation of the chain between the two cross-link points *A* and *B*, shown in Figure 7.2.

By definition, the force of deformation for a chain can now be calculated by:

$$F_c = \frac{d\psi_c}{d\lambda} \tag{7.5}$$

A statistical treatment for the free energy function in equation (7.4) that is valid for large stretches is provided by the Langevin model [161]. The probability density function would be of the form:

$$p(\lambda) = p_0 \exp\left[-N\left(\frac{\lambda}{\sqrt{N}}\beta + \ln\frac{\beta}{\sinh\beta}\right)\right] \tag{7.6}$$

where $\beta = \ell^{-1}(\frac{\lambda}{\sqrt{N}})$, $\ell(\beta) = \coth\beta - 1/\beta$ is the well-known Langevin function and p_0 is a constant. Inserting equation (7.6) into (7.4) gives the free energy of a single chain as:

$$\psi_c = NkT\left(\frac{\lambda}{\sqrt{N}}\ell^{-1}(\frac{\lambda}{\sqrt{N}}) + \ln\frac{\ell^{-1}(\frac{\lambda}{\sqrt{N}})}{\sinh\ell^{-1}(\frac{\lambda}{\sqrt{N}})}\right) + \psi_0 \tag{7.7}$$

where ψ_0 is a constant so that the free energy of the chain ψ_c would be zero in the undeformed state.

Substituting equation (7.7) into (7.5) gives the associated force acting on a chain as:

$$F_c = kT\sqrt{N}\ell^{-1}(\frac{\lambda}{\sqrt{N}}) \tag{7.8}$$

The Langevin function in the above equation can be approximated by [167]:

$$\ell^{-1}(\frac{\lambda}{\sqrt{N}}) \approx \frac{\lambda}{\sqrt{N}}\left(3 - (\frac{\lambda}{\sqrt{N}})^2\right)\Big/\left(1 - (\frac{\lambda}{\sqrt{N}})^2\right) \tag{7.9}$$

Thus, the force acting on a single chain takes the final form:

$$F_c = kT\lambda\cdot\frac{3 - (\lambda^2/N)}{1 - (\lambda^2/N)} \tag{7.10}$$

From this, a network model of aggregate chains can be developed, linked to the deformation at the tissue level, which directly exploits the energy function. As outlined earlier, the free energy of a network of n chains per unit volume is equal to the sum of the elastic free energy of the individual chains [161,164]. Assuming the network consists of n chains of equal Kuhn segment length l per unit volume, the free energy of the network will then be:

$$\psi_n = \sum_{i=1}^{n}\psi_c^i = n\psi_c \tag{7.11}$$

However, to be able to define the macroscopic deformation energy of the network, i.e. the deformation of the network due to application of load at the tissue (macro)

level, it is necessary to link the deformation of the chain to the macroscopic deformation of the tissue continuum. In a broad classification, the macro-to-micro transition of the deformation assumes either an *affine* or *non-affine* transformation [168]. Under the affine assumption, the chain stretch λ is a linear function of the macro stretch $\bar{\lambda}$, i.e. $\lambda = a\bar{\lambda} + b$, where a and b are constant coefficients [168]. The non-affine deformation assumes a non-linear transformation of strain map, which in the general case takes the relation $\lambda = f(\bar{\lambda})$, where f is a non-linear function that acts on the affine stretch [168]. The assumption of affine deformation may idealise the deformation of some polymeric chains [169,170]. However, it was shown in chapter 5 that the strain transfer from tissue level to the micro-structure in AV tissue specimens under tensile deformation is non-affine. As such, it becomes necessary to derive a relationship between the macro (tissue level) stretch ($\bar{\lambda}$) and the induced micro stretch (λ), based on the network geometry defined in Figure 7.2.

Consider the single chain in the undeformed network shown in Figure 7.2b. The unstrained end to end distance of the chain, r_0, is then $r_0 = a_0\sqrt{2}$. After deformation, the end-to-end chain length vector will be given by $\bar{r} = a_0(\bar{\lambda}_1\hat{i} + \bar{\lambda}_2\hat{j})$, where $\bar{\lambda}_1$ and $\bar{\lambda}_2$ are the principal macro stretches, and i and j are the unit vectors, in x and y directions respectively. Hence, the magnitude of $\bar{r}$ is:

$$r = a_0\sqrt{\bar{\lambda}_1^2 + \bar{\lambda}_2^2} \tag{7.12}$$

Substituting this into equation (7.1):

$$\lambda = \sqrt{\frac{\bar{I}_1}{2}} \tag{7.13}$$

where $\bar{I}_1$ is the first principal invariant of the Cauchy-Green deformation tensor in the macro level principal reference system, and is given by $\bar{I}_1 = \bar{\lambda}_1^2 + \bar{\lambda}_2^2$. Equation (7.13) represents the relationship between macro and micro stretches for the considered network.

Now, with the relationships for network energy ψ_n and the non-affine transformation of the macro to micro (equations (7.11) and (7.13) respectively) we

can derive the energy function for the elastin network with regards to the deformation at tissue level. This can be done through [168]:

$$\Psi_{elast} = \psi_n(\sqrt{\frac{\bar{I}_1}{2}}) \tag{7.14}$$

By inserting equations (7.7) and (7.11) into (7.14):

$$\Psi_{elast} = nkTN\left(\sqrt{\frac{\bar{I}_1}{2N}}\ell^{-1}(\sqrt{\frac{\bar{I}_1}{2N}}) + \ln\frac{\ell^{-1}(\sqrt{\frac{\bar{I}_1}{2N}})}{\sinh\ell^{-1}(\sqrt{\frac{\bar{I}_1}{2N}})}\right) + \psi_0 \tag{7.15}$$

and from equation (7.5), the forces can be calculated as:

$$F_i = \frac{\partial\Psi_{elast}}{\partial\bar{\lambda}_i}\ ,\ \ i = 1,2 \tag{7.16}$$

where i denotes the principal directions.

7.3. Results and analysis

Experimental studies regarding the mechanical behaviour of the AV elastin network in isolation are very rare in literature, mainly owing to the difficulties associated with isolating the intact elastin network from the other components of the AV matrix [20,171]. However, Vesely (1998) carried out a study attempting to look at the mechanical behaviour of the intact elastin network within the AV tissue by digesting other matrix components, and experimentally characterised the stress-strain relationship under uniaxial loading, in circumferential and radial loading directions [20]. To establish if the developed model is capable of characterising the behaviour of elastin network, the model is fitted to the data provided in the study. However, the digestion procedure may alter the initial structural architecture of the elastin network within the tissue, especially at the inter-fibre connections with the surrounding collagen fibres, and subsequently the overall behaviour of the network. One should note that such effects can not be avoided in experimental investigations, and are inherent to the adopted protocols, and hence the resulting data.

Under uniaxal deformation, assuming that the principal direction is $i=1$, then $\bar{\lambda}_2 = 0$. Thus Ψ_{elast} in equation (7.15) simplifies to:

$$\Psi_{elast} = nkTN\left(\frac{\bar{\lambda}_1}{\sqrt{2N}}\ell^{-1}\left(\frac{\bar{\lambda}_1}{\sqrt{2N}}\right) + \ln\frac{\ell^{-1}\left(\frac{\bar{\lambda}_1}{\sqrt{2N}}\right)}{\sinh\ell^{-1}\left(\frac{\bar{\lambda}_1}{\sqrt{2N}}\right)}\right) + \psi_0 \tag{7.17}$$

and therefore the force will be:

$$F_1 = nkT\sqrt{N}\ell^{-1}\left(\frac{\bar{\lambda}_1}{\sqrt{2N}}\right) \tag{7.18}$$

which can be expressed in light of equation (7.9) as:

$$F_1 = \frac{1}{2}nkT\bar{\lambda}_1 \cdot \frac{3-(\bar{\lambda}_1^2/2N)}{1-(\bar{\lambda}_1^2/2N)} \tag{7.19}$$

Equation (7.19) was fitted to the experimental force-strain data provided in the work of Vesely [20]. The results for the circumferential and radial directions are shown in the graphs of Figures 7.3a and 7.3b, respectively. The model provides a good fit, with R^2 values in excess of 0.98. Values for the constants and network parameters are summarized in Table 7.1. The network parameters are close to the values reported for other soft tissues such as arteries [166,172]. However, characterisation of these parameters within the AV is currently lacking in the literature for a direct comparison, to the knowledge of author.

Table 7.1 Model parameters.

Constants		**Network Parameters**			
k (JK^{-1})	T (K)	Circumferential		Radial	
		n (mm^{-3})	N	n (mm^{-3})	N
1.38×10^{-23}	300	9.58×10^{17}	4.03	6.15×10^{17}	2.43

(a)

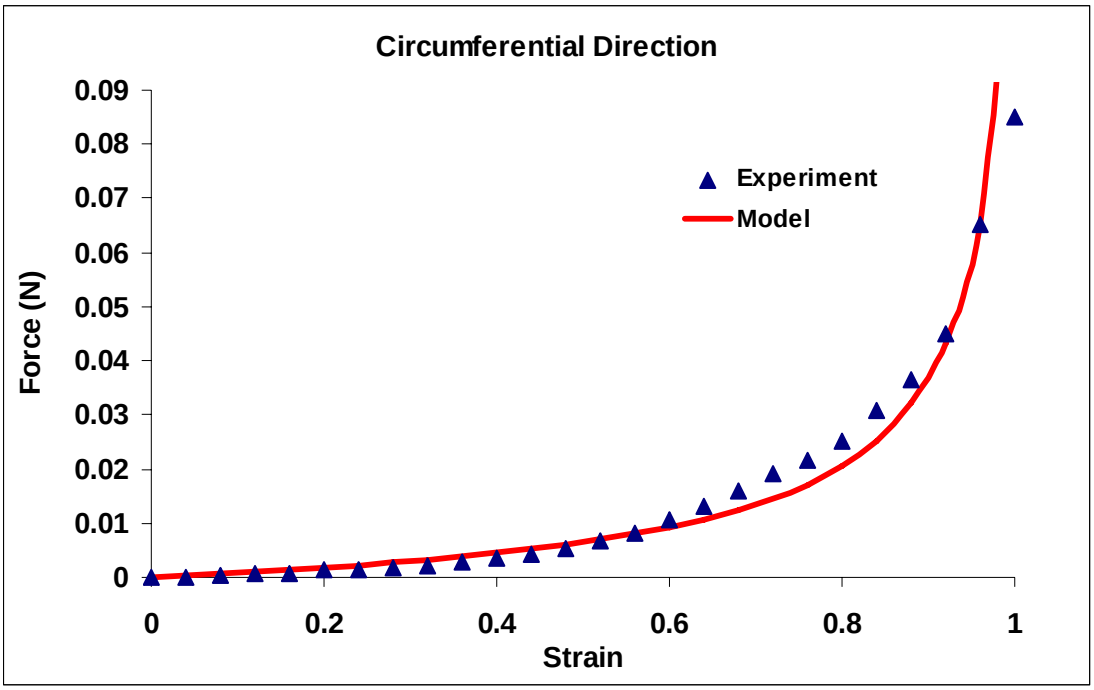

(b)

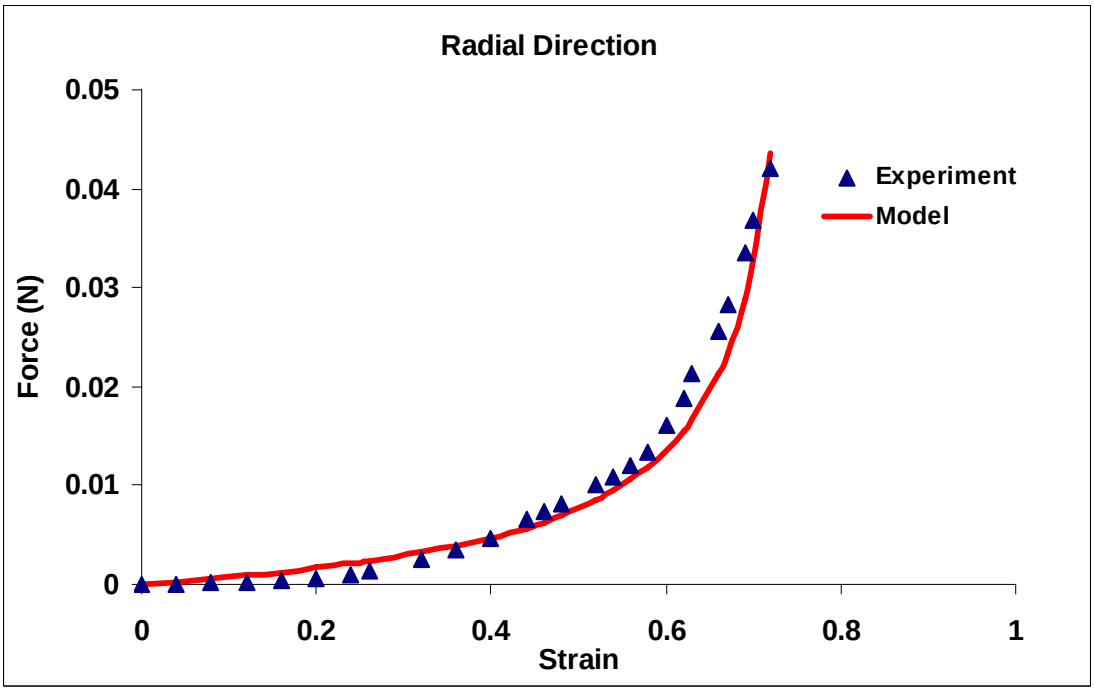

Figure 7.3 Experimental force-strain data for the intact elastin network of the AV in isolation compared with modelling outputs for: (a) the circumferential direction; and (b) the radial direction.

7.4. Discussion

A modelling criterion was introduced and developed in this chapter, to characterise the contribution of the elastin network to AV mechanical behaviour. The model demonstrates how a network of free elastin fibres can show non-linear mechanical behaviour, under tissue-level deformation.

With regards to the choice of probability distribution function introduced in equation (7.6), an alternative to the considered Langevin function is the Gaussian probability, used in the classical statistical theories of single polymer and rubber chains [173]. It should be noted that the first term of the Taylor series expansion of the Langevin model reproduces the Gaussian model (Appendix E). However, as evident from equation (F5, Appendix E), the Gaussian model leads to a linear relationship between the force and elongation for the network, which is not supported by the experimental data. A comparison between the two models is shown graphically in Figure 7.4. It becomes evident from the process of deriving the Gaussian model that it implicitly assumes that the entire network undergoes only small deformations (equation (F7)), contrary to the experimental data. This is also reflected in the graphs shown in Figure 7.4, as the forces in Gaussian model and Langevin model are close only at small strains. Generally, the choice of a Gaussian probability distribution to describe the geometrical characteristics of the fibrous constituents of the AV does not seem likely to result to an accurate description. Indeed, it was demonstrated in chapter 6 that the angular distribution of collagen fibres follows a Lorentzian pattern, rather than a Gaussian (normal).

It must therefore be emphasised that descriptions which limit the contribution of the elastin network to only small strains in the AV mechanical behaviour do not analytically hold true, as this would lead to a Gaussian probability of the configuration of the network of elastin chains and a linear stress-strain relationship. However, the experimental and modelling results both indicate that the overall nonlinearity of AV stress-strain curves may not be entirely a result of the gradual recruitment of the initially wavy collagen fibres, but that the elastin network can further exacerbate the nonlinearity, especially at increasing strains.

(a)

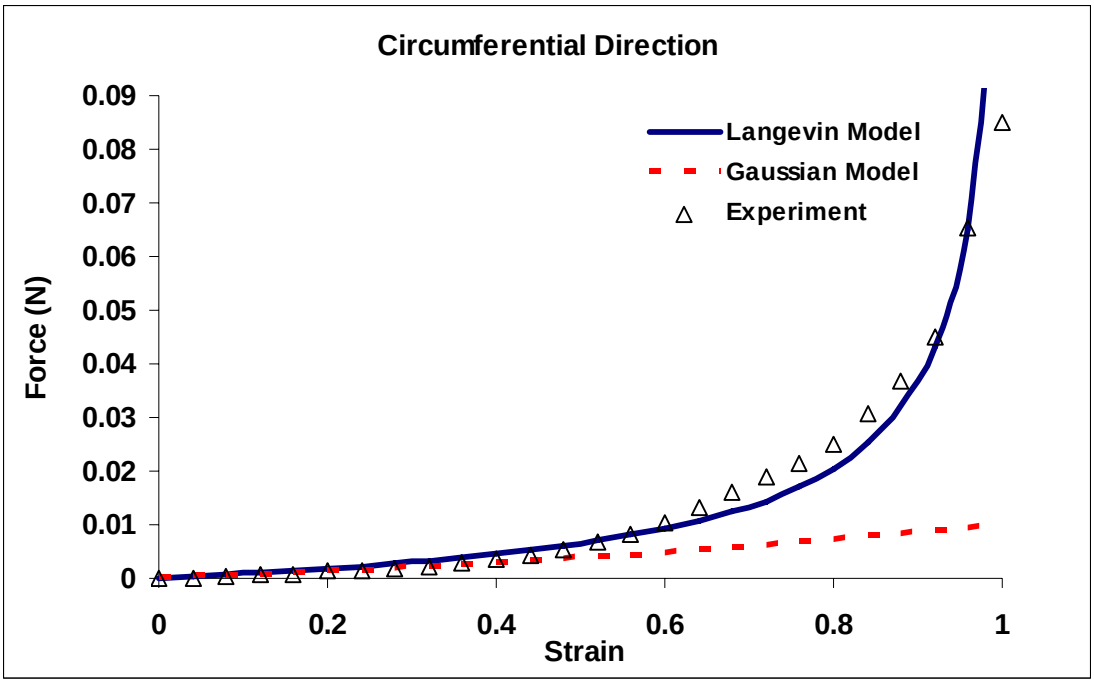

(b)

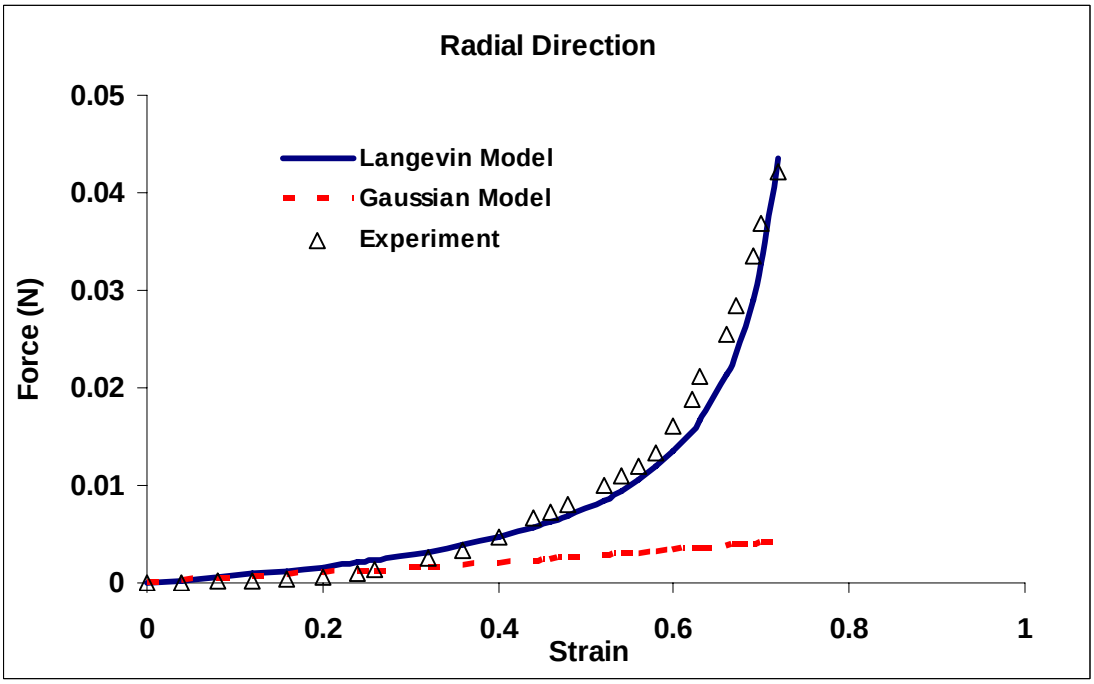

Figure 7.4 Langevin versus Gaussian model in describing the mechanical behaviour of the intact elastin network in isolation: (a) the circumferential direction, (b) the radial direction. The Gaussian model produces forces similar to the Langevin model and the experimental data only at small strains.

The AV is considered a planar tissue when modelling and characterising its mechanical behaviour, a principal also assumed in this chapter, when describing the geometry of the elastic fibres and their network. However, a recent study has shown that the elastic fibres may form an interconnecting component between the layers, spanning through the thickness of the leaflet [171], effectively constructing a 3D network. The modelling criterion introduced in this study can easily be extended for a 3D network, as the relationship between the λ and $\bar{\lambda}$ given in equation (7.13) for the case of 3D network will take the form:

$$\lambda = \sqrt{\frac{\bar{I}_1}{3}} \tag{7.20}$$

as shown in Appendix F. This can be substituted into the equation for the elastic energy of the network (7.14), and the forces in each direction can then be derived accordingly.

Chapter 8

Can the quasi-linear viscoelasticity (QLV) theory explain the time-dependent behaviour of the aortic valve based on its microstructure?

8.1. Synopsis

AV micromechanics under quasi-static loading was analysed in chapters 6 and 7, characterising the contribution of the load-bearing extracellular matrix constituents to the overall tissue mechanics. In the following chapters, the time-dependent behaviour of the AV will be investigated and analysed from a microstructural perspective. Time-dependant matrix reorganisation will be experimentally examined, and its relationship with tissue level behaviour modelled and quantified.

As the first step in this chapter, it is investigated that if the QLV theory, as the well-accepted modelling criteria for characterising the viscoelastic behaviour of collagenous soft tissues, can explain the time-dependant behaviour of the AV based on its microstructure, or if alternative explanations and models are required.

Quasi-linear viscoelasticity (QLV) theory has been widely employed in studies concerning the viscoelastic behaviour of several soft tissues, from tendons and ligaments [148,174] to cardiac muscles [175] and heart valves [5]. It has enabled the mathematical principles applied to linear viscoelasticity to be employed in the analysis of time-dependent behaviour observed in biological tissues [176]. However, studies investigating stress-relaxation of the AV have reported discrepancies in the values of the relaxation parameters quantified through QLV, as a consequence of the relatively poor fit to the experimental data [5,55,72]. The question therefore arises as to whether quasi-linear viscoelasticity is an intrinsic behaviour of the AV tissue, or if QLV is essentially a phenomenological model that is not supported by the underlying micro-structural mechanisms inherent to time-dependent behaviour in the AV. This is of particular interest, as the answer would clarify if the quantified time-dependant parameters by the QLV are physically meaningful, or only a result of a numerical fitting procedure.

8.2. The modelling criteria

The hereditary integral constitutive equation for viscoelastic response of a solid, under the assumption that the response of that solid to a multi-step strain history can

be approximated by a linear combination of responses to single strain histories $R[\varepsilon(t),t]$, has shown to be [176,177]:

$$\sigma(t) = \int_{-\infty}^{t} d_{\varepsilon} R[\varepsilon(s), t-s] \tag{8.1}$$

where $d_{\varepsilon} R[\varepsilon,t]$ denotes a differential with respect to the first argument of $R[\varepsilon,t]$.

With a strain history such that:

$$\varepsilon(s) = 0 \quad \text{for} \quad s \in (-\infty, 0) \tag{8.2}$$

the stress in equation (8.1) can be expressed as [176,177]:

$$\sigma(t) = R[\varepsilon(0),t] + \int_{0}^{t} \frac{\partial R[\varepsilon(s),t-s]}{\partial \varepsilon(s)} \cdot \frac{d\varepsilon(s)}{ds} \cdot ds \tag{8.3}$$

The model proposed by Fung, known as quasi-linear viscoelasticity (QLV), assumes that $R[\varepsilon,t]$ can be expressed by [71]:

$$R[\varepsilon,t] = \sigma^{e}(\varepsilon) \cdot G(t) \tag{8.4}$$

where $G(t)$ is a stress-relaxation function and $\sigma^{e}(\varepsilon)$ is the immediate elastic response [71]. By substituting (8.4) into (8.3):

$$\sigma(t) = \sigma^{e}(\varepsilon(0)) \cdot G(t) + \int_{0}^{t} G(t-s) \frac{d\sigma^{e}(\varepsilon(s))}{d\varepsilon(s)} \cdot \frac{d\varepsilon(s)}{ds} \cdot ds \tag{8.5}$$

or equivalently:

$$\sigma(t) = \sigma^{e}(\varepsilon(0)) \cdot G(t) + \int_{0}^{t} G(t-s) \frac{d\sigma^{e}(\varepsilon)}{d\varepsilon} \cdot \frac{d\varepsilon}{ds} \cdot ds \tag{8.6}$$

8.2.1. Stress-relaxation

The elastic response function $\sigma^{e}(t)$ in collagenous soft tissues has been proposed by Lanir [143,147], as discussed in details in chapters 6. For simplicity of the

formulations, an alternative form of $\sigma^e(t)$ will be used, as introduced by Lanir (1986) [178], in which:

$$\sigma^e(\varepsilon) = \int_0^{\varepsilon} V \cdot K \cdot \frac{\varepsilon - \varepsilon_s}{1+2\varepsilon_s} D(\varepsilon_s) d\varepsilon_s \tag{8.7}$$

where K is the elastic modulus of a single fibre (Chapter 7, equation 7.14) , $D(\varepsilon_s)$ is the distribution function representing the fraction of fibres that are straight at a strain of ε_s, and V is the volume fraction of fibres within the tissue [178]. Using a gamma distribution function for $D(\varepsilon_s)$, equation (8.7) can be rewritten as:

$$\sigma^e(\varepsilon) = K \cdot V \int_0^{\varepsilon} \frac{\varepsilon - \varepsilon_s}{1+2\varepsilon_s} \cdot \frac{1}{\beta^{\alpha}\Gamma(\alpha)} \varepsilon_s^{\alpha-1} \exp(-\frac{\varepsilon_s}{\beta})\ d\varepsilon_s \tag{8.8}$$

Now, substituting (8.8) into (8.6), and assuming that both stress and strain at 0 are equal to zero, i.e. $\varepsilon(0) = 0$ and $\sigma(0) = 0$, and strain rate is constant upon applying the ramp, i.e. $\frac{d\varepsilon}{ds} = C = const$, we will arrive at:

$$\sigma(t) = \int_0^t G(t-s) \frac{d\sigma^e(\varepsilon)}{d\varepsilon} \cdot C \cdot ds \tag{8.9}$$

from equation (8.8):

$$\frac{d\sigma^e}{d\varepsilon} = K \cdot V \int_0^{\varepsilon} \frac{D(\varepsilon_s)d\varepsilon_s}{1+2\varepsilon_s} = K \cdot V \int_0^{\varepsilon} \frac{1}{1+2\varepsilon_s} \frac{1}{\beta^{\alpha}\Gamma(\alpha)} \varepsilon_s^{\alpha-1} \exp(-\frac{\varepsilon_s}{\beta})\ d\varepsilon_s \tag{8.10}$$

thus:

$$\sigma(t) = K \cdot V \cdot C \int_0^t G(t-s) \left(\int_0^{\varepsilon} \frac{1}{1+2\varepsilon_s} \frac{1}{\beta^{\alpha}\Gamma(\alpha)} \varepsilon_s^{\alpha-1} \exp(-\frac{\varepsilon_s}{\beta}) d\varepsilon_s \right) ds \tag{8.11}$$

Under the assumption of linear elasticity of the fibre, one can consider the straightening strain of the fibre, ε_s, is independent of time. The argument in the brackets in equation (8.11) will thus be a constant and comes out of the integral:

$$\frac{\sigma(t)}{K \cdot V \cdot C\int_0^{\varepsilon} \frac{1}{1+2\varepsilon_s} \frac{1}{\beta^{\alpha}\Gamma(\alpha)} \varepsilon_s^{\alpha-1} \exp(-\frac{\varepsilon_s}{\beta}) d\varepsilon_s} = \int_0^t G(t-s)\, ds \tag{8.12}$$

In a stress-relaxation test, the left side of the above equation is the stress history of the specimen during the course of relaxation. Thus, the right-hand side of the above equation can take the form of any function that would follow the same trend. This implies that the relaxation function $G(t)$ is not necessarily a specific type of function, but is essentially selected through fitting to the experimental data that appear on the left-hand side of the equation (8.12). Indeed, it was shown in chapter 4 that the relaxation of the AV typically follows a Maxwell-type exponential decay mode. Thus the above equation should have lead to a specific solution in the form an exponentially decaying function. This indicates that the QLV remains a phenomenological model in describing the stress-relaxation behaviour of the AV.

8.2.2. Creep

Corresponding to the stress-relaxation function $G(t)$ is a creep function $J(t)$. In QLV theory these are related to each other by [176]:

$$1 = J(0)G(t) + \int_0^t G(s)\frac{dJ(t-s)}{d(t-s)} ds = G(0)J(t) + \int_0^t J(s)\frac{dG(t-s)}{d(t-s)} ds \tag{8.13}$$

where $G(0) = J(0) = 1$.

Considering equation (8.13), and that $G(0) = J(0) = 1$, equation (8.6) describing creep behaviour will take the form [176]:

$$\sigma(\varepsilon(t)) = \sigma(0)J(t) + \int_0^t J(t-s)\frac{d\sigma^e}{ds} ds \tag{8.14}$$

Equation (8.14) can be rearranged by the chain rule as:

$$\sigma(\varepsilon(t)) = \sigma(0)J(t) + \int_0^t J(t-s)\frac{d\sigma^e}{d\varepsilon_s}\frac{d\varepsilon_s}{d\varepsilon}\frac{d\varepsilon}{ds} ds \tag{8.15}$$

The term $\frac{d\sigma^e}{d\varepsilon_s}$ is given in equation (8.10), and $\frac{d\varepsilon_s}{d\varepsilon}$ will be a constant, shown hereafter as C_1. Additionally, similar to the relaxation case, strain rate is assumed constant upon applying the creep loading protocol, i.e. $\frac{d\varepsilon}{ds} = C_2 = const$. Equation (8.15) can now be re-written:

$$\sigma(\varepsilon(t)) = \int_0^t J(t-s)\left(K \cdot V \frac{\varepsilon - \varepsilon_s}{1+2\varepsilon_s} \frac{1}{\beta^\alpha \Gamma(\alpha)} \varepsilon_s^{\alpha-1} \exp(-\frac{\varepsilon_s}{\beta}) \right) C_1 C_2 ds \tag{8.16}$$

Substituting for ε in the above equation from equation (D6) in appendix D leads to:

$$\sigma(\varepsilon(t)) = \int_0^t J(t-s)\left(K \cdot V \varepsilon_t \frac{1}{\beta^\alpha \Gamma(\alpha)} \varepsilon_s^{\alpha-1} \exp(-\frac{\varepsilon_s}{\beta}) \right) C_1 C_2 ds \tag{8.17}$$

Under the assumption of linear elasticity of a fibre, one can consider ε_t to be independent of time, and ε_s to be an intrinsic property of the fibres within the tissue. Thus (8.17) can be rearranged as:

$$\sigma(\varepsilon(t)) = A \frac{1}{\beta^\alpha \Gamma(\alpha)} \varepsilon_s^{\alpha-1} \exp(-\frac{\varepsilon_s}{\beta}) \int_0^t J(t-s) ds \tag{8.18}$$

where A is the multiplication of all the constants in (8.17). Substituting for ε_s in equation (8.18) in the light of equation (D6, appendix D):

$$\sigma(\varepsilon(t)) = A \frac{1}{\beta^\alpha \Gamma(\alpha)} \left(\frac{\varepsilon - \varepsilon_t}{2\varepsilon_t + 1} \right)^{\alpha-1} \exp\left(-\frac{\varepsilon - \varepsilon_t}{\beta(2\varepsilon_t + 1)} \right) \int_0^t J(t-s) ds \tag{8.19}$$

and thus:

$$\frac{\sigma(\varepsilon(t))}{A \frac{1}{\beta^\alpha \Gamma(\alpha)} \left(\frac{\varepsilon - \varepsilon_t}{2\varepsilon_t + 1} \right)^{\alpha-1} \exp\left(-\frac{\varepsilon - \varepsilon_t}{\beta(2\varepsilon_t + 1)} \right)} = \int_0^t J(t-s) ds \tag{8.20}$$

Since stress $\sigma(\varepsilon(t))$ remains constant during creep, it becomes clear from equation (8.20) that the creep function $J(t)$ will be of the general form:

$$J(t) := \gamma(t)^{\alpha-1} \exp\left(\frac{\gamma(t)}{\beta}\right) \tag{8.21}$$

where: $\gamma(t) = \dfrac{\varepsilon(t) - \varepsilon_t}{2\varepsilon_t + 1}$.

It was shown in chapter 4 that primary creep strain in the AV follows a Maxwell-type exponential mode. However equation (8.21) clearly indicates that the analytical form of the creep function resulting from QLV contains an additional power-term, $\gamma(t)^{\alpha-1}$. This form of creep function provides a poor fit to the experimental data, and does not follow the linear secondary creep observed in the experiments (Figure 4.6, Chapter 4).

8.3. Concluding remark

The QLV model has been very successful in characterising the time-dependent behaviour of a wide range of soft tissues. However, it does not facilitate structural insights into the observed time-dependent behaviour in the AV tissue, and remains phenomenological when accounted for stress-relaxation phenomenon. When applied to creep, it was shown that QLV will lead to creep modes that are not experimentally observed (power term in equation (8.21)). Thus for an accurate characterisation of the structure-function relationship of the time-dependant behaviour in the AV, alternative modelling criteria should be developed based on the tissue microstructure and the experimentally observed underlying mechanisms. The reorganization of the AV microstructure during stress-relaxation and creep, and how it contributes to the tissue level behaviour, will be experimentally investigated and analytically modelled in the following chapters.

Chapter 9

Micromechanics of stress-relaxation in the aortic valve

9.1. Synopsis

Stress-relaxation is an important mechanical feature of the native AV, as its structural durability is generally thought to be linked with its ability to dampen (relax) the transient stresses created by the sudden change in pressure gradient at systole during each cardiac cycle [76,179]. Indeed, the structural failure of substitute valves may be a consequence of a lack of stress-relaxation compared to the native tissue [76,179]. Additionally, it has been hypothesised that valve calcification may be exacerbated by a reduction in the stress-relaxation ability of the AV. This reduction may result in damage to the AVICs membrane and haemolysis, as the cells will be exposed to excessive loading levels [34]. However, despite these potentially critical roles for stress-relaxation behaviour in the normal function of the AV, the micro-structural mechanisms involved in AV stress-relaxation have received minimal attention, and are poorly understood [69].

The mode of stress-relaxation in valvular tissues has shown to be a Maxwellian exponential type [69,75]. In chapter 4 it was further showed that AV stress-relaxation in the radial direction followed a single Maxwell mode, whereas circumferential relaxation followed a single mode only at low strain levels but switched to two Maxwell modes at higher strains (Chapter 4, Table 4.3). Each mode is an indicator of a structural mechanism contributing to the overall relaxation at the macro level [180,181]. Furthermore, the type of the relaxation mode also reflects the nature of the underlying mechanism causing the relaxation [170-182]. Indeed, many materials have been shown to undergo non-exponential relaxations [182], such as power-law modes [180,181,183], and even a specific logarithmic relaxation mode for lung tissue [180], stemming from different underlying mechanisms causing the relaxation. Of the very few studies examining the structural basis of time-dependent behaviour in valvular tissues, it has been reported that the collagen fibril D-period decreases during stress-relaxation, while it remains approximately constant during creep, when the tissues are subjected to equi-biaxial loading [69,75]. This mechanism, termed as the “fibril-level locking” mechanism, has been hypothesised to allow the stress to relax, by dissipating the deformation energy to reduce the D-period spacing in collagen fibrils, but preventing this change under [69,75]. However, it does not provide a clear

explanation of the exponential stress-relaxation mode, nor the number of relaxation modes, observed at the tissue level.

In this chapter, the structural origins of stress-relaxation in the AV at the micro level are investigated, using confocal microscopy to track the interstitial cell movements during relaxation. The interstitial cells are known to be bonded to the fibres [23,121,184], and thus by tracking the ICs movement, the fibre kinematics (i.e. rotation and movement) can be tracked and characterised. A mathematical description is also derived and developed to show how these structural reorganization mechanisms will lead to the exponential stress-relaxation modes observed at the tissue level.

9.2. Materials and methods

6 porcine hearts were used in this investigation. Tested specimens were prepared according to the protocol described in §2.1, excised circumferentially from AV leaflets. This yielded a total of 18 circumferential samples.

9.2.1. Stress-relaxation tests

Samples were divided in two analysis groups in order to investigate the ventricularis and fibrosa layers individually: 9 samples were viewed from the ventricularis side, and 9 from the fibrosa side, along the central region of the sample length. Imaging was carried out at a depth of 50 to 80 μm into the designated valve layer.

Each sample was incrementally strained from 0% to 20% in 2% increments, at a rate of 60%/min, using the uniaxial rig described in §2.3.3, and held at each strain level for 300 s to be consistent with the experiments for the tissue-level relaxation, described in chapter 4. Stress-relaxation tests for each layer were repeated for nine samples ($n = 9$).

9.2.2. Cell tracking

The technique for imaging and tracking the AVICs within the tissue matrix followed that discussed in §2.3. Images were recorded during the 300s relaxation period at a rate of 1 frame per second, and the movement of cells tracked using particle tracking software (IMARIS®, Bitplane AG) to determine the (x, y) coordinates of the centroid of the nuclei. From these data, the displacement and the velocity of each nucleus during the relaxation period was calculated and used to analyze the structural re-organization occurring during each relaxation increment within the AV.

9.2.3. Statistical analysis

Statistical comparisons between the values associated with fibre kinematics in the ventricularis and fibrosa layers were performed using paired *t*-tests. The statistical significance was set at $p < 0.05$. Values plotted in the figures are presented as the mean and standard deviation.

9.3. Results

The microscopy images documented no detectable movement of the AVICs at strain levels $\varepsilon \leq 4\%$, implying no microstructural re-organisation within the AV during stress-relaxation at those strain levels. However, the movement of the cell nuclei during the relaxation period became evident for strain levels of $\varepsilon \geq 6\%$. Typical microscopic images highlighting the movement of the cell nuclei are shown in Figure 9.1. While the movement of the nuclei was curvilinear at lower strains (Figure 9.1a), straight-line movement in the straining direction became dominant as the strain levels increased (Figure 9.1b). This can also be observed by reconstructing the trajectory of the nuclei, using their (x, y) coordinates at each time-point in each frame during relaxation. Figure 9.2 shows a typical trajectory of a cell nucleus during the 300 s relaxation period, at a range of different strain increments. As can be seen, the movement becomes straighter as the strain increases.

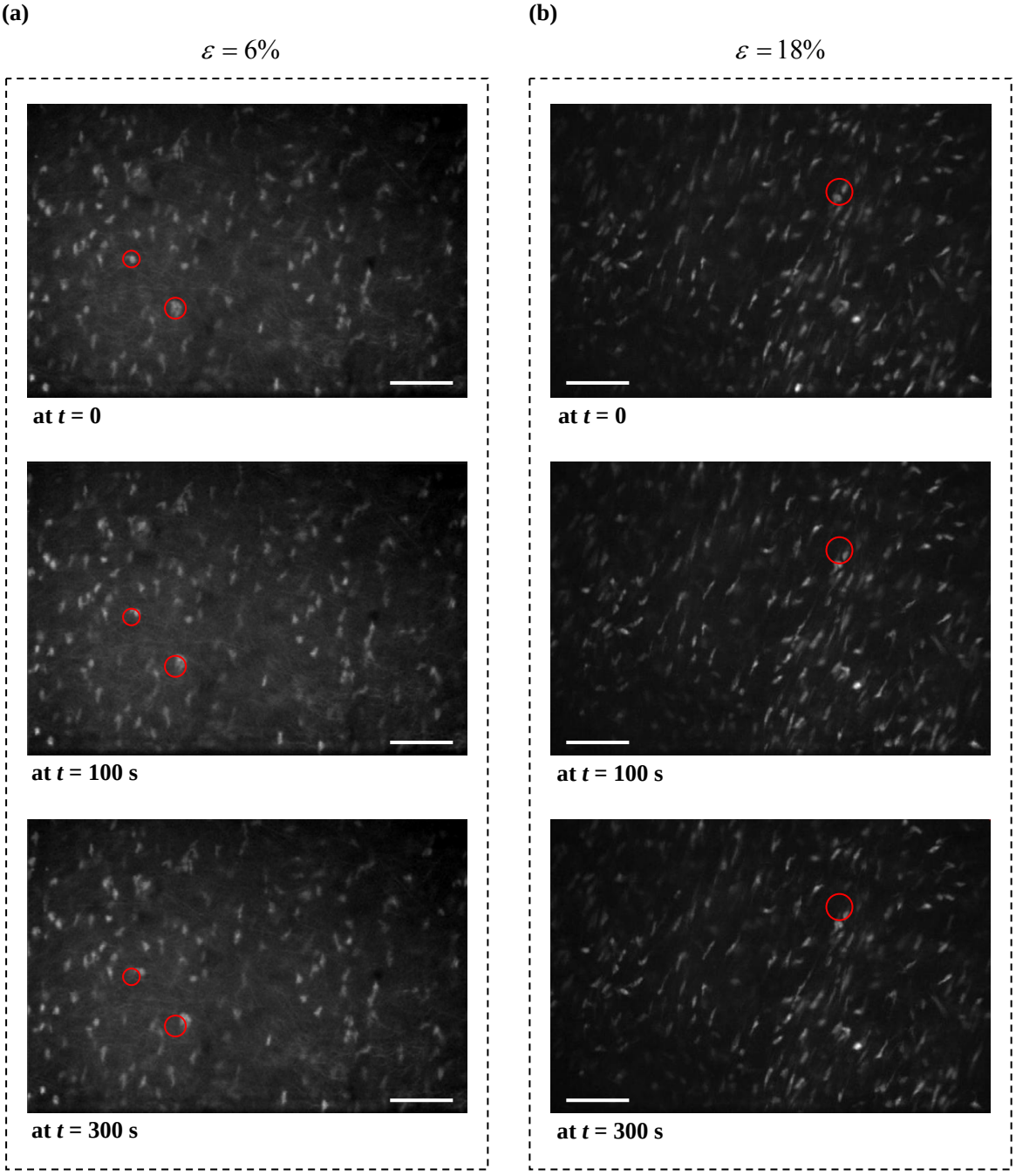

Figure 9.1 Sequence of images documenting the movement of the cell nuclei during relaxation: (a) rotation of the nuclei through a curvilinear motion at low strain levels ($\varepsilon = 6\%$); (b) linear displacement of the nuclei at higher strain levels ($\varepsilon = 18\%$). The time sequence increases in each panel from top to bottom. The circles show the same location of the indicated nuclei at t = 0. The scale bar shows 100 μm.

To calculate the angle of rotation (θ in Figure 9.2), the (x, y) coordinates of the nuclei from the start to the end of the 300 s relaxation period were curve fitted to a quadratic polynomial and the radius of curvature was calculated at both the start and

end point of the curvature, i.e. r_i and r_f in Figure 9.2. The angle θ was then calculated using the values of r_i, r_f and the coordinates of the start and end point of the curvature.

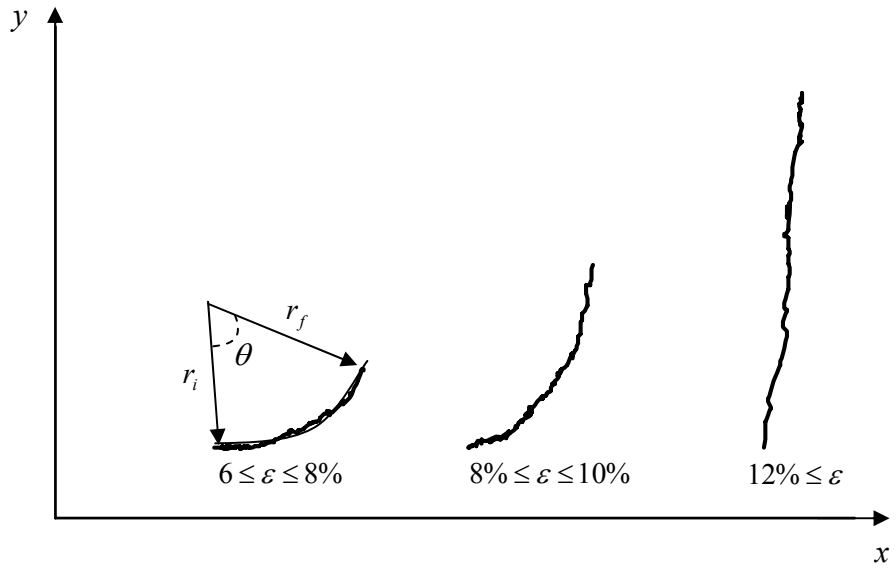

Figure 9.2 A typical trajectory of the movement of the nuclei during stress relaxation at different strain levels. At lower strains, curvilinear movement is prevalent. However, with increasing strain levels, the movement gradually transfers to straight line motion.

The calculated mean values for the angle of rotation for both the ventricularis and fibrosa layers at each strain level are shown in Figure 9.3a. Results show that the rotation decreases as the strain increases in both layers, while the angle of rotation is significantly larger in the ventricularis layer at all strain levels. Additionally, rotation in the ventricularis layer occurred at strain levels up to 16%, while negligible rotation was observed in fibrosa layer at strains above 10% (Figure 9.3a). However, as the strain increased, the curvilinear motion gradually switched to a linear motion (Figure 9.2). The average displacements of the nuclei were calculated using their (x, y) co-ordinations at the start and the end of the 300 s relaxation period. The values are shown in Figure 9.3b. In contrast to anglular rotation, linear displacement is more dominant in the fibrosa layer.

(a)

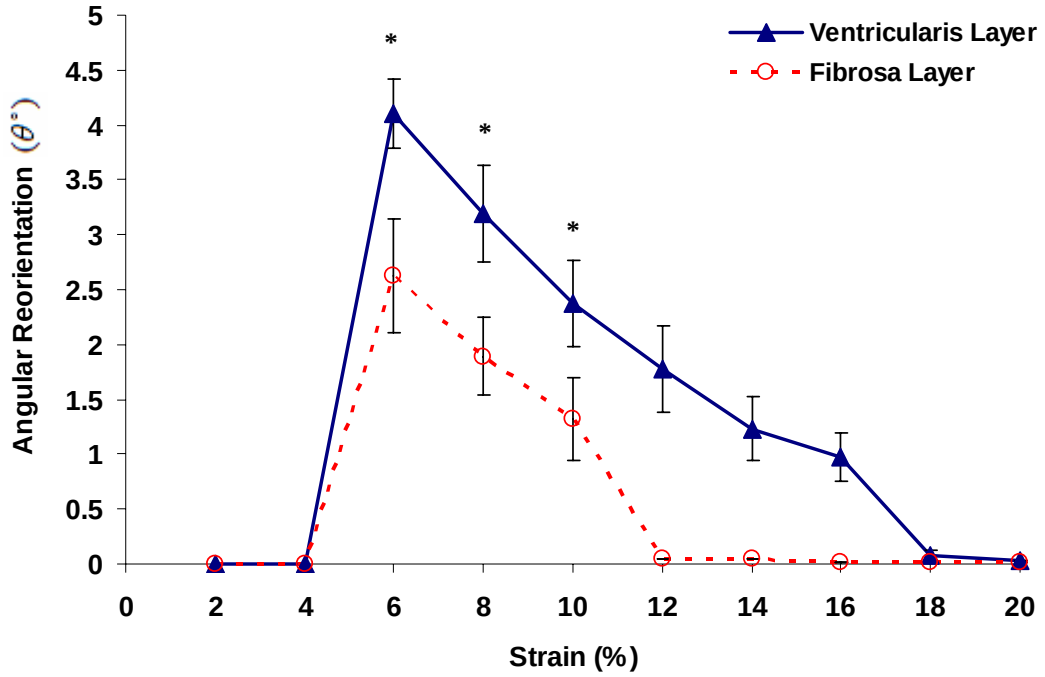

(b)

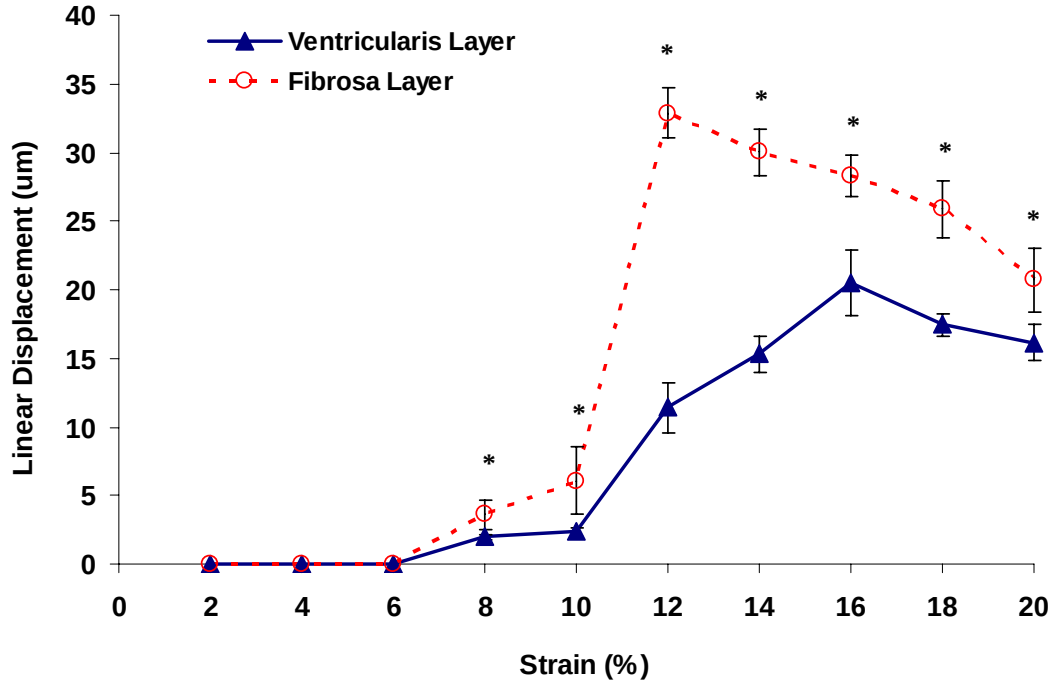

Figure 9.3 The movement of cell nuclei during relaxation: (a) values for angular rotation; (b) values for linear displacement. There is a statistically significant difference between the two layers at all corresponding strain levels, shown by *. The values are presented as Mean ± SD. No detectable movement of the cell nuclei was observed at strain levels $\varepsilon \leq 4\%$.

The velocity of the linear motion of the nuclei was also calculated by the distance they travelled, using their (x, y) coordinates at each frame. The typical trends and values are shown in Figure 9.4a and 9.4b, for the ventricularis and the fibrosa layers respectively. The values show an exponential decrease over the time, at all the strain levels in both layers. Comparing equivalent strain levels, the values are higher in the fibrosa layer. The characteristic decay times for the velocity, calculated using a single exponential decay function, are summarized in Table 9.1 for each strain level for the both layers. For comparison, the slow relaxation times at the tissue level established in chapter 4, are provided for comparable strain levels.

Table 9.1 Characteristic decay times for the linear motion of the cell nuclei in both the ventricularis and fibrosa layers of the AV, and the corresponding relaxation times at the tissue level.

ε (%)	Tissue level slow relaxation time (s) (from chapter 4)	Characteristic decay time (s)	
		Ventricularis	Fibrosa
12	---	---	87.33 ± 5.08
14	---	---	56.16 ± 8.73
16	88.48 ± 6.21	---	58.40 ± 10.26
18	108.173 ± 8.75	41.52 ± 11.62	51.72 ± 10.44
20	152.02 ± 14.70	64.13 ± 6.38	60.29 ± 9.15

(a)

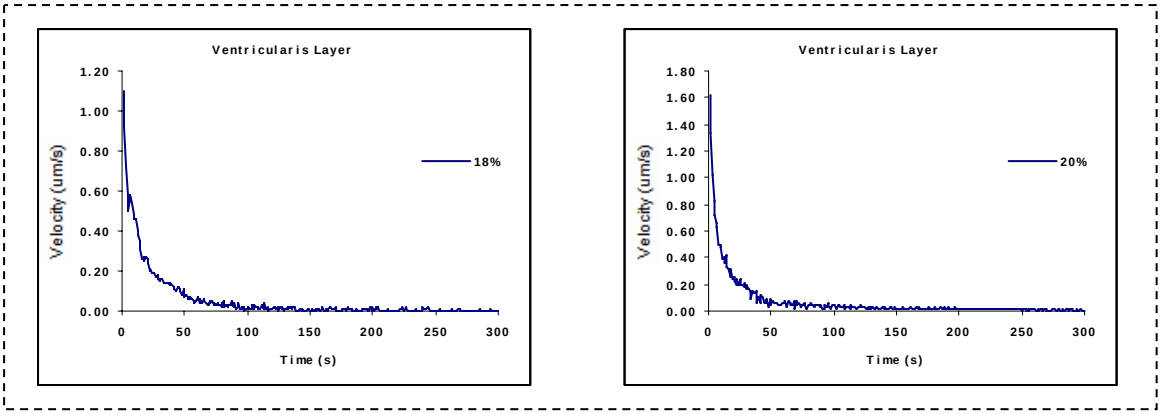

(b)

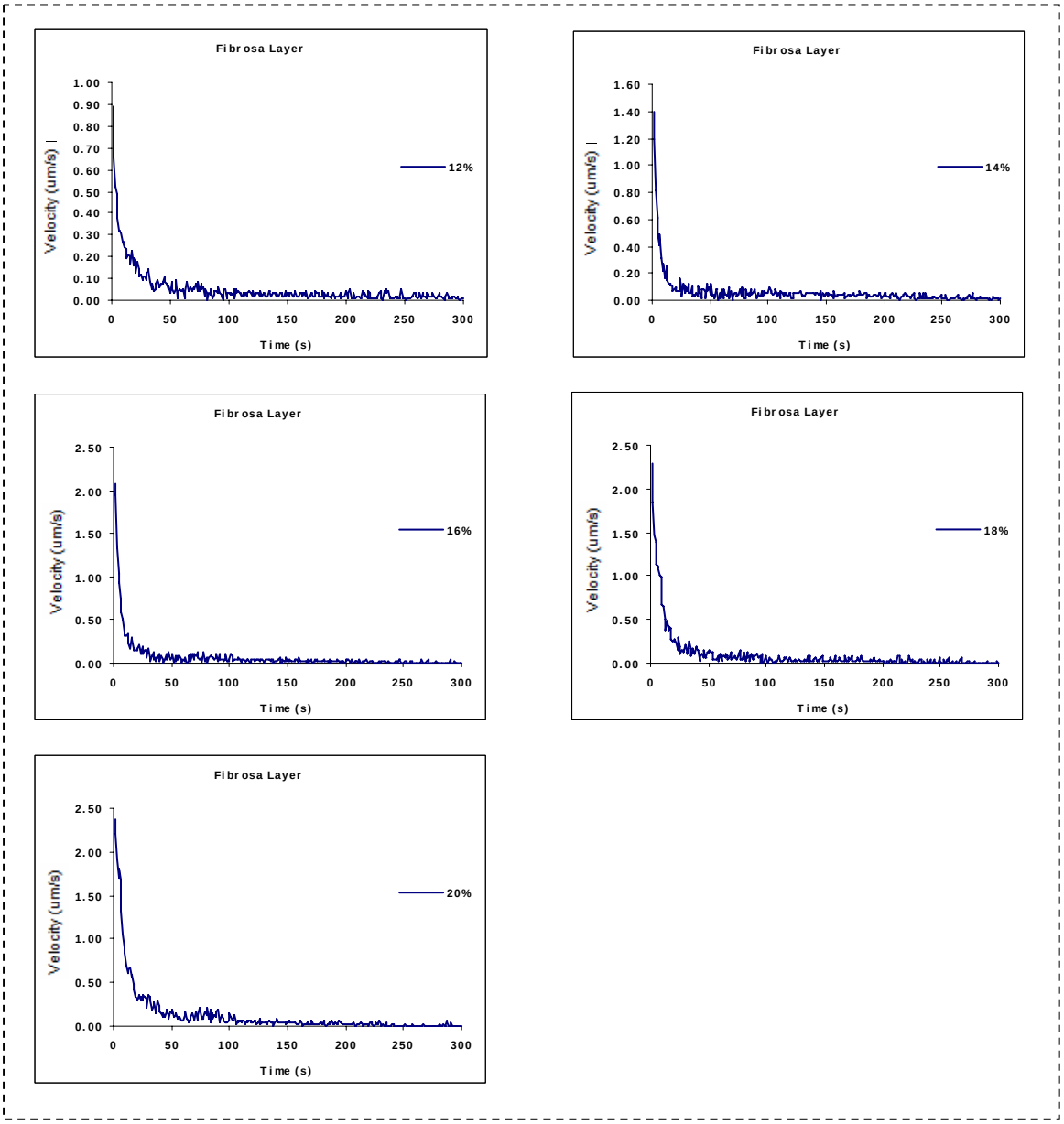

Figure 9.4 Average velocity of the linear movement of the cell nuclei during relaxation in: (a) ventricularis layer; and (b) fibrosa layer, at a range of different applied strain levels.

9.4. Discussion

Histological observations and biochemical analysis have indicated that cells are bonded to the fibres within the AV ECM [23,121,184]. Movement of the AVIC nuclei was therefore adopted as an indicator of fibre reorganization in this st Assuming that the movement of the cells reflect a similar kinematics to that of the fibres, data indicate that during stress-relaxation fibres undergo reorientation at low strain levels, while at higher strains they displace linearly. In the following, it will be shown how such fibre kinematics during relaxation would lead to an exponential decay of stress at the tissue level.

For simplicity of the kinematics, analysis starts with the linear motion mode occurring at higher strains, where a larger fraction of the fibres are straight. It is well established that, due to the fibre movement, there are frictional contacts between the fibres and the surrounding ECM elements [113]. A theoretical criterion is formulated in the following to describe the relaxation of stress, due to sliding of adjacent fibres against each other, and the surrounding ECM, upon their linear movement. This criterion is based on the principles primarily introduced in [113], adjusted and modified to be applicable for planar collagenous tissues such as the AV.

Consider two straight adjacent collagen fibres in a tissue sample, as shown in Figure 10.5, that interact with each other along their length through a contact force that has two components: (i) a normal component to the surface of each fibre denoted here as N; and (ii) a tangential component to the surface of each fibre denoted here as T. Physically, N may represent the transverse mechanical loads (e.g. Poisson ratio effects), as well as any other microenvironment originated loading, and T can be interpreted as the frictional force between the two fibres.

When the fibres displace linearly and sliding between the two fibres occur, the tangential component T at any given point of x will depend on time (t), the relative velocity between the fibres at that point $V_{rel}(x,t)$, and the normal component acting on that point $N(x)$ [113]. Assuming that the two fibres are in some parts in direct sliding contact, whereas in other parts they are separated by a very thin layer of other

ECM components, such as GAGs, the tangential traction T over the length of dx at time t and point x will be:

$$T(x,t) = \pm \mu N(x) + C_d V_{rel}(x,t) \tag{9.1}$$

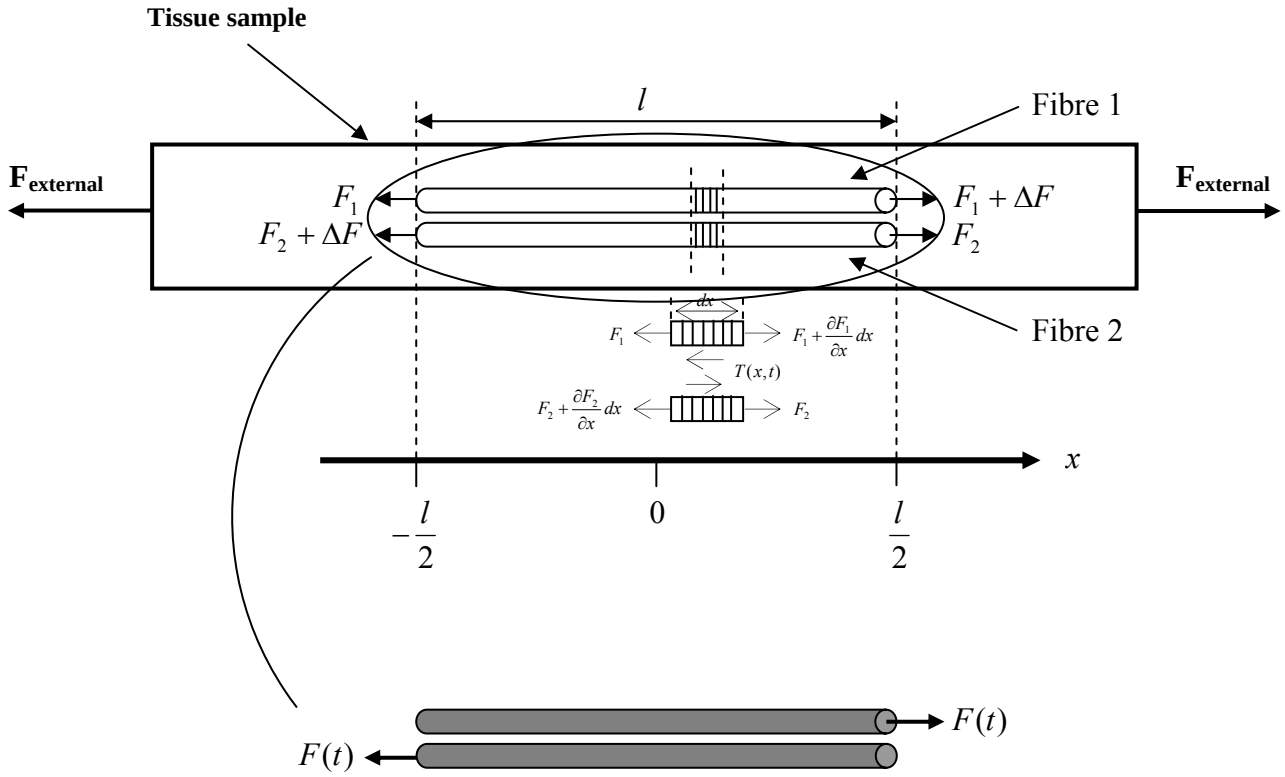

Figure 9.5 Schematic of two adjacent fibres moving and sliding relative to each other during stress-relaxation.

Note that the first term in equation (9.1), $\mu N(x)$, is the classic Coulomb friction law, and the second term, $C_d V_{rel}(x,t)$ is the Newtonian viscous force. Data in chapter 3 highlighted that that the viscous damping coefficient in AV tissue appears to be rate dependant, and thus the viscous effects are non-Newtonian. However, in the current model, a Newtonian case is considered for simplicity.

Consider that the application of uniaxial strain to the tissue corresponds to an external load $\boldsymbol{F_{external}}$ acting on the tissue sample (Figure 9.5), which is held constant

to allow for stress-relaxation to occur. In such a configuration, consider the applied force at the fibres ends to be $F(t)$ (Figure 9.5). Let's assume that $F(t)$ loads the opposite end of the two adjacent fibres (Figure 9.5). This assumption assures that mechanically, only sliding between the two fibres would occur, without any slippage. The force in fibre 1 changes from F_1 to $F_1 + \Delta F$, and from F_2 to $F_2 + \Delta F$ in fibre 2, over the total interface length, *l*, between the two fibres (Figure 9.5). ΔF is the total differential force exerted by one fibre on the other, due to the above described interactions between the two fibres. Thus, at equilibrium, ΔF should be in balance with the total tangential traction *T* over the whole length *l* at any time:

$$\Delta F = \int_0^l T(x,t)dx \tag{9.2}$$

By the above definition, ΔF is transferred entirely from fibre 1 to fibre 2, or vice versa, along the interface length *l*, due to the tangential traction *T*. Since ΔF is the only force acting upon the two fibres at equilibrium at any time point, it should be equal to the $F(t)$:

$$F(t) = \Delta F = \int_0^l T(x,t)dx \tag{9.3}$$

As evident in Figure 9.5, the local equilibrium is obtained when:

$$\frac{\partial F}{\partial x} = T(x,t) \tag{9.4}$$

From the theory of linear elasticity:

$$\frac{F}{A} = E\frac{\partial u}{\partial x} \tag{9.5}$$

where *u* is the displacement, $\frac{\partial u}{\partial x}$ is the Cauchy strain [138], *E* is the elastic modulus, and *A* is the cross-sectional area. Combining equations (9.4) and (9.5), and assuming that linear elasticity theory applies for the stress-strain relationship of a collagen fibre [156] gives:

$$AE\frac{\partial^2 u(x,t)}{\partial x^2} = T(x,t) \tag{9.6}$$

where $u(x,t)$ is the fibre displacement at position x and time t.

Writing equation (9.6) for fibres 1 and 2:

$$\begin{cases} A_1 E_1 \dfrac{\partial^2 u_1(x,t)}{\partial x^2} = T(x,t) \\ A_2 E_2 \dfrac{\partial^2 u_2(x,t)}{\partial x^2} = -T(x,t) \end{cases} \tag{9.7}$$

where A_1 and A_2 are the cross-sectional areas, E_1 and E_2 are the elastic moduli, and u_1 and u_2 are the fibre displacements for fibre 1 and fibre 2 respectively. Equation (9.7) describes the displacement fields for the two interfacing fibres. Summing the two field equations in (9.7) gives a second order partial differential equation:

$$\frac{\partial^2 (u_1 + u_2)}{\partial x^2} = 0 \tag{9.8}$$

Multiplying both sides of the equation (9.8) by *AE*, the first integration of the equation gives the equilibrium equation of the form in (9.4), where $AEC_1(t)$ is equal to the force *F(t)*. $C_1(t)$ is an arbitrary function resulting from first integration. Thus the general solution of the field equations becomes:

$$u_1(x,t) + u_2(x,t) = \frac{F(t)}{AE} x + C_2(t) \tag{9.9}$$

During stress-relaxation, the universal displacement of the continuum is kept constant, thus one may assume that the transverse mechanical loading effects are no longer present, and the normal component *N* may approach zero. Hence equation (9.1) can be approximated as:

$$T(x,t) = C_d \frac{\partial}{\partial t}(u_1 - u_2) \tag{9.10}$$

where $u_1 - u_2$ is the relative displacement of the two fibres, and $\dfrac{\partial}{\partial t}(u_1 - u_2)$ is equal to V_{rel}.

Combining the equations (9.10), (9.9) and (9.7) will result in the following differential equation:

$$AE\frac{\partial^2 u_1}{\partial x^2} = \frac{F(t)}{2AE}x - u_1(x,t) + 2C_d \tag{9.11}$$

where the boundary conditions would be:

$$\begin{cases} u_1(\frac{l}{2},t) = \frac{1}{2}U(t) \\ \frac{\partial}{\partial x}u_1(x,0) = \frac{F(0)}{2AE} \end{cases} \tag{9.12}$$

where $U(t)$ is the elongation at time *t*.

The partial differential equation in (9.11) with the above boundary conditions in (9.12) is of the same form as that which appears in diffusion problems, specific to the non-steady state diffusion in plane sheets [185]. Using this analogy, the solution for the displacement will be [185]:

$$u_1(x,t) = \frac{F(t)}{2AE}x + \frac{1}{2}U_0\left(1 - \sum_{n=1}^{\infty}\frac{2\cos(\gamma_n\frac{2x}{l})\sec\gamma_n}{2+\gamma_n^2}\exp\left(-(\frac{2\gamma_n^2 AE}{l^3 C_d})t\right)\right) \tag{9.13}$$

where γ_n are positive roots of $\gamma_n \tan\gamma_n = 1$, and U_0 is the initial elongation of the fibres.

Substituting equation (9.13) into (9.5), for the loaded end at $x = \frac{l}{2}$, gives the relaxation force as:

$$F(t) = \frac{2AEU_0}{l}\sum_{n=1}^{\infty}\frac{2}{2+\gamma_n^2}\exp\left(-(\frac{2\gamma_n^2 AE}{l^3 C_d})t\right) \tag{9.14}$$

Equation (9.14) explicitly shows how the force, and hence the stress, decays exponentially with time when a collagenous tissue such as the AV is strained and the strain is kept constant over time, i.e. stress-relaxation loading conditions.

Linear movement of the fibres is the dominant reorganization mode of the fibrous network architecture in the AV sample at strain levels $\varepsilon \geq 12\%$ in fibrosa layer and

$\varepsilon \geq 18\%$ in ventricularis layer (Figures 9.1b & 9.3b). This linear movement would inevitably provide sliding between the fibres and the surrounding matrix that would lead to an exponential decay in stress, described mathematically in equations (9.1) through (9.14).

For the case of lower strains, i.e. $6\% \leq \varepsilon \leq 10\%$ in fibrosa layer and $6\% \leq \varepsilon \leq 16\%$ in ventricularis layer, experimental data implies that rotational movement of fibres dominates during relaxation (Figures 9.1a & 9.3a). The following derivation demonstrates how this mode of fibre reorganization would also lead to the observed exponential stress-relaxation trends at the tissue level, at the corresponding strains, established in chapter 4.

Consider two adjacent fibres which are wavy at lower applied strains, with an initial angle between their axes (Figure 9.6a). During relaxation, each fibre rotates by an arbitrary amount to give a final configuration, such as that shown in Figure 9.6b. For simplicity in the geometry, let us assume that the axis of one the fibres is parallel to the x axis, e.g. fibre 1 in Figure 9.6b.

For small rotational angles of less than 6°, the rotational movement may be linearized to a 2D movement in the x and y directions. From the theory of 2D elasticity [186]:

$$\frac{F}{A} = \frac{E}{1-\upsilon^2}\left[\frac{\partial u}{\partial x} + \upsilon\frac{\partial u}{\partial y}\right] \tag{9.15}$$

where υ is the Poisson's ratio.

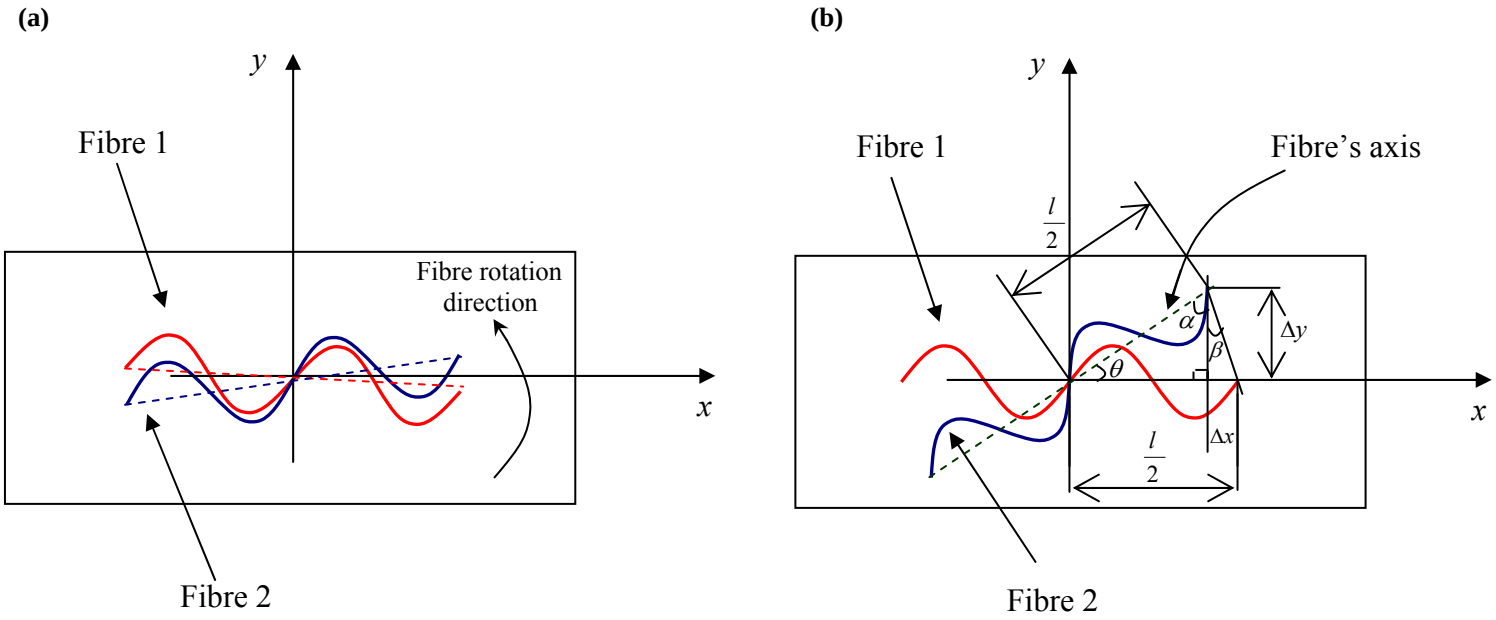

Figure 9.6 Configuration of two adjacent wavy fibres: (a) before rotation, (b) after rotation during stress-relaxation.

From the geometry of the configuration of the fibres after relaxation in Figure 9.6:

$$2(\alpha+\beta)+\theta=180 \tag{9.16}$$

and:

$$\theta+\alpha=90 \;\rightarrow\; \alpha=90-\theta \tag{9.17}$$

Substituting for α from (9.17) to (9.16):

$$\beta=\frac{\theta}{2} \tag{9.18}$$

From Figure 9.6b:

$$\tan\beta=\frac{\Delta x}{\Delta y} \tag{9.19}$$

and by substituting (9.18) into (9.19):

$$\tan\frac{\theta}{2}=\frac{\Delta x}{\Delta y} \tag{9.20}$$

For small rotational angles, equation (9.20) can be re-written as:

$$\tan\frac{\theta}{2}=\frac{\theta}{2}=\frac{dx}{dy} \tag{9.21}$$

Substituting for dy from equation (9.21) into (9.15):

$$F=\frac{AE}{1-\upsilon^2}\left(1+\frac{\upsilon\theta}{2}\right)\frac{\partial u}{\partial x} \tag{9.22}$$

Taking the differential with respect to x from both sides the above equation:

$$\frac{\partial F}{\partial x}=\frac{AE}{1-\upsilon^2}\left(1+\frac{\upsilon\theta}{2}\right)\frac{\partial^2 u}{\partial x^2} \tag{9.23}$$

The rest of the analysis follows similar steps similar to those described for fibre sliding (equation (9.5) to (9.13)), which finally results in the following displacement field equation:

$$u(x,t)=\frac{F(t)\left[1-\upsilon^2\right]}{2AE\left(1+\frac{\upsilon\theta}{2}\right)}x+\frac{1}{2}U_0\left(1-\sum_{n=1}^{\infty}\frac{2\cos(\gamma_n\frac{2x}{l})\sec\gamma_n}{2+\gamma_n^2}\exp\left(-(\frac{2\gamma_n^2AE(2+\upsilon\theta)}{l^3(1-\upsilon^2)C_d})t\right)\right) \tag{9.24}$$

with the boundary conditions:

$$\begin{cases}\dfrac{\partial}{\partial x}u(\dfrac{l}{2},t)=\dfrac{F(t)[1-\upsilon^2]}{AE(1+\dfrac{\nu\theta}{2})}=\dfrac{1}{2}U(t)\\[2ex]\dfrac{\partial}{\partial x}u(0,t)=\dfrac{F(t)[1-\upsilon^2]}{2AE(1+\dfrac{\upsilon\theta}{2})}\end{cases} \tag{9.25}$$

Substituting equation (9.24) into (9.22) gives the force during relaxation as:

$$F(t)=\frac{2AE(1+\frac{\upsilon\theta}{2})U_0}{l(1-\upsilon^2)}\sum_{n=1}^{\infty}\frac{2}{2+\gamma_n^2}\exp\left(-(\frac{2\gamma_n^2AE(2+\upsilon\theta)}{l^3(1-\upsilon^2)C_d})t\right) \tag{9.26}$$

The parameters have the same definition as detailed in equation (9.14).

Equation (9.26) expresses that if the rotational movement of the two adjacent fibres during stress-relaxation is approximated by a 2D linear movement (i.e. the rotational angle is smaller than 6°), the sliding between that two fibres during this movement would again lead to an exponential decay of the stress. Thus, the sliding between the fibres, as a result of the structural reorganization of the fibres during relaxation, i.e. rotation at lower strains and linear movement at higher strains, will result in the exponential decay of stress observed at the tissue level during the stress-relaxation, as characterised by equations (9.14) and (9.26).

The γ_n in equations (9.14) and (9.26) are the positive roots of $\gamma_n \tan\gamma_n = 1$, thus: $\gamma_1 = 0.86$, $\gamma_2 = 3.42$, $\gamma_3 = 6.43$, ... [185]. Hence, the numerical values of the argument inside the operator Σ would be negligible for $n \geq 2$, since the values would be 10^{-6}, 10^{-20}, 10^{-42} … times smaller in $n = 2$, 3, 4 … respectively, compared to that for $n = 1$. Thus the relaxation due to the both rotation and linear movement of the fibres at lower and higher strains can be approximated as:

$$\begin{cases} F(t) = \dfrac{2AE(1+\dfrac{\upsilon\theta}{2})U_0}{l(1-\upsilon^2)} \cdot \dfrac{2}{2+\gamma_1^2} \exp\left(-(\dfrac{2\gamma_1^2 AE(2+\upsilon\theta)}{l^3(1-\upsilon^2)C_d})t\right) & (9.27a) \\ \text{and} \\ F(t) = \dfrac{2AEU_0}{l} \cdot \dfrac{2}{2+\gamma_1^2} \exp\left(-(\dfrac{2\gamma_1^2 AE}{l^3 C_d})t\right) & (9.27b) \end{cases}$$

or in terms of stress:

$$\begin{cases} \sigma(t) = \dfrac{2E(1+\dfrac{\upsilon\theta}{2})U_0}{l(1-\upsilon^2)} \cdot \dfrac{2}{2+\gamma_1^2} \exp\left(-(\dfrac{2\gamma_1^2 AE(2+\upsilon\theta)}{l^3(1-\upsilon^2)C_d})t\right) & (9.28a) \\ \text{and} \\ \sigma(t) = \dfrac{2EU_0}{l} \cdot \dfrac{2}{2+\gamma_1^2} \exp\left(-(\dfrac{2\gamma_1^2 AE}{l^3 C_d})t\right) & (9.28b) \end{cases}$$

where $\sigma(t)$ is the stress at time t.

For strain levels $\varepsilon < 6\%$, no detectable movement of the ICs was observed, suggesting that no structural reorganization of fibrous architecture is occurring in those strain levels. Similarly, in separate experiments performed on 12 radially cut samples, 6 viewed from the fibrosa and 6 viewed from the ventricularis layer, no movement of the cell nuclei was detected at any strain level. Chapter 4 demonstrated that the relaxation mode in AV samples in circumferential direction at low strain levels, and in the radial direction at all strain levels, is single, with a fast decay of stress in a short relaxation time. Additionally, chapter 3 highlighted that the GAG constituent of the AV, mainly present in the spongiosa layer, can be modelled as a viscous fluid, with viscous damping effects in the tensile deformation of the AV. Separate experimental studies on concentrated proteoglycan solutions have also confirmed such viscous fluid like characteristics [102]. Hence, it seems reasonable to suggest that the fast relaxation in radial direction, and at strain levels below 6% in the circumferential direction, originates from the viscous behaviour of the fluid-like GAG constituent of the AV ECM, which leads to a single exponential relaxation mode.

The secondary relaxation mode observed in the circumferential direction at higher strains appears to be the result of reorganization of the fibre architecture within AV; either rotation or linear movement. The modelling has demonstrated that this will lead to an exponential decay of stress in the form presented in equations (9.14) and (9.26), or equivalently equations (9.28a) and (9.28b). Furthermore, it is evident that the characteristic slow-relaxation times observed at the tissue level are close to the sum of the characteristic decay times of the linear motion of the fibres in the ventricularis and fibrosa layers, given in Table 9.1. Such a response further reinforces the argument that fibre kinematics is closely associated with the tissue relaxation process.

These findings are in a strong analogy with polymeric gels, which also show two exponential relaxation modes [180,181]. By exertion of external forces, a velocity gradient is induced in the polymeric gel, which continuously alters the equilibrium distribution of the configurations of polymer molecules. These long molecules are in a coordinated thermal or Brownian motion, the driving force of which is the thermal energy. Because they are moving in a viscous fluid, this leads to dissipation of the deformation energy. This relaxation mechanism is known as the ‘Rouse’ mechanism in polymers [181]. Another ongoing process consists of the gradual disengagement of

one long flexible molecule chain from its environment by performing "worm-like" displacements inside the polymeric gel. The interactions between the chain and the neighbouring molecules results in the dissipation of energy. This relaxation mechanism is known as 'reptation' [181]. For short time scales the conformational changes of the chains are Rouse-like, whereas at longer times the important behaviour is that of reptation, leading to the two relaxations modes, i.e. fast and slow [180,181]. The 'Rouse' mechanism resembles the damping effects of a viscous fluid like GAG in the AV at lower strains, and the 'reptation' mechanism is similar to the dissipative effects of the sliding of the fibres against each other, due to either their rotational or linear movement.

Due to the nature of the imaging technique employed in this study, the correlation between individual cells and fibres within the field of view could not have been explicitly elucidated. Therefore, the values associated with the rotation and the linear movement of the fibres at different strain levels (presented in Figures 9.2, 9.3 and 9.4) were calculated based on the assumption that the movement of each cell represented the mode of the movement of a fibre. However, it may well be the case that a group of cells *in situ* might be attached to a same fibre, or a cell might be attached to more than a single fibre. Subsequently, the recorded movement of some of the cells may represent the kinematics of a single fibre, while some others may indicate the resultant kinematics of a group of fibres attached to a same cell. However, the reported values in this chapter have been calculated by averaging over the entire group of cells within the field of view, which will reduce the overall influence of such effects. Furthermore, the nature of the mechanism and the theoretical criterion developed in this chapter will not be altered, as the movement of the cells is an indicator of the movement of the fibres which will inflict fibre-fibre and fibre-matrix sliding effects, irrespective of how many cells are attached to the same or different fibres.

The nature of the mechanisms leading to the exponential decay of stress in equations (9.14) and (9.27) is independent of the loading mode, i.e. uniaxial or biaxial. Sliding between the fibres under rotation or linear movement is independent of the loading conditions, and will lead to an exponential decay regardless of the loading mode applied to the tissue, as the same mathematics would apply. Indeed, even though uniaxial loading was used in the current study, the analysis was extended

to 2D elasticity in equations (9.15) to (9.26). Additionally, the viscous behaviour of the GAG constituent in the AV extracellular matrix would occur under the both uniaxial and biaxial loading modes, and hence would not be changed by the loading boundary conditions. However, the amount of rotation or the linear movement of the fibres, and the strain levels at which each of the two would occur, would probably be different under biaxial loading, to the values observed in this study.

Chapter 10

Micromechanics of creep in the aortic valve

10.1. Synopsis

Another aspect of time-dependant behaviour is manifested in the creep phenomenon, which describes the elongation of a specimen upon the application of constant load. It is a common assumption that the structural mechanism(s) responsible for the stress-relaxation and creep phenomena in collagnenous soft tissues are uncoupled [69,70,75]. This chapter investigates structural reorganization within the AV ECM during creep, following a similar approach to that employed in chapter 9.

10.2. Materials and methods

6 porcine hearts were used in this investigation. Specimens were prepared according to the protocol described in §2.1, excised circumferentially from AV leaflets. This yielded a total of 18 circumferential samples.

10.2.1. Creep tests

Samples were divided in two analysis groups in order to investigate the ventricularis and fibrosa layers individually: 9 samples were viewed from ventricularis side, and 9 samples from fibrosa side, along the central region of the sample length. Imaging was carried out at a depth of 50 to 80 μm into the designated valve layer.

Samples were loaded from zero to seven predefined loads (f), between $f = 0.5$ N and $f = 3.5$ N in 0.5 N increments using the uniaxial rig described in §2.3.3. A loading rate of 6%/min was used, and samples were kept at each loading level for 300 s, to be consistent with the experiments for tissue-level creep discussed in chapter 4. The loading set-up followed that described in §2.3.3. Each sample was loaded through all the increments, and the incremental creep tests for each layer repeated for nine samples.

10.2.2. Cell tracking

The technique for imaging and tracking the AVICs within the tissue matrix followed that discussed in §2.3. Images were recorded during the 300s creep period at a rate of 1 frame per second, and the movement of cells tracked using particle tracking software (IMARIS®, Bitplane AG) to determine the (x, y) coordinates of centroid of the nuclei. From these data, the displacement and the velocity of each nucleus during the creep period was calculated and used to analyze the structural re-organization within the AV.

10.2.3. Statistical analysis

Statistical comparisons between the values associated with fibre kinematics in the ventricularis and fibrosa layers were performed using paired *t*-tests. The statistical significance was set at $p < 0.05$. Values plotted in the figures are presented as the mean and standard deviation.

10.3. Results

Microscopy images documented movement of the cell nuclei, implying microstructural re-organization, during the creep period for all circumferential loading levels. Typical microscopy images, showing the movement of cell nuclei over time are shown in Figure 10.1. Similar to the observations for stress-relaxation, the movement of the cell nuclei during creep also followed curvilinear (Figure 10.1a) and straight-line (Figure 10.1b) movement patterns.

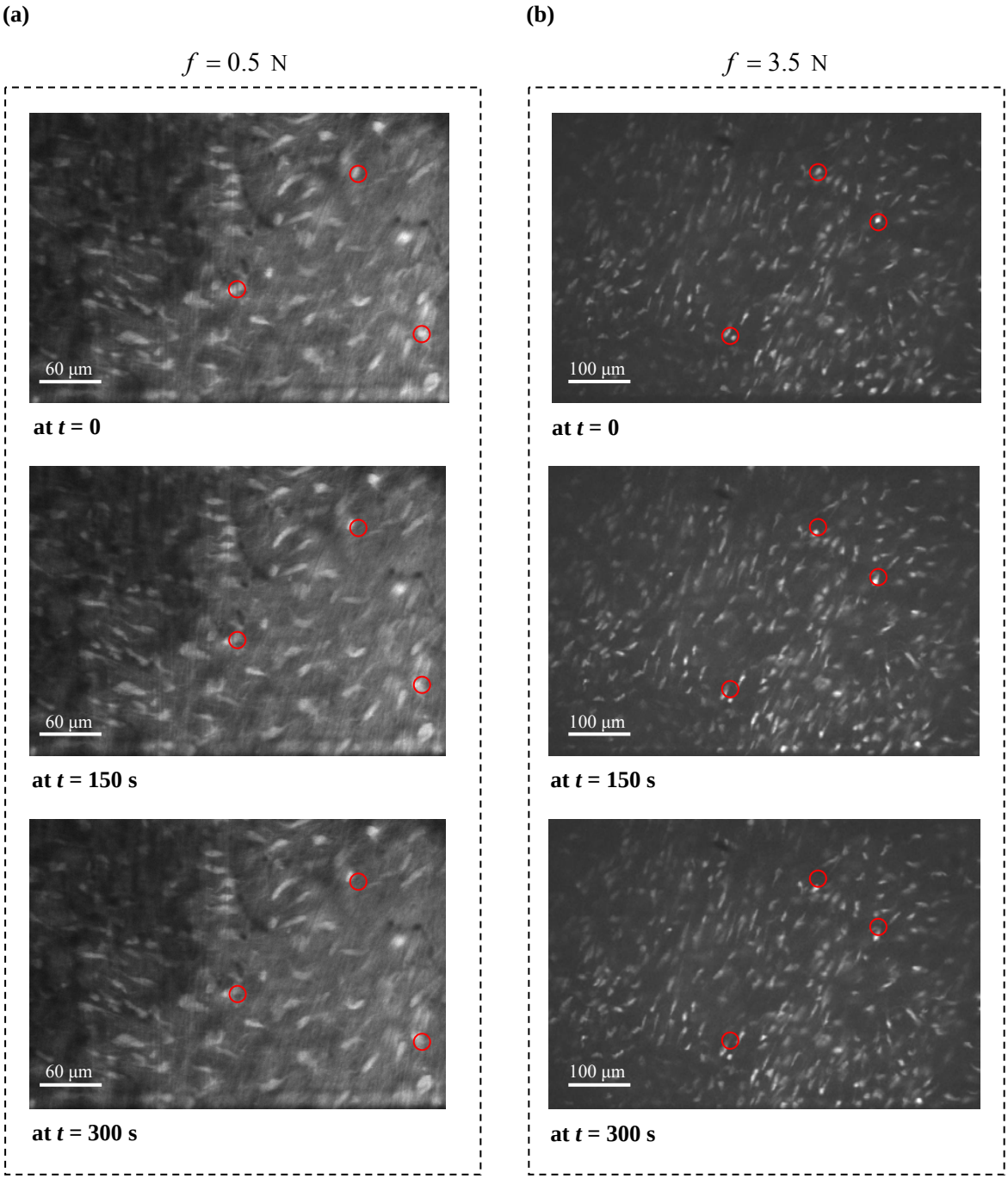

Figure 10.1 Sequence of images documenting the movement of the cell nuclei during creep: (a) rotation of the nuclei through a curvilinear motion in lower load levels ($f = 0.5$ N); (b) linear displacement of the nuclei at higher loading levels ($f = 3.5$ N). The time sequence increases in each panel from top to bottom. The circles show the original location of the indicated nuclei at $t = 0$.

Using the same method as described in §9.3, the angle of rotation and the linear displacement of the nuclei at every increment were calculated and are shown in Figure 10.2.

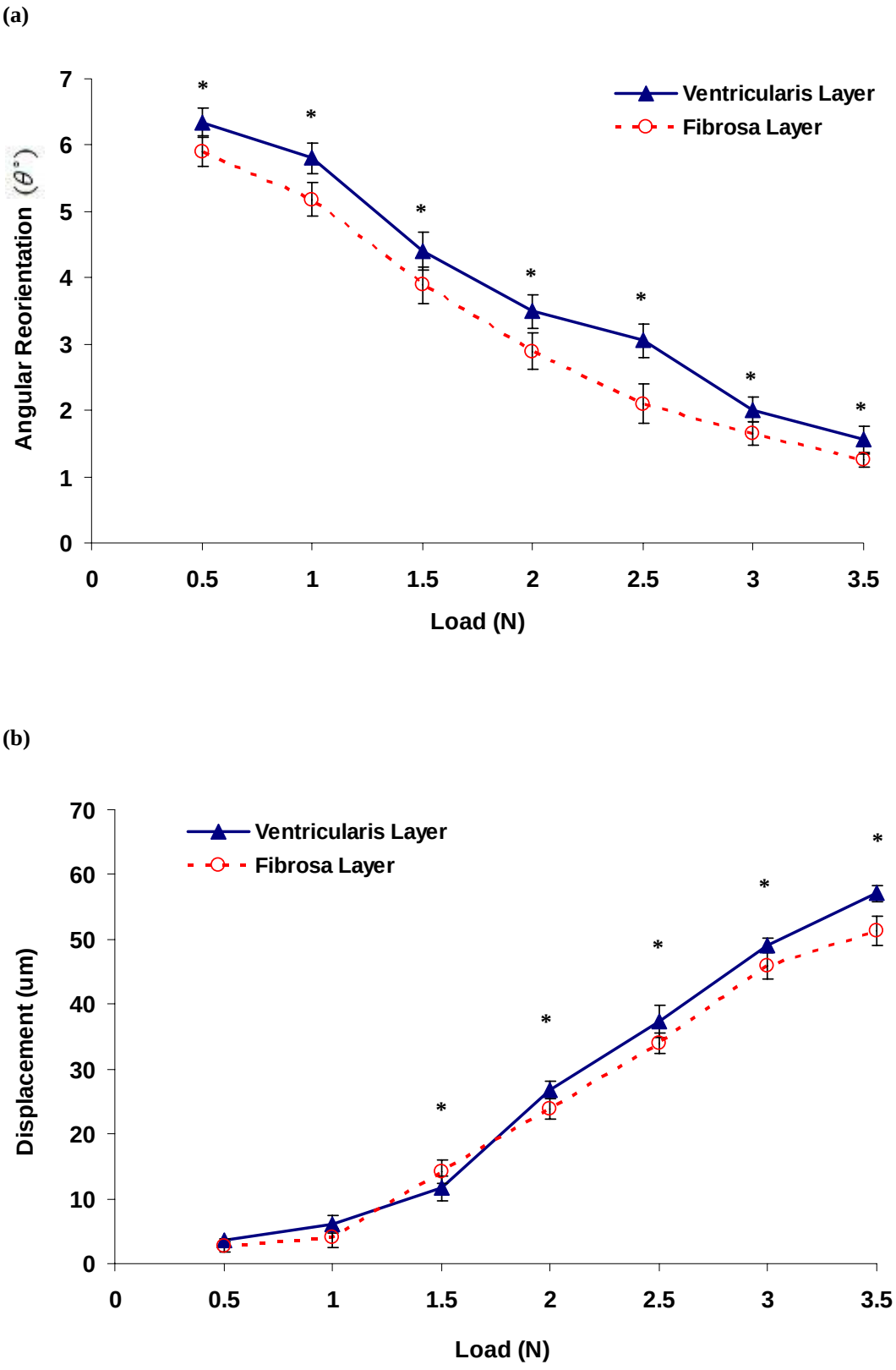

Figure 10.2 The movement of cell nuclei during creep: (a) values for angular rotation; (b) values for linear displacement. There is a statistically significant difference (indicated by *) between the values of angular reorientation within the two layers at all corresponding load levels (panel a). The asterisk indicates a statistically significant difference between the displacement values within each layer in panel b. The values are presented as Mean ± SD.

At corresponding strain levels, the angles of reorientation and the levels of displacement are both higher during creep than stress-relaxation. Table 10.1 compares the loading levels used in the creep tests and the corresponding strain levels. Additionally, the rotational motion in the fibrosa layer persisted to higher equivalent strain levels than those observed in stress-relaxation tests. Similar to results in stress-relaxation, the angular reorientation within the ventricularis layer is significantly higher than that within the fibrosa.

Table 10.1 Loading levels used in the creep tests and their corresponding strain levels.

Loading level used in creep tests (N) (f)	**Corresponding strain levels (%)** (ε)	**% of failure load** ($\%L_{failure}$)
0.5	6.64 ± 0.73	~5%
1	9.41 ± 0.61	~10%
1.5	11.25 ± 1.08	~14%
2	12.83 ± 0.88	~18%
2.5	14.79 ± 1.52	~22%
3	15.17 ± 0.33	~27%
3.5	16.52 ± 0.51	~30%

10.4. Discussion

From a structural perspective, the fibre reorganization mechanisms occurring during circumferential creep appear to be similar to those in stress relaxation, incorporating both fibre reorientation and linear movement. However, the values of reorientation and linear movement are noticeably higher in creep, compared to stress-relaxation. This may be due to the fact that samples are elongating with time during creep, so the physical dimensions of the samples are constantly changing. Owing to the Poisson's ratio effects, while the length of the tissue is increasing, the lateral dimension (width) is decreasing and the samples become narrower with time (Figure 10.3). This constant change in sample dimensions will add to the detected movement of the cells in the images, and subsequently results in higher values compared to stress-relaxation. It is

important to note that the elongation is kept constant during stress-relaxation, thus no changes occur in the physical dimensions of the samples.

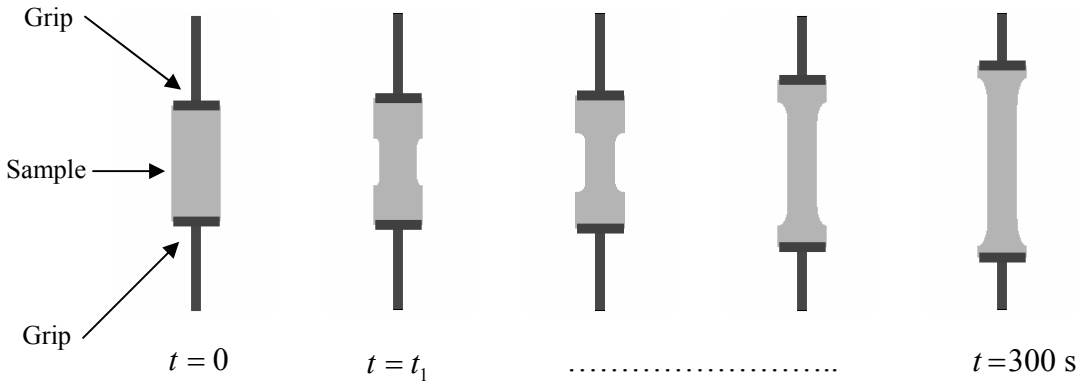

Figure 10.3 Change in the dimensions of the sample during creep, as it elongates within time. The sample length increases, while it becomes narrower in the lateral dimension.

Since the fibre kinematics during creep was experimentally observed to be similar to that in stress-relaxation, it is reasonable to assume similar governing equations for the displacement of fibres. The displacement field equation for the case of linear movement of fibres was shown to be (equation 9.11, chapter 9):

$$AE\frac{\partial^2 u_1}{\partial x^2} = \frac{F(t)}{2AE}x - u_1(x,t) + 2C_d \tag{10.1}$$

All parameters have the same definition as in §9.4.

However, the boundary conditions are different, as the loading conditions differ between creep and stress-relaxation. While the boundary conditions in stress-relaxation are determined through the applied strain (equation 9.12), they should be converted to incorporate load in the case of creep. Such boundary condition would thus translate to:

$$\begin{cases} \dfrac{\partial}{\partial x}u_1\left(\dfrac{l}{2},0\right) = \dfrac{F(t)}{AE} \\ \\ u_1(0,t) = \dfrac{1}{2}U(t) \end{cases} \tag{10.2}$$

The partial differential equation in (10.1) with the above boundary conditions is of the same form that appears in diffusion of a substance with a constant flux at a surface [185]. Using this analogy, the solution for the displacement will be [185]:

$$u_1(x,t)=\frac{F(t)l}{2AE}\left[\left(\frac{3x}{l}\right)+\left(\frac{2AE}{l^2C_d}\right)t-\frac{2}{\pi^2}\sum_{n=1}^{\infty}\frac{(-1)^n}{n^2}\exp\left(-(\frac{2n^2\pi^2AE}{l^2C_d})t\right)\cdot\cos\left(\frac{2n\pi x}{l}\right)\right] \tag{10.3}$$

Substituting equation (10.3) into (9.5) gives the creep elongation as:

$$U(t)=\frac{F(t)l}{2AE}\left[\frac{4}{3}+\left(\frac{2AE}{l^2C_d}\right)t-\frac{2}{\pi^2}\sum_{n=1}^{\infty}\frac{1}{n^2}\exp\left(-(\frac{2AEn^2\pi^2}{l^2C_d})t\right)\right] \tag{10.4}$$

For the case reorientation, fibre kinematics is analogous to that described in §9.4, equation (9.15) through (9.23). Hence:

$$u(x,t)=\frac{F(t)\left[1-\upsilon^2\right]}{2AE\left(1+\frac{\upsilon\theta}{2}\right)}l\left[\left(\frac{3x}{l}\right)+\left(\frac{2AE(2+\upsilon\theta)}{l^2(1-\upsilon^2)C_d}\right)t-\frac{2}{\pi^2}\sum_{n=1}^{\infty}\frac{(-1)^n}{n^2}\exp\left(-(\frac{2n^2\pi^2AE(2+\upsilon\theta)}{l^2(1-\upsilon^2)C_d})t\right)\cdot\cos\left(\frac{2n\pi x}{l}\right)\right] \tag{10.5}$$

And subsequently:

$$U(t)=\frac{F(t)[1-\upsilon^2]}{2AE\left(1+\frac{\upsilon\theta}{2}\right)}l\left[\frac{4}{3}+\left(\frac{2AE(2+\upsilon\theta)}{l^2(1-\upsilon^2)C_d}\right)t-\frac{2}{\pi^2}\sum_{n=1}^{\infty}\frac{1}{n^2}\exp\left(-(\frac{2AEn^2\pi^2(2+\upsilon\theta)}{l^2(1-\upsilon^2)C_d})t\right)\right] \tag{10.6}$$

Equations (10.4) and (10.6) describe the creep based on fibre linear movement and fibre rotation, respectively. They can be rearranged in terms of creep strain as:

$$\varepsilon(t)=\frac{F}{2AE}\left[\frac{4}{3}+\left(\frac{2AE}{l^2C_d}\right)t-\frac{2}{\pi^2}\sum_{n=1}^{\infty}\frac{1}{n^2}\exp\left(-(\frac{2AEn^2\pi^2}{l^2C_d})t\right)\right] \tag{10.7a}$$

$$\varepsilon(t)=\frac{F[1-\upsilon^2]}{2AE\left(1+\frac{\upsilon\theta}{2}\right)}\left[\frac{4}{3}+\left(\frac{2AE(2+\upsilon\theta)}{l^2(1-\upsilon^2)C_d}\right)t-\frac{2}{\pi^2}\sum_{n=1}^{\infty}\frac{1}{n^2}\exp\left(-(\frac{2AEn^2\pi^2(2+\upsilon\theta)}{l^2(1-\upsilon^2)C_d}\right)t\right] \tag{10.7b}$$

Since the applied load is kept constant with time during creep, $F(t)$ has been replaced by a constant value F. The equations above are analogous to the creep

relationship at the tissue level detailed in chapter 4, equation (4.5), used to describe the primary and secondary creeps occurred during the time course of the experiments.

It must be noted that the values of the exponential terms in the above equations for $n \geq 2$ are significantly smaller compared to $n = 1$, in order of 10^{-5}, 10^{-9}, 10^{-16}, … for $n = 2$, $n = 3$, $n = 4$, …, respectively. Thus the terms for $n \geq 2$ can be neglected, and the final form of the equations (10.7a) and (10.7b) will be:

$$\varepsilon(t) = \frac{F}{2AE}\left[\frac{4}{3} + \left(\frac{2AE}{l^2 C_d}\right)t - \frac{2}{\pi^2}\exp\left(-\left(\frac{2AE\pi^2}{l^2 C_d}\right)t\right)\right] \tag{10.8a}$$

$$\varepsilon(t) = \frac{F[1-\upsilon^2]}{2AE\left(1+\frac{\upsilon\theta}{2}\right)}\left[\frac{4}{3} + \left(\frac{2AE(2+\upsilon\theta)}{l^2(1-\upsilon^2)C_d}\right)t - \frac{2}{\pi^2}\exp\left(-\left(\frac{2AE(2+\upsilon\theta)\pi^2}{l^2(1-\upsilon^2)C_d}\right)t\right)\right] \tag{10.8b}$$

Equations (10.8a) and (10.8b) are similar in form to the functions that were fitted to experimental tissue-level creep data to describe the behaviour in chapter 4: a constant term, a linear term with respect to time, and an exponentially decreasing term. At small times t, the value of the exponential term determines the creep behaviour. However, as the time increases, the value of the exponential term decreases, and becomes small compared to the value of the linear term. Hence the linear term becomes the dominant contributor to creep, giving rise to the secondary creep observed in the tissue behaviour at higher time points (Chapter 4). Indeed, the secondary creep in AV tissue was observed to have a linear relationship with time, similar to the linear term in the above equations.

The assumptions regarding the correlation between the movement of the cells and the movement of the fibres during the creep are the same as those discussed in §9.4, for stress-relaxation. Similar to the stress relaxation analysis, cell movement is simply an indicator of the movement of the fibres, as analysed within the propsed mechanism and the developed theoretical criterion in this chapter.

Data regarding the time-dependant behaviour of the AV is scarce in the literature, particularly in addressing the creep phenomena. The general understanding in

valvular tissue is that the tissue doesn't show creep, while stress-relaxation is observed to occur, when loading the samples equi-biaxially [69,75]. It has also been reported that the collagen fibril D-period decreases during stress-relaxation, while it remains approximately constant during creep [69,75]. These data suggest that creep may not be an intrinsic behaviour of valve tissue, and furthermore that the possible underlying mechanisms are also decoupled. However, these suggestions vary considerably with studies examining the changes in the collagen D-period for other collagenous soft tissues, which report a sustained increase in collagen D-period in creep tests [187,188]. Additionally, the data presented in this chapter shows that creep does occur in the AV, along with the associated structural reorganisation.

In conclusion, the current data highlights that fibre sliding, occurring during either fibre reorientation or fibre linear displacement, is the mechanism responsible for the creep behaviour of the AV. This mechanism is similar in nature to that observed for stress-relaxation in chapter 10. However, since the boundary conditions (loading conditions) are different in the two phenomena, the outcomes reflect two different behaviours at the tissue level. Thus the structural mechanism governing the time-dependant behaviour in the AV can be explained at fibre level, and by the kinematics associated with fibre sliding during reorientation and linear movement.

Chapter 11

Final discussion, conclusions and recommendations for future work

11.1. Final discussion

AV biomechanics has received increasing attention over the past years, and remains an active research area in the field of medical engineering. Failure of current clinical substitutes, mortalities related to these failures, costs of the medical interventions arising from these shortcomings, and an annual financial turn over of nearly $1 billion pertaining to the substitute valve industry, have prompted multi-disciplinary research interests in this area.

Despite the progress in understanding the native valve function and properties, an optimal clinical substitute has not yet been introduced. This, from the author's point of view, may stem from the current paradigms and approaches adopted in studying AV biomechanics. As outlined in Chapter 1, the analysis of AV biomechanics has focused in three discrete areas [3,32]: dynamics of valve-blood interactions, tissue level mechanical behaviour and characteristics, and the properties and functions of valve cellular constituents. However, of equal importance, is the interrelationship between these approaches, which remains poorly understood. Key questions arise, such as [23,32]: how are the haemodynamics forces arising from the valve-blood interaction translated and transformed into the the structural components of the valve? How do structural responses influence the valve's mechanical behaviour? How is the micromechanical environment surrounding the residing cells perceived by them, and how do they respond to this?

To address some of these aspects of AV biomechanics, a fundamental study of AV structure-function relationships was carried out in this thesis, investigating the relationships between tissue-level behaviour and the structural mechanisms and responses contributing to that behaviour. Understanding these relationships provides a better platform for characterising valve function and properties, and will facilitate the design of more efficient substitutes, to mimic native valve behaviour more effectively. It will also help to quantify the micromechanical environment perceived by the residing cells, which can have significant implications for designing successful cell-mediated valve tissue engineering strategies, as an alternative to the currently available valve replacements.

Under physiological function, the AV opens in the systolic phase, and closes at the end-systolic phase, in each cardiac cycle [4]. The principal mode of AV deformation *in vivo* is flexion [7,77-79]. This translates to multiaxial tension of the ventricularis, and multiaxial compression of the fibrosa when the valve opens, reversing as the valve closes [78]. However, due to the technical complications associated with experimentally recreating physiological flexion *in vitro*, particularly in experiments employing microscopy imaging that requires in-plane focusing, biaxial and uniaxial tensile loading modes have alternatively been employed in studies of AV mechanics. Biaxial loading may more closely mimic the loading boundary conditions of the AV compared to uniaxial loading; however neither fully represent the natural loading mode of the valve *in vivo*. Nevertheless, when investigating structure-function relationships, loading modes will have minimal effects on the nature of the underlying structural mechanisms, nor how they would contribute to the tissue level behaviour. For example, structural reorganisation mechanisms such as the fibre recruitment, reorientation and sliding, observed and analysed in chapters 5 to 10 will occur, and indeed have been reported, under both uniaxial and biaxial loading modes [5,19,65,113,161]. However it is likely that the amount of the structural reorganization, and the loading and strain levels at which different reorganisation would occur, may differ depending on the loading mode.

The biomechanics of the AV at tissue level was characterised and presented in Chapters 3 and 4. While both chapters reflect aspects of the viscoelastic behaviour of the tissue, the nature of the viscoelastic behaviour addressed in each chapter is very different. Chapter 3 investigates the viscous effects of deformation of the tissue, while chapter 4 is addressing the time-dependent characteristics reflected in stress-relaxation and creep phenomena. Based on the intrinsic differences in biomechanics associated with each of these behaviours (quasi-static versus time-dependent), different models were adopted to address each aspect, and to quanity the associated biomechanical parameters. Such an approach followed that of traditionally adopted in the literature. A survey of the literature regarding the AV biomechanics indicates that no unified theories or models have been yet employed or proposed to characterise the entire range of the biomechanical characteristics of the AV, to the knowledge of the author. Indeed, models addressing the quasi-static behaviour of the AV have been mainly developed within the criterion of the hyperelasticity theory, while time-

dependent studies have mainly employed viscoelastic models. Furthermore, employment of a single viscoelastic model, i.e. either a Kelvin element or a Maxwell element based model, cannot thoroughly characterise both the stress-relaxation and creep behaviours of the valve's time-dependent spectra, as Kelvin model is known to be insufficient in characterising the stress-relaxation, and Maxwell model can only predict the primary creep behaviour of a subject tissue. The complex structural organisation of the AV ECM indeed facilitates stress-relaxation, and primary and secondary creep, as described in chapter 4, and possibly even tertiary creep if allowed the appropriate time-course. However, employing a unified model to characterise the different biomechanical parameters of the AV would be beneficial, as it enables comparing the obtained values in different studies in the literature, and it may further facilitate investigating the inter-relationships between the various associated parameters within the criterion of a unified theory. While this remains a challenging task in the literature, the author has attempted to formulate a unified theory for modelling stress-relaxation and creep in chapters 9 and 10, as a first step towards achieving this objective.

The mechanical behaviour of the AV under quasi-static loading was investigated in Chapter 3. The stress-strain curves were obtained under three different strain rates, covering a 100-fold increase in the level of applied strain rates. The associated parameters were characterised using a Kelvin-Voigt element-based model, by fitting the model to the experimental data. The stress-strain curves showed marked rate-dependency, i.e. the toe-in region and the ultimate failure strain decreased while the ultimate failure stress increased, with increasing strain rates (Figure 3.2). As discussed in §3.5, application of a tare load may influence the extent of the toe-in region and the estimation of failure stresses and strains. However, ensuring a consistent reference position in the curves necessitates employment of tare load protocols. Literature indicates that different protocols have been used in different studies, suggesting a level of arbitration in the choice of applied load, and subsequently the definition of the reference position. Nevertheless, a comparison of the data obtained in this study to the reported values in the literature reflected consistent values and trends, as discussed in §3.5.

The basis of the model developed in Chapter 3 originates from the assumption that total stress in the viscoelastic AV tissue could be considered as the sum of the stresses associated with the viscous fluid part (GAG) and the solid parts, i.e. two springs representing the contribution of elastin and collagen contents (equation 3.2). However, the mode and the extent of deformation in fluid and solid states could argueably be different, particularly at the large strains experienced by the samples in the performed tensile tests. This implies that the model may not be accurately applicable to the entire range of applied strains, particularly to the larger end of the deformation spectra. This could potentially result in errors in the estimation of model parameters, introducing uncertaintities to the calculated values. However, the model was seen to provide a good fit to the experimental data at all the employed strain rates (Figure 3.4), with small deviations from the experimental stress-strain curves even at larger strains.

The stress-strain curves under quasi-static loading showed marked rate-dependency (Chapter 3). Additionally, modelling results revealed that the viscous damping coefficient η values were also rate dependent, addressing a 'shear-thinning' behaviour, with reduced effective viscosity at higher strain rates (Table 3.3). The tangent modulus E, calculated numerically from the first derivative of the $\sigma - \varepsilon$ curve also reflected this rate dependency, as the values of E increased with increase in strain rate (Figure 3.3). However, the relationship between stress and strain was characterised by the model in equation (3.13) as:

$$T = \frac{E}{2}\left(\lambda^2 - \lambda^{-2}\right) + 4\eta\left(\frac{\dot{\lambda}}{\lambda}\right) - 4\eta\dot{\lambda} \tag{11.1}$$

and thus the first derivative of stress with respect to stretch ratio would be:

$$\frac{dT}{d\lambda} = \frac{E}{2}\left(2\lambda + 2\lambda^{-3}\right) - 4\eta\dot{\lambda}\lambda^{-2} \tag{11.2}$$

assuming that the stretch rate $\dot{\lambda}$ is constant.

In large deformations, where values of λ are large, $\lambda^{-4} \approx \lambda^{-3} \cong 0$, and therefore eq. (11.2) can be re-written as:

$$\frac{dT}{d\lambda} = E \tag{11.3}$$

Therefore the first derivative of stress with respect to deformation leads to the tangent modulus E only when the deformations are large. As such, the calculations of modulus may only be theoretically accurate for the third region of the stress-strain curves, defined in §3.4, where the values of strain are large compared to the other two regions. However, the *in vivo* strain values of the AV are approximately 10.1% and 30.8% in the circumferential and radial directions, respectively [7,8], which are small compared to the ultimate tensile strains in the respective direction (Table 3.1).

These data indicate that Eq. (11.2) would be a better representative of the first derivative of the stress, and hence the tangent modulus. As can be observed, the viscous damping coefficient also influences the tangent modulus, and therefore the measure of stiffness. Since the viscous effects are generally thought to be associated with the presence of the GAG constituent of the valve ECM [17,102], it is reasonable to conclude that the GAG component of the AV also contributes to the stiffness of the tissue. The change in tangent modulus with η at *in vivo* strain level is shown in Figure 11.1, for both loading directions, calculated by Eq. 11.2. The values of tangent modulus calculated numerically from the $\sigma - \varepsilon$ curves (Figure 3.3) are also shown for comparison. The results suggest that the GAG contribution to the overall tangent modulus of the tissue at *in vivo* strain levels increases, as the damping coefficient decreases, with increasing strain rates. This effect is more pronounced in the circumferential direction. Therefore, although it is generally accepted that the numerical first derivative of the $\sigma - \varepsilon$ curve can be used to determine the tangent modulus for an assessment of stiffness, it may underestimate the overall stiffness of the samples, particularly at small strains. It is therefore suggested that the constitutive equations describing sample stress-strain behaviour be used for establishing the modulus, by taking the mathematical derivate resulting to the tangent of the curve at each point.

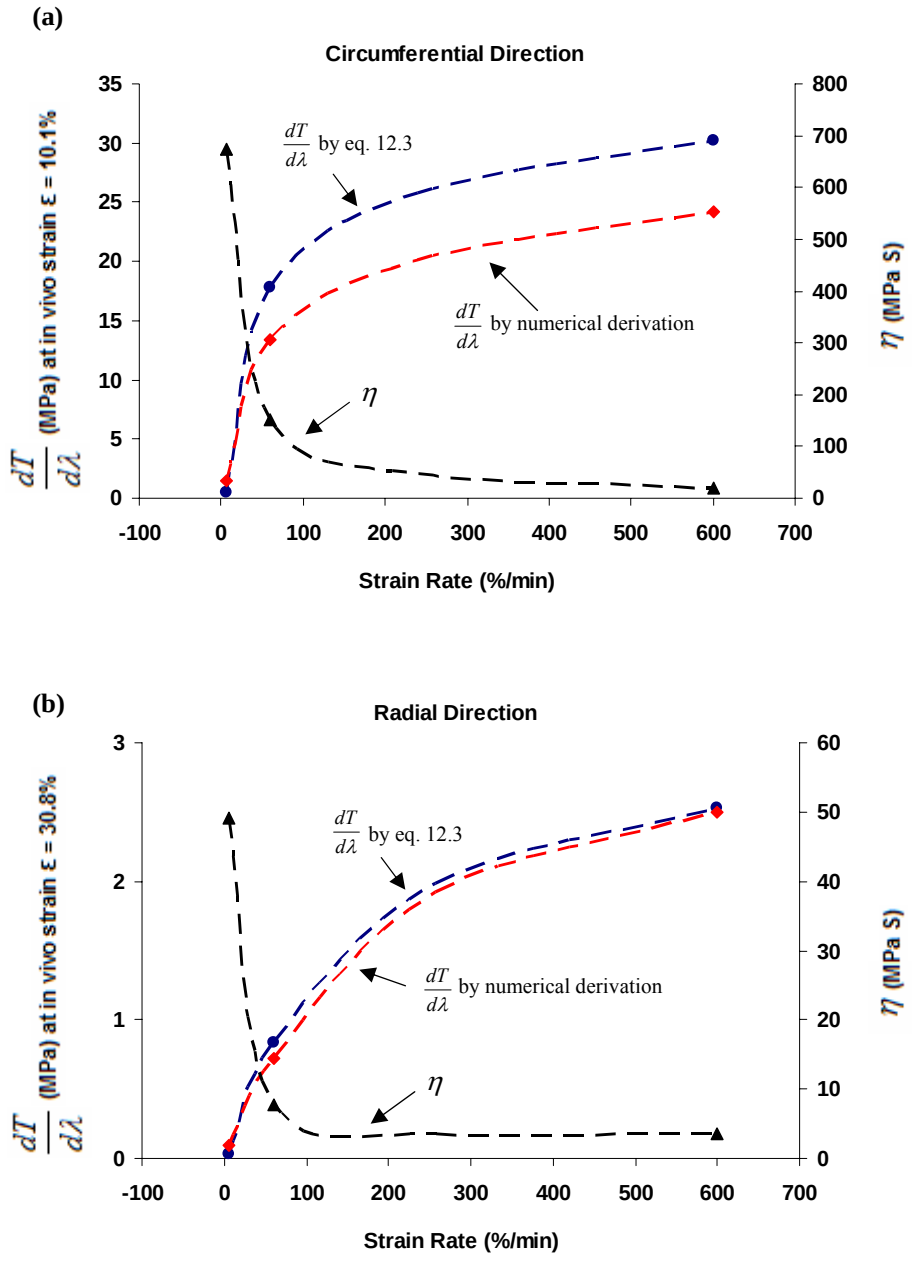

Figure 11.1 The first derivative of stress with respect to strain, $\frac{dT}{d\lambda}$, comparing the values calculated from Eq. 11.2 with ones numerically calculated from the stress-strain curves, at different strain rates. The value of the viscous damping coefficient η at each strain rate is also presented, to highlight the influence of η on $\frac{dT}{d\lambda}$.

In a simple form, collagen fibres can generally be considered to be elements that reinforce soft connective tissues, embedded in a gel-like GAG, sometimes referred to as ground substance [190]. Chapter 3 demonstrated that that the GAG within the AV can be modelled as a viscous fluid that tends to flow upon the application of load to the tissue, showing non-Newtonian viscous fluid properties. As a result, the interface between the collagen fibres and GAG will be under shear, which causes the fibres to

stretch [190]. The condition for a fibre to be able to provide an effective reinforcement is that its length should be comparable to a critical length, l_c, which in the theory of composite materials is defined by [190]:

$$l_c = \frac{r\sigma_f}{\tau} \tag{11.4}$$

where r is the radius of the fibre, σ_f is the failure stress of the fibre, and τ is the shear stress exerted on the fibre by the flow of GAG. Physically, the critical length is the minimum length that a fibre must have for the induced stresses in that fibre to reach σ_f in the centre of the fibre [190].

In terms of fibre length l and the critical length l_c, three possibilities can exist in the AV matrix, shown schematically in Figure 11.2 [190]: (a) the fibre is longer than the critical length, in which case the maximum transferable stress to the fibre σ_m can be reached and therefore the fibre provides effective reinforcement; (b) the fibre length is equal to the critical length, only allowing for the centre of the fibre to reach the maximum stress; and (c) the length of the fibre is less than the critical length, where the maximum stress can never be transferred to the fibre, leading to ineffective reinforcement.

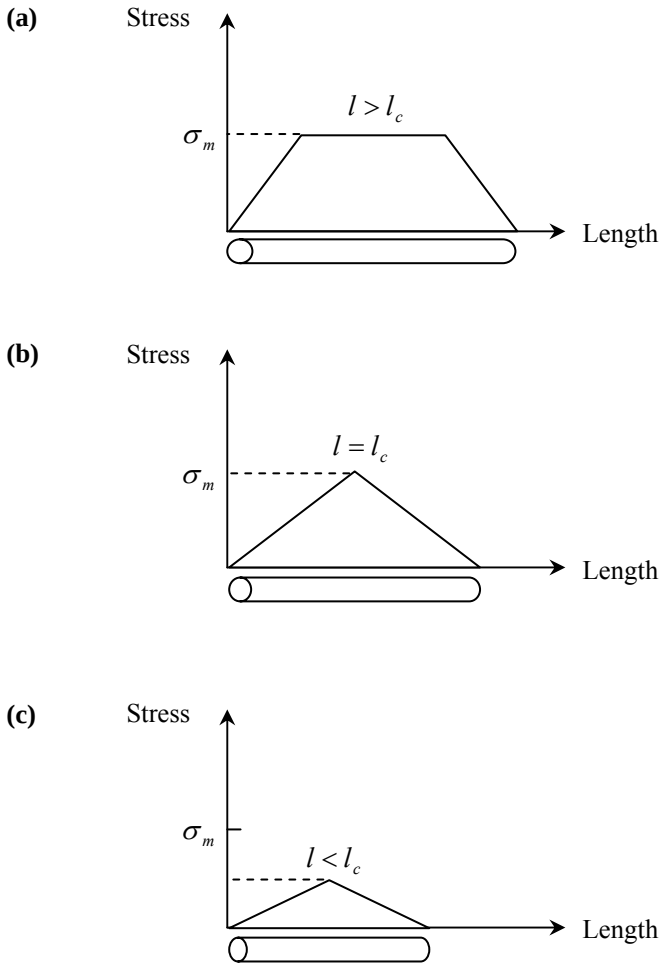

Figure 11.2 Fibre length and its relationship with stress bearing: (a) $l > l_c$, (b) $l = l_c$, and (c) $l < l_c$. σ_m is the maximum stress which can be transferred to the fibre (redrawn from [190]).

It was shown in Chapter 3 that there is a repeatable sudden transient decrease in stress, when samples were strained to failure in the circumferential direction (Figure 3.2). It was discussed that this may be due to the failure of the collagen fibre network within the ventricularis layer. In light of equation (11.4), it can be further observed that this failure could also be a result of larger l_c values for fibres within the ventricularis layer, due to the geometrical differences of fibres distributed between the layers. Fibres in the ventricularis may possibly possess higher radii, compared to the fibres present in the fibrosa layer. A larger l_c in the ventricularis would increase the possibility of fibres having lengths shorter than or equal to l_c. If $l = l_c$, and a group of fibres fail, other fibres will be overloaded and subsequently total failure will occur. If

$l < l_c$, then the fibres can not reach their potential maximum load bearing capacity, and thus will not effectively reinforce the ventricularis layer. Both cases will result in faster failure of the ventricularis layer. It was additionally shown in Chapter 5 that the fibrous network in the ventricularis endures less shear stresses and strains, compared to the fibrosa (Figures 5.5, 5.7 and 5.8). This, in light of equation (11.4), will also increase the l_c, which can be an additional factor contributing to the failure of the network in this layer prior to the fibrosa.

The modelling results in Chapter 3 showed that the viscous damping coefficient of the AV tissue reduces with increase in strain rate, tested across strain rates of 6%/min, 60%/min and 600%/min (Table 3.3). However, the *in vivo* strain rates correspond to 15000%/min, for samples with similar dimensions to the ones used in this study [95]. Extrapolating the values of η to the physiological rates implied that the AV tissue may offer minimal shearing resistance against blood flow in each cardiac cycle. This shear thinning behaviour, similar to the effects of the viscous damping coefficient on the tangent modulus and stiffness of the tissue (discussed in the beginning of this chapter and illustrated in Figure 11.1), can not be elucidated and formulated under elastic deformation assumptions and criteria. However, hyperelasticity theory has been the widely accepted criterion in formulating and developing microstructural based models for collagnenous soft tissues [144,145]. Within the hyperelasticity theory, only the contribution of the collagen fibres, as the main load bearing element of the tissue ECM, is considered [144,145], and the viscous effects are generally neglected under the quasi-static loading assumptions.

Based on the hyperelasticity assumptions, and the theoretical criteria developed by Lanir [143,147], a microstructural based models was developed and introduced to address the observed non-linearity of the tissue stress-strain curves, incorporating the response of the collagen fibres (Chapters 6). The contribution of wavy fibres to the overall mechanical behaviour of the tissue was formulated and characterised by the model, describing their behaviour from the wavy to the straight and further strained configurations (Chapter 6). The modelling results indicated that straightening of the fibres allowed the AV tissue to undergo circumferential strains of up to 15% (Figure 6.7), with failure strain of the fibres around 10% [155]. This is in a good agreement

with the experimental observations, reporting that collagen fibres straightened at tissue strains of approximately 17% [19]. Characterising the contribution of the wavy fibres to AV mechanical behaviour is important, since the *in vivo* circumferential strains are reported to be around 10% [7,8], at which point the fibres may not be fully straight. Thus, common assumptions that suggest only straight fibres can contribute to the mechanics of a tissue may not be applicable for the AV. The model introduced in Chapter 6 attempts to address this, by considering the contribution of the fibres in the general case of being wavy. Furthermore, as the AVICs are attached to the fibres, fibre elongation would also impose deformations to the cells, even when the fibres are wavy. Thus, characterisation of fibre strains before the fibres are fully straight would help to better understand and quantify the cell deformations, particularly at *in vivo* strain levels.

A key feature of the model developed in Chapter 6 is the assumption of non-affine transformation of strain from the tissue to the microstructure. This was experimentally investigated and concluded in Chapter 5, where no direct translation between the applied strains at the tissue level and collagen fibre network deformations was observed (Figure 5.4 and 5.5). Additionally, it was observed that the applied loading modes were different to those induced in the microstructure, as tissue level tensile deformations resulted in additional internal shearing within the collagen fibre network (Figures 5.7 and 5.8). The general assumption in formulating the previous microstructural based models is that strain transfer is affine [66,122,147], an assumption which was not supported experimentally (Chapter 5). The model in chapter 6 addresses this, formulating the first AV microstructural based model with non-affine strain transfer, known to the author.

Another aspect of fibre contribution to tissue behaviour may stem from fibre rotation, as the fibres have been reported to reorient towards the principle stretch axis under quasi-static loading [191]. Fibre rotation has previously been estimated to be approximately 10.5° under uniaxial loading in the circumferential direction [191]. The rotation of fibres was estimated also in Chapter 9, amounting to approximately 14° and 6° for the ventricularis and fibrosa layers respectively, during stress-relaxation (Figure 9.3). The average fibre rotation in the two layers is close to the reported value in [191]. However, to the knowledge of the author, there are no microstructural

models developed, to date, to characterise this behaviour in the AV tissue, and to enable the estimation of angular reorientation of the fibres directly ftom the quasi-static stress-strain data.

Another load bearing element within the valve ECM is the elastin, present as a network of elastic fibres [13]. To characterise the contribution of elastin to the overall mechanical behaviour of the AV, a model was developed in chapter 8 based on the principles of statistical mechanics for entropic elasticity, under the non-affine strain transfer assumption established in Chapter 5. The model explained how a network of elastin fibres can show non-linear mechanical behaviour, under tissue-level deformation. Modelling results indicated that the overall nonlinearity of AV stress-strain curves observed in Chapter 3 (Figure 3.2) may not entirely be due to the gradual recruitment of the initially wavy collagen fibres, but that the elastin network can further exacerbate the nonlinearity, especially at increasing strains (Figure 7.3). Elastin has previously been reported to contribute to the load-bearing capacity of AV tissue at small strains, and to restore the contracted configuration of the valve leaflet after the stretch induced during the diastolic phase of each cardiac cycle [5,19,20]. However, it was analytically shown that descriptions which limit the contribution of elastin network to only small strains, would mathematically assume a Gaussian probability distribution for the configuration of the network of elastic chains, which leads to a linear stress-strain relationship (Figure 7.4, Appendix E). Such behaviour is not supported experimentally, and both the experimental and modelling data confirmed the nonlinear contribution of the elastin network to tissue behaviour continued up to large strain levels.

Another aspect of the AV biomechanics is the time-dependent behaviour, manifested by stress-relaxation and creep phenomena [5,55,69]. It was established in Chapter 3 that the AV shows non-Newtonian viscous-fluid characteristics under quasi-static loading. In Chapter 4, stress-relaxation and creep characteristics of the tissue were investigated. The results indicate that the time-dependent behaviour of the AV is non-linear, i.e. the amount of stress-relaxation or tissue creep both change with the level of applied strain or load (Figures 4.4 and 4.6; Tables 4.3 and 4.4). The non-linear nature of AV time-dependent behaviour does not agree with the quasi-linear assumptions incorporated in the QLV theory (eq. 8.4, Chapter 8) to describe the tissue

behaviour. Further, it was shown in Chapter 8 that the QLV model may not be supported microstructurally, and hence its associated parameters are not likely to interpret the time-dependent behaviour of the AV accurately. This is supported by the high standard deviations observed when characterising tissue relaxation times using the QLV model [5,55,72].

Using a generalised Maxwell model, it was shown that AV relaxation in the radial direction followed a single mode (Table 4.3). Circumferential relaxation also followed a single mode at low strains. However, it switched to a double relaxation mode at higher strains (Table 4.3). Each mode is an indicator of a structural mechanism contributing to the overall relaxation at the macro level [180,181]. Furthermore, the type of the relaxation mode also reflects the nature of the underlying mechanism causing the relaxation [180-182]. This information could not have been elucidated from the tissue level behaviour, if models that incorporate continuous relaxation spectra were used to characterise stress-relaxation of the AV samples, such as the QLV.

The microstructural mechanisms associated with the time-dependent behaviour observed in Chapter 4 were studied in Chapters 9 and 10, for stress-relaxation and creep phenomena respectively. Reorganisation of the ECM was investigated by monitoring movement of the AVIC nuclei during stress-relaxation and creep. The AVICs are known to be bonded to the fibres [23,121,184], and therefore their movement may be an indicator of the movement of the fibres. These movements were imaged during the time course of the experiments, and from these images, fibre kinematic parameters were quantified. As discussed in §9.4 and §10.4, calculation of fibre kinematic parameters were made under the assumption that the movement of each cell represented the mode of the movement of a fibre. In practice, however, more than one cell might be attached to any one fibre, or a cell might be attached to more than a single fibre. While this will influence the values associated with rotation/linear movement of fibres reported in Chapters 9 and 10, the underlying mechanism and the theoretical analysis presented will still apply, as the movement of the cells is an indicator of the movement of the fibres which will inflict fibre-fibre and fibre-matrix sliding effects, irrespective of the number of cells attached to any particular fibre.

Based on these assumptions, results indicated that at lower load or strain levels, the fibres rotate during the creep or stress-relaxation (Figures 9.1, 9.3, 10.1 and 10.2). However, as the loading or strain levels increased, linear displacement became the dominant mode of movement (Figures 9.1, 9.3, 10.1 and 10.2). The values associated with fibre kinematics were also significantly different between the ventricularis and fibrosa layers (Figures 9.3 and 10.2). To explain how this fibre reorganisation contributes to tissue-level time-dependent behaviour, the mathematics of the observed kinematics was introduced and developed. In contrast to the microstructural based models developed in Chapters 6 and 7 to analyse the quasi-static behaviour of the AV, the viscous effects of the ECM due to the presence of GAG was also considered, as well as the fibre-fibre interactions (Chapter 9). The outcomes indicated that the frictional effect between two fibres, and between fibre and the viscous fluid-like GAG, is one mechanism for stress-relaxation, resulting in one of the observed relaxation modes at the tissue level. However, no detectable movement of the nuclei was apparent in the radial direction, nor at lower strains in the circumferential direction, indicating a different relaxation mode. The lack of fibre movements in these cases suggests that the relaxation mode may come from the flow of the GAG, which was shown to have non-Newtonian fluid characteristics in Chapter 3. These findings are in a good analogy with stress-relaxation behaviour observed in polymeric gels, in which two microstructural mechanisms, namely 'Rouse' and 'reptation', are responsible for the two relaxation modes observed at the macro-level [180,181].

The fibre kinematics observed during creep were similar to those during stress-relaxation, with the same mathematical principles resulting in the same governing equations (Chapter 10). However, the loading boundary conditions are different in the two phenomena (equations 9.12 and 10.2), which leads to two kinds of behaviour. Contrary to studies suggesting that the structural mechanisms for the two phenomena in valvular tissues may be uncoupled [69,75], the current data and analysis show that the frictional effects between fibres, and between fibres and the surrounding GAG, provide the principal mechanism contributing to the time-dependent behaviour of the AV. In investigating the underlying mechanisms contributing to the time-dependant behaviour of soft tissues, there are studies that have tried to examine the roots of these mechanisms in length scales below the fibre level, such as the fibril level [69,75,192], or down to the molecular level [187,188]. However, the choice of length scale is

essentially a matter determined by how the resulting data are able to explain the macro-level behaviour. For AV tissue, based on the experimental data and mathematical analysis presented in this thesis, fibre-level mechanisms seem to explain both the type and number of modes, observed at the tissue level, during the time-dependent behaviour.

11.2. Conclusions

11.2.1. At the tissue level

- The quasi-static behaviour of the AV is strain rate-dependent, with the tissue becoming stiffer at higher strain rates. The UTS in the circumferential direction was determined to be 3.44 ± 0.57 MPa at 6%/min, while it was observed to be 4.45 ± 0.13 MPa at 600%/min. However, the failure strain decreased from $45.07\% \pm 1.25$ to $27.56\% \pm 1.96\%$, between 6%/min and 600%/min. A similar trend was also observed in the radial direction, with the UTS increasing from 0.34 ± 0.03 MPa to 0.84 ± 0.05 MPa, and the corresponding failure strain reducing from $87.6\% \pm 1.78\%$ to $61.11\% \pm 0.63\%$, at strain rates of 6%/min and 600%/min, respectively.

- A mathematical model was developed based on the three morphological layers of the AV, to account for the rate effects. From the results of the model it became evident that rate dependency stems from the GAG constituent of the AV ECM, showing a shear-thinning behaviour. By extrapolating the results to physiological loading rates, the viscous damping coefficients were determined to be $\eta_{cir} = 8.3$ MPa s and $\eta_{rad} = 3.9$ MPa s in the circumferential and radial loading directions, respectively. This non-Newtonian viscous property of the native valve is likely a critical aspect in optimising substitute valves, as it indicates that the native AV tissue offers minimal resistance to the shear stresses induced by blood flow. The thromboembolism and coagulation-related problems associated with the current substitute valve designs may be, in part, due to the mismatch in shear-thinning behaviour, as increasing shear stress in the valve-blood interaction can damage the blood cells.

- The time-dependent behaviour of the AV is anisotropic, but is also non-linear, meaning the associated parameters change with the level of applied strain or load. The tissue exhibits both stress-relaxation and creep, implying that they are intrinsic characteristics of the tissue. The time-dependent behaviour is a particularly important mechanical feature of the native AV, as structural durability of AV is thought to be linked with its ability to relax the induced stresses.

- The stress-relaxation modes are different depending on the level of applied strain, and the loading direction. While a single relaxation mode suffices to explain the relaxation behaviour of the AV in the radial direction and also at lower strain in the circumferential direction, it switches to two relaxation modes at higher circumferential strains. The number of modes is important since it indicates the number and the nature of the mechanisms involved in the phenomena.

- Creep behaviour is also directional dependent, with creep strains consistently reporting higher values in the radial direction. Except for samples under lower applied circumferential load, the tissue exhibited both primary and secondary creep during the time course of the experiment.

11.2.2. At the micro level

- Strain transfer from tissue to ECM is likely to be non-affine, i.e. there was no direct nor linear translation and transformation of strains applied at tissue level to the micro level strains. The strain distribution within the fibrous network (FN) was also non-homogenous, possessing higher values in the central (belly) region, reducing towards the commissural region. The non-affinity of strain transfer is an important feature of the tissue when it comes to modelling its behaviour, based on the microstructure.

- The end-effects were quantified both experimentally, and analytically. The characteristic decay length, the distance after which the gripping effects become

negligible, was quantified for both the circumferential and radial loading directions, and investigated experimentally at tissue and micro levels. The analysis indicated that the end effects influenced considerably longer sample length in the radial direction, compared to the circumferential loading direction.

- A 3D map of strain distribution was constructed within the ECM, and internal shearing was quantified accordingly. The FN within the fibrosa layer elongates less than the ventricularis, and thus the network and residing cells bear more shear stress in that layer. The shear stress is also higher in the circumferential direction compared to the radial direction. The distribution profile of strain within the FN, together with the induced shear stresses, may be linked to the higher levels of collagen biosynthesis in the fibrosa layer, and the preferred orientation of collagen fibres in the circumferential direction.

- Incorporating the assumption of non-affinity of strain transfer, two microstructural based models were developed to characterise the contribution of collagen fibres to the non-linear stress-strain relationship of the tissue. The first model included the gradual contribution of the fibres, from their wavy configuration to fully straight, and quantified single fibre strain during the tissue deformation. The second model incorporated fibre reorientation, quantifying the angle of reorientation of the population of the collagen fibres upon tissue-level deformations. Both models provided a good fit to the experimental tissue-level data, and indicated that contrary to the general assumption, the fibres should not necessarily be fully straight to contribute to load-bearing in the tissue, and that the angular distribution of the fibres may not be preserved during deformation. A new angular distribution function was also developed and introduced, based on the geometry of the fibres within the tissue, for a more accurate description of the fibre kinematics during tissue deformation.

- A model was proposed based on the principles of statistical mechanics in entropic elasticity, to characterise the contribution of the elastin network to the mechanics of the AV. Results of modelling the experimental data showed that the overall nonlinearity of the stress-strain curves observed in AV tensile deformation tests may not entirely be due to the gradual recruitment of the

initially wavy collagen fibres, but that the elastin network can further exacerbate nonlinearity, especially at increasing strains. Previous descriptions of the function of the elastin constituent of the AV ECM have mainly remained descriptive, limited to 'providing an elastic returning mechanism' for the AV tissue after stretching [19,20]. The model developed in chapter 7 can be superimposed into that developed for collagen fibres in chapter 6, for a more accurate micro-mechanical based characterisation of the mechanical behaviour of the AV by a unified model.

- With regard to time-dependent behaviour, it was shown mathematically that the QLV model is not structurally based, and remains phenomenological in describing stress-relaxation and creep behaviour of the AV. Thus, alternative modelling criteria were needed to describe the time-dependent behaviour of the AV based on its microstructure.

- The ECM reorganizes during stress-relaxation, with two distinct fibre kinematic features observed experimentally: reorientation and linear movement. It was shown mathematically that the dissipative effects due to fibre-fibre and fibre-matrix interactions during the reorientation and the linear sliding would result in Maxwell-type exponential stress-relaxation. One of the relaxation modes observed at tissue-level thus results from such fibre kinematics, and the other relaxation mode is most likely related to the viscous effects of GAGs.

- Similar ECM reorganization was observed during the creep, i.e. fibre reorientation and movement. It was shown that the mathematics of fibre kinematics is similar in creep and stress-relaxation, and the observed creep behaviour at the tissue-level results from the same set of equations, with only the boundary conditions differing between creep and stress-relaxation. This structural mechanism results in both the primary and secondary creep behaviours, observed at the tissue-level.

- Experimental observations and modelling results both confirmed that the same microstructural mechanism is responsible for stress-relaxation and creep phenomena in the AV at the fibre level.

11.3. Recommendations for future work

The areas for future work associated with the current study may be divided into three separate categories, each pertaining different time scales: modelling criteria, experimental work, and tissue engineering perspective.

11.3.1. Modelling criteria

The microstructural based models developed in this work enable the quantification of strains, and accordingly stresses, of a single and a network of fibres within the AV during deformation, both under quasi-static and time-dependant loading modes. An exciting prospect for future developments to this work would be to introduce the derived equations to finite element codes and models that simulate the deformation of the AV cusp under physiological loading conditions. This could quantify the local micro strains and stresses within the ECM, within the native functioning valve.

Another aspect providing further insights into the micromechanics of the AV is to investigate the mechanisms of AVIC adhesion to the fibres, which could result in clarification of how the strains and stresses are transferred to the cells, from the fibres. This is particularly a challenging task, and may therefore be persuaded in longer time scales, since in addition to the associated biological and biochemical complications, biologists and modellers need to arrive at a common understanding and consent for a representative model. Once this is achieved, the strains and stresses undergone by cells can also be quantified from the tissue-level deformation data. This would significantly contribute to our understanding of AVIC mechanobiology, and can lead to the design of optimised loading protocols which can be implemented in bioreactors for cell-mediated ECM biosynthesis, and eventually tissue-engineered valves. All this can be achieved by coupling finite element models investigating tissue deformation with the micromechanical based models developed in this study, and knowledge of how the cells are attached to the fibres. This is shown schematically in Figure 11.3.

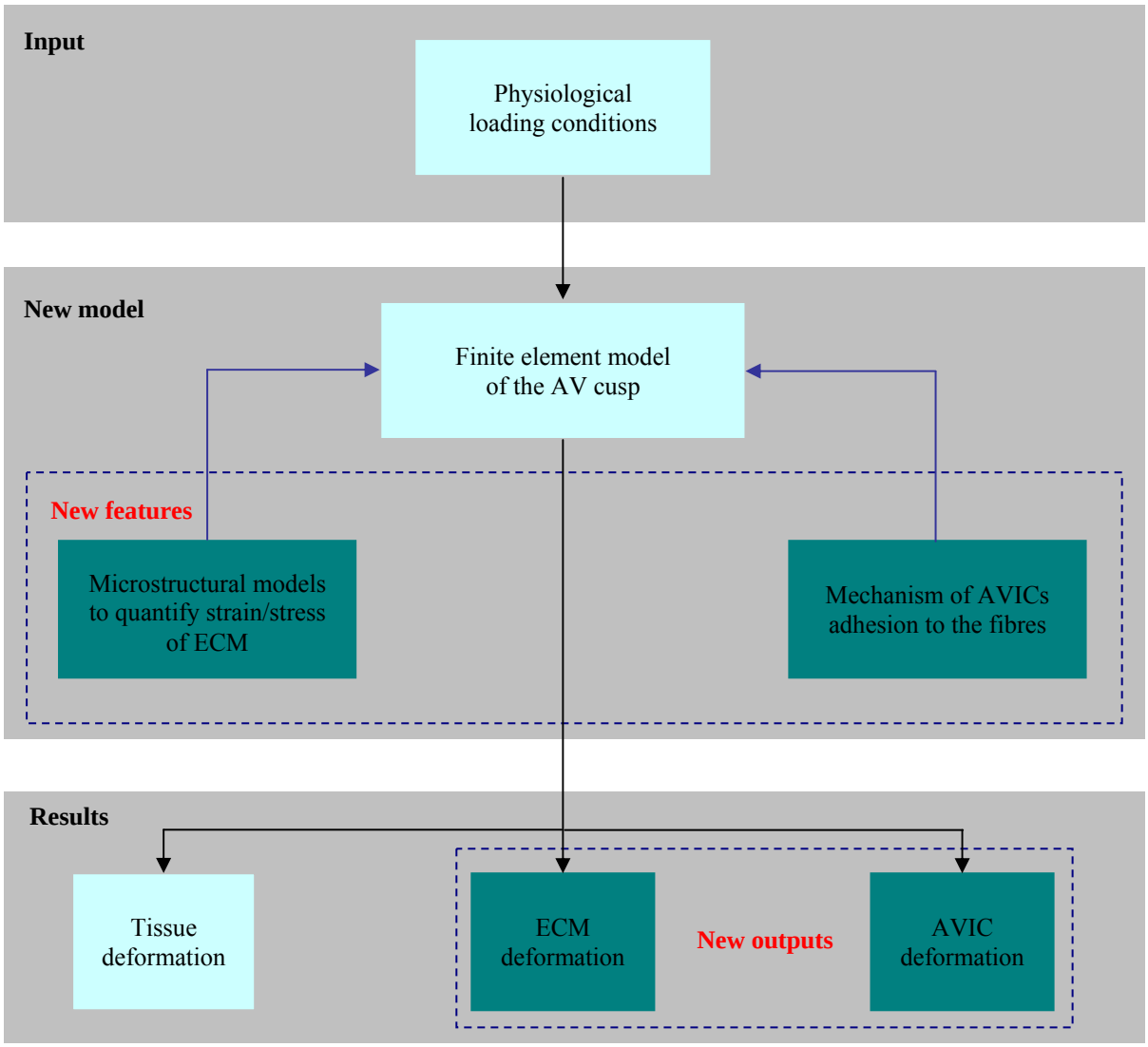

Figure 11.3 Possible new developments to build into conventional finite element models, generating new outputs.

11.3.2. Experimental work

From an experimental point of view, further work should employ a biaxial loading protocol, as a means to create loading boundry conditions more closely matched with those in AV physiological loading. Of particular interest is the investigation of AVIC deformation *in situ* under biaxial deformation of the AV; information which is currently lacking from the literature. The outcomes of this study can be of significant benefit when linked with the data from mechanobiology studies of single-cell models investigating the influence of cell deformation on ECM biosynthesis, to draw more

accurate conclusions about the rate of ECM metabolism and turnover in the native valve.

When studying AV mechanics under biaxial loading, it would also be interesting to investigate the time-dependent behaviour of the tissue under non equi-biaxial loading regimes, to elucidate the extent of such effects on the native functioning AV. Current data fall short in describing creep behaviour of the AV under non equi-biaxial loading, which is the likely loading mode in the native valve. This information can prove crucial when designing substitute mechanical valves, for a more optimized material selection to mimic the behaviour of the native valve more closely.

In prepration for these studies, a biaxial loading rig was designed and developed during the course of this work. A picture of the rig, together with a schematic showing the different components, is presented in Figure 11.4. The rig allows for the application of quasi-static and time-dependent loading modes on tissue samples, under both load and displacement control. It has been designed to fit on the stage of confocal microscope, facilitating imaging of the residing cells and ECM upon deformation of the sample in real time. The technical drawings of the rig are included in Appendix G.

(a)

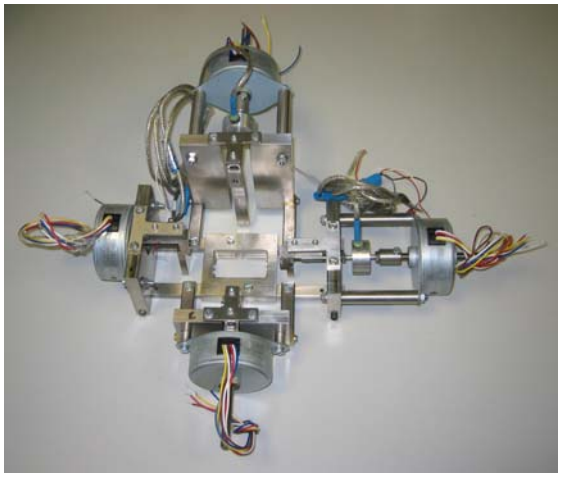

(b)

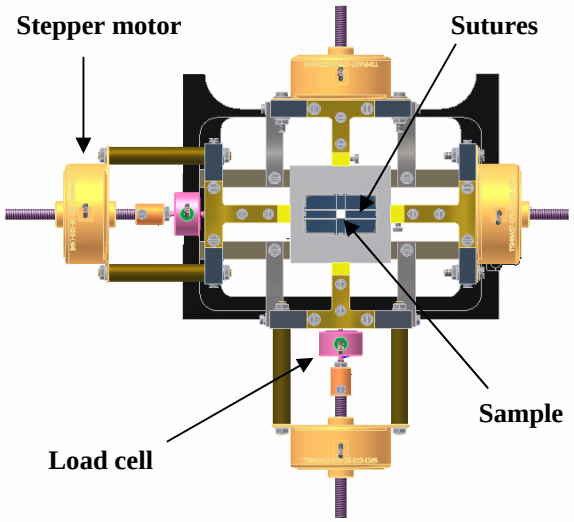

(c)

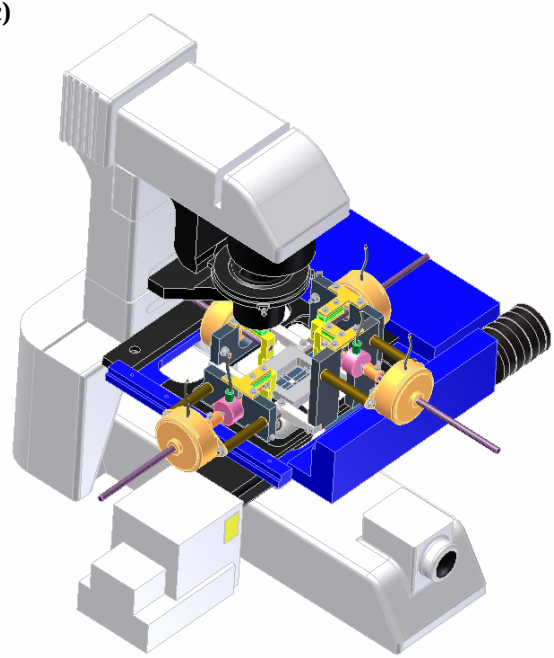

Figure 11.4 (a) a picture of the biaxial rig; (b) schematics of the rig; showing its different parts; (c) schematics of the rig on confocal microscope stage.

11.3.3. A tissue engineering perspective

My view is that, in a broader perspective, the ultimate goal of studies investigating structure-function relationships in biological tissues should be to implement the gained knowledge into strategies that would lead to tissue-engineered replicates of the subject tissue. This is further encouraged in the case of AV, as none of the current

prosthetic or bioprosthetic valves are reliable long-term alternatives to the dysfunctional native valve.

The current paradigms adopted in tissue engineering of the AV mainly include the use of decellularized allogeneic or xenogeneic valve matrices, followed by seeding and repopulating with endothelial and interstitial cells [193,194]. This would create a non-thrombogenic surface for the valve matrix, and enables the remodelling of the ECM during the valve's function *in vivo*. However, a major drawback of this approach is the insufficient attachment of the cells to the matrix, particularly in the dynamic loading environment which the AV faces *in vivo* [193]. A better approach, in my view, is to seed the cells into a scaffold made of suitable biomaterials, and create the optimum biological and mechanical environment for the complex in a bioreactor, to stimulate ECM biosynthesis and a viable replacement valve.

In this regard, I propose a cell-mediated tissue engineering strategy that includes three stages: (i) design of appropriate choice of scaffolds for the AVICs to be seeded on; (ii) *in vitro* tissue formation, by creating the native metabolic and mechanical environment for the seeded cells on the scaffold inside a bioreactor as a control; seeding endothelial cells to the construct to creat a non-thrombogenic sheath on the valve leaflets; and (iii) *in vivo* animal models to check the viability and functionality of the produced tissue. A breakdown of each stage, with details of the processes that may be included in each stage, is described in the diagram in the following page. It must also be acknowledged that this approach is a highly multi-disciplinary research area, requiring much broader time horizons to be implemented and achieving its objectives, compared to the other two recommended developments in this section.

This strategy is in line with the principles of a paradigm known as 'Functional Tissue Engineering' (FTE), addressed by the United States National Committee on Biomechanics (USNCB). The general principles of FTE are [195,196]:

1) Understanding the biomechanical properties of native tissues.
2) Prioritisation of specific biomechanical properties of the native tissue.
3) The use of physical factors to enhance tissue generation and regeneration.
4) Investigation of the effects of mechanical factors on tissue repair.
5) Measurement of *in vivo* stresses and strains in native valve.

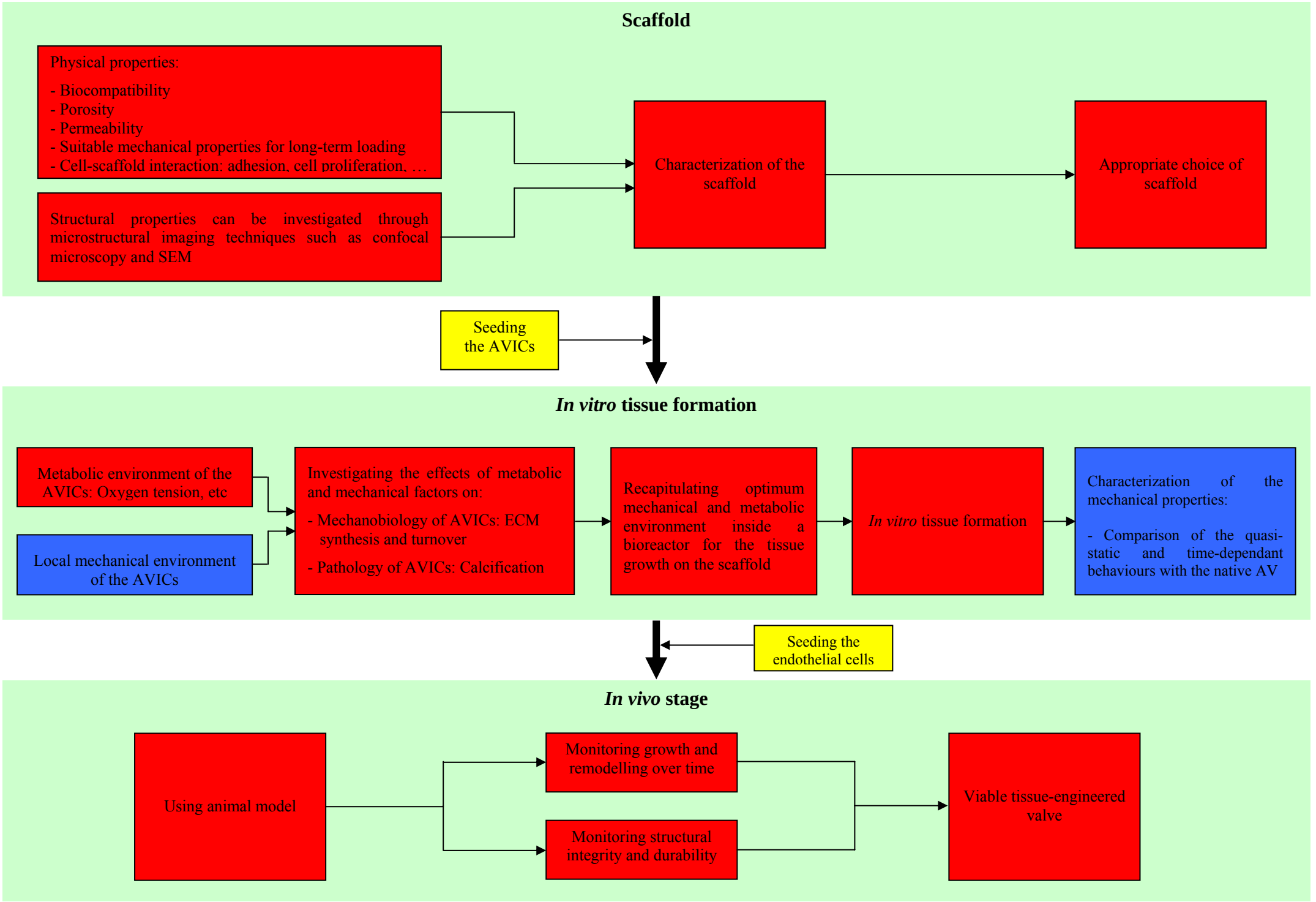
Scaffold
Physical properties:
- Biocompatibility
- Porosity
- Permeability
- Suitable mechanical properties for long-term loading
- Cell-scaffold interaction: adhesion, cell proliferation, …
Structural properties can be investigated through microstructural imaging techniques such as confocal microscopy and SEM
Characterization of the scaffold
Appropriate choice of scaffold
Seeding the AVICs
In vitro tissue formation
Metabolic environment of the AVICs: Oxygen tension, etc
Local mechanical environment of the AVICs
Investigating the effects of metabolic and mechanical factors on:
- Mechanobiology of AVICs: ECM synthesis and turnover
- Pathology of AVICs: Calcification
Recapitulating optimum mechanical and metabolic environment inside a bioreactor for the tissue growth on the scaffold
In vitro tissue formation
Characterization of the mechanical properties:
- Comparison of the quasi-static and time-dependant behaviours with the native AV
Seeding the endothelial cells
In vivo stage
Using animal model
Monitoring growth and remodelling over time
Monitoring structural integrity and durability
Viable tissue-engineered valve

The proposed strategy here encompasses the FTE specifications, incorporated in different stages of the strategy as illustrated in the graph; however it also provides more specific details for each stage of the strategy. The 1st, 2nd and 3rd principles are addressed in the *in vitro* tissue formation stage, while the 4th principle is incorporated into the *in vivo* stage. The 5th principle provides the data for benchmarking the properties of the obtained tissue with respect to the native tissue, as indicated in the blue box in the *in vitro* tissue formation stage. The blue boxes in the diagram indicate the data that can be elucidated from this study through the experimental and modelling results, or by incorporating the developed analytical models into the computational finite element models, as described in §11.3.1. The red boxes indicate the scope of the work needed to be done to achieve the goals of this strategy.

Appendices

Appendix A

Characteristic decay length based on Saint-Venant's principle

Amongst the different descriptions of the Saint-Venant's principal, a well accepted representation is described by Love as [125]: "According to this principal, the strains that are produced in a body by the application, to a small part of its surface, of a system of forces statically equivalent to zero force and zero couple, are of negligible magnitude at distances which are large compared with the linear dimensions of the part". This distance, known as the characteristic decay length, is the length along a test specimen at which gripping effects gradually decay and become negligible.

For a general case of 2D elasticity, it has been shown that the exponential decay in strain energy is of the form [128]:

$$E(x) \le 2E(0)e^{-\frac{2kx}{b}} \tag{A1}$$

where $E(x)$ is the stored elastic strain energy beyond the distance x from the loaded end, $E(0)$ is the total stored energy upon deformation, k is the *universal constant* and is equal to 1.4, and b is the maximum dimension of the cross-sectional area. Employing the mean value theorem for biharmonic functions, the stress will also decay exponentially in the form [128]:

$$\sigma(x,y) \le 5\sqrt{\frac{2}{\pi}}\frac{\sqrt{E(0)}}{\delta}e^{-\frac{2kx}{b}} \tag{A2}$$

where δ is the distance between point (x,y) from the loading boundary.

Since biological soft tissues are generally anisotropic, the results obtained by Knowles (1966) [128] must be expanded for the case of anisotropic elasticity. The stress-strain relationships for an anisotropic solid with one plane of elastic symmetry (e.g. the 1,2 plane) are given as [138]:

$$\begin{cases} \varepsilon_{11} = E_{11}\sigma_{11} + E_{12}\sigma_{22} + E_{13}\sigma_{33} + E_{16}\sigma_{12} \\ \varepsilon_{22} = E_{21}\sigma_{11} + E_{22}\sigma_{22} + E_{23}\sigma_{33} + E_{26}\sigma_{12} \\ \varepsilon_{33} = E_{31}\sigma_{11} + E_{32}\sigma_{22} + E_{33}\sigma_{33} + E_{36}\sigma_{12} \\ \varepsilon_{23} = \frac{1}{2}\left(E_{44}\sigma_{23} + E_{45}\sigma_{31}\right) \\ \varepsilon_{31} = \frac{1}{2}\left(E_{54}\sigma_{23} + E_{55}\sigma_{31}\right) \\ \varepsilon_{12} = \frac{1}{2}\left(E_{61}\sigma_{11} + E_{62}\sigma_{22} + E_{63}\sigma_{33} + E_{66}\sigma_{12}\right) \end{cases} \tag{A3}$$

where E_{ij}, ε_{ij} and σ_{ij} are the elastic moduli, strain and stress components respectively. In a plane deformation, the non-zero strain components of the equation (A3) will be:

$$\begin{cases} \varepsilon_{11} = \alpha_{11}\sigma_{11} + \alpha_{12}\sigma_{22} + \alpha_{16}\sigma_{12} \\ \varepsilon_{22} = \alpha_{21}\sigma_{11} + \alpha_{22}\sigma_{22} + \alpha_{26}\sigma_{12} \\ \varepsilon_{12} = \frac{1}{2}\left(\alpha_{61}\sigma_{11} + \alpha_{62}\sigma_{22} + \alpha_{66}\sigma_{12}\right) \end{cases} \tag{A4}$$

where:

$$\alpha_{ij} = E_{ij} - \frac{E_{i3}E_{j3}}{E_{33}}, \quad i, j = 1, 2, 6 \tag{A5}$$

The Airy stress function, φ, is by definition related to the Cauchy stress and strain tensor as [138]:

$$\sigma_{ij} = \beta_{ij}\frac{\partial^2\varphi}{\partial x_i \partial x_j} \tag{A6}$$

where β_{ij} is the two-dimensional alternator that: $\beta_{11} = \beta_{22} = 0$, $\beta_{12} = -\beta_{21} = 1$.

In the absence of body force:

$$\nabla^2(\sigma_{11} + \sigma_{22}) = 0 \ \therefore \ \nabla^4\varphi = 0 \tag{A7}$$

Therefore, using the equation (A4), the above equation leads to a fourth order differential equation of the form:

$$\alpha_{11}\varphi_{,2222} + \alpha_{22}\varphi_{,1111} + \left(2\alpha_{12} + \alpha_{66}\right)\varphi_{,1122} - 2\alpha_{16}\varphi_{,1222} - 2\alpha_{26}\varphi_{,1112} = 0 \tag{A8}$$

where the operator (,) denotes the partial differential operator.

The total strain energy for a plane deformation in anisotropic materials is given by:

$$E_{total} = \iint W dA \tag{A9}$$

where W is the strain energy density function, and in an elastic deformation is given by [100]:

$$W \equiv \frac{1}{2} E\varepsilon^2 \tag{A10}$$

which for an anisotropic elastic material, using equation (A4) will be of the form:

$$W = \frac{1}{2}\left(\alpha_{11}\sigma_{11}^2 + \alpha_{22}\sigma_{22}^2 + \alpha_{66}\sigma_{12}^2 + 2\alpha_{12}\sigma_{11}\sigma_{22} + 2\alpha_{16}\sigma_{11}\sigma_{12} + 2\alpha_{26}\sigma_{22}\sigma_{12}\right) \tag{A11}$$

or in a matrix format:

$$W = \frac{1}{2} C^T B C \tag{A12}$$

where:

$$C = \begin{bmatrix} \sigma_{11} \\ \sigma_{22} \\ \dfrac{\sigma_{12}}{\sqrt{2}} \end{bmatrix} \tag{A13}$$

and:

$$B = \begin{bmatrix} \alpha_{11} & \alpha_{12} & \dfrac{\alpha_{16}}{\sqrt{2}} \\ \alpha_{12} & \alpha_{22} & \dfrac{\alpha_{26}}{\sqrt{2}} \\ \dfrac{\alpha_{16}}{\sqrt{2}} & \dfrac{\alpha_{26}}{\sqrt{2}} & \dfrac{\alpha_{66}}{\sqrt{2}} \end{bmatrix} \tag{A14}$$

It has been shown that the strain energy described by equations (A10) and (A11), for the stress field characterised in equation (A8) will decay exponentially following the form [129]:

$$E(x) \le 2E(0)e^{-2kx} \tag{A15}$$

and subsequently the stress decay would be [129]:

$$\sigma \le Ke^{-kx} \tag{A16}$$

where K is a constant proportional to $\sigma(0)$, and $1/k$ is the characteristic decay length.

Now, k must be calculated. The plane deformation of an anisotropic material is given by equation (A3) and (A4). However, by further assuming that the material is transversely isotropic about one axis, say axis 3, the deformation equations reduce to [138]:

$$\begin{cases} \varepsilon_{ij} = \dfrac{1+\upsilon'}{E'}\sigma_{ij} - \left(\dfrac{\upsilon'}{E'}\sigma_{nn} + \dfrac{\upsilon}{E}\sigma_{33}\right)\delta_{ij} \ , \ i,j = 1,2 \\ \varepsilon_{33} = \dfrac{1}{E}\sigma_{33} - \dfrac{\upsilon}{E}\sigma_{ii} \ , \ \varepsilon_{3i} = \dfrac{1}{2G}\sigma_{3i} \end{cases} \tag{A17}$$

where δ_{ij} is the Kronecker delta. For a plane deformation using the Airy stress function:

$$P\varphi_{,1111} + Q\varphi_{,1133} + R\varphi_{,3333} = 0 \tag{A18}$$

where:

$$P = \frac{1}{E}\left(1 - \upsilon^2\frac{E'}{E}\right),\ Q = \frac{1}{G} - \frac{2\upsilon}{E}(1+\upsilon'),\ R = \frac{1-(\upsilon')^2}{E'} \tag{A19}$$

For a fibre-reinforced composite material, with the constraint of incompressibility in direction 3, it has been shown that the following assumptions are valid [139]:

$$\frac{G}{E} << 1,\ \frac{E'}{E} << 1,\ 1-\upsilon' << 1 \tag{A20}$$

Thus the coefficients in equation (A19) will become:

$$P \cong \frac{1}{E},\ Q \cong \frac{1}{G} \tag{A21}$$

For a deformation described by equation (A18), with material coefficients defined in (A21) and (A19) (P, Q, and R), and boundary conditions given by (A17) which ensures the constraint of anisotropy with transversely isotropic axis, k (the inverse of characteristics decay length) can be derived by [129]:

$$k^2 = \frac{\pi^2}{2b^2} \cdot \frac{\lambda}{R} s \tag{A22}$$

where λ is the minimum eigenvalue of the equivalent matrix to B in equation (A14) under the assumptions given in (A20) which would be:

$$\begin{bmatrix} \frac{1}{E} & 0 & 0 \\ 0 & \frac{1-(\upsilon')^2}{E'} & 0 \\ 0 & 0 & \frac{1}{2G} \end{bmatrix} \tag{A23}$$

and s can be given by [129]:

$$s = \sqrt{\left(\left(\frac{E'}{2G(1-(\upsilon')^2}\right)^2 + 1\right)} - \frac{E'}{2G(1-(\upsilon')^2)} \cong O\left((1-(\upsilon')^2)\frac{2G}{E'}\right) \tag{A24}$$

From the definition of λ described earlier above:

$$\frac{\lambda}{R} = \min\left(\left(\frac{E'}{E(1-(\upsilon')^2}\right), 1, \frac{G}{2E}\right) \tag{A25}$$

Thus:

$$\frac{\lambda}{R} = O\left(\frac{E'}{E(1-(\upsilon')^2}\right) \tag{A26}$$

Therefore, considering (A26), (A24) and (A22):

$$k = O\left(\frac{(G/E)^{0.5}}{b}\right) \tag{A27}$$

Thus, finally, the characteristic decay length would be:

$$l = 1/k = O\left((E/G)^{0.5} b\right) \tag{A28}$$

Appendix B

3D viscolasticity for a Kelvin-Voigt solid under uniaxial deformation

In a 3D Kelvin-Voigt viscoelastic solid under uniaxial stress [140]:

$$\begin{cases} E_i\varepsilon_i + \eta_i\dot{\varepsilon}_i = \sigma_i \\ \\ E_i\gamma_{ij} + \eta_i\dot{\gamma}_{ij} = 0 \end{cases}, \quad i,j = 1,2,3 \tag{B1}$$

where E and η are the elastic and viscous damping moduli respectively, ε and σ denote strain and stress, γ is the shear strain, and $\dot{\varepsilon}$ and $\dot{\gamma}$ are the time derivatives of the normal and shear strains, respectively. 1, 2 and 3 are the principal directions (Figure 5.7).

The amount of shear strain in the 1-3 plane due to elongation in direction 1 (the loading direction) can be determined by $E_1\gamma_{13} + \eta_1\dot{\gamma}_{13} = 0$; where E_1 and η_1 are the elastic modulus and the viscous damping coefficients in either the circumferential or radial direction, as relevant. The values for η_1 and E_1 at different strain levels, have been evaluated and calculated by incorporating experimental data and a Kelvin-Voigt model in Chapter 3.

From Mohr's circle [141]:

$$\gamma_{13} = 2\varepsilon_3 \tag{B2}$$

For the strain in direction 3, ε_3, due to the uniaxial engineering stress in direction 1, σ_1, one can write [142]:

$$\varepsilon_3 = -\upsilon\varepsilon_1 \tag{B3}$$

The time derivative of the above equation would be:

$$\dot{\varepsilon}_3 = -\upsilon\dot{\varepsilon}_1 \tag{B4}$$

and from equation (B2):

$$\dot{\gamma}_{13} = 2\dot{\varepsilon}_3 \tag{B5}$$

Substituting equation (B5) into (B4):

$$\dot{\gamma}_{13} = -2\upsilon\dot{\varepsilon}_1 \tag{B6}$$

Considering the AV tissue as incompressible (Chapter 3), one may substitute $\upsilon = 0.5$ into equation (B6):

$$\dot{\gamma}_{13} = -\dot{\varepsilon}_1 \tag{B7}$$

Thus, from equation (B1):

$$\gamma_{13} = \frac{\eta_1}{E_1}\dot{\varepsilon}_1 \tag{B8}$$

Appendix C

The 2nd Piola-Kirchhoff stress in a fibrous soft tissue

The strain energy density function for a fibrous tissue with a population of randomly distributed collagen fibres can be written as [156,160]:

$$W = \int R(\theta) w_{fibre} d\theta \tag{C1}$$

where $R(\theta)$ is the statistical distribution function of the angular distribution of the collagen fibres, with θ being the Eulerian angle describing the direction of the oriented fibres, and w_{fibre} the fibre strain energy function. For a planar 2 dimensional tissue continuum, $R(\theta)$ must be symmetric in the range of $-\frac{\pi}{2} \le \theta \le \frac{\pi}{2}$, subjected to the normalization constraint [156]:

$$\int_{-\frac{\pi}{2}}^{\frac{\pi}{2}} R(\theta) = 1 \tag{C2}$$

Thus equation (C1) becomes [156,160]:

$$W = \int_{-\frac{\pi}{2}}^{\frac{\pi}{2}} R(\theta) w_{fibre} d\theta \tag{C3}$$

By definition, the 2nd Piola-Kirchhoff stress tensor, S, is [122]:

$$S = \frac{\partial W}{\partial \varepsilon} \tag{C4}$$

where ε is the Green strain tensor. Substituting equation (C3) in (C4) gives:

$$S = \int_{-\frac{\pi}{2}}^{\frac{\pi}{2}} R(\theta) \frac{\partial w_{fibre}}{\partial \varepsilon} d\theta \tag{C5}$$

Applying the chain rule in differentiation to equation (C5) leads to:

$$S = \int_{-\frac{\pi}{2}}^{\frac{\pi}{2}} R(\theta) \frac{\partial w_{fibre}}{\partial \varepsilon_{fibre}} \cdot \frac{\partial \varepsilon_{fibre}}{\partial \varepsilon} d\theta \tag{C6}$$

where $\frac{\partial w_{fibre}}{\partial \varepsilon_{fibre}}$ itself would be the 2nd Piola-Kirchhoff stress of the fibre, and $\frac{\partial \varepsilon_{fibre}}{\partial \varepsilon}$ would be given by $\left[\vec{N} \otimes \vec{N}\right]$, where $\vec{N}$ is the unit vector representing the direction of the fibre as: $\vec{N} = \cos\theta\ \hat{i} + \sin\theta\ \hat{j}$ [122].

$$S = \int_{-\frac{\pi}{2}}^{\frac{\pi}{2}} R(\theta) S_{fibre} [\vec{N} \otimes \vec{N}] d\theta \tag{C7}$$

Note that $\otimes$ is the external multiplication operator such that $\left[\vec{N} \otimes \vec{N}\right]_{ij} = \vec{N}_i \vec{N}_j$ [122]. Thus, in component format:

$$\begin{cases} S_{11} = \int_{-\frac{\pi}{2}}^{\frac{\pi}{2}} R(\theta) S_{fibre} \cos^2\theta\ d\theta \\ S_{22} = \int_{-\frac{\pi}{2}}^{\frac{\pi}{2}} R(\theta) S_{fibre} \sin^2\theta\ d\theta \\ S_{12} = S_{21} = \int_{-\frac{\pi}{2}}^{\frac{\pi}{2}} R(\theta) S_{fibre} \cos\theta \sin\theta\ d\theta \end{cases} \tag{C8}$$

Appendix D

True strain of a wavy fibre

Fibre true strain, ε_t, is related to the stretch ratio λ_t by:

$$\varepsilon_t = \frac{\lambda_t^2 - 1}{2} \tag{D1}$$

where:

$$\lambda_t = \frac{L}{L_s} \tag{D2}$$

L is the current length of the fibre, and L_s is the straight length of the fibre. Equation (D2) can be re-arranged by the chain rule as:

$$\lambda_t = \frac{L}{L_s} = \frac{L}{L_0} \cdot \frac{L_0}{L_s} = \frac{\lambda_{fibre}}{\lambda_s} \tag{D3}$$

Substituting (D3) into (D1):

$$\varepsilon_t = \frac{\lambda_{fibre}^2 - \lambda_s^2}{2\lambda_s^2} \tag{D4}$$

and by definition:

$$\varepsilon_{fibre} = \frac{\lambda_{fibre}^2 - 1}{2}\ ,\ \varepsilon_s = \frac{\lambda_s^2 - 1}{2} \tag{D5}$$

Substituting λ_{fibre} and λ_s from (D5) into (D4) one gets:

$$\varepsilon_t = \frac{\varepsilon_{fibre} - \varepsilon_s}{1 + 2\varepsilon_s} \tag{D6}$$

Appendix E

Deriving the Gaussian model from the Taylor series expansion of the Langevin model

The Gaussian probability density has the form [173]:

$$p(\lambda) = p_0 \exp\left(-\frac{3}{2}\lambda^2\right) \tag{E1}$$

where p_0 is a constant. Inserting equation (E1) into equation (8.4):

$$\psi_c = \frac{3}{2}kT\lambda^2 + \psi_0 \tag{E2}$$

The parameters in the above equation are the same as those defined in equation (8.7). The force acting on a single chain can be calculated in light of equation (8.5):

$$F_c = 3kT\lambda \tag{E3}$$

Now, following the procedure described through equations (8.11) to (8.19):

$$\Psi_{elast} = \frac{3}{2}nkT\frac{\overline{\lambda_1}^2}{2} + \psi_0 \tag{E4}$$

and:

$$F_1 = \frac{3}{2}nkT\overline{\lambda_1} \tag{E5}$$

which assumes a linear relationship between force and stretch.

The Taylor series expansion of a function around an arbitrary point a is:

$$\sum_{n=0}^{\infty}\frac{f^{(n)}(a)}{n!}\cdot(x-a)^n \tag{E6}$$

Inserting the Langevin model given in equation (8.19) into (E6), its Taylor expansion around $a = 0$ would be:

$$\frac{3}{2}nkT\overline{\lambda_1} + nkT\overline{\lambda_1}^3 + \ldots \tag{E7}$$

For small deformations $\bar{\lambda}_1 >> \bar{\lambda}_1^n$, thus the power terms bear negligible values compared to the first term of the expansion in (E7), and can be eliminated. The first term of the above expansion is equal to the force in Gaussian model given in (E5).

Appendix F

Relationship between the deformation of an elastin chain and the macroscopic deformation of the tissue in 3D

Consider a single chain in a 3D cube element, shown in Figure F1. The unstrained end to end distance of the chain, r_0, is then $r_0 = a_0\sqrt{3}$. After deformation, the end-to-end chain length vector will be given by $\vec{r} = a_0(\bar{\lambda}_1\hat{i} + \bar{\lambda}_2\hat{j} + \bar{\lambda}_3\hat{k})$, where $\bar{\lambda}_1$, $\bar{\lambda}_2$ and $\bar{\lambda}_3$ are the principal macro stretches, i, j and k are the unit vectors, in the x, y and z directions respectively. Hence, the magnitude of $\vec{r}$ is:

$$r = a_0\sqrt{\bar{\lambda}_1^2 + \bar{\lambda}_2^2 + \bar{\lambda}_3^2} \tag{F1}$$

Substituting this into equation (8.1):

$$\lambda = \sqrt{\frac{\bar{I}_1}{3}} \tag{F2}$$

where $\bar{I}_1$ is the first principal invariant of the Cauchy-Green deformation tensor in the macro level principal reference system and is given by $\bar{I}_1 = \bar{\lambda}_1^2 + \bar{\lambda}_2^2 + \bar{\lambda}_3^2$.

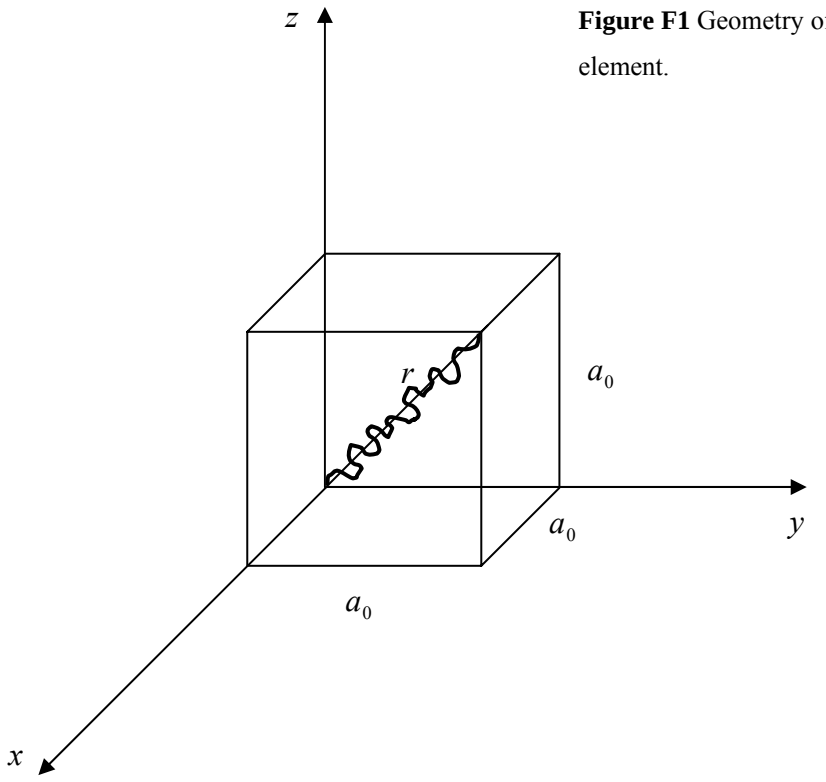

Figure F1 Geometry of a single chain in a 3D cube element.

Appendix G

Technical drawings of the biaxial loading rig

Bibliography

1- Stella, J. A., Sacks, M. S. (2007) On the biaxial mechanical properties of the layers of the aortic valve leaflet, J. Biomech. Eng., 129, 757-766.

2- Misfeld, M., Sievers, H. H. (2007) Heart valve macro- and microstructure, Phil. Trans. R. Soc. B, 362, 1421-1436.

3- Sachs, M. S., Yoganathan, A. P. (2007) Heart valve function: a biomechanical perspective, Phil. Trans. R. Soc. B, 362, 1369-1391.

4- Guyton, A. C., Hall, J. E. (2001) Textbook of medical physiology, 10th edition, Saunders, USA, pp: 96-106.

5- Sauren, A. A. H. J., Van Hout, M. C., Van Steenhoven, A. A., Veldpaus, F. E., Janssen, J. D. (1983) The mechanical properties of porcine aortic valve tissues, J. Biomech., 16, 327-337.

6- Mavrilas, D., Missirlis, Y. (1991) An approach to the optimization of preparation of bioprosthetic heart valves, J. Biomech., 24, 331-339.

7- Thubrikar, M., Piepgrass, W. C., Bosher, L. P., Nolan, S. P. (1980) The elastic modulus of canine aortic valve leaflets in vivo and in vitro, Circ. Res., 47, 792-800.

8- Thubrikar, M., Aouad, J., Nolan, S. P. (1986) Comparison of the in-vivo and in-vitro mechanical properties of aortic valve leaflets, J. Thorac. Cardiovasc. Surg., 92, 29-36.

9- Merryman, W. D., Bieniek, P. D., Guilak, F., Sacks, M. S. (2009) Viscoelastic properties of the aortic valve interstitial cell, J. Biomech. Eng., 131, 041005.

10- Butcher, J. T., Mahler, G. J., Hockaday, L. A. (2011) Aortic valve disease and treatment: The need for naturally engineered solutions, Adv. Drug Deliv. Rev., doi: 10.1016/j.addr.2011.01.008.

11- Hwai Yap, C., Kim, H-S, Balachandran, K., Weiler, M., Haj-Ali, R., Yoganathan, A. P. (2010) Dynamic deformation characteristics of porcine aortic valve leaflet under normal and hypertensive conditions, Am. J. Physiol. Heart Circ. Physiol., 298, H395-H405.

12- Schoen, F. J. (1997) Aortic valve structure-function correlations: role of elastic fibers no longer a stretch of the imagination, J. Heart Valve Dis., 6, 1-6.

13- Schoen, F. J., Levy, R. J. (1999) Tissue heart valves: current challenges and future research perspectives, J. Biomed. Mater. Res., 47, 439-465.

14- Balguid, A., Rubbens, M. P., Mol, A., Bank, R. A., Bogers, A. J. J. C., Van Kats, J. P., De Mol, B. A. J. M., Baaijens, F. P. T., Bouten, C. V. C. (2007) The role of collagen cross-links in biomechanical behaviour of human aortic heart valve leaflets - relevance for tissue engineering, Tissue Eng., 13, 1501-1511.

15- Mol, A., Bouten, C. V. C., Baaijens, F. P. T., Zünd, G., Turina, M. I., Hoestrup, S. P. (2004) Tissue engineering of semilunar heart valves: current status and future developments, J. Heart Valve Dis., 13, 272-280.

16- Vesely, I. (2005) Heart Valve Tissue Engineering, Circ. Res., 97, 743-755.

17- Brody, S., Pandit, A. (2004) Microarchitectural characterization of the aortic heart valve, in: Hasirci, N., Hasirci, V. (Eds.), Biomaterials: from molecules to engineered tissues, pp: 167-186, Kluwer Academic/Plenum Publishers.

18- Talman, E. A., Boughner, D. R. (1996) Internal shear properties of fresh porcine aortic valve cusps: Implications for normal valve function, J. Heart Valve Dis., 5, 152-159.

19- Scott, M., Vesely, I. (1995) Aortic valve cusp microstructure: the role of elastin, Ann. Thorac. Surg., 60, S391-S394.

20- Vesely, I. (1998) The role of elastin in aortic valve mechanics, J. Biomech., 31, 115-123.

21- Mulholland, D. L., Gotlieb, A. I. (1996) Cell biology of valvular interstitial cells, Can. J. Cardiol., 12, 231-236.

22- Taylor, P. M., Batten, P., Brand, N. J., Thomas, P. S., Yacoub, M. H. (2003) The cardiac valve interstitial cell, Int. J. Biochem. Cell Bio., 35, 113-118.

23- Huang, H. Y. S., Liao, J., Sacks, M. S. (2007) In-situ deformation of the aortic valve interstitial cell nucleus under diastolic loading, J. Biomech. Eng., 129, 880-889.

24- Chester, A. H., Taylor, P. M. (2007) Molecular and functional characteristics of heart-valve interstitial cells, Phil. Trans. R. Soc. B, 362, 1437-1443.

25- Rabkin, E., Hoerstrup, S. P., Aikawa, M., Mayer Jr., J. E., Schoen, F. J. (2002) Evolution of cell phenotype and extracellular matrix in tissue-engineered heart valves during in-vitro maturation and in-vivo remodelling, J. Heart Valve Dis., 11, 308-314.

26- Butcher, J.T., Nerem, R. M. (2004) Porcine aortic valve interstitial cells in three-dimensional culture: comparison of phenotype with aortic smooth muscle cells, J. Heart Valve Dis., 13, 478-486.

27- Butcher, J. T., Penrod, A. M., García, A. J., Nerem, R. M. (2004) Unique morphology and focal adhesion development of valvular endothelial cells in static and fluid flow environments, Arterioscler Thromb. Vasc. Biol., 24, 1429-1434.

28- Butcher, J. T., Simmons, C. A., Warnock, J. N. (2008) Review: mechanobiology of the aortic heart valve, J. Heart Valve Dis., 17, 62-73.

29- Leask, R. L., Jain, N., Butany, J. (2003) Endothelium and valvular diseases of the heart, Microsc. Res. Tech., 60, 129-137.

30- Lloyd-Jones, D., Adams, R. J., Brown, T. M., Carnethon, M., Dai, S., De Simone, G., Ferguson, T. B., Ford, E., Furie, K., Gillespie, C., Go, A., Greenlund, K., Haase, N., Hailpern, S., Ho, P. M., Howard, V., Kissela, B., Kittner, S., Lackland, D., Lisabeth, L., Marelli, A., McDermott, M. M., Meigs, J., Mozaffarian, D., Mussolino, M., Nichol, G., Roger, V., Rosamond, W., Sacco, R., Sorlie, P., Stafford, R., Thom, T., Wasserthiel-Smoller, S., Wong, N. D., Wylie-Rosett, J. (2010) Heart disease and stroke statistics 2010 update: A report from the American Heart Association, Circ., 121, e46-e215.

31- Yacoub, M. H., Cohn, L. H. (2004) Novel approaches to cardiac valve repair: from structure to function: part I, Circ., 109, 942-950.

32- Sacks, M. S., Merryman, W. D., Schmidt, D. E. (2009) On the biomechanics of heart valve function, J. Biomech., 42, 1804-1824.

33- Merryman, W. D. (2010) Mechano-potential etiologies of aortic valve disease, J. Biomech., 43, 87-92.

34- Schoen, F. J., Levy, R. J. (2005) Calcification of tissue heart valve substitute: progress toward understanding and prevention, Ann. Thorac. Surg., 79, 1072-1080.

35- De Hart, J. (2002) Fluid-structure interaction in the aortic heart valve, Ph.D. thesis, Eindhoven University of Technology, Eindhoven, Netherlands.

36- Jamieson, W. R. (1993) Modern cardiac valve devices-bioprostheses and mechanical prostheses: state of the art, J. Cardiac Surg., 8, 89-98.

37- Schoen, F. J., Levy, R. J., Piehler, H. R. (1992) Pathological considerations in replacement cardiac valves, Cardiovasc. Pathol., 1, 29-52.

38- Schoen, F. J. (2005) Cardiac valves and valvular pathology: update on function, disease, repair, and replacement, Cardiovasc. Pathol., 14, 189-194.

39- Thubrikar, M., Skinner, J. R., Aouad, J., Finkelmeier, B. A., Nolan, S. P. (1982) Analysis of the design and dynamics of aortic bioprostheses in vivo, J. Thorac. Cardiovasc. Surg., 84, 282-290.

40- Smith, D. B., Sacks, M. S., Vorp, D. A., Thornton, M. (2000) Surface geometric analysis of anatomic structures using biquintic finite element interpolation, Ann. Biomed. Eng., 28, 598-611.

41- Yoganathan, A. P. (1988) Fluid mechanics of aortic stenosis, Eur. Heart J., 9, 13-17.

42- Kunzelman, K. S., Cochran, R. P., Chuong, C., Ring, W. S., Verrier, E. D., Eberhart, R. D. (1993) Finite element analysis of the mitral valve. J. Heart Valve Dis., 2, 326-340.

43- Kunzelman, K. S., Cochran, R. P., Verrier, E. D., Eberhart, R. C. (1994) Anatomic basis for mitral valve modelling, J. Heart Valve Dis., 3, 491-496.

44- Kunzelman, K. S., Reimink, M. S., Cochran, R. P. (1998) Flexible versus rigid ring annuloplasty for mitral valve annular dilatation: a finite element model, J. Heart Valve Dis., 7, 108-116.

45- Kim, H., Lu, J., Sacks, M. S., Chandran, K. B. (2006) Dynamic simulation pericardial bioprosthetic heart valve function. J. Biomech. Eng., 128, 717-724.

46- De Hart, J., Peters, G. W., Schreurs, P. J., Baaijens, F. P. (2003) A three-dimensional computational analysis of fluid-structure interaction in the aortic valve, J. Biomech., 36, 103-112.

47- Boerboom, R. A., Driessen, N. J. B., Bouten, C. V. C., Huyghe, J. M., Baaijens, F. P. T. (2003) Finite element model of mechanically induced collagen fiber synthesis and degradation in the aortic valve, Annals Biomed. Eng., 31, 1040-1053.

48- Driessen, N. J. B., Bouten, C. V. C., Baaijens, F. P. T. (2005) Improved prediction of the collagen fiber architecture in the aortic heart valve, J. Biomech. Eng., 127, 329-336.

49- Balguid, A., Driessen, N. J. B., Mol, A., Schmitz, J. P. J., Verheyen, F., Bouten, C. V. C., Baaijens, F. P. T. (2008) Stress related collagen ultrastructure in human aortic valves-implications for tissue engineering, J. Biomech., 41, 2612-2617.

50- De Hart, J., Peters, G. W., Schreurs, P. J., Baaijens, F. P. (2000) A two-dimensional fluid- structure interaction model of the aortic valve. J. Biomech., 33, 1079-1088.

51- Grande, K. J., Cochran, R. P., Reinhall, P. G., Kunzelman, K. S. (1998) Stress variations in the human aortic root and valve: the role of anatomic asymmetry, Ann. Biomed. Eng., 26, 534-545.

52- Clark, R. E. (1973) Stress-strain characteristics of fresh and frozen human aortic and mitral leaflets and chordae tendineae: Implications for clinical use, J. Thorac. Cardiovasc. Surg., 66, 202-208.

53- Missirlis, Y. F., Chong, M. (1978) Aortic valve mechanics - Part I: material properties of natural aortic valves, J. Bioeng., 2, 287-300.

54- Chong, M., Missirlis, Y. F. (1978) Aortic valve mechanics part II: a stress analysis of the porcine aortic valve leaflets in diastole, Biomat. Med. Dev. Art. Org., 6, 225-244.

55- Rousseau, E. P. M., Sauren, A. A. H. J., Van Hout, M. C., Van Steenhoven, A. A. (1983) Elastic and viscoelastic material behaviour of fresh and glutaraldehyde-treated porcine aortic valve tissue, J. Biomech, 16, 339-348.

56- Sauren, A. A. H. J., Kuijpers, W., Van Steenhoven, A. A., Veldpaus, F. E. (1980) Aortic valve histology and its relation with mechanics-preliminary report, J. Biomech., 13, 97-104.

57- Broom, N. D. (1977) The stress/strain and fatigue behaviour of glutaraldehyde preserved heart-valve tissue, J. Biomech., 10, 707-724.

58- Brewer, R. J., Mentzer, R. M., Deck, J. D., Ritter, R. C., Trefil, J. S., Nolan, S. P. (1977) An in vivo study of the dimensional changes of the aortic valve leaflets during the cardiac cycle, J. Thorac. Cardiovasc. Surg., 74, 645-650.

59- Kasyanov, V. A., Purinya, B. A., Ose, V. P. (1985) Structure and mechanical properties of the human aortic valve, Mech. Composite Mat., 20, 637-647.

60- Broom, N. D., Thomson, F. J. (1979) Influence of fixation conditions on the performance of glutaraldehyde-treated porcine aortic valve: towards a more scientific basis, Thorax, 34, 166-176.

61- Lee, T. C., Midura, R. J., Hascall, V. C., Vesely, I. (2001) The effect of elastin damage on the mechanics of the aortic valve, J. Biomech., 34, 203-210.

62- Christie, G. W., Barratt-Boyes, B. G. (1995) Mechanical properties of porcine pulmonary valve leaflets: How do they differ from aortic leaflets?, Ann. Thorac. Surg., 60, S195-S199.

63- Christie, G. W., Barratt-Boyes, B. G. (1995) Age-dependent changes in the radial stretch of human aortic valve leaflets determined by biaxial testing, Ann. Thorac. Surg., 60, S156-S159.

64- Christie, G. W., Barratt-Boyes, B. G. (1995) Biaxial mechanical properties of explanted aortic allograft leaflets, Ann. Thorac. Surg., 60, S160-S164.

65- Billiar, K. L., Sacks, M. S. (2000) Biaxial mechanical properties of the natural and glutaraldehyde treated aortic valve cusp - part I: experimental results, J. Biomech. Eng., 122, 23-30.

66- Billiar, K. L., Sacks, M. S. (2000) Biaxial mechanical properties of the natural and glutaraldehyde treated aortic valve cusp – part II: a structural constitutive model, J. Biomech. Eng., 122, 327-335.

67- Vesely, I., Lozon, A. (1993) Natural preload of aortic valve leaflet components during glutaraldehyde fixation: Effects on tissue mechanics, J. Biomech., 26, 121-131.

68- Pioletti, D. P., Rakotomanaana, L. R. (2000) On the independence of time and strain effects in the stress relaxation of ligaments and tendons, J. Biomech., 33, 1729-1732.

69- Stella, J. A., Liao, J., Sacks, M. S. (2007) Time dependent biaxial mechanical behaviour of the aortic heart valve leaflet, J. Biomech., 40, 3169-3177.

70- Thornton, G. M., Oliynyk, A., Frank, C. B., Shrive, N. G. (1997) Ligament creep cannot be predicted from stress relaxation at low stress: a biomechanical study of the rabbit medial collateral ligament, J. Orthop. Res., 15, 652-656.

71- Fung, Y. C. (1993) Biomechanics: Mechanical properties of living tissue, 2nd edition, Springer-Verlag New York Inc., New York.

72- Sauren, A. A. H. J., Rousseau, E. P. M. (1983) A concise sensitivity analysis of the quasi-linear viscoelastic model proposed by Fung, J. Biomech. Eng., 105, 92-95.

73- Carew, E. O., Garg, A., Barber, E., Vesely, I. (2004) Stress relaxation preconditioning of porcine aortic valves, Ann. Biomed. Eng., 32, 563-572.

74- Doehring, T. C., Carew, E. O., Vesely, I. (2004) The effect of strain rate on the viscoelastic response of aortic valve tissue: a direct-fit approach, Ann. Biomed. Eng., 32, 223-232.

75- Liao, J., Yang, L., Grashow, J., Sacks, M. S. (2007) The relation between collagen fibril kinematics and mechanical properties in the mitral valve anterior leaflet, J. Biomech. Eng., 129, 78-87.

76- Robinson, P. S., Tranquillo, R. T. (2009) Planar biaxial behavior of fibrin-based tissue-engineered heart valve leaflets, Tissue Eng. Part A, 15, 2763-2772.

77- Thubrikar, M., Piepgrass, W. C., Deck, J. D., Nolan, S. P. (1980) Stress of natural versus prosthetic aortic valve leaflets in vivo, Ann. Thorac. Surg., 30, 230-239.

78- Merryman, W. D., Huang, H. Y. S., Schoen, F. J., Sacks, M. S. (2006) The effects of cellular contraction on aortic valve leaflet flexural stiffness, J. Biomech., 39, 88-96.

79- Mirnajafi, A., Raymer, J. M., McClure, L. R., Sacks, M. S. (2006) The flexural rigidity of the aortic valve leaflet in the commissural region, J. Biomech., 39, 2966-2973.

80- Merryman, W. D., Youn, I., Lukoff, H. D., Krueger, P. M., Guilak, F., Hopkins, R. A., Sacks, M .S. (2006) Correlation between heart valve interstitial cell stiffness and transvalvular pressure: implications for collagen biosynthesis, Am. J. Physiol. Heart Circ. Physiol., 290, H224-H231.

81- Merryman, W. D., Liao, J., Parekh, A., Candiello, J. E., Lin, H., Sacks, M. S. (2007) Differences in tissue-remodeling potential of aortic and pulmonary heart valve interstitial cells, Tissue Eng., 13, 2281-2289.

82- Guilak, F., Ting-Beall, H. P., Baer, A. E., Trickey, W. R., Erickson, G. R., Setton, L. A. (1999) Viscoelastic properties of intervertebral disc cells. Identification of two biomechanically distinct cell populations, Spine, 24, 2475-2483.

83- Hochmuth, R. M. (2000) Micropipette aspiration of living cells, J. Biomech., 33, 15-22.

84- Rabkin-Aikawa, E., Farber, M., Aikawa, M., Schoen, F. J. (2004) Dynamic and reversible changes of interstitial cell phenotype during remodeling of cardiac valves, J. Heart Valve Dis., 13, 841-847.

85- Kershaw, J. D. B., Misfeld, M., Sievers, H-H., Yacoub, M. H., Chester, A. H. (2004) Specific regional and directional contractile responses of aortic cusp tissue. J. Heart Valve Dis., 13, 798-803.

86- Liu, A. C., Joag, V. R., Gotlieb, A. I. Gotlieb (2007) Review: the emerging role of valve interstitial cell phenotypes in regulating heart valve pathobiology, Am. J. Path., 171, 1407-1418.

87- Lim, K. O., Boughner, D. R. (1976) The low frequency dynamic viscoelastic properties of human aortic valve tissue, Circ. Res., 39, 209-214.

88- Anssari-Benam, A. (2010) Uniaxial mechanical behaviour of aortic valve leaflet in vitro, MPhil/PhD transfer report, Queen Mary, University of London, UK.

89- Screen, H. R. C., Lee, D. A., Bader, D. L., Shelton, J. C. (2003) Development of a technique to determine strains in tendons using the cell nuclei, Biorheo., 40, 361-368.

90- Screen, H. R. C., Lee, D. A., Bader, D. L., Shelton, J. C. (2004) An investigation into the effects of the hierarchical structure of tendon fascicles on micromechanical properties, Proc. Insts. Mech. Engrs. Part H: J Engineering in Medicine, 218, 109-119.

91- Screen, H. R. C., Bader, D. L., Lee, D. A., Shelton, J. C. (2004) Local strain measurements within tendons, Strain, 40, 157-163.

92- Jones, C. W., Smolinski, D., Keogh, A., Kirk, T. B., Zheng, M. H. (2005) Confocal laser scanning microscopy in orthopaedic research, Prog. Histochem. Cytochem., 40, 1-71.

93- Bader, D. L., Knight, M. M. (2008) Biomechanical analysis of structural deformation in living cells, Med. Biol. Eng. Comput., 46, 951-963.

94- Screen, H. R. C. (2003) The contribution of structural components to tendon mechanics, Ph.D. thesis, Queen Mary, University of London, London, UK.

95- Leeson-Dietrich, J., Boughner, D., Vesely, I. (1995) Porcine pulmonary and aortic valves: a comparison of their tensile viscoelastic properties at physiological strain rates, J. Heart Valve Dis., 4, 88-94.

96- Love, E. R. (1952) Linear superposition in visco-elasticity and theories of delayed effects, Austral. J. Phys., 9, 1-12.

97- Drapaca, C. S., Tenti, G., Rohlf, K., Sivaloganathan, S. (2006) A quasi-linear viscoelastic constitutive equation for the brain: Application to hydrocephalus, J. Elasticity, 85, 65-83.

98- Pioletti, D. P., Rakotomanana, L. R., Benvenuti, J. F., Leyvraz, P. F. (1998) Viscoelastic constitutive law in large deformations: application to human knee ligaments and tendons, J. Biomech., 31, 753-757.

99- Li, J., Luo, X. Y., Kuang, Z. B. (2001) A nonlinear anisotropic model for porcine aortic heart valves, J. Biomech., 34, 1279-1289.

100- Anssari-Benam, A., Viola, G., Korakianitis, T. (2010) Thermodynamic effects of linear dissipative small deformations, J. Therm. Anal. Calorim., 100, 941-947.

101- Teng, Z., Tang, D., Zheng, J., Woodard, P. K., Hoffman, A. H. (2009) An experimental study on the ultimate strength of the adventitia and media of human atherosclerotic carotid arteries in circumferential and axial directions, J. Biomech., 42, 2535-2539.

102- Ratcliffe, A., Mow, V. C. (1996) Articular cartilage In: Comper, W. D. (ed) Extracellular matrix, Vol.1, pp. 268-272. Harwood academic publishers, Amsterdam.

103- Baumgaertel, M., Winter, H. H. (1992) Interrelation between continuous and discrete relaxation time spectra, J. Non-Newtonian Fluid Mech., 44, 15-36.

104- Provenzano, P. P., Lakes, R. S., Corr, D. T., Vanderby Jr., R. (2002) Application of nonlinear viscoelastic models to describe ligament behaviour, Biomechan. Model. Mechanobiol., 1, 45-57.

105- Segawa, W. (1961) Rheological equations of generalized Maxwell model and Voight model in three-dimensional, non-linear deformation, J. Phys. Soc. Jap., 16, 320-323.

106- Gerlach, S., Matzenmiller, A. (2005) Comparison of numerical methods for identification of viscoelastic line spectra from static test data, Int. J. Numer. Meth. Engng., 63, 428–454.

107- Rehal, D., Guo, X., Lu, X., Kassab, G. S. (2006) Duration of no-load state affects opening angle of porcine coronary arteries, Am. J. Physiol. Heart Circ. Physiol., 290, 1871-1878.

108- Rao, Y. Q., Farris, R. J. (2008) Fatigue and creep of high-performance fibres: Deformation mechanics and failure criteria, Int. J. Fatigue, 30, 793-799.

109- Bevington, P. R., Robinson, D. K. (1992) Data reduction and error analysis for the physical sciences, 2nd edition. McGraw-Hill Inc., New York, pp. 141-167.

110- Johnson, G. A., Tramaglini, D. M., Levine, R. E., Ohno, K., Choi, N. Y., Woo, S. L. Y. (1994) Tensile and viscoelastic properties of human patellar tendon, J. Orthop. Res., 12, 796-803.

111- Einat, R., Lanir, Y. (2009) Recruitment viscoelasticity of the tendon, J. Biomech. Eng., 131, 111008.

112- Burt, H., Wilshire, B. (2004) Theoretical and practical implications of creep curve shape analyses, Metal. Mater. Trans. A, 37A, 1691-1701.

113- Mijailovich, S. M., Stamenovic, D., Fredberg, J. J. (1993) Towards a kinetic theory of connective tissue micromechanics, J. App. Physio., 74, 665-681.

114- Dean, G. D., Tomlins, P. E., Read, B. E. (1995) A model for nonlinear creep and physical aging in Poly(Vinyl Chloride), Poly. Eng. Sci., 35, 1282-1289.

115- Adamczyk, M. M., Lee, T. C., Vesely, I. (2000) Biaxial strain properties of elastase-digested porcine aortic valves, J. Heart Valve Dis., 9, 445-453.

116- Adamczyk, M. M., Vesely, I. (2002) Biaxial strain distributions in explanted porcine bioprosthetic valves, J. Heart Valve Dis., 11, 688-695.

117- Aritan, S., Olutunde Oyadiji, S., Bartlett, R. M. (2008) A mechanical model representation of the in vivo creep behaviour of muscular bulk tissue, J. Biomech., 41, 2760-2765.

118- Hooley, C. J., Cohen, R. E. (1979) A model for the creep behaviour of tendon, Int. J. Biolog. Macromolecules, 1, 123-132.

119- Wren, T. A. L., Lindsey, D. P., Beaupre, G. S., Carter, D. R. (2003) Effects of creep and cyclic loading on the mechanical properties and failure of human Achilles tendons, Ann. Biomed. Eng., 31, 710-717.

120- Stella, J. A., Liao, J., Hong, Y., Merryman, W. D., Wagner, W. R., Sacks, M. S. (2008) Tissue-to-cellular level deformation coupling in cell micro-integrated elastomeric scaffolds, Biomat., 29, 3228-3236.

121- Bax, D. V., Rodgers, U. R., Bilek, M. M. M., Weiss, A. S. (2009) Cell adhesion to tropoelastin is mediated via the C-terminal GRKRK motif and integrin $\alpha_V\beta_3$, J. Biolog. Chem., 284, 28616-28623.

122- Sacks, M. S. (2003) Incorporation of experimentally-derived fiber orientation into a structural constitutive model for planar collagenous tissues, J. Biomech. Eng. 125, 280-287.

123- Ku, C-H., Johnson, P. H., Batten, P., Sarathchandra, P., Chambers, R. C., Taylor, P. M., Yacoub, M. H., Chester, A. H. (2006) Collagen synthesis by mesenchymal stem cells and aortic valve interstitial cells in response to mechanical stretch, Cardiovasc. Res., 71, 548-556.

124- Vesely, I., Nosesorthy, R. (1992) Micromechanics of the fibrosa and the ventricularis in aortic valve leaflets, J. Biomech., 25, 101-113.

125- Love, A. E. H., A treatise on the mathematical theory of elasticity, 1944, Dover Publications, New York, pp. 132.

126- Toupin, R. A. (1965) Saint-Venant's principle, Arch. Rational Mech. Anal., 18, 83-96.

127- Arridge, R. G. C., Folkes, M. J. (1976) Effect of sample geometry on the measurement of mechanical properties of anisotropic materials, Polymer, 17, 495-500.

128- Knowles, J. K. (1966) On Saint-Venant's principle in the two-dimensional linear theory of elasticity, Arch. Rational Mech. Anal., 21, 1-22.

129- Horgan, C. O. (1972) On Saint-Venant's principle in plane anisotropic elasticity, J. Elasticity, 2, 169-180.

130- Cross, M. M. (1979) Relation between viscoelasticity and shear-thinning behaviour, Rheol. Acta, 18, 609-624.

131- Waldman, S. D., Lee, J. M. (2002) Boundary conditions during biaxial testing of planar connective tissue. Part 1: Dynamic behaviour, J. Mater. Sci.: Mater. Med., 13, 933-938.

132- Waldman, S. D., Sacks, M. S., Lee, J. M. (2002) Boundary conditions during biaxial testing of planar connective tissue. Part II: Fiber orientation, J. Mater. Sci. Let., 21, 1215-1221.

133- Sun, W., Sacks, M. S. (2005) Effects of boundary conditions on the estimation of the planar biaxial mechanical properties of soft tissues, J. Biomech. Eng., 127, 709-715.

134- Jimenez, M. L., Brown, T. D., Brand, R. A. (1989) The effects of grip proximity on perceived local *in vitro* tendon strain, J. Biomech., 22, 949-955.

135- Waldman, S. D., Lee, J. M. (2005) Effect of sample geometry on the apparent biaxial mechanical behaviour of planar connective tissues, Biomat., 26, 7504-7513.

136- Driessen, N. J. B., Bouten, C. V. C., Cox, M. A. J., Baaijens, F. P. T. (2008) Remodelling of the angular collagen fiber distribution in cardiovascular tissues, Biomechan. Model Mechanobiol., 7, 93-103.

137- Carew, E. O., Talman, E. A., Boughner, D. R., Vesely, I. (1999) Quasi-Linear viscoelastic theory applied to internal shearing of porcine aortic valve leaflets, J. Biomech. Eng., 121, 386-392.

138- Mase, G. T., Mase, G. E., Continuum mechanics for engineers, 2nd edition, 2000, CPC Press, Florida.

139- Choi, I., Horgan, C. O. (1977) Saint-Venant's principal and end effects in anisotropic elasticity, J. Appl. Mech., 44, 424- 430.

140- Nyashin, Y., Lokhov, V., Kolenda, J. (2007) On the stress-strain relations in viscoelastic solids, Mar. Technol. Trans., 18, 75-84.

141- Beer, F. P., Johanston, E. R., Mechanics of materials, 2nd edition, 1992, McGraw-Hill Inc., London, pp. 353-366.

142- Popov, E. P., Mechanics of materials, 2nd edition, 1996, Prentice-Hall Inc., New Jersey, pp. 43-45.

143- Lanir, Y. (1979) A structural theory for the homogeneous biaxial stress-strain relationships in flat collagenous tissues, J. Biomech., 12, 423-436.

144- Sacks, M. S. (2000) Biaxial mechanical evaluation of planar biological materials, J. Elasticity, 61, 199-246.

145- Sacks, M. S., Sun, W. (2003) Multiaxial mechanical behavior of biological materials, Annu. Rev. Biomed. Eng., 5, 251-284.

146- Engelmayr Jr., G. C., Sacks, M. S. (2006) A structural model for the flexural mechanics of nonwoven tissue engineering scaffolds, J. Biomech. Eng., 128, 610-622.

147- Lanir, Y. (1983) Constitutive equations for fibrous connective tissues, J. Biomech. 16, 1-12.

148- Woo, S. L-Y., Johnson, G. A., Smith, B. A. (1993) Mathematical modeling of ligaments and tendons. J. Biomech. Eng., 115, 468-473.

149- Fisén, M., Mägi, M., Sonnerup, L., Viidik, A. (1969) Rheological analysis of soft collagenous tissue, Part I: Theoretical considerations, J. Biomech., 2, 13-20.

150- Fisén, M., Mägi, M., Sonnerup, L., Viidik, A. (1969) Rheological analysis of soft collagenous tissue, Part II: Experimental evaluations and verifications, J. Biomech., 2, 21-28.

151- Diamant, J., Keller, A., Baer, E., Litt, M., Arridge, R. G. C. (1972) Collagen; ultrastructure and its relation to mechanical properties as a function of ageing, Proc. R. Soc. Lond. B, 180, 293-315.

152- Katz, J. L. (1971) Hard tissue as a composite material, I: Bounds on the elastic behaviour, J. Biomech., 4, 455-473.

153- Freed, A. D., Doehring, T. C. (2005) Elastic model for crimped collagen fibrils, J. Biomech. Eng., 127, 587-593.

154- Grytz, R., Meschke, G. (2009) Constitutive modeling of crimped collagen fibrils in soft tissues, J. Mech. Behav. Biomed., 2, 522-533.

155- Aspden, R. M. (1994) Fibre reinforcing by collagen in cartilage and soft connective tissues, Proc. R. Soc. Lond. B, 258, 195-200.

156- Bischoff, J. E. (2006) Continuous versus discrete (invariant) representations of fibrous structure for modelling non-linear anisotropic soft tissue behaviour, Int. J. Non-Linear Mech., 41, 167-179.

157- Hurschler, C., Loitz-Ramage, B., Vanderby Jr., R. (1997) A structurally based stress-stretch relationship for tendon and ligament, J. Biomech. Eng., 119, 392-399.

158- Cowan, G. (1998) Statistical data analysis, Oxford university press, Oxford.

159- Sasaki, N., Odajima, S. (1996) Elongation mechanism of collagen fibrils and force-strain relations of tendon at each level of structural hierarchy, J. Biomech., 29, 1131-1136.

160- Cortes, D. H., Lake, S. P., Kadlowee, J. A., Soslowsky, L. J., Elliot, D. M. (2010) Characterising the mechanical contribution of fibre angular distribution in connective tissue: comparison of two modelling approaches, Biomech. Model Mechanobiol., 9, 651–658.

161- James, H. M., Guth, E. (1943) Theory of the elastic properties of rubber, J. Chem. Phys., 11, 455-481.

162- Treloar, L. R. G. (1954) The photoelastic properties of short-chain molecular networks, Trans. Faraday Soc., 50, 881-896.

163- Bischoff, J. E., Arruda, E. M., Grosh, K. (2002) Orthotropic hyperelasticity in terms of an arbitrary molecular chain model, J. Appl. Mech., 69, 198-201.

164- Elias-Zuniga, A., Beatty, M. F. (2002) Constitutive equations for amended non-Gaussian network models of rubber elasticity, Int. J. Eng. Sci., 40, 2265-2294.

165- Kuhl, E., Garikipati, K., Arruda, E. M., Grosh, K. (2005) Remodeling of biological tissue: mechanically induced reorientation of a transversely isotropic chain network, J. Mech. Phys. Solids, 53, 1552-1573.

166- Zhang, Y., Dunn, M. L., Drexler, E. S., McCowan, C. N., Slifka, A. J., Ivy, D. D., Shandas, R. (2005) A microstructural hyperelastic model of pulmonary arteries under normo- and hypertensive conditions, Annals Bioemd. Eng., 33, 1042-1052.

167- Cohen, A. (1991) A Padé approximant to the inverse Langevin function, Rheol. Acta, 30, 270-273.

168- Miehe, C. (2003) Computational micro-to-macro transitions for discretized micro-structures of heterogeneous materials at finite strains based on the minimization of averaged incremental energy, Comput. Methods Appl. Mech. Eng., 192, 559-591.

169- Arruda, E. M., Boyce, M. C. (1993) A three-dimensional constitutive model for the large stretch behavior of rubber elastic materials, J. Mech. Phys. Solids, 41, 389-412.

170- Boyce, M. C., Arruda, E. M. (2000) Constitutive models of rubber elasticity: a review. Rubber Chem. Technol., 73, 504-523.

171- Tseng, H, Grande-Allen, K. J., (2011) Elastic fibers in the aortic valve spongiosa: a fresh perspective on its structure and role in overall tissue function, Acta Biomater., Doi: 10.1016/j.actbio.2011.01.022.

172- Zou, Y., Zhang, Y. (2009) An experimental and theoretical study on the anisotropy of elastin network, Annals Bioemd. Eng., 37, 1572-1583.

173- Treloar, L. R. G. (1975) The physics of rubber elasticity, 3rd Edition, Clarendon Press, Oxford.

174- Sarver, J. J., Robinson, P. S., Elliott, D. M. (2003) Methods for quasi-linear viscoelastic modelling of soft tissue: application to incremental stress-relaxation experiments, J. Biomech. Eng., 125, 754-758.

175- Pinto, J. G., Patitucci, P. J. (1980) Visco-elasticity of passive cardiac muscle, J. Biomech. Eng., 102, 57-61.

176- Rajagopal, K. R., Wineman, A. S. (2008) A quasi-correspondence principle for quasi-linear viscoelastic solids, Mech. Time-Depend. Mater., 12, 1-14.

177- Pipkin, A.C., Rogers, T. G. (1968) A non-linear integral representation for viscoelastic behaviour, J. Mech. Physic. Solids, 16, 59-72.

178- Lanir, Y. (1986) On the structural origins of the quasilinear viscoelastic behaviour of tissues, in: Schmid-Schonbein, G. W., Woo, S. L-Y., Zweifach, B. W. (Eds.), Frontiers in biomechanics, pp:130-136, Springer-Verlag New York Inc.

179- Sacks, M. S. (2001) The biomechanical effects of fatigue on the porcine bioprosthetic heart valve, J. Long. Term Eff. Med. Implants, 11, 231-247.

180- Suki, B., Barabasi, A-L., Lutchen, K. R. (1994) Lung tissue viscoelasticity: a mathematical framework and its molecular basis, J. Appl. Physiol., 76, 2749-2759.

181- Yoshioka, N., Obata, Y., Kawai, H. (1967) Theoretical approaches to the mechanical relaxation mechanisms in semicrystalline polymers, J. Macromol. Sci-Phys., B1, 567-585.

182- Fricker, H. S. (1973) On the theory of stress relaxation by cross-link reorganization, Proc. R. Soc. Lond. A., 335, 289-300.

183- Kapnistos, M., Lang, M., Vlassopoulos, D., Pyckhout-Hintzen, W., Richter, D., Cho, D., Chang, T., Rubinstein, M. (2008) Unexpected power-law stress relaxation of entangled ring polymers, Nature Mater., 7, 997-1002.

184- Meng, X., Ao, L., Song, Y., Babu, A., Yang,X., Wang, M., Weyant, M. J., Dinarello, C. A., Cleveland, Jr., J. C., Fullerton, D. A. (2007) Expression of functional Toll-like receptors 2 and 4 in human aortic valve interstitial cells: potential roles in aortic valve inflammation and stenosis, Am. J. Physiol. Cell Physiol., 294, C29-C35.

185- Crank, J. (1979) The mathematics of diffusion, 2nd edition, Oxford University Press, London, UK.

186- Akin, J. E. (1994) Finite elements for analysis and design, p: 223, Academic Press INC, San Diego, California.

187- Purslow, P. P., Wess, T. J., Hukins, D. W. L. (1998) Collagen orientation and molecular spacing during creep and stress-relaxation in soft connective tissue, J. Exp. Biol., 201, 135-142.

188- Mosler, E., Folkhard, W., Knorzer, E., Nemetschek-Gansler, H., Nemetschek, T. (1985) Stress-induced molecular rearrangement in tendon collagen, J. Molec. Biol., 182, 589-596.

189- Prot, V., Skallerud, B., Sommer, G., Holzapfel, G. A. (2010) On modelling and analysis of healthy and pathological human mitral valves: Two case studies, J. Mech. Behave. Biomed. Mat., 3, 167-177.

190- Aspden, R. M., Hukins, D. W. L. (1985) Composition and properties of connective tissues, Trends Biochem. Sci., 10, 260-264.

191- 159- Billiar, K. L., Sacks, M. S. (1997) A Method to quantify the fiber kinematics of planar tissues under biaxial stretch, J. Biomech., 30, 753–756.

192- Gupta, H. S., Seto, J., Krauss, S., Boesecke, P., Screen, H. R. C. (2010) *In situ* multi-level analysis of viscoelastic deformation mechanisms in tendon collagen, J. Struc. Biol., 169, 183-191.

193- Zimmerman, W-H., Eschenhagen, T. (2003) Tissue engineering of aortic heart valves, Cardiovasc. Res., 60, 460-462.

194- Yacoub, M. H., Takkenberg, J. J. M. (2005) Will heart valve tissue engineering change the world?, Nat. Clin. Prac. Cardiovasc. Med., 2, 60-61.

195- Guilak, F. (2000) Functional tissue engineering - The role of biomechanics in reparative medicine, Ann. N. Y. Acad. Sci., 961, 193-195.

196- Butler, D. L., Goldstein, S. A., Guilak, F. (2000) Functional tissue engineering: the role of biomechanics, J. Biomech. Eng., 122, 570-575.